

A Viscoelastic Model for High Strain Rate Loading of the Human Calvarium

A Viscoelastic Model for High Strain Rate Loading of the Human Calvarium

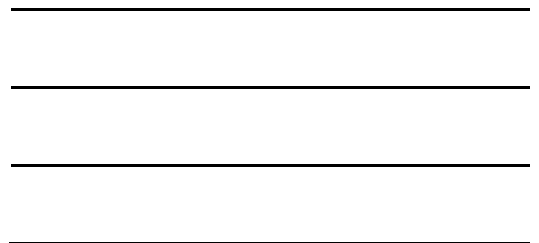
Sourabh Boruah
Guwahati, Assam, India

Bachelor of Technology, Indian Institute of Technology, Guwahati, 2008

A Dissertation presented to the Graduate Faculty
of the University of Virginia in Candidacy for the Degree of
Doctor of Philosophy

Department of Mechanical and Aerospace Engineering

University of Virginia
May, 2016



APPROVAL SHEET

The dissertation
is submitted in partial fulfillment of the requirements
for the degree of
Doctor of Philosophy

Norman Bourke P.

AUTHOR

The dissertation has been read and approved by the examining committee:

[Signature]

Advisor

[Signature]

[Signature]

[Signature]

[Signature]

[Signature]

Accepted for the School of Engineering and Applied Science:

CCB

Craig H. Benson, Dean, School of Engineering and Applied Science

August

2016

Acknowledgements

I would like to express my wholehearted appreciation towards my advisor Dr. Jeff Crandall for the patient guidance and strategic advice he has provided throughout my time as a graduate student. I would like to acknowledge Dr. Robert Salzar, for the continuous support and supervision, the painstaking review of my writing, and most importantly, for the professional freedom he has allowed. I appreciate Dr. Damien Subit, for sharing his research experience and expertise, and dispensing pleasant humor. I would like to thank Dr. Barry Shender for recognition of the importance of this research. This research was sponsored by the U.S. Naval Air Warfare Center, Aircraft Division, Patuxent River, MD (contract no. N00421-11-C-0004).

I would like to recognize the immense help provided by my colleagues at the laboratory. Especially, Varun Bollapragada, Lee Gabler, and Dr. Edward Spratley, for their support in running simulations, John Christopher, Kyvory Henderson, and Jonathan Foster, for their assistance in experimentation, Ted Miller and Mark McCardell, for logistics, and Jim Bolton, and Brian Overby, for help in fabrication of test equipment. I am truly thankful to my PhD committee members, Drs. Richard Kent, Silvia Blemker, and Mark Sochor, whose thought-provoking suggestions, constructive criticism and friendly counsel have directly resulted in improvement of the research.

Finally, I would like to convey my utmost gratitude to my family and friends for their support and understanding of the demands and vagaries of PhD research. Especially my wife, Ipchita, for the innumerable sacrifices she has made while I continued pursuing this degree, my parents Pradip and Kalyanee for their moral support through the trials and tribulations of graduate student life, and my sister Soujanya for the inspiration to follow the path less taken.

Abstract

Brain injury resulting from exposure to blast continues to be a significant problem in the military community. In order to understand the response of the human brain under various high-rate mechanical insults to the head, the way in which the load is transmitted through the skull must be accurately characterized. The bones of the human calvarium comprise a sandwich structure with two dense layers of cortical bone separated by porous cancellous bone. Although the high strain-rate behavior of human calvarium cortical bone has been previously studied, the viscoelasticity of the porous diploe layer has remained to be characterized. Due to the presence of fluids in the porous layer, the diploe may be expected to exhibit considerable strain-rate related stiffening and dissipative properties. The primary objective of this dissertation is to investigate the viscoelasticity of the calvarium at strain-rates characteristic of blast loading.

For modeling the stiff bending response while retaining accurate through-the-thickness response of the calvarium sandwich structure, it is essential to describe the thicknesses and mechanical properties of the individual layers. As a secondary objective, the layer thicknesses and how they vary across the calvarium, which is unavailable in the literature, was studied through micro computed tomography (μ CT) of through-the-thickness cylindrical samples (cores) from the calvarium using an objective methodology of distinction of the three layers. It was established that the outer cortical table is at an average 68% thicker than the inner.

The same cores were tested under dynamic compression and cyclic compression-tension loading (1 to 20 kHz) in the direction normal to the surface of the skull, for obtaining viscoelastic properties of the calvarium. These composite properties, which included the contribution of the two cortical layers and the diploe layer, were decomposed into effective properties of the

individual layers using geometrically accurate FE models of the composite core specimens built using their μ CT images.

Dynamic tension tests were conducted on coupon samples from the cortical layer. Two phase micro finite element (μ FE) models specific to each tested coupon, developed from their μ CT images, were used to account for specimen porosity and identify the Young's modulus of the bone phase (18.5 ± 3.5 GPa) through optimization to match the coupon structural response (12.0 ± 3.3 GPa). The cortical modulus was found to vary between the superior and inferior aspects of the calvarium. These properties were used in the cortical layers of the FE models of the cores for derivation of the effective viscoelastic properties of the diploe layer. Interestingly, the effective diploe layer quasi-static modulus (273 ± 125 MPa) and the fractional viscoelastic modulus (3.3 ± 1.2) varied between the frontal and parietal bones. The extent of viscoelastic stiffening of the porous diploe layer is much greater than that observed for cortical bone and it was capable of dissipating far more energy. The viscoelastic model of the calvarium, including the material properties and geometric measurements, developed in this study can be used by researchers to accurately model the effect of blast on the human brain for understanding the mechanism of blast-induced traumatic brain injury.

A simplified plane-strain FE model using the layer thicknesses and properties found in this study showed that viscoelasticity of the calvarium and its between subjects variation may have very little influence on brain deformation caused by blast. On the other hand variation in calvarium layer thicknesses could result in substantial change of brain deformation, caused by blast. The effect of variation in layer thicknesses was found to be comparable to the combined influence of the scalp and the cerebrospinal fluid layers.

List of papers

Paper I

Boruah, S., Paskoff, G.R., Shender, B.S., Subit, D.L., Salzar, R.S., Crandall, J.R., 2015. *Variation of bone layer thicknesses and trabecular volume fraction in the adult male human calvarium*. Bone 77, 120–34. doi:10.1016/j.bone.2015.04.031.

Paper II

Boruah, S., Subit, D.L., Paskoff, G.R., Shender, B.S., Crandall, J.R., Salzar, R.S., 2016. *Influence of bone microstructure on the mechanical properties of skull cortical bone – A combined experimental and computational approach*. J. Mech. Behav. Biomed. Mater. doi: 10.1016/j.jmbbm.2016.09.041.

Paper III

Boruah, S., Paskoff, G.R., Shender, B.S., Subit, D.L., Crandall, J.R., Salzar, R.S., 2016. *Dynamic compression response of the human calvarium diploe layer and its dependence on location*. Submitt. to J. Mech. Behav. Biomed. Mater.

Paper IV

Boruah, S., Paskoff, G.R., Shender, B.S., Crandall, J.R., Salzar, R.S., 2016. *Viscoelastic compression response of the human skull diploe layer and a viscoelastic model of the calvarium for the study of blast exposure*. Submitt. to J. Mech. Behav. Biomed. Mater.

Paper V

Boruah, S., Henderson, K., Subit, D.L., Salzar, R.S., Shender, B.S., Paskoff, G.R., 2013.

Response of human skull bone to dynamic compressive loading, in: Proc. IRCOBI Conf.

Paper VI

Boruah, S., Subit, D.L., Crandall, J.R., Salzar, R.S., Shender, B.S., Paskoff, G., 2014. *A lumped-mass model to simulate through-the-thickness transmission of vibration in the adult human skull*. in: Proc. IRCOBI Conf.

Conference presentations of included work

Boruah, S., Subit, D.L., Crandall, J.R., Salzar, R.S. *Location based variation of material properties of the adult human skull*. 83rd Annual Scientific Meeting of the Aerospace Medical Association, Atlanta, Georgia, 2012.

Boruah, S., Henderson, K., Subit, D.L., Salzar, R.S., Shender, B.S., Paskoff, G.R. *Response of human skull bone to dynamic compressive loading*, IRCOBI Conference, Gothenburg, Sweden, 2013.

Boruah, S., Subit, D.L., Crandall, J.R., Salzar, R.S., Shender, B.S., Paskoff, G., *Development of a material model to simulate through-the-thickness transmission of vibration in the adult human skull*. 10th Annual Injury Biomechanics Symposium, Columbus, Ohio, 2014.

Boruah, S., Subit, D.L., Crandall, J.R., Salzar, R.S., Shender, B.S., Paskoff, G., *A lumped-mass model to simulate through-the-thickness transmission of vibration in the adult human skull*. IRCOBI Conference, Berlin, Germany, 2014.

Contents

1	Introduction.....	1
1.1	Traumatic brain injury	1
1.2	Blast induced Traumatic Brain Injury (bTBI).....	3
1.3	Blast pressure wave.....	5
1.4	Geometry of the human cranial vault.....	6
1.5	Structure of the cranial vault.....	8
1.6	Microstructure of the calvarium.....	10
1.7	Studies of the mechanical properties of the calvarium	12
1.8	Techniques of characterization of viscoelasticity	15
1.9	Finite element models of the head	16
1.10	Brain injury models.....	18
1.11	Specific objectives	20
1.12	Summary.....	21
2	Test subjects and test specimens.....	23
2.1	Post mortem human surrogates.....	23
2.2	Sample harvest locations.....	24
2.3	Cores – Through-the-thickness cylindrical samples	26
2.4	Coupons – cuboidal specimens from the outer cortical layer	27
3	Three dimensional geometry of the calvarium and its microstructure.....	29

3.1	Objective	29
3.2	Methodology	29
3.2.1	Micro computed tomography	30
3.2.2	Use of arbitrary apparent density scale	30
3.2.3	Density distribution from μ CT and soft segmentation.....	31
3.2.4	Probabilistic crisp segmentation and Monte Carlo	32
3.2.5	Thickness estimation and curvature compensation.....	33
3.2.6	Statistics: averaging at the scale of interest and resulting expected value and uncertainty.....	35
3.2.7	Alber's projection of the skull and interpolation of measurements	36
3.3	Results.....	37
3.3.1	Gross geometry and amount of data	37
3.3.2	Monte Carlo and regional averaging.....	39
3.3.3	Cancellous layer volume fraction	47
3.4	Discussion	47
3.5	Conclusions.....	50
4	Coupon tensile tests	52
4.1	Objective	52
4.2	Methodology	52
4.2.1	Micro computed tomography	52
4.2.2	Segmentation and finite element mesh	53

4.2.3	Tensile test setup.....	56
4.2.4	Strain from image stereo-correlation	58
4.2.5	Micro FE model and optimization	58
4.3	Results.....	60
4.3.1	Linear elastic response.....	60
4.3.2	Influence of bone microstructure – Implicit finite element model.....	63
4.3.3	Variance with subject and location on the calvarium	63
4.4	Discussion	68
4.4.1	Effective properties of cortical coupons	68
4.4.2	Comparison to other studies of cortical coupons	69
4.4.3	Properties of cortical bone at the micro scale	69
4.5	Conclusions.....	70
5	Core compression tests	71
5.1	Objective.....	71
5.2	Methodology	71
5.2.1	Specimen potting	71
5.2.2	Dynamic compression test setup.....	72
5.2.3	McElhaney’s porous block model.....	73
5.2.4	Core simplified finite element model and optimization.....	76
5.2.5	Material properties and boundary conditions.....	78
5.3	Results.....	80

5.3.1	Typical compression response	80
5.3.2	Composite structural Young's modulus.....	82
5.3.3	McElhaney's porous block model.....	83
5.3.4	Simplified finite element model.....	84
5.4	Discussion	87
5.4.1	Effective modulus of the cancellous diploe layer	87
5.4.2	Current FE models	89
5.5	Conclusions.....	89
6	Core transmissibility tests	90
6.1	Objective	90
6.2	Methodology	90
6.2.1	Transmissibility test setup.....	90
6.2.2	Viscoelastic material model for the diploe.....	93
6.2.3	Experimental and FE model boundary conditions	93
6.2.4	Inertia.....	96
6.3	Results.....	96
6.3.1	Data from cyclic loading tests.....	96
6.3.2	Mesh sensitivity and viscoelasticity parameter optimization.....	98
6.3.3	Viscoelastic modulus	99
6.4	Discussion	100

6.4.1	Rationale for use of low-rate dynamic properties as quasi-static properties and choice of viscoelastic time constant.....	100
6.4.2	Comparison to other modes of testing, and need for finite element modeling	101
6.4.3	Dependence on location.....	102
6.4.4	Material loss tangent – $\tan\delta$	103
6.4.5	Comparison to in vivo blast loading	104
6.5	Conclusions.....	105
7	Simplified plane-strain finite element model of the calvarium.....	106
7.1.1	Objective	106
7.2	Methodology	106
7.2.1	Plane strain model.....	107
7.2.2	Brain tissue injury criteria.....	109
7.3	Results.....	113
7.3.1	Eulerian air mesh response	113
7.3.2	Time history of brain deformation	114
7.3.3	Peak brain deformation	117
7.4	Influence of viscoelasticity – spectral analysis	121
7.5	Discussion	123
7.5.1	Bending stiffness.....	124
7.6	Conclusions.....	127
8	Hypotheses.....	128

8.1	Variance with subject.....	128
8.1.1	H0 – Layer thicknesses do not vary between subjects.....	128
8.1.2	H0 – Mechanical properties do not vary between subjects.....	129
8.2	Variance with location	129
8.2.1	H0 – Layer thicknesses do not vary with location on the calvarium	130
8.2.2	H0 – Mechanical properties do not vary with location on the calvarium	131
8.3	Influence on blast brain injury	131
9	Limitations	132
9.1	Effect of fluid content in the diploe layer	132
9.2	Distinction of layers of the calvarium.....	133
9.3	Isotropy of the cortical and diploe layers.....	133
9.4	Assumption of linear viscoelasticity	134
10	Contributions.....	135
10.1	Methodology for layer thickness estimation.....	135
10.2	Methodology for determination of viscoelasticity in bone	135
10.3	Influence of cortical bone microstructure on its structural response	136
10.4	Dependence on location.....	136
10.5	Analysis of mechanical properties and microstructure of same samples.....	136
10.6	Integrated model of the calvarium	137
10.7	Impact of variation of properties of the calvarium on brain deformation.....	137
10.8	Summary	138

11	Future work.....	140
11.1	Detailed blast-brain FE study.....	140
11.2	Micro scale properties of trabecular bone.....	140
12	Conclusion	141
13	References.....	142
14	Appendix.....	168
14.1	Tables.....	169
14.2	Radiographic imaging	181
14.2.1	Distribution of measurements over the calvarium of each subject	181
14.2.2	Tabulated results	186
14.2.3	Statistical test results.....	196
14.3	Coupon tensile testing.....	210
14.3.1	Experimental data	210
14.3.2	Tabulated results	212
14.3.3	Statistical test results.....	230
14.3.4	Distribution of cortical layer mechanical properties over the calvarium of each subject.....	232
14.4	Micro computed tomography cross-sections of the core and coupon samples, and their mechanical properties	238
14.5	Core compression testing.....	322
14.5.1	Experimental data	322

14.5.2	Tabulated results	324
14.5.3	Statistical test results	329
14.5.4	Distribution of quasi-static modulus over the calvarium of each subject	331
14.6	Core transmissibility testing	333
14.6.1	Sample wise Force and Acceleration magnitude spectra	333
14.6.2	Resultant Modulus magnitude spectra from experiment and optimized simulations	344
14.6.3	Sample wise Force and Acceleration phase spectra	355
14.6.4	Tabulated results	366
14.6.5	Statistical test results	371
14.6.6	Distribution of viscoelastic modulus over the calvarium of each subject	373
14.7	Simplified plane-strain blast model	375
14.7.1	Shock wave propagation in Eulerian air mesh	375
14.7.2	Statistical results	377

Figures

Figure 1.1 Friedlander waveform; the ideal blast shockwave; numbers are arbitrary.	5
Figure 1.2 The human cranial vault; mid-sagittal section (Gray, 1918); box shows region of the cranial vault which does not have the sandwich structure.	8
Figure 1.3 Cylindrical core samples from the human calvarium. Section view perpendicular to skull surface showing the sandwich structure (top) and tangential to skull surface (bottom) showing lack of regular trabecular orientation.	10
Figure 1.4 Flowchart of the dissertation showing the different tasks undertaken and the various secondary objectives achieved before the accomplishment of the primary objective.	22
Figure 2.1 Sample harvest locations marked on the calvarium; through-the-thickness cylindrical samples (cores) from the right half (bottom left of this image) and cortical coupon samples from the left half of the calvarium (top right of this image).....	25
Figure 2.2 Skull core samples were obtained from the right calvarium using a circular abrasive drill press.....	26
Figure 2.3 A sample skull core.	27
Figure 2.4 0.5 mm thick cortical bone wafer being machined on a Buehler Isomet low-speed saw.	28
Figure 2.5 Cortical Bone wafers being milled.	28
Figure 2.6 Dimensions of a coupon sample (left) and A few finished coupons (right).	28

Figure 3.1 Clockwise from left; Core holder jig for μ CT of through-the-thickness samples; Cores loaded in a falcon tube for scanning; A typical μ CT slice image (parallel to calvarium surface); Image showing a transverse section reconstruction and slice direction..... 30

Figure 3.2 μ CT slice of core showing comparable measured density of cortical and trabecular bone..... 31

Figure 3.3 Typical distribution of apparent density in a skull core (blue); hypothetical distribution of bone (magenta) and pore content (green dotted); Bone probability as a function of apparent density (red broken). 32

Figure 3.4 Curvature of skull core surface indicated by partial visibility in slice; mesh-size ~ 2.25 mm; red hatched areas denote the spatial extent of core; this μ CT image is not filtered..... 34

Figure 3.5 Illustration showing location dependency of cortical layer thickness within a skull core..... 35

Figure 3.6 The average 3D shape of the cranium with azimuth and elevation isolines shown on the outer surface. Numbers at intersection of contours show azimuth, elevation angles (left). Color represents the distance of the outer cranium from the origin. Alber’s projection of the human cranium (right). The coronal, sagittal and lambdoid sutures (dotted lines) are shown. 38

Figure 3.7 Left: Average normalized distance to skull outer surface from origin (radius); Right: Standard deviation of normalized radius; These distances have been normalized to the interporion distance. Diamonds: core harvest locations, Squares: Coupon harvest locations. 39

Figure 3.8 Effects of averaging on estimated thickness from Monte Carlo simulation, showing progressive convergence (left to right) with more and more averaging. Thickness measurements (Blue circles on left axis) and their Standard deviation (Red line on right axis; log-scale)..... 40

Figure 3.9 Distribution of regional thicknesses of a typical core sample from Monte Carlo Simulations; width of the bars show the range of averaged regional thickness..... 41

Figure 3.10 Boxplot of cortical layer thicknesses, and diploe layer thickness and bone volume fraction (BVF) highlighting differences between parietal vs. frontal bones and superior vs. inferior aspects of the calvarium; box – inner quartile distance; line – 95% interval; marker – median.....	42
Figure 3.11 Histogram of ratios of outer cortical layer to inner cortical layer thickness. This distribution includes data from subject 7.	45
Figure 3.12 Contour on left: outer cortical layer thickness; right: inner cortical layer thickness; Within each plot, left: average across subjects; right: mirror image of the left showing distribution of standard deviation.....	46
Figure 3.13 Contour on left: average cancellous layer thickness across subjects; right: standard deviation.....	46
Figure 3.14 Contour on left: average cancellous layer bone volume fraction across subjects; right: standard deviation.	46
Figure 3.15 Skull thickness and diploe bone volume fraction data (near the vertex of the skull) from the literature, in chronological order.	47
Figure 4.1 Coupon holder jig for μ CT imaging (left; broken line shows slice direction) and a typical slice image of ten coupons.	53
Figure 4.2 Distribution of apparent density in a typical coupon (solid lines) and corresponding distribution in a core harvested from a symmetric location on the opposite side of the skull (dashed lines). Blue lines show total distributions and magenta lines show hypothetical distributions in the bone phase. Probability function used in segmentation is shown by the red line. Color grid on the top-right shows the binning of bone elements into different parts on the basis of their density.	55

Figure 4.3 Micro CT slice of a coupon gage area (left; color indicates bone probability: white – 0, black – 1) and corresponding two-phase FE mesh (right).	55
Figure 4.4 A multi-phase FE mesh of a coupon for studying the influence of apparent density on Young’s modulus of the bone phase. Color scale in Figure 4.2.	56
Figure 4.5 Self aligning coupon testing jig mounted on clevises of the 8874 servo-hydraulic system.	57
Figure 4.6 Tensile test setup.	57
Figure 4.7 Ten coupons before (top) and after testing (bottom). Two coupons break outside gage area (number 1 and 6 from the left).	61
Figure 4.8 Strain fields on the outer (top) and inner surface of a coupon during a typical test. Color map shows strain along the vertical axis. Failure occurred between 4.6 and 4.8 ms.....	62
Figure 4.9 Typical force (blue) and strain (green) time histories (left) and corresponding engineering stress vs. engineering strain curves (right). Solid lines show data from commencement of loading to time of failure.	62
Figure 4.10 Effective Young’s modulus and failure stress of calvarium cortical coupons as it varies with coupon bone volume fraction. Both y axes and the x axis are on logarithmic scales. 63	63
Figure 4.11 Effective structural modulus as predicted from implicit μ FE models vs. experimentally measured. A constant bone phase Young’s modulus of 18.51 GPa was used.	63
Figure 4.12 Effective structural Young’s modulus (top), failure stress (middle) and failure strain (bottom) of the outer cortical layer. Contour map on right shows mean values across different subjects and on the left shows the standard deviations.	64
Figure 4.13 Young’s modulus of calvarium cortical bone derived using empirical power law (left) and implicit FE models (right).	67

Figure 5.1 A skull core being potted (top) for mounting on the test device and two typical potted cores (bottom).	72
Figure 5.2 Compression test setup.	73
Figure 5.3 Porous block model used by (McElhaney et al., 1970).	75
Figure 5.4 Median and 95% range of through-the-thickness variation of porosity in the calvarium.	75
Figure 5.5 μ CT Cross-section image (top) and corresponding FE mesh. Red – potting, dark gray – cortical layers, light gray – diploe layer (bottom).	78
Figure 5.6 Three dimensional rendering of the FE mesh. Red – potting (elements have been shrunk for visibility), dark gray – cortical layers, light gray – diploe layer (shown as a wireframe).	78
Figure 5.7 Calvarium core samples, belonging to subject 3, before (columns 1 and 3) and after (columns 2 and 4) testing. Failure cases have been shown by the red boxes.	80
Figure 5.8 Typical force and displacement time histories in failure cases (top) and corresponding engineering stress vs. engineering strain curve (bottom).	81
Figure 5.9 Engineering stress vs. engineering strain for samples belonging to a particular subject. The response of potting material (polyester) is also shown.	82
Figure 5.10 Composite structural Young's modulus in through-the-thickness compression. Contour map on left shows mean values across different subjects and on the right shows the standard deviations.	83
Figure 5.11 Typical relationship between diploe elastic modulus and structural modulus (force response normalized to strain and cross-section area) calculated using the simplified FE model (shown in circles).	84

Figure 5.12 Effective elastic modulus of the diploe layer under compression in the normal direction. Contour map on left shows mean values across different subjects and on the right shows the standard deviations.....	86
Figure 6.1 Transmissibility Test setup; Shaker and shaker-side instruments (left); Index table and table-side instruments (right); please note that an aluminum placeholder sample is installed in the image on right.	90
Figure 6.2 Schematic of test setup; skull core specimen sandwiched between two pseudo rigid transducers consisting of mounting hardware, accelerometer and load-cell sprung mass.	91
Figure 6.3 Schematic of the test control system; the controller (LABVIEW software in PC) communicates via TCP / IP with data acquisition system and via NI-VISA with the waveform generator.	92
Figure 6.4 Illustration of methodology used for obtaining viscoelastic properties of the diploe layer of the calvarium. The diploe material is represented by the standard linear solid element with three parameters.	94
Figure 6.5 Typical results from cyclic loading tests. Magnitudes are plotted on the left and phases on the right. Horizontal axes are on a logarithmic scale.	97
Figure 6.6 Typical set of results showing force response (normalized to cross-section area and magnitude of strain) from simulation with optimized viscoelastic modulus (triangles) compared against the experimental results (circles). Magnitudes are plotted on the left and phases on the right.....	98
Figure 6.7 Viscoelastic modulus (left: absolute; right: fractional, relative to quasi-static modulus) of the cancellous diploe layer. Average values across nine subjects are shown on the contour map on the left and the standard deviations are shown on the right.	101

Figure 6.8 Variation of material loss tangent ($\tan\delta$) of the cancellous diploe layer (solid line – average values; shaded area – ± 1 S.D) compared to loss tangent of polyester potting material (broken line), loss tangent of cortical bone from human tibia (Garner et al., 1999, dashed line) and , two term Prony series (Johnson et al., 2010) fit to human calvarium cortical bone dynamic tensile tests (Wood, 1971), (dotted line).	104
Figure 7.1 Simplified Lagrangian mesh of the skull brain system used in free-field blast simulation from Panzer et al. (2012). Blast impact occurs from the anterior aspect (bottom of this image).	106
Figure 7.2 Blast overpressure time-history used in the simplified plane-strain simulations.	109
Figure 7.3 Free field and reflected pressure at blast impact location, compared to target pressure time history.	113
Figure 7.4 Pressure at different locations inside the brain (blast impact occurs in the frontal side), showing transient response (left; letters at the peaks indicate the location) and long term response (right).	115
Figure 7.5 Frequency spectrum of pressure at frontal and central brain (left). Deformation of the skull in anterior to posterior and right to left directions.....	115
Figure 7.6 Bending mode of the skull (displacement amplified by a factor of 40).	115
Figure 7.7 Von Mises stress at different locations inside the brain (left), and corresponding frequency spectra (right; letters at the peaks indicate the location).	116
Figure 7.8 Maximum shear strain at different locations inside the brain (left), and corresponding frequency spectra (right; letters at the peaks indicate the location).	116
Figure 7.9 Maximum shear strain rate at different locations inside the brain (left), and corresponding frequency spectra (right; letters at the peaks indicate the location).	116

Figure 7.10 Peak deformation metrics (from top to bottom) across the brain for the different simulation cases (from left to right). MSS – maximum shear strain; VM – Von Mises. Color scale limits are shown on right.....	120
Figure 7.11 Spectrograms of pressure in the frontal (left) and central (right) brain. From top to bottom cases DEM Q, DEM I and Median.....	122
Figure 11.1 A cross-section view of a micro FE model of a composite core specimen.	141
Figure A.1 Individual Cranial vault outer shapes	181
Figure A.2 Individual outer cortical layer thickness; left: average; right: standard error.	182
Figure A.3 Individual inner cortical layer thickness; left: average; right: standard error.	183
Figure A.4 Individual cancellous layer thickness; left: average; right: standard error.	184
Figure A.5 Individual cancellous layer bone volume fraction; left: average; right: standard error.	185
Figure A.6 Engineering stress vs. strain for coupon tensile tests combined by subject.....	210
Figure A.7 Engineering stress vs. strain for coupon tensile tests combined by location.	211
Figure A.8 Effective structural Young's modulus of cortical coupons.	233
Figure A.9 Effective structural failure stress of cortical coupons.....	234
Figure A.10 Effective structural failure strain of cortical coupons.....	235
Figure A.11 Cortical bone phase Young's modulus, as derived from BVF based power law model.	236
Figure A.12 Cortical bone phase Young's modulus, as derived from implicit micro FE models.	237
Figure A.13 Stress vs. strain for core compression tests combined by subject.....	322

Figure A.14 Stress vs. strain for core compression tests combined by location	323
Figure A.15 Effective composite through-the-thickness modulus.....	331
Figure A.16 Effective cancellous layer modulus derived using implicit FE models.....	332
Figure A.17 Effective diploe layer viscoelastic modulus (absolute values).	373
Figure A.18 Effective diploe layer viscoelastic modulus (fractional value relative to quasi-static modulus).	374

Tables

Table 1.1 Categorization of the studies in the literature pertaining to mechanical properties of the calvarium	12
Table 1.2 Brain tissue deformation metrics found to correlate with experimental brain injury in animal models	20
Table 2.1 Anthropometry of test subjects	24
Table 2.2 Descriptions of cranial landmarks used (all lie on the outer surface of the skull)	26
Table 3.1 μ CT specifications and settings	29
Table 3.2 Albers projection transformation parameters.....	37
Table 3.3 Number of subject combinations with significantly different layer thicknesses, expressed as absolute values and as ratios to total thickness, and BVF.	44
Table 3.4 Number of subjects with significantly different layer thicknesses, expressed as absolute values and as ratios to total thickness, and BVF. Strong effects are shaded.....	45

Table 4.1 Simulation matrix – coupon μ FE models run using LSDYNA implicit.....	60
Table 4.2 Linear elastic material parameters for effective tensile response of human calvarium cortical bone from this study (shown in bold) and the literature.	65
Table 4.3 Elastic modulus for bone phase at the length scale of osteons (in GPa).....	66
Table 4.4 Effective mechanical properties from this study compared to other coupon tensile studies of human cortical bone	69
Table 5.1 Simulation matrix – core simplified FE models run using LSDYNA implicit for identification of quasi-static modulus.....	85
Table 5.2 Linear elastic modulus for the effective response of porous bone under compression from this study (shown in bold) and the literature (in MPa).....	87
Table 5.3 Diploe elastic modulus from this study (shown in bold) and diploe layer thickness compared to values used in current head FE models.	89
Table 6.1 Simulation matrix – core simplified FE models run using LSDYNA explicit for identification of viscoelastic parameters.....	99
Table 6.2 Optimized standard linear solid model parameters. (± 1 S.D. are shown).....	99
Table 7.1 Linear viscoelastic materials used for the scalp and the brain in the simplified plane strain model.....	110
Table 7.2 Layer thickness and material parameters used in plane-strain free-field blast simulation cases.	111
Table 7.3 Brain deformation metrics tested as hypothetical brain injury criteria.	112

Table 7.4 Predictor variables used in linear model for each simulation case.	118
Table 7.5 Statistics of linear model fit to the simulation data to predict stress based deformation metrics.....	119
Table 7.6 Statistics of linear model fit to the simulation data to predict strain based deformation metrics.....	121
Table 7.7 Linear model coefficients expressed as percentage of intercept.	122
Table 7.8 Case wise peak reflected overpressure and maximum peak brain pressure in kPa.	123
Table 7.9 Average values of stiffness under pure bending of the calvarium from the literature.	126
Table A.1 Summary of trabecular diploe or skull composite mechanical studies.	169
Table A.2 Summary of skull cortical layer mechanical studies.....	172
Table A.3 Summary of current head FE models.....	175
Table A.4 Summary of head / brain injury studies.	177
Table A.5 Format of sample unique identification numbers.....	180
Table A.6 List of core samples and their harvest locations.	186
Table A.7 List of core samples and their microstructural parameters.	191
Table A.8 Results of normality tests (p-values from Shapiro-Wilk test) of layer thicknesses and diploe layer BVF measurements for each subject.....	196
Table A.9 Significance (p-values from non-parametric Wilcoxon rank sum test) of difference in layer thickness and diploe layer bone volume fraction measurements between frontal and parietal bones.	197
Table A.10 Difference in median values of layer thickness (mm) and diploe layer bone volume fraction between the frontal and parietal bones.	198

Table A.11 Significance (p-values from non-parametric Wilcoxon rank sum test) of difference in layer thickness and diploe layer bone volume fraction measurements between the superior and inferior aspects of the calvarium.	199
Table A.12 Difference in median values of layer thickness (mm) and diploe layer bone volume fraction between the superior and inferior aspects of the calvarium.	200
Table A.13 Significance (p-values from non-parametric Wilcoxon rank sum test) of difference in ratios of layer thicknesses to total thickness between parietal and frontal bones and the superior and inferior aspects of the calvarium.	201
Table A.14 Difference in median values of ratios of layer thicknesses to total thickness between parietal and frontal bones and the superior and inferior aspects of the calvarium.	202
Table A.15 Significance (top right half, p-values from non-parametric Wilcoxon rank sum test) of difference and, difference in median values (bottom left half in mm) of outer cortical layer thicknesses between subjects.	203
Table A.16 Significance (top right half, p-values from non-parametric Wilcoxon rank sum test) of difference and, difference in median values (bottom left half in mm) of diploe layer thicknesses between subjects.	204
Table A.17 Significance (top right half, p-values from non-parametric Wilcoxon rank sum test) of difference and, difference in median values (bottom left half in mm) of inner cortical layer thicknesses between subjects.	205
Table A.18 Significance (top right half, p-values from non-parametric Wilcoxon rank sum test) of difference and, difference in median values (bottom left half) of diploe layer BVF between subjects.....	206
Table A.19 Significance (top right half, p-values from non-parametric Wilcoxon rank sum test) of difference and, difference in median values (bottom left half) of ratios of outer cortical layer thickness to total thickness between subjects.	207

Table A.20 Significance (top right half, p-values from non-parametric Wilcoxon rank sum test) of difference and, difference in median values (bottom left half in mm) of ratios of diploe layer thicknesses to total thickness between subjects.	208
Table A.21 Significance (top right half, p-values from non-parametric Wilcoxon rank sum test) of difference and, difference in median values (bottom left half in mm) of ratios of inner cortical layer thickness to total thickness between subjects.	209
Table A.22 List of coupon samples and their harvest locations.	212
Table A.23 Repetitions at same location and failure outside gage-area status for each coupon sample.	218
Table A.24 List of coupon samples and their mechanical properties.	224
Table A.25 Results of normality tests (p-values from Shapiro-Wilk test) of mechanical properties of the calvarium cortical layer for each subject.	230
Table A.26 Results of one-way ANOVA tests of mechanical properties of the calvarium cortical layer.	231
Table A.27 List of core samples and their quasi-static mechanical properties.	324
Table A.28 Results of normality tests (p-values from Shapiro-Wilk test) of quasi-static mechanical properties of the core samples for each subject.	329
Table A.29 Results of one-way within subjects ANOVA tests of quasi-static mechanical properties of the core samples.	330
Table A.30 List of core samples and their viscoelastic properties.	366
Table A.31 Results of normality tests (p-values from Shapiro-Wilk test) of viscoelastic modulus of the diploe layer for each subject.	371
Table A.32 Results of one-way within subjects ANOVA tests of viscoelastic modulus of the diploe layer.	372
Table A. 33 Case wise spatial distributions (as percentiles) of peak pressure [kPa]	377

Table A. 34 Case wise spatial distributions (as percentiles) of peak Von-Mises stress [kPa].....	378
Table A. 35 Case wise spatial distributions (as percentiles) of peak maximum shear strain [%]	379
Table A. 36 Case wise spatial distributions (as percentiles) of peak maximum shear strain rate [s ⁻¹].....	380

Equations

Equation 4.1 Power law relationships.....	62
Equation 5.1 McElhaney's porous block model	74
Equation 5.2 McElhaney's porous block model extended for peak stress and strain	76
Equation 7.1 Formulae for calculation of chosen brain deformation metrics	113
Equation 7.2 Stiffness under pure bending as a function of homogenized effective modulus	125
Equation 7.3 Stiffness under pure bending as a function of heterogenous modulus	125

1 Introduction

Prevention and mitigation of head injuries require the knowledge of the mechanical behavior of the head. Impact experiments have been conducted on the whole human head by various researchers in an attempt to relate kinematic indicators of impact to head injury, inclusive of skull fractures and brain injury (Got et al., 1978; Hodgson et al., 1970; Nahum et al., 1968). The earliest studies to characterize the mechanical response of the various components of the head, including the skull, were motivated by the requirement to identify artificial materials for the development of physical models of the head, to be used as test devices for assessment of head injury potential. The development of complex mathematical models of the head using digital computers and numerical methods has only expanded the scope and value of the description of mechanical response of the various components of the skull. However, the creation of advanced computational models of the head requires better knowledge of the link between bone microstructure and its mechanical behavior to ultimately predict the risk of injury not only to the skull, but also to the other components of the head.

1.1 Traumatic brain injury

Traumatic Brain Injury (TBI) is an important public health problem in the United States (Faul et al., 2010) and across the world. 2.6 million TBIs occurred among the United States civilian population in 2010. Over the past decade, percentage of ER visits has been on the rise while the percentages of hospitalization and death have been declining (Centers for Disease Control and Prevention, NCIPC, Atlanta, GA). This apparent change in outcome could be caused by changes in injury codification, improvements in diagnostic technologies, or more importantly improvements in preventive devices and medical evacuation and treatment (Ghajar, 2000; Zasler et al., 2012). It was estimated in 1996, that globally at least 10 million TBIs occur annually that

were serious enough to lead to death or hospitalization and that 62% of the global TBI related outcomes were caused by road traffic accidents (Murray and Lopez, 1996).

Among the military population in the United States, incidences of TBIs have been on the decline since the 90s (Summers et al., 2009); however, an unusual form of brain injury is surfacing within this community. In the last decade (2000 – 2010) there were 178,876 cases of TBI in the U. S. military and 95% of these cases were closed head injuries (Fischer, 2010). Exposure to explosive blasts caused 80 to 90% of injuries sustained by soldiers in Iraq (Hoge et al., 2008) from Improvised Explosive Devices (IEDs) or mines. The fact that a large fraction of survivors were diagnosed with Post Traumatic Stress Disorder (PTSD) (Hoge et al., 2008), is another unusual characteristic of this group. Researchers have found that the pathobiology of blast induced TBI (bTBI) is significantly different from other classical types of brain injury, like impact induced brain injury (Cernak and Noble-Haeusslein, 2010; Mac Donald et al., 2011), and involve significant axonal trauma and white matter disruptions which have been detected by advanced techniques like Diffusion Tensor Imaging (DTI). Due to the rampant prevalence of bTBI amongst Iraq veterans, it has been called the “signature wound” of the war in Iraq (Elder and Cristian, 2009; Ling et al., 2009). bTBI is not limited to military personnel. Civilians in current and former war zones are frequently injured by landmines and unexploded ordnance (Bilukha et al., 2008). Also, more and more civilians have become victims in terrorist attacks where explosive weapons were used. Exposure to blast may cause instant death or injuries. It may also cause latent injuries that manifest symptoms much later. Bulk of the blast injury research has been in the area of thoracic injury owing to the large number of fatalities in the world wars due to injuries to lungs or bowel or other air containing organs. In all of these cases the thoracic organs were severely injured without any external indication. Researchers have identified the cause of such injuries as the blast shock front being transmitted into the body and not due to gross compression of the

thorax, and have succeeded in designing countermeasures that use stress wave decoupling (Cooper, 1996; Cooper et al., 1991; Cripps and Cooper, 1996). However, there is dearth of knowledge regarding mechanism of blast induced brain injury. Devastating axonal damage with the absence of external indications such as head penetration suggests that the mechanism of injury may be similar to blast induced thoracic injury, with direct transmission of the shock front into the cranial vault being the causative agent.

1.2 Blast induced Traumatic Brain Injury (bTBI)

Blast injuries can be classified into three groups by cause; primary blast injury is caused by the blast stress wave travelling through the body; secondary blast injury is caused by projectiles that have been launched by the explosion; and tertiary blast injury is caused by the head impacting another object. The mechanisms of brain injury associated with the secondary and tertiary forms of blast injury are similar to the mechanisms involved in automotive accidents or assault, which are more commonly seen in the civilian population. These mechanisms have been studied extensively through experimentation (Gurdjian and Lissner, 1961; Gurdjian et al., 1968, 1966; Nahum and Smith, 1976; Stalnaker et al., 1977b) and numerical modelling (Deck and Willinger, 2008; Kleiven, 2006). The primary mode of blast injury to the brain, however, has not been studied thoroughly and is a subject of intensive research. Primary bTBI usually occurs in combination with secondary and tertiary modes of injury; therefore, it is extremely difficult to obtain clinical cases where only primary blast injury has occurred.

Clinical outcomes of primary blast brain injury range from short periods of confusion to severe coma. Severe primary bTBI injuries, such as skull fractures and hematoma, may be apparent through traditional imaging like computed tomography (CT) and magnetic resonance imaging (MRI). The mild injuries are difficult to detect even with high resolution imaging. Diffuse trauma to the brain may manifest in the form of diffuse cerebral edema indicating disruption of the

blood-brain barrier (BBB) (Chen and Huang, 2011; Ling et al., 2009; Unterberg et al., 2004), or lowered fractional anisotropy in diffusion tensor imaging (DTI) indicating disruption of white matter (Davenport et al., 2012; Jorge et al., 2012; Magnuson et al., 2012). The causative agent of injury is the stress that is transmitted into the cranial vault, either through vasculature, or through the skull itself, and injury occurs within a short time from exposure (few milliseconds) even before gross motion of the head is established. The specific cause of injury, whether dilation (including cavitation) (Denny-Brown and Russell, 1940; Gross, 1958; Lubock and Goldsmith, 1980; Stålhammar and Olsson, 1975; Stålhammar, 1975a, 1975b; Suh et al., 1972) or shear (Gurdjian and Lissner, 1961; Holbourn, 1943; Strich, 1961) of nerve tissue is a topic of debate and, finite element (FE) models of the head are already playing a crucial role in this research (Panzer et al., 2013). For accurate numerical simulation of blast exposure of the head, it is essential to understand the geometry and material properties of the entire head, including the skull and the brain. The study of bTBI will undoubtedly require the knowledge of the mechanical behavior of the calvarium at high strain rates. Apart from the potential of FE models as tools for studying injury mechanisms, due to the unrepeatable, expensive and time-consuming nature of cadaver studies, FE models of the human body have been used as a tool for safety assessment in the automotive and military industry. They also find use in the medical industry for design and simulation of medical procedures like surgery and devices like prosthetics. Correct geometry and material response properties of the head, including knowledge of the variation of these properties, are a requirement for the accurate modelling of the head.

1.3 Blast pressure wave

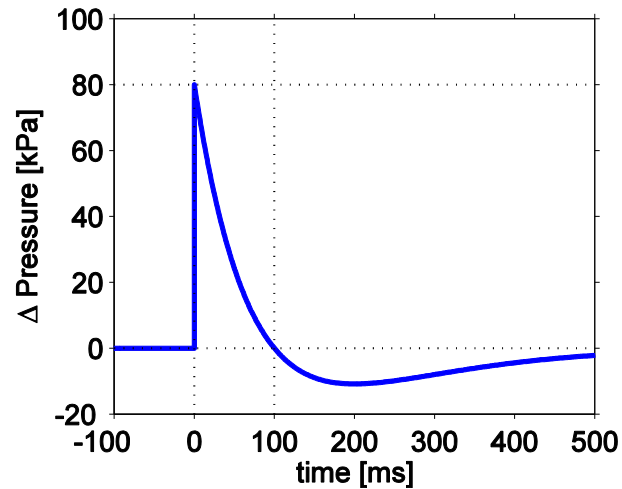


Figure 1.1 Friedlander waveform; the ideal blast shockwave; numbers are arbitrary.

The suitability of material properties depends on the type of loading; therefore, it is important to study the boundary conditions on the skull in a blast scenario. The ideal blast pressure wave involves a positive step in pressure followed by decay to pressures lesser than the initial pressure. This wave is called the Friedlander waveform. Figure 1.1 shows a Friedlander wave with a peak overpressure of 80 kPa and positive phase duration of 100 ms. The discontinuity in the ideal blast wave results in an infinitely wide frequency spectrum; however, due to interactions with the surroundings, the high-frequency contents are attenuated rapidly (Chandra et al., 2012). Data from strain gages affixed to skulls in shock tube studies show significant energy content at frequencies of up to 20 kHz (Chafi et al., 2011; Ganpule et al., 2012), after transmission through the scalp.

The material properties used in an FE model designed to study effects of blast must use material models that can predict response at such large deformation rates. Viscoelasticity may play a big role in the response through stiffening of the skull and also through damping. Research of the viscoelasticity of bone has been confined to pure cortical bone and the viscoelasticity of the skull

has not been studied. The presence of porous trabecular bone may result in skull bone having significantly different viscoelastic properties as compared to cortical bone.

In addition to the material properties used for skull bone, the skull geometry can be expected to play a large role in the response to blast. The skull is not perfectly spherical and homogenous. Also, because of the time and space dependent nature of the blast pressure wave, the pressure exerted at the various points on the skull at any given instant will be different. Due to these two reasons, in addition to compression along the normal direction, the skull may undergo significant bending (Moss et al., 2009). Stiffness of the dense cortical layers which are present on the inner and outer surface of the cranial vault will regulate the bending mode of deformation.

1.4 Geometry of the human cranial vault

The human skull has been studied and measured since the beginning of the nineteenth century. Historically, these studies have been motivated by anthropological questions, such as correlation of measurements with growth, race, and evolution, or medical questions, such as correlation with pathological conditions (Gould, 1993; Haggare and Rönning, 1995; Haller, 1970; Huxley, 1867; Kosif et al., 2013; Krogman, 1951; Relethford, 2010; White et al., 2003). Special devices were built in the 1910s to aid location of landmarks both inside and outside the anthropoid skull (Keith, 1910). The most comprehensive study of the variation of cranial morphology in humans was done by Howells (1973). More than 1,000 skulls were studied with almost a hundred measurements for each. The early studies have always used two dimensional (2D) measurements and have focused on distances and angles between landmarks. A device to capture the three dimensional (3D) shape of the cranium was developed by Oyen and Walker (1977) and christened the “stereoplotting craniostat.” He also introduced the idea of representing cranial measurements on a 2D figure. With the advent of computed tomography (CT), studying the 3D shape of the skull was simplified. Mathematical models of the head in injury studies have utilized CT for their 3D

geometrical description, but they have always been based on the skull of a unique individual (Ackerman, 1998; Gayzik et al., 2011). Current literature addressing the three dimensional shape of the human cranium and its variation in the population is extremely limited.

The three dimensional geometry of the human head can be derived from imaging using multiple modalities such as X-ray computed tomography (CT), magnetic resonance imaging (MRI) and microtomy. A multi-modality approach allows discerning of the various components of the head which is not entirely possible using a single modality. The Visible Human Project has been used by many researchers as the source for 3D morphological data of the human body (Collins et al., 1998; Spitzer and Whitlock, 1998). Because of the time consuming nature of such imaging studies, they are often augmented by anthropometric studies (Gordon et al., 1989) which can provide a statistical distribution of geometrical parameters in the population. A more recent study Gayzik et al. (2011) uses an individual more closely resembling the 50th percentile male. In human safety research, the importance of the three dimensional shape of the cranium has only recently been acknowledged (Lee et al., 2014).

1.5 Structure of the cranial vault

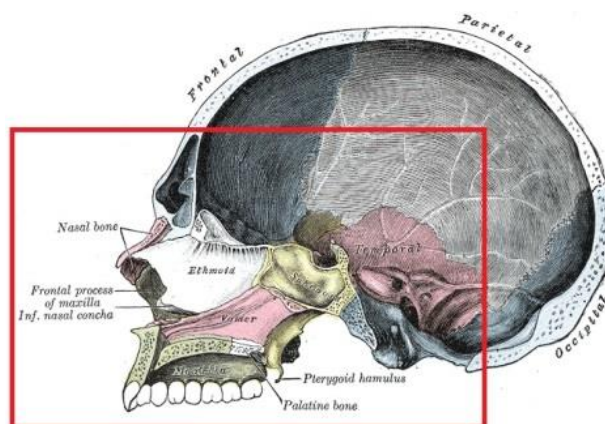


Figure 1.2 The human cranial vault; mid-sagittal section (Gray, 1918); box shows region of the cranial vault which does not have the sandwich structure.

Apart from the maxillofacial region and the foramen magnum (box in Figure 1.2), the cranial vault is composed of three layers. Two dense layers of cortical bone on the inner and outer surface of the cranial vault, called the cortical tables, are separated by a porous layer of cancellous bone called the diploe. The thicknesses of these layers determine the rigidity of the cranial vault and are particularly important for accurate mathematical modelling of the head. Several studies have looked at the variation of total thickness, but the number of studies regarding the thicknesses of the individual layers is very limited.

Todd (1924) observed the total cranial thickness at four cranial landmarks and their relationship with age. It was observed that cranial thickness increases with age until around 60 years of age. Todd also notes the remarkable variability in thickness. McElhaney et al. (1970) determined layer thicknesses from 180 specimens harvested from 14 donors. They noted that the diploe layer was thicker away from the sutures. However, the regional variation of this thickness and the strategy of measurement were not discussed. Ross et al. (1976) found that skulls of women were significantly thicker than men. All of these measurements have been made at the plane of

dissection using calipers, with or without photography and averaging. Similar visual techniques are still in use (de Souza Fernandes et al., 2011; Hodgson et al., 1970; Hwang et al., 1997; Ishida and Dodo, 1990; Jung et al., 2003; Lynnerup, 2016; Moreira-Gonzalez et al., 2006; Pensler and McCarthy, 1985; Peterson and Dechow, 2002; Sullivan and Smith, 1989). In addition to the limited number of points on the skull where thickness has been measured, there is no clear and precise methodology, beyond visual inspection, for distinguishing the different layers. Due to this, the measurements for the different layers may be very subjective. Thickness measurement of the skull has also been done using X-Ray and magnetic resonance imaging (Adeloye et al., 1975; Anzelmo et al., 2015; Baer and Harris, 1969; Baral et al., 2014; Hatipoglu et al., 2008; Lillie et al., 2015; Lynnerup et al., 2005; Sabancioğulları et al., 2013, 2012). Lynnerup et al. (2005) found that diploe layer thickness in the frontal bone is significantly greater in males than in females. Ultrasound methods have also been used for thickness measurement (Elahi et al., 1997; Ruan and Prasad, 2001; Tretbar et al., 2009). The objective of these studies was to find any correlation between thickness and age, sex, race, or general body build in order to exploit this relationship usually in forensic or anthropological studies, or to explore the cranium to find suitable donor sites for harvesting bone grafts. The mechanical response of the cranium may be highly sensitive to the presence of pores in the material. Therefore development of a mathematical model of the head that describes its mechanical response requires a more detailed and objective study of the thicknesses of the different layers of the skull. No systematic and objective study of cranial vault thickness across the calvarium exists in the literature. The advent of micro CT (μ CT) has offered much greater resolution, allowing detection of much smaller pores and discerning of individual bone trabeculae in porous bone. Lillie et al. (2015) have used μ CT imaging to validate a new approach to determine cortical layer thickness from clinical CT.

1.6 Microstructure of the calvarium

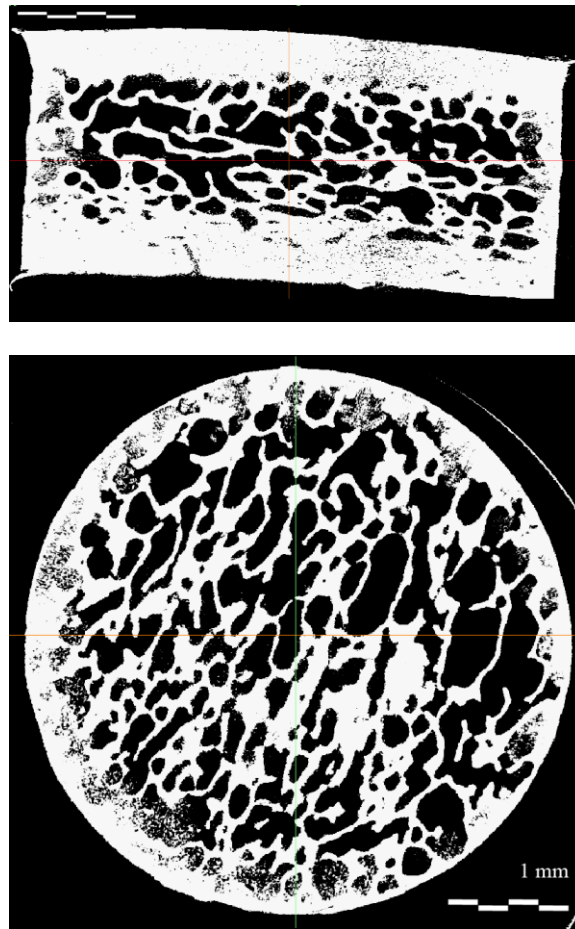


Figure 1.3 Cylindrical core samples from the human calvarium. Section view perpendicular to skull surface showing the sandwich structure (top) and tangential to skull surface (bottom) showing lack of regular trabecular orientation.

At the length scales of interest for current mechanical models of the head, the cortical shells may be assumed to be homogenous. Researchers for more than a century have observed that the building blocks of biological tissues have a grain orientation. Arrangement of osteons in cortical bone may lend anisotropy to its macroscopic mechanical behavior, making it stiffer under deformation along the grain as compared to the transverse directions. Although grain patterns have been demonstrated on the skull cortical layers, they are oriented in random directions in the

majority of the cranial vault. They appear to have a common directionality only when the shape of the bone deviates from the smooth sphere and ridges or troughs appear (Benninghoff, 1925; Dempster, 1967). Considering the random orientation of grain in the cortical tables, their mechanical response may be assumed to be transversely isotropic.

The cancellous diploe layer (Figure 1.3) is inhomogeneous and therefore, apart from its thickness, the histology of this layer may be of interest, especially for predicting its mechanical response. It is known that mechanical properties of cancellous bone depend on the volume fraction of bone (Currey, 1988; Keaveny et al., 2001). Surgeons have studied the remodeling of parietal bone using light microscopy on microtome sections (Hwang et al., 2000; Le Lorc'h-Bukiet et al., 2005; Torres-Lagares et al., 2010). However the relationship of volume fraction of trabecular bone in the cranium with mechanical properties has not been studied.

Wolff (1893) proposed that stress exerted on bone may influence bone remodeling and architecture. Wolff's law has evolved over time and gained consensus among researchers. It has been confirmed in several experiments (Hayes and Snyder, 1981; Kushner, 1940; Lanyon, 1974) and has led to the idea that bone remodeling is guided by the objective of attaining isotropic strain (Turner, 1992). The calvarium does not bear large loads and significant anisotropy in the cancellous bone could be expected only at muscle or tendon anchor points especially of the temporal muscle at the temporal fossa which drives mastication. From shear tests done at different angles, McElhaney et al. (1970) have concluded that skull bone as a whole is transversely isotropic with the plane of isotropy being tangential to the skull.

1.7 Studies of the mechanical properties of the calvarium

Table 1.1 Categorization of the studies in the literature pertaining to mechanical properties of the calvarium		
	Static	Dynamic rate (automotive)
Composite sandwich structure		
Compression / tension	Robbins and Wood (1969)	Halgrin et al. (2012)
	Barber et al. (1969)	
	McElhaney et al. (1970)	
	Schueler et al. (1994)	
Bending	Hubbard (1971)	Motherway et al. (2009)
	Delille et al. (2007)	
	Rahmoun et al. (2014)	
Shear	McElhaney et al. (1970)	
	Schueler et al. (1994)	
Cortical layer		
Compression / tension	Robbins and Wood (1969)	Melvin et al. (1970)
		Wood (1971)
Bending	Hubbard (1971)	Motherway et al. (2009)
	Delille et al. (2007)	
	Rahmoun et al. (2014)	
Ultrasound		Peterson and Dechow (2002)
Cancellous diploe layer		
Compression		Melvin et al. (1970)

The different components of the calvarium have been previously tested, either separately or in combination, under uniaxial tension, compression or, simple shear (Barber et al., 1969; Evans and Lissner, 1957; Halgrin et al., 2012; McElhaney et al., 1970; Melvin et al., 1970; Robbins and Wood, 1969; Schueler et al., 1994; Wood, 1971). More recently, mechanical characterization of the calvarium has focused on bending tests of composite bone (Auperrin et al., 2014; Delille et al., 2007; Hubbard, 1971; Motherway et al., 2009; Rahmoun et al., 2014). A few researchers have attempted to use ultrasound to calculate mechanical properties (Peterson and Dechow, 2003, 2002). Although few authors have noted differences in specimens harvested from the left and right calvarium, and also anisotropy in the cortical (Evans and Lissner, 1957) and cancellous bone (McElhaney et al., 1970), significance of this difference and evidence to the contrary (Benninghoff, 1925; Dempster, 1967) far overwhelm this notion.

The first comprehensive study of tensile and compressive failure properties of cortical bone from the skull was published in Evans and Lissner (1957). More than a decade later, the mechanical stiffness at quasi-static and dynamic rates was reported by Robbins and Wood (1969) and Wood (1971) respectively. Wood (1971) had studied 120 skull cortical bone specimens from thirty subjects at various rates of loading. Although a sample was tested, no objective distinction of the different layers of the calvarium was done. Moreover, material inhomogeneity within the skull cortical bone samples was not addressed in any of these studies. Therefore, it is unknown to what extent, if any, the microstructure of cortical bone influences the macroscopic mechanical properties.

Properties of cortical bone have also been derived from composite skull bone bending tests (Auperrin et al., 2014; Delille et al., 2007; Hubbard, 1971; Motherway et al., 2009; Rahmoun et al., 2014). Inhomogeneity and porosity in the material used in a composite skull bending study was accounted for using a three-layer model by Hubbard (1971) and the layer thicknesses were

calibrated through visual inspection. Delille et al. (2007) and Auperrin et al. (2014) have used mineral (ash) percentage to calibrate the thicknesses of a hollow beam models of samples from the calvarium in their bending study. Microstructure from micro-radiology was used in conjunction with bending tests only recently by Motherway et al. (2009). However, in all these cases, curvature of the skull was ignored and a simplified straight beam model was assumed. Ultrasound transmission was used by Peterson and Dechow (2002) to estimate the Young's modulus of human skull cortical bone.

In the only studies where micro computed tomography (μ CT) was used (Motherway et al., 2009; Rahmoun et al., 2014), it was assumed, despite evidence to the contrary (Rho et al., 1997; Zysset et al., 1999), that the bone in the cortical layers and the cancellous diploe layer had equal modulus. It is also unknown if the mechanical properties vary with location on the skull.

Biomaterials are viscoelastic in nature, and bone from the human calvarium is no exception. The analysis and measurement of viscoelasticity of bone is essential for modeling and simulation of impact and other high strain rate events. There are very few studies of the dynamic response of either the diploe layer or composite bone from the human calvarium. To date composite bone from the calvarium was tested at dynamic rates by only Motherway et al. (2009) and Halgrin et al. (2012). Motherway et al. (2009) have tested composite specimens in bending and derived dynamic properties of the bone phase using material distribution description from μ CT. Halgrin et al. (2012) have used an inverse FE method to optimize effective dynamic elastic modulus of composite specimens to match similar dynamic compression tests done on a Split Hopkinson Bar setup. The variance of the optimized modulus was not quantified. Cuboidal samples from the human skull diploe layer were tested at dynamic rates in compression by Melvin et al. (1970). While this is the only paper in the literature that has reported the effective modulus of the diploe

layer, the strain-rate dependency was not characterized and number of samples tested was unknown.

Wood (1971), in the only study of viscoelasticity of bone from the human calvarium, reported the dynamic ramp response of cortical bone samples from the human calvarium at strain rates ranging from 0.005 to 150 sec^{-1} . Although a viscoelastic model for cortical bone can be derived from this data, viscoelasticity of the diploe layer and the calvarium as a whole may be different. Due to the presence of fluid filled and interconnected pores, the diploe layer perhaps exhibits increased dissipative effects. Viscoelasticity of the human calvarium diploe layer has not been studied. Compared to the studies of bovine compact bone (Buechner et al., 2001; Schaller et al., 2004), bovine trabecular bone shows significantly greater material loss tangent (Dong et al., 2004). Even if the pores are neglected, previous research (Shepherd et al., 2011) has shown that due to differences in microstructural features, the bone in the diploe layer itself may have different viscoelastic properties compared to bone from the cortical layers. Human skull bone material studies have been summarized in Table A.1 and Table A.2.

1.8 Techniques of characterization of viscoelasticity

A few early researchers used dynamic ramp loading tests to quantify the extent of stiffening that bone undergoes as a result of increasing strain rate (Crowninshield and Pope, 1974; Lewis and Goldsmith, 1975; Linde et al., 1991; McElhaney, 1966; Wood, 1971). While this method indicates the existence of viscoelasticity, it does not directly provide a viscoelastic constitutive model that is suitable for simulation of arbitrary loading profiles. Nonetheless, several papers describe viscoelastic models fit to bone ramp loading test data (Johnson et al., 2010; Lewis and Goldsmith, 1975).

Step loading, for observation of either stress relaxation or creep function, was used by several others (Deligianni et al., 1994; Lakes et al., 1979; Quaglioni et al., 2009; Sasaki et al., 1993; Shepherd et al., 2011). Step loading tests are ideal for quantification of viscoelastic effects, but because of the practical limitation of finite rate of application of the step, in reality these tests are ramp and hold tests. Test samples incur significant relaxation even before the desired step loading is fully completed and viscoelastic decay that occurs before finishing of the ramp cannot be observed (Myers et al., 1991). Therefore, viscoelastic effects that have decay times greater than 100 ms (10 Hz) can be studied using this approach.

A usable viscoelastic constitutive model, with accurate instantaneous and initial transient responses, can be derived from cyclic loading tests by studying the magnitude and phase relationship between stress and strain. The desired accuracy of instantaneous and initial transient response is determined by the simulation scenario for which the model is to be used. This accuracy is improved with increasing loading frequency, which in turn is limited by different factors including test setup and sample size. Cyclic loading tests were previously done on bone samples from various sources (Black and Korostoff, 1973; Boruah et al., 2014; Buechner et al., 2001; Dong et al., 2004; Frasca et al., 1981; Garner et al., 1999; Lakes et al., 1979; Mano, 2005; Schaller et al., 2004; Yamashita et al., 2001). All of these tests were done on small samples with simple geometry allowing direct calculation of stress and strain.

1.9 Finite element models of the head

Most FE models of the head that are currently used for injury research utilize a single isotropic material for the entire skull. In order to simulate the correct bending stiffness of the skull, these FE models are typically very stiff under through-the-thickness deformation. In order to simultaneously simulate stiff bending and soft compression using an isotropic material, the skull must be modeled as a three layer sandwich structure with different properties for the diploe and

cortical layers. Head models that use different materials for these three layers (Asgharpour et al., 2014; Horgan and Gilchrist, 2003; Panzer et al., 2012) use a fixed ratio of thicknesses of the three layers of the skull. Mechanical properties of these layers are derived from mechanical tests done on samples obtained from the skull (McElhaney et al., 1970). With the advent of μ CT, it is now possible to verify if these samples were representative of the specific skull layer for which their properties are used in the FE models.

All of the contemporary FE models of the head in use in the automotive industry (Asgharpour et al., 2014; Gilchrist et al., 2001; Horgan and Gilchrist, 2003; Mao et al., 2013) have skull geometry identical to one individual, whose head geometry may not match the median head geometry in the population. The geometry data is usually derived from studies like the Visible Human project (Ackerman, 1998). While most of these models employ a constant ratio of diploe layer thickness to total thickness, some models do not distinguish the different layers of the skull at all and take an empirical approach by optimizing material properties of the skull to fit existing whole head experimental data (Hodgson et al., 1970; Nahum et al., 1977).

There are several head FE models that have been designed to simulate head exposure to explosive blasts (M S Chafi et al., 2009; Moore et al., 2009; Moss et al., 2009; Nyein et al., 2010; Panzer et al., 2012; Singh et al., 2014; Taylor and Ford, 2009). These models have small element size (~ 1 mm) to be able to simulate wave propagation effects. All blast head FE models use a single material model for all layers of the cranium, except (Panzer et al., 2012). An isotropic material which has been tuned to predict either bending, or normal or, tangential compression will fail to accurately predict the other two modes because of the sandwich structure in the calvarium. More importantly, all but two of these models consider the skull to be linear elastic. Panzer et al. (2012) and Moss et al. (2009) have incorporated a viscoelastic material in their skull FE models. And the viscoelastic parameters used in both of these models is based on dynamic ramp tensile tests done

on pure cortical bone from the skull. A few important current head FE models have been summarized in Table A.3.

1.10 Brain injury models

The earliest head injury models were developed to cope with the rising problem of head injury during motor vehicle crashes (Gadd, 1966; Versace, 1971). These studies led to the development of the head injury criteria (HIC) and the physical head-form for assessment of vehicle safety.

Although the HIC is a widely accepted injury criteria for brain contusion and is based on animal and cadaver head impact studies with intracranial pressure monitoring (Gurdjian et al., 1954; Lissner et al., 1960), it is not applicable in injuries with excessive head rotations. These injuries are common among football players. Although still a topic of contention, several criteria have been proposed to assess or predict injury caused by excessive rotation of the head (Kimpara and Iwamoto, 2011; Newman et al., 2000; Rowson and Duma, 2013). Research of criteria for brain injury due to blast is very limited. Rafaels et al. (2012) proposed that a combination of external peak air pressure and duration may be used as an effective blast induced brain injury criteria.

Most of the whole head kinematics-based brain injury criteria (Gadd, 1966; Kimpara and Iwamoto, 2011; Newman et al., 2000; Rowson and Duma, 2013; Versace, 1971) are empirical in nature and are not based on any hypothetical or proven injury mechanism of the brain tissue.

Only the HIC (Gadd, 1966; Versace, 1971) is based on research (Gurdjian et al., 1954) that shows that pressure may be a cause of neuronal damage. However, rotation is not directly coupled to pressure in the head and therefore pressure is unsuitable to predict brain injury caused by rotation.

Due to the difficulty of measuring strain in the in-vivo brain, researchers have used brain FE models to correlate strain metrics to known real world injury cases (Antona-Makoshi et al., 2013; Kimpara and Iwamoto, 2011; Takhounts et al., 2003). These FE models have been validated to a study of brain motion using high speed bi-planar x-ray on neutral density targets implanted in the

brain (Hardy et al., 2001). It is perhaps the only study that shows internal brain motion. Patterns of diffuse axonal injury found from animal studies (Gennarelli et al., 1982) matched patterns of maximum shear strain in physical models exposed to identical kinematic insult (Margulies et al., 1990).

Galbraith et al. (1993) tested individual squid giant axons while monitoring their electrical functionality to establish damage criteria. Laplaca et al. (1997) used neuron like cells in a shear device and observed that damage was sensitive to shear strain rate. Bain and Meaney (2000) tested guinea pig optic nerve and resulting sensory deficit and electrical response to derive injury criteria, but it cannot be said for certain that the mechanical behavior of the neurons in humans will be identical to that in other animals. Morrison III et al. (2003) developed a methodology to bond human neuron cell cultures to a membrane and apply biaxial strain to it. This device has been used with fluorescent dye photography to observe cell damage.

Although there is no tissue level injury criteria for the brain under blast loading, there is consensus that strain, strain-rate, or a combination of the two, is the cause of neuron damage. King et al. (2003) stated that “Brain response governs injury and not the input acceleration”. Closed-head blast-induced brain trauma is often characterized by diffuse axonal injury (Chen and Huang, 2011; Davenport et al., 2012; Jorge et al., 2012; Ling et al., 2009; Magnuson et al., 2012; Unterberg et al., 2004) leading to varying degrees of morbidity depending on the number of axons damaged (Blumbergs et al., 1995; Povlishock and Christman, 1995). Due to the distributed nature of brain function, Takhounts et al. (2003) proposed that the cumulative strain damage measure (CSDM, Bandak and Eppinger, 1994), which represents the fraction of neurons that exceeded the damage strain limit, would be better suited as an injury predictor and used FE models validated to (Hardy et al., 2001) brain kinematic dataset coupled with animal injury studies (Abel et al., 1978; Meaney et al., 1993; Nusholtz et al., 1984; Stalnaker et al., 1977a) to

derive CSDM based injury risk curves. He subsequently used data from instrumented helmets of football players who have suffered head injury in several studies (Takhounts et al., 2013, 2011, 2008) and established that CSDM level was indeed a good predictor of brain injury produced by head impacts. Head and brain injury studies in the literature have been summarized in Table A.4.

For the purpose of assessment of the geometry and mechanical properties of the calvarium and their between subjects variation found in this study in context of blast brain injury, a list of prime brain tissue injury criteria was compiled. This list is shown along with their proponents in Table 1.2.

Table 1.2 Brain tissue deformation metrics found to correlate with experimental brain injury in animal models

Deformation metric	Proponent	Specific injury
Strain based		
Maximum principal strain	(Antona-Makoshi et al., 2015)	Diffuse axonal injury
Maximum principal strain	(Antona-Makoshi et al., 2012)	Concussion
Maximum principal strain	(Takhounts et al., 2003)	Diffuse axonal injury
Maximum shear strain	(Margulies et al., 1990)	Diffuse axonal injury
Stress based		
Pressure	(Takhounts et al., 2003)	Contusion
Von Mises Stress	(Antona-Makoshi et al., 2012)	Concussion

1.11 Specific objectives

The primary objective of this study is the characterization of the viscoelastic properties of the calvarium in through-the-thickness deformation mode. As a secondary objective, for accurate

bending response of the skull, the layer thicknesses were estimated and cortical specimens from the calvarium were tested. The dissertation has been divided into the following parts.

Three-dimensional imaging: Three-dimensional x-ray computed tomography was used to characterize the geometry of the cranium and skull bone layer thicknesses. The volume fraction of bone in the porous diploe layer was also measured.

Dynamic tensile tests: For determination of skull cortical layer elastic modulus.

Dynamic compression tests: For determination of relatively low-rate mechanical characteristics of the diploe layer in through-the-thickness deformation mode.

Transmissibility tests: For determination of through-the-thickness viscoelastic properties of the diploe layer. A time-domain viscoelastic model for use by FE modelers was developed.

Integrated calvarium material model: Data from all tests and imaging was combined into an FE material model for accurate through-the-thickness and tangential deformation response and bending response and applicable in the study of blast exposure. The effect of variation of material parameters on brain deformation under blast was assessed using a simplified plane-strain model of the head.

1.12 Summary

This dissertation presents the development of a viscoelastic material model for the cancellous diploe layer of the human calvarium. Despite its inhomogeneity and complex microstructure, the diploe layer was treated as a homogenous and isotropic material at the continuum level. μ CT was used to distinguish the three layers of the calvarium in composite through-the-thickness samples and compatible mechanical properties of the cortical layers was developed using micromechanical FE models of tested cortical coupons. The dependence of the aforementioned

geometric and mechanical properties on anatomical location on the calvarium was evaluated using statistical techniques. Finally, the mechanical and geometric properties found were applied in a simplified model of the calvarium to study the effect of calvarium viscoelasticity and its variance on brain deformation under blast loading. The influence of variation of layer thicknesses was also investigated. The research is shown in the form of a flowchart in Figure 1.4.

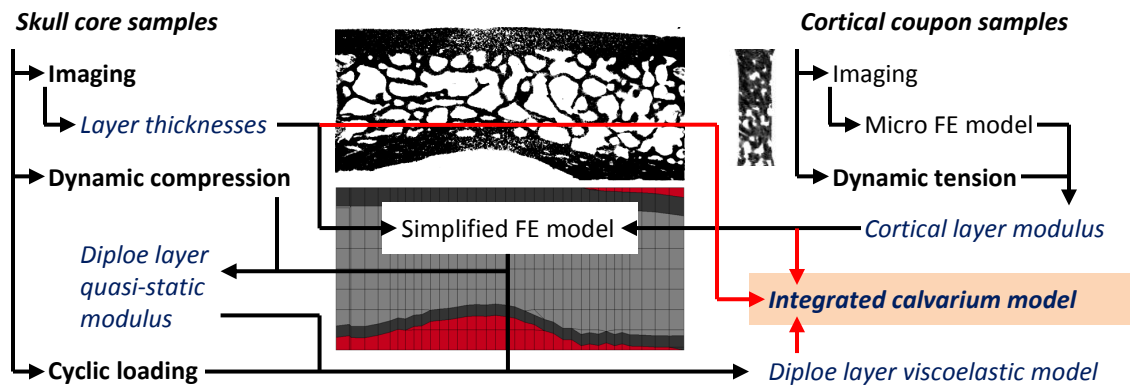


Figure 1.4 Flowchart of the dissertation showing the different tasks undertaken and the various secondary objectives achieved before the accomplishment of the primary objective.

2 Test subjects and test specimens

2.1 Post mortem human surrogates

Test samples were obtained from the calvaria of ten adult male post-mortem human surrogates, with an upper age limit of 70 years (Table 2.1). All test subjects were frozen post-mortem and thawed for use. Torimitsu et al. (2014) found that freezing-thawing cycles have no significant effect on the mechanical properties of bone. All subjects were screened for hepatitis A, B, C, and HIV and for pre-existing pathology that may influence bone properties, such as trauma and metastatic or wasting diseases. Pre-test radiographs were analyzed to verify that specimens with existing bone conditions, such as osteoporosis or osteopenia, on the basis of bone mineral density at the lumbar vertebrae and the femoral head (measured using dual-energy X-ray absorptiometry), were excluded from the study. All test procedures were approved by the University of Virginia Institutional Review Board for Human Surrogate Use. Clinical CT was performed on all subjects at an in-plane resolution of 0.980 mm/voxel, and a slice thickness of 0.625 mm in order to identify potential locations of harvesting specimens.

Obtaining PMHS specimens of age comparable to military populations is difficult. The average age of the identified donors is 55 years. Previous studies have found that porosity of bone increases with age, but that bone mineralization remains unchanged. Age has a significant influence on failure properties, but not on the elastic modulus of cortical bone (McCalden et al., 1993). Since the primary goal of this study is to find sub-failure properties, the influence of age will be addressed only as far as looking at the statistical correlation of the results with donor age.

Table 2.1 Anthropometry of test subjects

Subject no.	Age [years]	Height [cm]	Weight [kg]	Cause of death
1	58	188	104	Lung cancer
2	41	180	71	Cirrhosis of the liver / failure
3	49	175	57	Metastatic lung cancer
4	51	173	91	Cardiopulmonary arrest
5	66	178	70	Alzheimer
6	59	173	68	Pneumonia
7	61	175	104	Cadiac arrest, ventricular fibulation and HBP
8	45	191	73	Salivary gland cancer
9	49	175	101	Brain injury
10	70	173	77	Congestive heart failure

2.2 Sample harvest locations

Ten locations with relatively less curvature were identified on the left half of the calvarium. These locations varied slightly from skull to skull, if needed, to avoid unsuitable anomalies and the sutures. Bone samples were harvested from the outer cortical layer at these locations. These samples were machined into coupons. Ten locations on the right half of the calvarium, symmetric to those on the left, were marked for harvesting through-the-thickness cylindrical skull bone specimens (cores). These locations were distributed across the frontal bone and the parietal bone. Cortical bone samples were harvested from the outer cortical layer at symmetric points on the left half of the calvarium. Following thawing of the head and removal of the scalp, these locations

were marked on the skull surface (Figure 2.1). The harvest locations varied from skull to skull due the presence of unsuitable anomalies and curvature and also to avoid the sutures.

The actual positions of the harvest locations were measured and recorded for each skull relative to an anatomical landmark based head coordinate system. The origin of the head coordinate system was at the centroid of the nasion, bregma, lambda and the two porions. The horizontal plane was parallel to the Frankfort plane and $n\pi$ (n is any integer) azimuth corresponded to a plane perpendicular to the line joining the two porions. A brief description of these cranial landmarks is provided in Table 2.2. The harvest locations of the samples from each skull are shown in terms of azimuth and elevation angles, relative to this coordinate system, separately in Figure A.1 and together in Figure 3.7. The locations have been tabulated in Table A.6 and Table A.22. The calvarium was then removed using a circular oscillating saw and split into the right and left halves.



Figure 2.1 Sample harvest locations marked on the calvarium; through-the-thickness cylindrical samples (cores) from the right half (bottom left of this image) and cortical coupon samples from the left half of the calvarium (top right of this image)

Table 2.2 Descriptions of cranial landmarks used (all lie on the outer surface of the skull)

Nasion	Intersection of frontal and two nasal bones
Bregma	Intersection of the coronal and sagittal sutures
Lambda	Intersection of the lambdoid and sagittal sutures
Porions	Upper margin of the ear canals
Frankfort plane	Plane passing through the porions and the inferior margin of the left orbit

2.3 Cores – Through-the-thickness cylindrical samples

Skull core specimens were then harvested from the right half of the calvarium using a circular abrasive drill bit on a bench drill press (Figure 2.2). Bone hydration was maintained with saline solution throughout this process to prevent excessive heating. This process yielded skull cores with a diameter of approximately 18 mm (Figure 2.3). A total of 94 cores were harvested. They were stored submerged in saline solution at 5.5 °C.

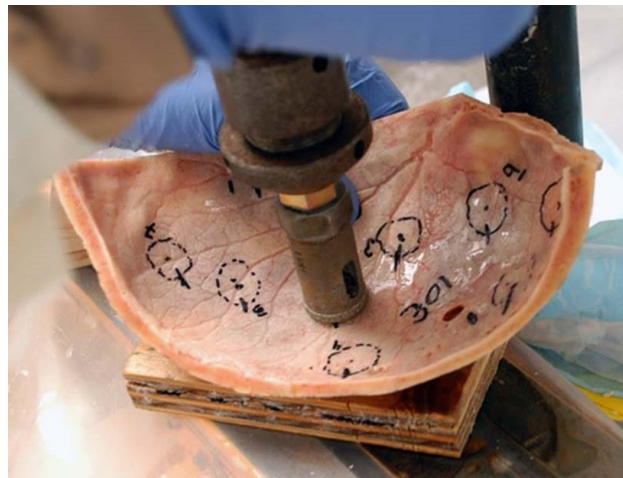


Figure 2.2 Skull core samples were obtained from the right calvarium using a circular abrasive drill press.

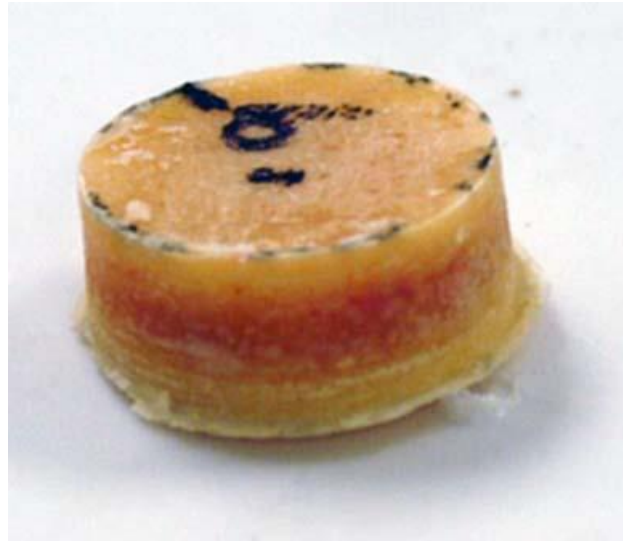


Figure 2.3 A sample skull core.

2.4 Coupons – cuboidal specimens from the outer cortical layer

The left calvarium was first cut into smaller segments using a band saw. These segments were machined under distilled water irrigation into 0.5 mm thick cortical bone wafers using an Isomet low-speed diamond wafering saw (Buehler, Lake Bluff, Illinois), which was equipped with a screw gauge (Figure 2.4). The cortical wafers thus obtained from the calvarium were mounted on a router and the final shape was milled (Figure 2.5). The thickness of the coupon was precisely ground to 0.5 mm using a custom sanding block. The dimensions of the finished coupons were based on previous work by (Subit et al., 2013, 2011) to allow the creation of test samples mostly composed of cortical bone (Figure 2.6). The harvested coupons were then stored submerged in saline solution inside polypropylene tubes at 5.5 °C. A total of 115 coupons were harvested.



Figure 2.4 0.5 mm thick cortical bone wafer being machined on a Buehler Isomet low-speed saw.



Figure 2.5 Cortical Bone wafers being milled.

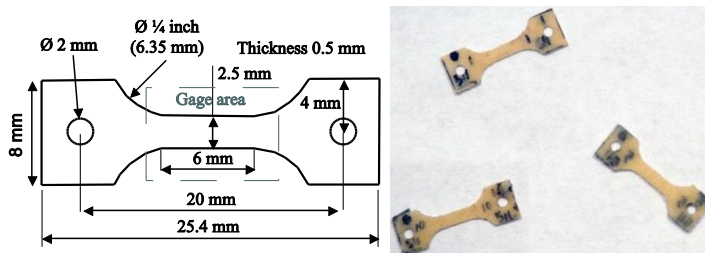


Figure 2.6 Dimensions of a coupon sample (left) and A few finished coupons (right).

3 Three dimensional geometry of the calvarium and its microstructure

3.1 Objective

The detailed geometry and microstructure of the cranium and its variation across the population is not well understood or documented. This study is aimed at exploring the variation of geometrical properties and bone volume fraction of the adult male human calvarium across the calvarium itself and between different subjects. This information can be used to develop statistical FE models of the head that are capable of predicting more accurately a complete spectrum of outcomes rather than a unique deterministic outcome.

3.2 Methodology

Table 3.1 μ CT specifications and settings

Type	High speed in vivo micro CT scanner
X-Ray	Microfocus X-Ray source; 5 or 7 μ m spot size
Detector	2048 \times 252 elements, 26 μ m pitch
Field of View	30.7 mm bore
Energy	45 kVp
Current	142 μ A
Integration time	800 ms
Resolution	30 μ m isotropic voxel size
Filter	3 \times 3 \times 3 Gaussian

3.2.1 Micro computed tomography

The skull cores were loaded onto a custom jig which fit inside a polypropylene tube. The jig was designed to hold the cores submerged in saline solution with the tables roughly perpendicular to the axis of the tube. The tube was then loaded into a Scanco VivaCT micro CT (μ CT) scanner (specifications and settings in Table 3.1). The slice direction was perpendicular to the axis of the tube (Figure 3.1).

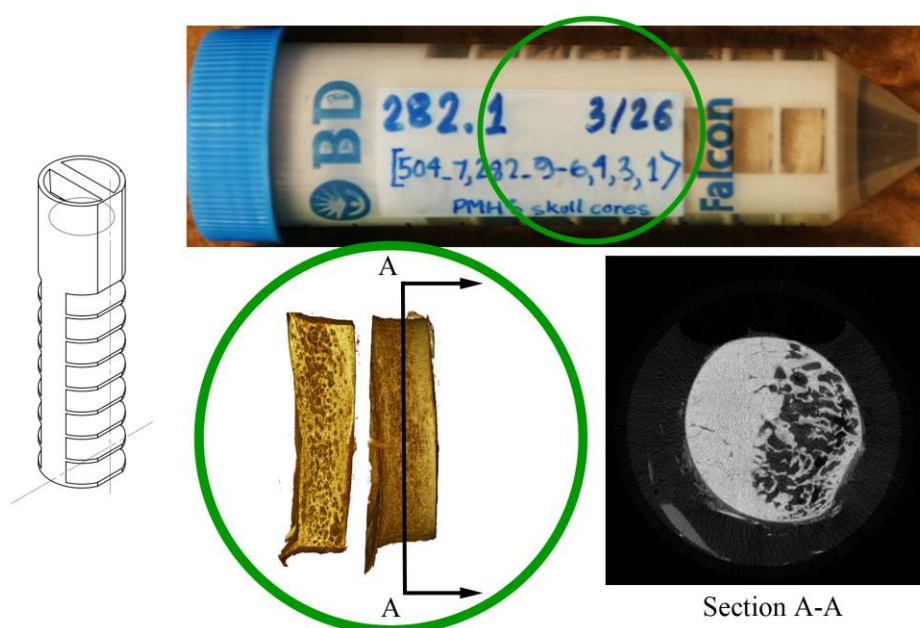


Figure 3.1 Clockwise from left; Core holder jig for μ CT of through-the-thickness samples; Cores loaded in a falcon tube for scanning; A typical μ CT slice image (parallel to calvarium surface); Image showing a transverse section reconstruction and slice direction.

3.2.2 Use of arbitrary apparent density scale

The quantitative density measurements from μ CT have been converted to apparent hydroxyapatite densities. The relationship between CT numbers (gray scale or the linear attenuation coefficients of each voxel) and apparent hydroxyapatite density is linear and is obtained from phantom ($0 - 800 \text{ mg HA/cm}^3$) based scanner calibration. Although theoretically,

this relationship is non-linear, it has been shown that a linear relationship may be sufficiently accurate for low energy X-ray (Brown et al., 2008). Because of its ability to resolve inter trabecular spacing and consequent lack of averaging of bone and pore material densities, the density of trabecular bone, in μ CT, is comparable to cortical bone (Figure 3.2). The inter trabecular space has non-zero density corresponding to its contents. The segmentation on which the findings are based is not dependent on the accuracy of the actual density numbers.

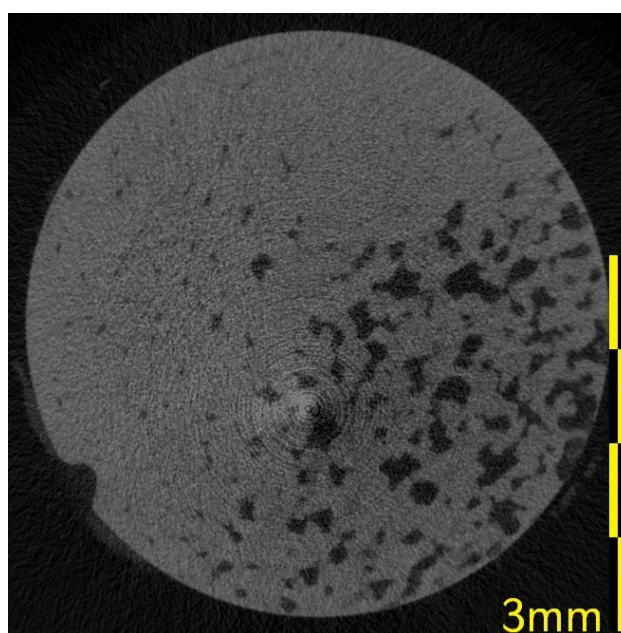


Figure 3.2 μ CT slice of core showing comparable measured density of cortical and trabecular bone.

3.2.3 Density distribution from μ CT and soft segmentation

The quantitative density measurements from μ CT of a skull core typically and primarily demonstrated a bimodal distribution (blue solid line; Figure 3.3). The second (denser and typically more prominent) mode at ~ 1000 mg Hydroxyapatite/cm³ (mg HA/cm³) is assumed to be actual bone and the rest is assumed to correspond to pore content. A generalized extreme value (gev) distribution was fit to the mode corresponding to bone (magenta line; Figure 3.3) as an estimate of actual bone content in the core. A gev distribution (widely used to model extreme

values of random variables; Jenkinson, 1955) has been used because it captures the skewed bell-curve very well. The difference between the total distribution from μ CT and this distribution of actual bone is, hypothetically, the distribution of pore content (green dotted line; labeled ‘other’ in Figure 3.3). The ratio of hypothetical actual bone density distribution to the measured total skull core density distribution was then used as the probability of a voxel belonging to bone as a function of the measured μ CT density (red broken line and labeled ‘Bone p.’ in Figure 3.3). This probability function was generated for each individual skull core and used to assign a probability value to each voxel (soft segmentation membership function of bone; Pham et al., 2000).

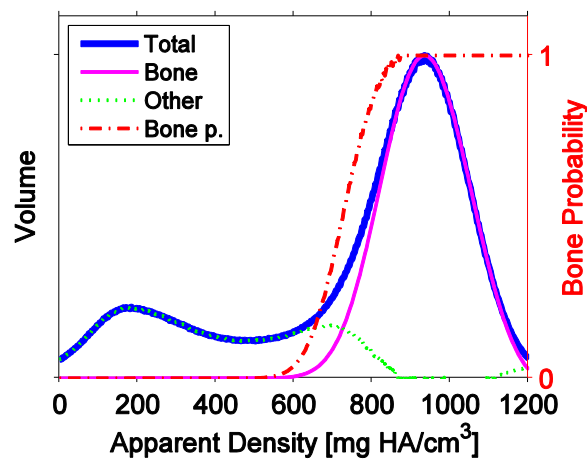


Figure 3.3 Typical distribution of apparent density in a skull core (blue); hypothetical distribution of bone (magenta) and pore content (green dotted); Bone probability as a function of apparent density (red broken).

3.2.4 Probabilistic crisp segmentation and Monte Carlo

Before measurement of thickness, a crisp segmentation of the bone volume is required. The MATLAB pseudo random number generator was used to randomly to assign a voxel to bone or pore. This process was biased using the soft segmentation probability value, explained in the previous section, such that the probability of a voxel being assigned to bone was equal to its membership function. The MATLAB (r2013b) pseudo-random number generator was used with

time as seed for this process. Since this process is random, the solution is not unique. In order to look at the influence of random probabilistic segmentation on the measured parameters, a Monte Carlo (MC) study was done by repeating the process 100 times. Each iteration cost ~100 s of computation time for each skull core on a quad core machine.

3.2.5 Thickness estimation and curvature compensation

Due to the curvature of the skull, the cortical layers on the core are not perfectly flat and parallel. Cancellous diploe layer appears in certain regions on the core before others, so also the core itself appears in certain regions in the slice before it appears on the others (Figure 3.4). Therefore, measurement of thickness is not straightforward. There were typically 3×10^5 voxels each on the inner and the outer surface of each skull core. For each of the voxels belonging to the outer surface of the skull core, traversal was made along the depth from outside the outer surface of the core until a voxel belonging to bone was encountered. This indicates commencement of the outer cortical layer. Further traversal was done until a voxel belonging to pore was encountered, indicating the commencement of cancellous bone. Similarly, traversal was made along the opposite direction from outside the inner surface of the core. Thus the thickness of the outer cortical layer, cancellous layer and the inner cortical layer corresponding to that particular outer surface voxel was measured.

This, however, does not account for curvature in the core in the sense that the stack of voxels traversed may not be locally perpendicular to the core surface. To overcome this problem, a mesh based approach was taken to fit a polynomial surface to the inner and outer layers of the cores. The entire slice was split into 64 square regions (shown in Figure 3.4). The location of the core outer and inner surfaces in each of these regions was calculated by averaging the locations corresponding to each outer surface voxel belonging to that particular region. This process of averaging resulted in the smoothing of surface curvatures at scales less than the mesh resolution

(~2.25 mm). A polynomial surface was then fit to the outer and inner surfaces of the core at this coarser resolution (red and blue surfaces in Figure 3.5). These polynomials were used to generate vectors perpendicular to the inner and outer surfaces at the points of measurement (black lines in in Figure 3.5) and the thickness measurements were projected onto these in order to achieve a thickness measurement adjusted for curvature.

The regional cortical layer thickness estimates for a typical core are shown in Figure 3.5 using cubic interpolation between the regional measurement points. Much variation in thickness was seen at the length scale of the core (18 mm). Measurements reported in this paper have been averaged at the regional level (~2.25 mm) since current head FE models have a similar mesh resolution.

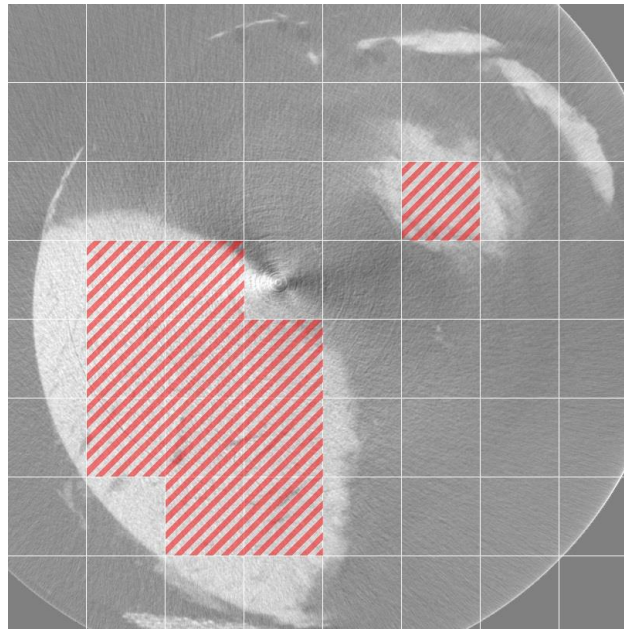


Figure 3.4 Curvature of skull core surface indicated by partial visibility in slice; mesh-size ~2.25 mm; red hatched areas denote the spatial extent of core; this μ CT image is not filtered.

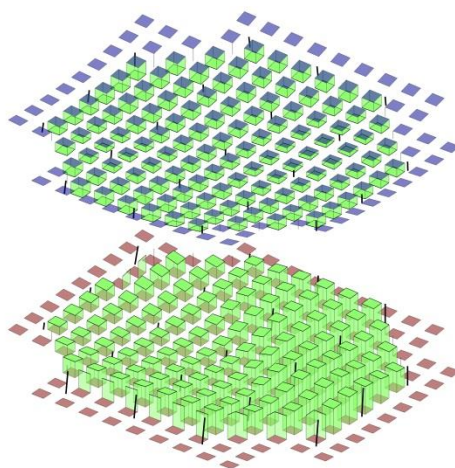


Figure 3.5 Illustration showing location dependency of cortical layer thickness within a skull core.

Figure 3.5 shows outer surface of core (red squares) and inner surface of core (blue squares). Cortical layer thickness measurements are along local normal at each region (black lines). Interpolated surfaces from discrete regional measurements are shown (green columns). Note – the inner and outer layers have been vertically offset to allow readers to discern them visually.

3.2.6 Statistics: averaging at the scale of interest and resulting expected value and uncertainty

Although the measurements, viz. the thickness and trabecular bone volume fraction, can be made at each surface voxel (30 μm across), they vary greatly from one voxel to the next. In fact, the measurements at the same surface voxel vary significantly with the MC iterations. Since current mathematical models have far lesser spatial resolution (compared to 30 μm), the measurements have been averaged across regions 2.25 mm across. This approach not only makes these measurements suitable for application to current models but also reduces the variation with the MC iterations. This effect is shown clearly in the subsequent results. This regional averaging decreases the variation due to the probabilistic segmentation to such an extent that this small variance has not been extensively reported. Because the variance is so small, the difference

between the average and median of the measurements from the MC iterations may be neglected. But it should be noted that the median values have been reported because the distribution is not generally symmetric.

Typically, each core sample has 30 square regions 2.25 mm across, and after regional averaging, the distribution of the measurements across these regions (~30 measurements) can be assessed. For depiction in a 2D projection of the calvarium, the average of the ~ 30 regional measurements (average values tabulated in Table A.7) has been considered the expected value of the metric at the particular sample location on the skull, and the standard error of the regional measurements has been considered to be the uncertainty. For statistical tests, all 30 regional measurements have been treated as separate measurements at that location. Because of the frequently skewed and uneven distributions, non-parametric Wilcoxon Rank sum tests were used to determine significance of difference in these measurements when grouped by subject and anatomical location.

In this way a location wise expected value and uncertainty map of each measurement has been generated for each subject. These discrete location wise measurements have been interpolated in order to generate smooth location dependent metrics. This interpolation method is explained in the next section. This interpolation also allows the comparison of the measurements across the different subjects.

3.2.7 Alber's projection of the skull and interpolation of measurements

The Alber's conic projection (Snyder, 1987) has been chosen to depict the results of this study due to its area preserving nature. As described in chapter 1, the origin of the Cartesian coordinate system was defined as the centroid of the nasion, bregma, lambda, and the two porions on the skull. The horizontal plane was aligned parallel to the Frankfort plane. Zero (and π) azimuth

corresponds to the plane perpendicular to the line joining the two Porions. The parameters used in the transformation of the 3D Cartesian coordinates to the 2D Alber's coordinates are summarized in Table 3.2. The various bones of the cranium and the sutures for the subjects are shown in Figure 3.6. The anterior aspect is towards the bottom and the posterior aspect is split along the sagittal plane and is seen on the top of this projection. The various bones are labeled in italics.

Latitude of origin	0
Longitude of origin	0
Latitude of standard parallel 1	$\pi/9$ radians
Latitude of standard parallel 2	$4\pi/9$ radians

Apart from measurements for the geometry of the outer surface of the cranial vault, all other measurements are available only at the sample locations. The sample locations on the Alber's map from all the skulls were combined to produce a standard mesh. The discrete measurements on each skull were interpolated onto this standard mesh using a linear triangulation algorithm. The averaging was done across all nine skulls at each node on the standard mesh and the results have been presented as one contour map representing the average skull. The variance has been shown in the mirror image of the particular half of the calvarium where measurements were done.

3.3 Results

3.3.1 Gross geometry and amount of data

The gross geometry of the outer surface of the cranial vault has been shown in terms of normalized distance from the origin to the outer surface (Figure 3.7 top). The measurements were normalized to the distance between the left and right porions (inter-porion distance). The inter-

porion distance in the nine subjects ranged from 94 to 122 mm and had a median value of 110 mm. The outer surface of the parietal bones was mostly at a constant distance from origin equal to half the inter-porion distance. Deviation from a spherical shape was noticeable somewhat on the anterior aspects of the parietal bones and the occipital bone and prominently on the frontal bone. The standard deviation of the normalized distance is also shown (Figure 3.7 bottom). A maximum standard deviation of ~ 8% was noted in the nine calvaria. The 12% deviation occurring at the brow is an artifact of the mismatched boundaries. The standard deviations are noticeably more asymmetrical than the average. Individual cranial vault outer shapes are presented in Figure A.1.

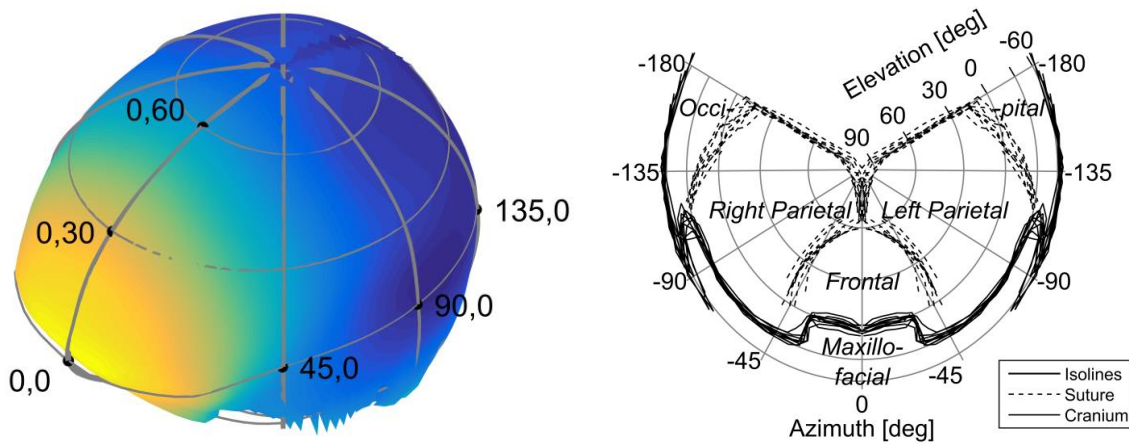


Figure 3.6 The average 3D shape of the cranium with azimuth and elevation isolines shown on the outer surface. Numbers at intersection of contours show azimuth, elevation angles (left). Color represents the distance of the outer cranium from the origin. Alber's projection of the human cranium (right). The coronal, sagittal and lambdoid sutures (dotted lines) are shown.

The data presented in this paper are from a total of 94 skull core samples harvested from ten PMHS specimens. Figure 3.7 shows the locations of samples harvested from all skulls, excluding subject no. 1. Few key landmarks in the CT images for Subject no. 1 were unavailable and therefore the 2D projection could not be developed. The figure also shows the coronal, sagittal and lambdoid sutures for the nine skulls. Each core sample typically had thirty-two 5 mm²

regions in which the measurements were averaged. There were a total of 2,850 regions in the 94 skull core samples that were studied. Of these, 954 regions were in the frontal bone and 1,896 regions in the parietal bone.

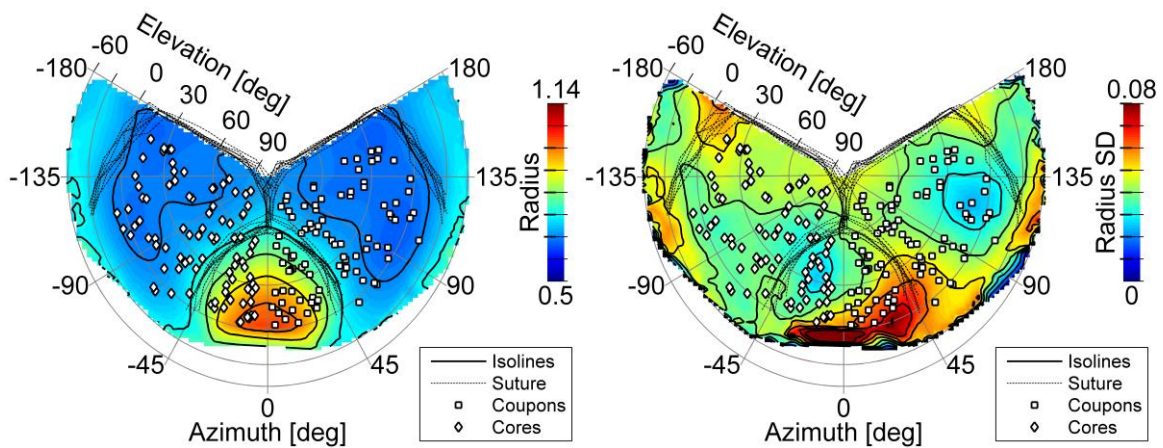


Figure 3.7 Left: Average normalized distance to skull outer surface from origin (radius); Right: Standard deviation of normalized radius; These distances have been normalized to the inter-porion distance. Diamonds: core harvest locations, Squares: Coupon harvest locations.

3.3.2 Monte Carlo and regional averaging

A typical set of thickness estimates from the 100 MC iterations are shown in Figure 3.8. On the left column are the thickness measurements at the same voxel, without any averaging. A wide variation of measurement can be seen due to the random nature of the segmentation.

Discretization of measurements to the μ CT resolution is clear at this level. Thickness measurements vary from 1.1 to 1.3 mm with an outlier at 0.6 mm. Upon averaging the thickness measurements at the $\sim 10^4$ voxels in a region from the coarse mesh (Figure 3.4), the variation drops below the μ CT resolution ($\sim 10 \mu\text{m}$). As shown in the middle column the measurements are clustered close together. The variation was $\sim 1 \mu\text{m}$ after averaging at the core level and the measurements from the 100 MC iterations are seen on top of each other (right column Figure 3.8).

The results of the MC simulations were distributed normally and when averaged at the region level, had a narrow variance (Figure 3.9). Especially, the calculated volume fraction exhibited a very small variance. This shows that reliable measurements can be obtained without the assumption of a threshold, as is done with traditional segmentation. The measurement values reported in this paper are medians of the results of the 100 MC iterations averaged at the region level (scale of 5 mm²). These figures also illustrate the large variation of these measurements from one region in a core to another.

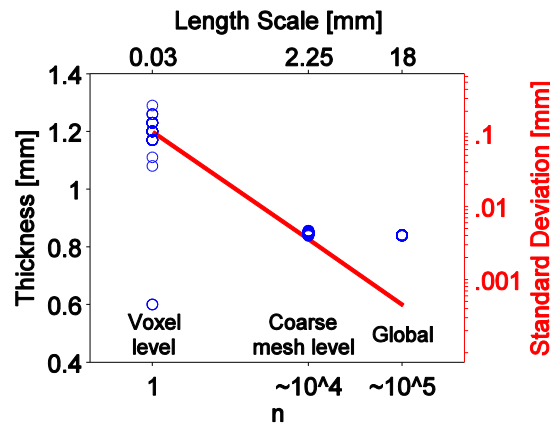


Figure 3.8 Effects of averaging on estimated thickness from Monte Carlo simulation, showing progressive convergence (left to right) with more and more averaging. Thickness measurements (Blue circles on left axis) and their Standard deviation (Red line on right axis; log-scale).

For analysis of inter-subject variation of the measurements, all combinations of the ten subjects were tested (45 total pairs). The absolute values of the thickness varied by more than 10% in almost 80% of the total subject pairs (Table 3.3). The ratio of the layer thicknesses to the total thickness also varied by more than 10% in majority of the cases.

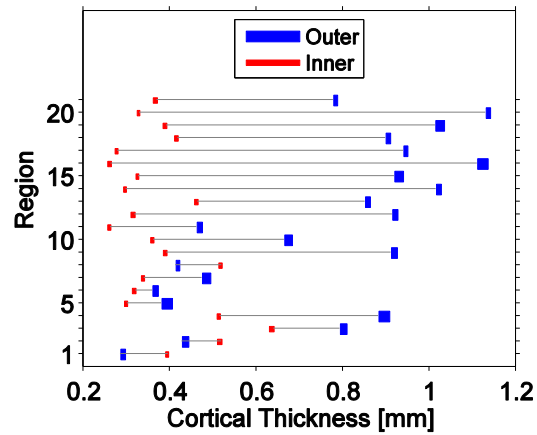


Figure 3.9 Distribution of regional thicknesses of a typical core sample from Monte Carlo Simulations; width of the bars show the range of averaged regional thickness.

Regional thickness measurements for a particular core were not normally distributed (Table A.8). Their subject-wise distribution is shown in the box-plots in Figure 3.10. They have been tested for difference using the Wilcoxon rank sum test ($\alpha=0.05$). The results of these tests are recorded in Table A.9 through Table A.21.

The variation with location on the calvarium was studied by grouping the measurements on the basis of whether they were obtained from the frontal or parietal bones and, additionally on the basis of whether they were obtained from the superior or inferior aspect of the calvarium.

Although there were significant differences in the majority of the tested pairs, the trend of variation was not consistent (Table 3.4). However, in eight out of ten subjects, diploe thickness was greater in the frontal bone.

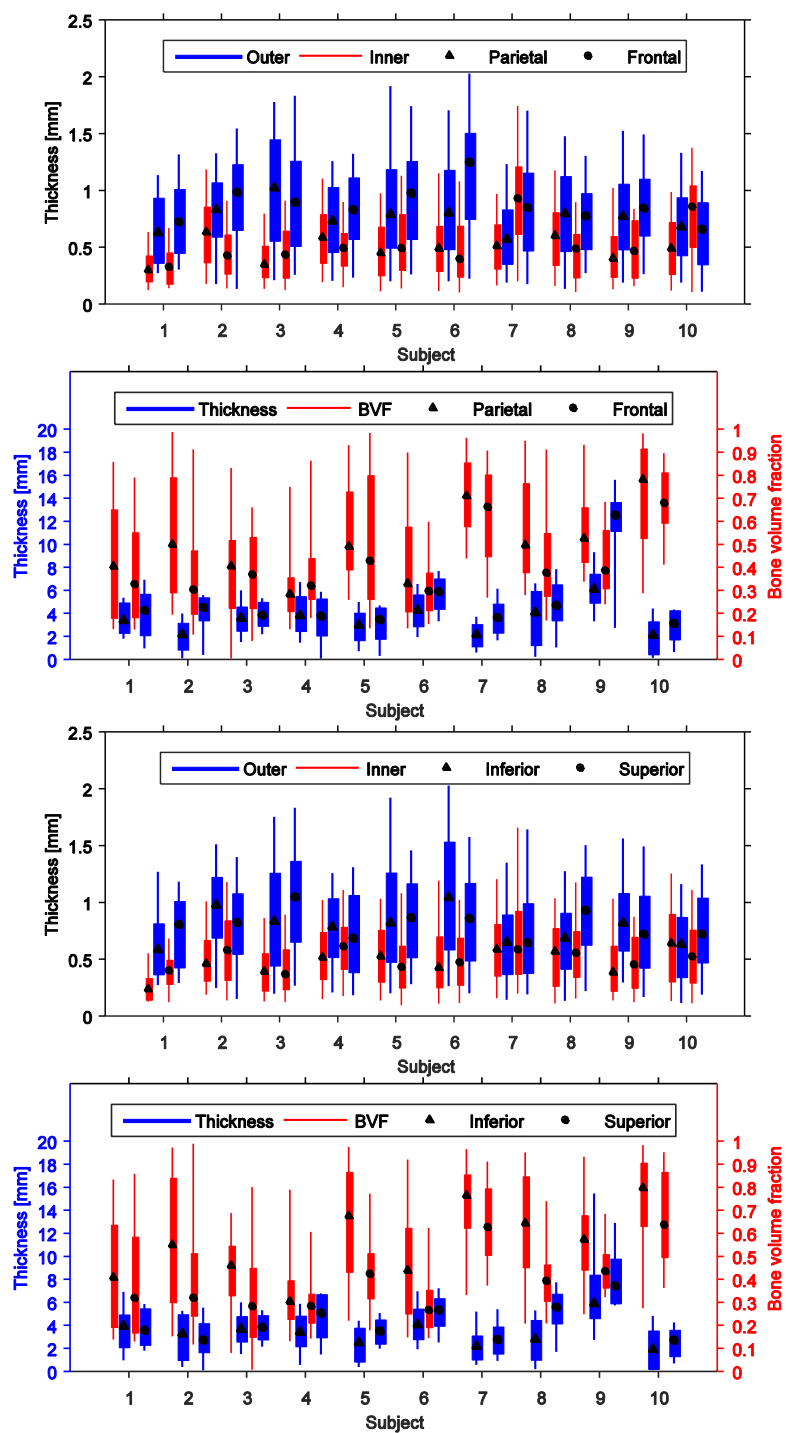


Figure 3.10 Boxplot of cortical layer thicknesses, and diploe layer thickness and bone volume fraction (BVF) highlighting differences between parietal vs. frontal bones and superior vs. inferior aspects of the calvarium;

box – inner quartile distance; line – 95% interval; marker – median.

Inner and outer cortical layer thicknesses were correlated and a t-test showed that their ratio was significantly different from unity ($p < 0.001$). Upon excluding subject 7, the median value of outer to inner cortical layer thickness ratio rises to 1.68 and the 95% confidence interval shifts to 0.55 to 5.14. Figure 3.12 shows the distribution of the average and variance of the outer and inner cortical layer. Individual outer and inner cortical layer thicknesses are shown in Figure A.2 and Figure A.3 respectively. Although the cancellous layer thicknesses varied significantly from the parietal to the frontal bone (except subject 7; Wilcoxon rank sum tests; $\alpha = 0.05$; summarized in Table A.9), there was no consistent trend. The distribution of the average cancellous layer thickness and its variance across the calvarium is shown in Figure 3.13. Subject 9 had an unusually thick skull. Individual cancellous layer thicknesses are shown in Figure A.4.

Table 3.3 Number of subject combinations with significantly different layer thicknesses, expressed as absolute values and as ratios to total thickness, and BVF.

	Percentage of pairs that are significantly different	Percentage of significant pairs that are more than 10% different	Median percentage absolute difference of all pairs
Absolute values			
Outer cortical thickness	73.3	86.7	15.0
Inner cortical thickness	73.3	68.9	22.0
Diploe thickness	91.1	86.7	33.8
Diploe BVF	86.7	77.8	33.3
Ratios to total thickness			
Outer cortical thickness	77.8	68.9	20.9
Inner cortical thickness	88.9	86.7	42.3
Diploe thickness	86.7	51.1	10.5
Strong effects are shown in bold. Total number of subject combinations is 45.			

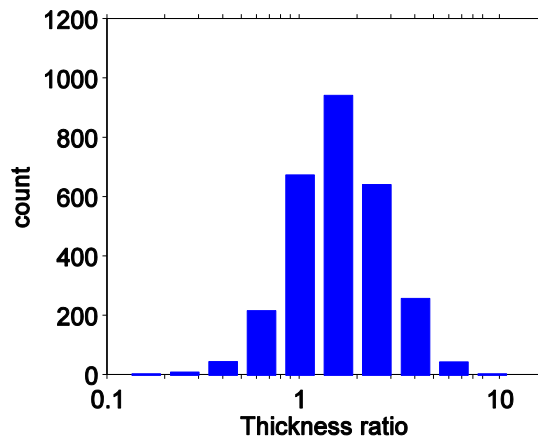


Figure 3.11 Histogram of ratios of outer cortical layer to inner cortical layer thickness. This distribution includes data from subject 7.

	Parietal vs. frontal			Inferior vs. superior		
	+	n	-	+	n	-
Absolute values						
Outer cortical thickness	0	5	5	3	3	4
Inner cortical thickness	3	4	3	2	5	3
Diploe thickness	1	1	8	0	3	7
Diploe BVF	6	3	1	9	1	0
Ratios to total thickness						
Outer cortical thickness	6	1	3	8	1	1
Inner cortical thickness	0	6	4	6	2	2
Diploe thickness	4	5	1	1	2	7

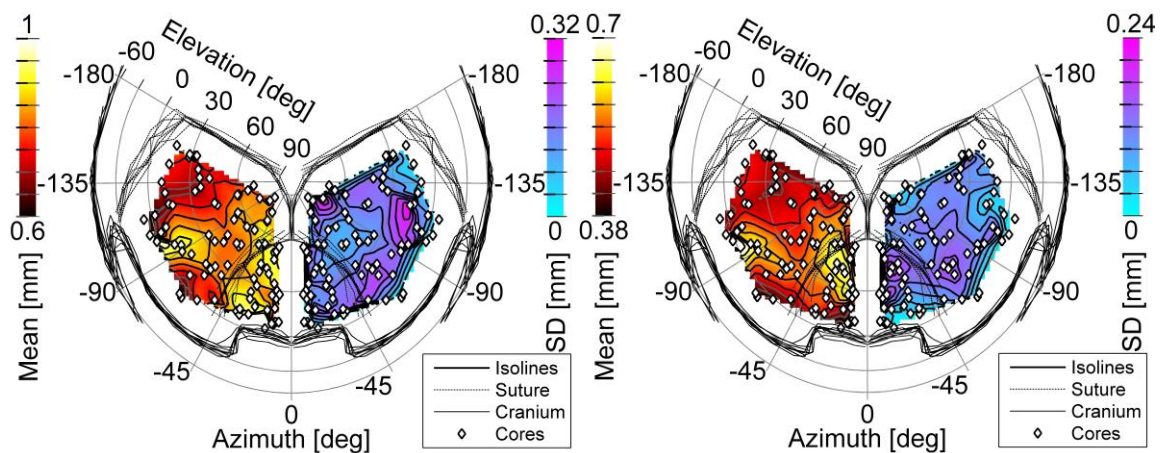


Figure 3.12 Contour on left: outer cortical layer thickness; right: inner cortical layer thickness; Within each plot, left: average across subjects; right: mirror image of the left showing distribution of standard deviation.

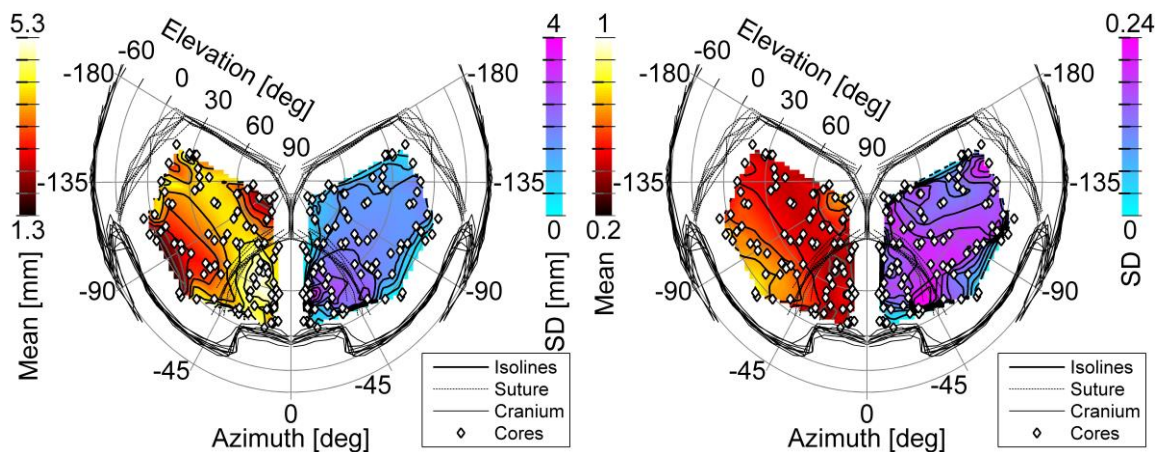


Figure 3.13 Contour on left: average cancellous layer thickness across subjects; right: standard deviation.

Figure 3.14 Contour on left: average cancellous layer bone volume fraction across subjects; right: standard deviation.

3.3.3 Cancellous layer volume fraction

In addition to layer thicknesses, bone volume fraction (BVF) in the trabecular diploe layer in the harvested skull core samples has been estimated. It had a median value of 0.47 (95% confidence interval [0.18 0.90]). Wilcoxon rank sum tests showed that BVF was significantly greater in the inferior aspect of the calvarium nine out of ten subjects (significance levels and median differences listed in Table A.9 through Table A.12). Bone volume fraction in parietal bone was significantly higher in three subjects and lower in three other subjects than in frontal bone. Figure 3.14 shows a map of the average bone volume fraction. Figure A.5 shows the distribution of BVF for each subject.

3.4 Discussion

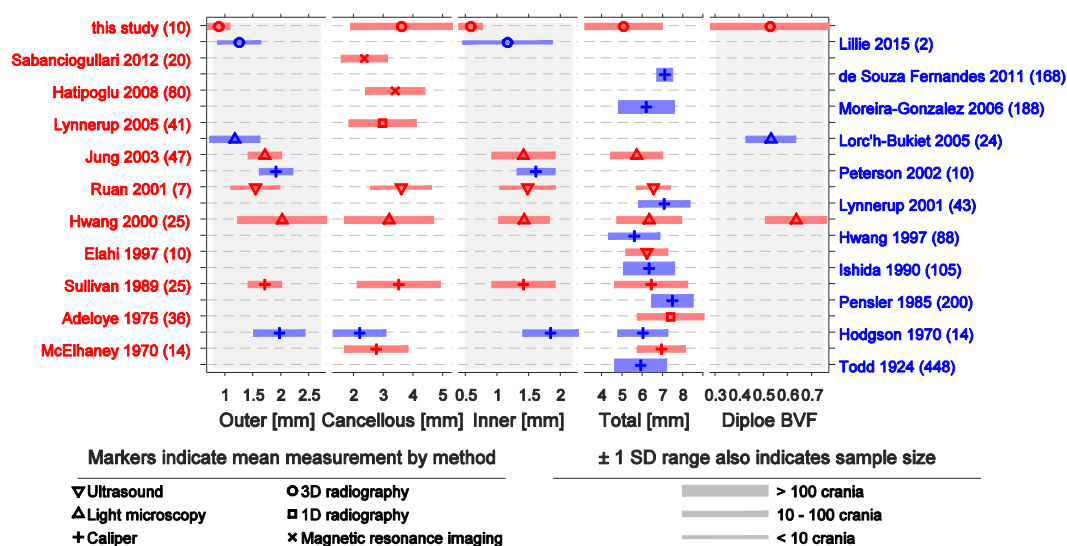


Figure 3.15 Skull thickness and diploe bone volume fraction data (near the vertex of the skull) from the literature, in chronological order.

Skull layer thickness and diploe bone volume fraction data from the literature has been presented in Figure 3.15. Most of the cranial landmarks are based on the suture joints of the various bones on the skull. Because of the variance in shape of the skull, defining a common reference point on

any skull bone is difficult. Most recently, the other researchers have used different grids that have been constructed with reference to the suture lines to relate their measurements to a location on the skull. This approach may be adequate for surgical procedures, but does not lend itself well to the creation of 3D numerical models. Application of geometric data to FE models using a 2D interpolated map, on the basis of a few cranial landmarks has been proposed and the data has been presented in this form. Such a statistical FE model will be suitable for research related to the protection of the brain. The measurements shown in Figure 3.15 correspond to a location that is as close as available in the literature, to the vertex of the skull of an adult white male.

At the onset, a large degree of variability can be seen in all of the metrics. This divergence in thickness of the cranial vault was observed by Todd (1924), who wrote “Cranial thickness is so variable that it appears unreasonable to imagine it under specific natural control as many (other) dimensions (of the body) seem to be”. Although the skull thickness undeniably grows during the first two decades of life (Roche, 1953), there are conflicting results about what happens later. Todd (1924) and Adeloje et al. (1975) found gradual increase in until the sixth decade of life, whereas Sullivan and Smith (1989) observed the opposite trend. Several other authors (Ishida and Dodo, 1990; Lynnerup, 2016; Moreira-Gonzalez et al., 2006; Pensler and McCarthy, 1985; Sullivan and Smith, 1989) found no correlation between age and skull thickness beyond 20 years of age. Keeping in mind that the data in this paper is aimed at the development of FE models of the adult calvarium, the changes with age has been neglected. Apart from the variability at the same location on the skulls, a large variability is also seen at different locations across the same skull. Statistical tests reported in this paper have revealed no significant trend in the variation of any of the measurements with anatomical location. However, studies with larger sample sizes (Hwang et al., 1997; Pensler and McCarthy, 1985) have reported increasing total thickness from anterior to posterior of the parietal bone.

The main weakness of almost all of the past literature that describes skull layer thicknesses is that the methodology of determining the extent of each layer is not clearly defined. As noted by Ruan and Prasad (2001), there is no clear and consistent demarcation between the three layers of the skull. This makes the process of visual measurement using a caliper, with or without microscopy, very subjective. This may be sufficient for the purpose of donor site determination for bone grafts, but a more rigorous approach is required for mathematical modeling. The compatibility of mechanical properties with each of the layers in FE model can only be ascertained once the distinction of these layers is properly defined. Although use of digital imaging (like CT, ultrasound, or MRI) allows elimination of subjectivity, a detailed description of the segmentation methodology is still required for choosing appropriate material properties.

Traditional three dimensional imaging does not have sufficient resolution to distinguish the different layers of the cranial vault. Historically, thicknesses of the cortical tables has been determined either visually or using a microscope. Using these techniques, measurements are made only on the plane of dissection, making the description of these metrics on the entire cranial vault nearly impossible. The advent of micro CT has solved this problem by allowing the analysis of these layers in three dimensions. Lillie et al. (2015) have used micro CT to determine inner and outer cortical layer thickness at seven locations on two skulls and used these measurements to validate a new technique of cortical thickness measurement from clinical CT. Apart from the small sample size, sufficient details of segmentation of the different layers in micro CT has not been provided for confident choice of corresponding material properties. This paper represents the first thorough description of layer thicknesses and cancellous bone volume fraction in the adult male calvarium, obtained from micro CT study of samples from a fairly large number of skulls.

With the emergence of imaging technologies with greater resolutions, finer discontinuities in the bone material become visible. Perhaps due to this, cortical layer thickness measurements have a diminishing trend with study time (Figure 3.15). This possibility highlights the importance of methodological details in the interpretation and use of these results.

This chapter also presents a probabilistic segmentation technique to account for uncertainties associated with partial volume effects. This technique allows quantification of errors introduced by the assumption of a threshold value in traditional segmentation. It was found that the variance of the measurements due to this uncertainty was negligibly small in this case of micro CT of the calvarium.

3.5 Conclusions

1. A new method of probabilistic segmentation of bone that does not require the assumption of any threshold value is presented. This technique allows the use of Monte Carlo methods to quantify any error in segmentation introduced by partial volume effects and noise. Variance in results due to probabilistic segmentation is found to be very small.
2. Detection of small pores in the calvarium, which was previously impossible, was enabled by μ CT and the thicknesses of the cortical tables were determined to be actually much less than the existing values in the literature.
3. The diploe layer thickness varied significantly between subjects (median value of 1.25 mm or 33.8%).
4. The outer cortical layer was found to be significantly thicker than the inner cortical layer (median ratio is 1.68).

5. Although there were significant differences in layer thicknesses across the calvarium, there was no common trend in this difference, except for diploe layer thickness which was greater for frontal bone in 8 out of the 10 subjects.
6. Diploe layer bone volume fraction was significantly greater in the inferior aspect of the calvarium in nine out of ten subjects.

4 Coupon tensile tests

4.1 Objective

The objective of this study was to examine the Young's modulus of cortical bone from the skull, specifically the calvarium, at a sub-osteon element size (50 μm), under the assumption that the bone behaves in an isotropic fashion at this length scale. Despite this assumption, at the macro scale, the porous bone samples may behave in an anisotropic fashion depending on the existence of any directionality in the bone scaffold. A three-step approach was designed. First, tensile coupons were harvested from the outer cortical layer of the calvarium and imaged using μCT to analyze the bone micro-structure. Second, the coupons were tested under dynamic tension. Third, coupon specific FE models were developed to account for the micro-structural arrangement of osteons and to identify the mechanical properties of bone at a microscopic scale.

In addition to the assessment of influence of microstructure on the mechanical properties of the cortical layers of the calvarium, the statistical difference in these properties between the frontal and parietal bones and between the superior and inferior aspects of the calvarium was also determined.

4.2 Methodology

4.2.1 Micro computed tomography

The coupon samples were loaded in a custom built jig (Figure 4.1 left) and submerged in saline solution inside falcon tubes. They were then scanned using a VIVACT40 μCT machine (resolution – 25 μm ; Scanco, Brüttisellen, Switzerland). All scan parameters, except field of view (25.4 mm bore) and resolution, were same as the radiological study of the core samples (Table

3.1). A μ CT slice showing the cross-section of two stacks of five coupons each is shown in Figure 4.1. The slice direction relative to the coupon holder is also shown in the same figure.

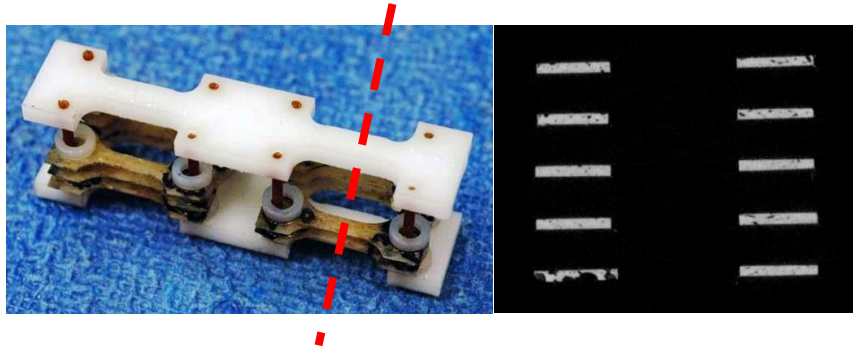


Figure 4.1 Coupon holder jig for μ CT imaging (left; broken line shows slice direction) and a typical slice image of ten coupons.

4.2.2 Segmentation and finite element mesh

Micro CT images of the coupons were segmented using a probabilistic segmentation method described in Section 3.2.3. In summary, the distribution of apparent density within the volume of each sample was analyzed to determine a hypothetical distribution of apparent density in the bone phase (Figure 4.2). This hypothetical distribution was used to generate a probability function which estimates the probability of any voxel belonging to the bone phase on the basis of its apparent density.

The distributions of apparent density are shown in Figure 4.2. In comparison with through-the-thickness cores samples obtained from symmetric locations on the right half of the calvarium, it was observed that part of the lower density components of bone was lost presumably through leaching during machining and storage of the coupons (as seen from the significantly higher density of the bone phase in the coupon samples; solid blue line vs. dashed blue line in Figure 4.2). This same effect was observed by Boothroyd (1964). Typically, the median bone density of the coupons was 13% more than that of the corresponding cores. Therefore, the probability functions used for coupon segmentation were generated from their corresponding core samples.

Because of the greater porosity of the core samples as compared to the coupons, their distributions had a pronounced bimodal shape, resulting in sharper probability functions.

The coupons were segmented using a random number generator that was biased using this probability function in conjunction with apparent density from μ CT. The bone volume fraction (BVF) of the gage area of each coupon was computed from the ratio of number of voxels belonging to bone to the number of total voxels in the coupon gage area (resolution of 25 μ m). This metric was used as a quantitative descriptor of the bone microstructure for looking at correlations with mechanical properties.

The FE mesh of the gage area of each coupon was built using the segmentation method described above. The meshes for the micro FE models of the gage area of each coupon were constructed at reduced resolution (50 μ m element size; Figure 4.3) because full resolution (25 μ m) meshes were computationally prohibitive. A mesh convergence study was not done. There were typically 50,000 cubical elements representing bone in the coupon gage area. It was assumed that the pores had no contribution to the tensile response and they were not meshed. For studying the hypothetical influence of apparent density on Young's modulus, in the case of a few coupons, the elements representing bone were separated into different parts on the basis of their apparent density (bin-size 100 mg HA/cm³; Figure 4.4 and Figure 4.2 top-right).

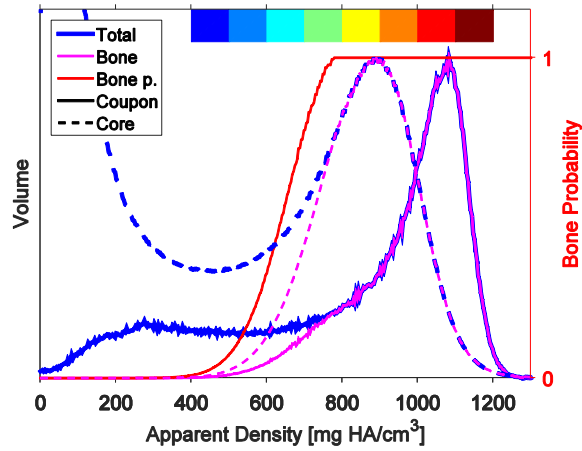


Figure 4.2 Distribution of apparent density in a typical coupon (solid lines) and corresponding distribution in a core harvested from a symmetric location on the opposite side of the skull (dashed lines). Blue lines show total distributions and magenta lines show hypothetical distributions in the bone phase. Probability function used in segmentation is shown by the red line. Color grid on the top-right shows the binning of bone elements into different parts on the basis of their density.

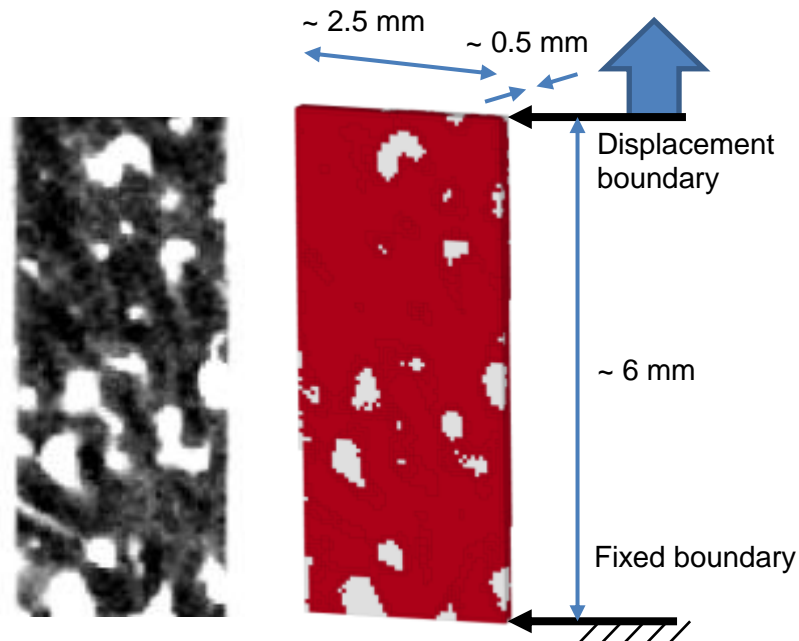


Figure 4.3 Micro CT slice of a coupon gage area (left; color indicates bone probability: white – 0, black – 1) and corresponding two-phase FE mesh (right).

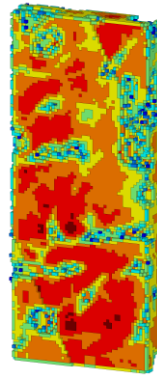


Figure 4.4 A multi-phase FE mesh of a coupon for studying the influence of apparent density on Young's modulus of the bone phase. Color scale in Figure 4.2.

4.2.3 Tensile test setup

After completion of μ CT imaging, the coupons were tested to failure with the tensile test setup described in Subit et al. (2011). It consisted of a custom built test fixture attached to the 8874 servo-hydraulic system (Instron, Norwood, Massachusetts). The test fixture, consisting of two clamps and ball joints, was designed to self-align in the direction of load (Figure 4.5). The lightweight clamps have a 0.5 mm wide slot for insertion of the coupons and a 2 mm screw to apply the clamping force. Ball joints accommodated the roller pins which attached the clamps to the clevises on the driving machine. The top clevis was attached to the hydraulic actuator and the bottom was attached to the stationary load-cell (Honeywell model 41). The roller-clevis joint constrained only vertical motion, allowing the coupon-clamp system to self-align to the vertical axis upon application of pre-load. A digital image correlation system was used to measure displacement and strain (Aramis v6.2, GOM mbH, Braunschweig, Germany). The entire setup is shown in Figure 4.6. Two high speed cameras (NAC GX-1, NAC image technology, Tokyo, Japan) recorded images at 5000 fps, using a 105 mm macro lens (NIKON AF-S VR Micro-Nikkor). These images were used to measure strain and displacement. The load-cell data was acquired at 100 kHz using a DEWE-2010 data acquisition system (Dewetron, Graz, Austria). The

tensile tests were conducted after application of a pre-load of $\sim 5\text{N}$. The Instron actuator was driven at a speed of 12 mm/s (target strain rate $200\text{ \%}/\text{s}$). All data was filtered using a low-pass butterworth filter with a cut-off frequency of 2 kHz .

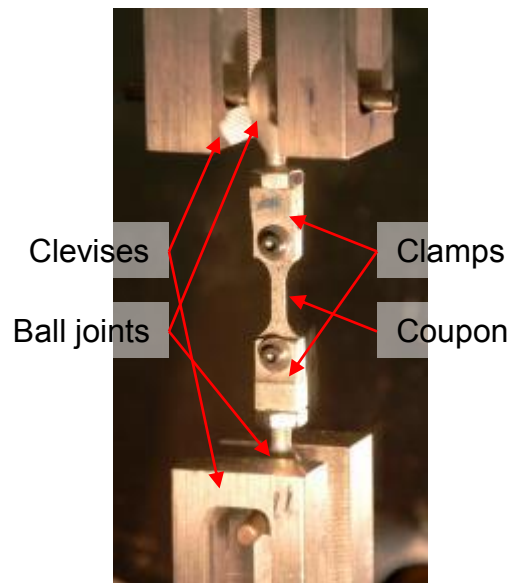


Figure 4.5 Self aligning coupon testing jig mounted on clevises of the 8874 servo-hydraulic system.

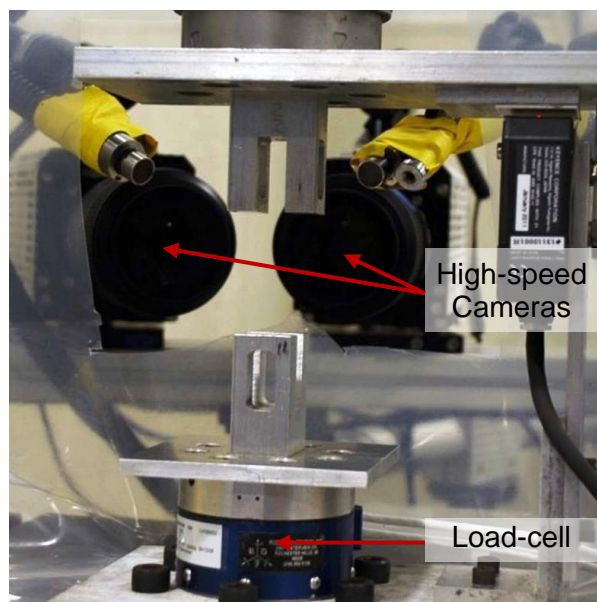


Figure 4.6 Tensile test setup.

4.2.4 Strain from image stereo-correlation

Before tests were conducted, a black and white speckle pattern (speckle size ~ 0.1 mm) was applied on the coupon surfaces. The software defines square facets several pixels across on the reference image, and tracks the speckle pattern within each facet to calculate displacements. The cameras remained stationary. The software is capable of assessment of out-of-plane motion using a pair of cameras calibrated for a test volume, yielding a full 3D displacement field of the surface under observation. In order to ascertain that there was no significant out-of-plane motion leading to incorrect 2D displacement field estimation, some tests were carried out with a calibrated pair of cameras looking at one surface of the coupon (such a setup is seen in Figure 4.6). Once it was confirmed that out-of-plane displacements were negligible, the remaining tests were conducted with the two cameras on opposite sides of the coupon, each looking at the inner and outer surfaces. Coupon surface displacement fields from image analysis were used to generate strain fields on the coupon surfaces. For finding effective mechanical properties at the length scale of the coupons, average vertical strain in the gage area was used in the analysis. Engineering stress was calculated by dividing force by the coupon gage cross-sectional area. Coupon gage cross-sectional area was the average area of the rectangular bounding box of the coupon gage area on a slice-by-slice basis calculated from μ CT.

4.2.5 Micro FE model and optimization

LS DYNA (R7.1.1, LSTC, Livermore, CA) implicit was used to solve the FE models to compute the structural stiffness of the coupons as a function of the elastic modulus of the bone phase. The nodes in the bottom of the gage area were constrained in the vertical axis, but were free to move along the transverse axes. The nodes at top were displaced along the vertical axis corresponding to 0.1% strain. They were also free in the transverse axes (Figure 4.3). This arrangement allowed

only force in the vertical axis and moments in the transverse axes at the top and bottom boundaries.

The bone elements were cubic constant stress solid elements. Their constitutive behavior was defined as isotropic linear elastic using the LS DYNA MAT_ELASTIC card. The models, where a variable, apparent density dependent, bone phase modulus was used (multi-phase mesh, Figure 4.4), showed insignificant improvement over the constant models (Two-phase mesh, Figure 4.3 right). For each coupon, the optimal value of the slope and intercept of the mineral density dependent bone phase modulus were not unique and, even a negative slope of modulus with respect to density could yield the experimentally observed effective structural response.

Therefore, it was not possible to make any deduction about the dependence of the Young's modulus of the bone phase on its apparent density and the simulations done with the multi-phase mesh is not included in the simulation matrix. Keeping this in mind, a constant Young's modulus was used for all the bone elements in each coupon, and this modulus was optimized to match the experimental force response. This modulus is referred to as the bone phase modulus in this article. The effect of microstructural arrangement of bone, at a length scale of greater than 50 μm , was cancelled from the structural response of the coupon in this manner.

The determination of coupon specific Young's modulus through parameter identification was computationally intensive. To increase the tractability of the computational work, a sensitivity analysis of the simulation results to the simulation inputs was performed on a subset of five coupons (Table 4.1). The FE models of these coupons were loaded to four different strains using a bone phase modulus of 16 GPa. The force response was perfectly linear with respect to strain in all five cases. Similarly, simulations were run for five coupons using four different bone phase moduli to a strain of 0.1%. The force response was again perfectly linear. On the basis of these observations, all optimization simulations were run to a strain of 0.1% using two seed values of

bone phase moduli: 12.00 and 21.00 GPa. The optimum bone phase modulus for each coupon was then obtained through linear interpolation. A third simulation was run using this optimal bone phase modulus to confirm if it yielded the experimentally observed force. The force response was insensitive to the Poisson's ratio and a value of 0.40 was used (Dong and Guo, 2004; Robbins and Wood, 1969).

Table 4.1 Simulation matrix – coupon μ FE models run using LSDYNA implicit.

Number of coupons	Strain [%]	Modulus [GPa]
Preliminary		
5	0.05, 0.1, 0.5, 2.0	16.00
5	0.1	12.00, 15.00, 18.00, 21.00
Final		
97	0.1	12.00, 21.00, sample dependent value

4.3 Results

The results for 97 successfully tested calvarium coupon samples are presented here. Eighteen coupons were damaged during mounting on the test setup.

4.3.1 Linear elastic response

A few coupons before and after testing are shown in Figure 4.7. The strain field was measured on both coupon surfaces (Figure 4.8). Typically engineering stress varied linearly with engineering strain (Figure 4.9), and the effective linear elastic modulus of the coupon was estimated from linear regression of stress vs. strain data within 20% to 80% of the failure strain. Non-linearity at the extreme ends of stress and strain was discounted in this manner. Ratio of stress to strain deviated more than 10% from the effective modulus in half of the tests near the failure point. In 23 out of 97 successful tests, the coupons failed outside the gage area (Table A.23). In these cases

the maximum stress and strain that were attained in the gage area were less than the failure stress and strain, because failure did not occur in the gage area, and these values were discarded in the statistical analysis of failure properties. However, the sub-failure stress vs. strain relationship is still valid for the gage area and effective elastic modulus can be derived.

The stress-strain plots, for all successfully tested coupons, combined by subject and by location are shown in Figure A.6 and Figure A.7 respectively. The linear elastic material parameters for the effective or structural response of the 97 cortical bone coupons have been summarized in Table 4.2. Effective Young's modulus of the coupons had a weak correlation ($R^2 = 0.51$) with BVF in the coupon gage area. Similarly, the failure stress for the coupons that broke in the gage area, had a weak correlation with BVF ($R^2 = 0.50$; Figure 4.10). Power law models were chosen for functional representation of these relationships (Equation 4.1). Failure strain had no discernable trend with BVF.

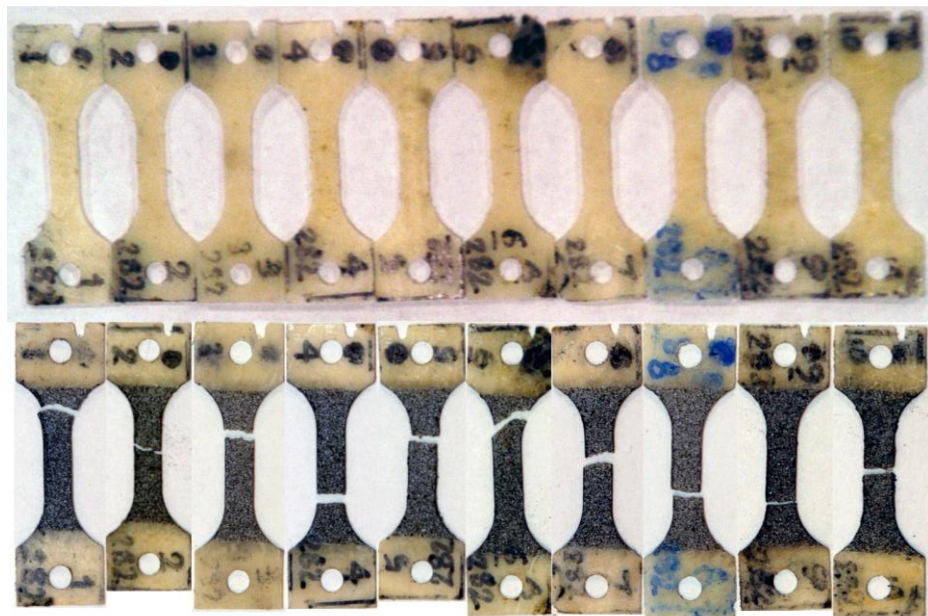


Figure 4.7 Ten coupons before (top) and after testing (bottom). Two coupons break outside gage area (number 1 and 6 from the left).

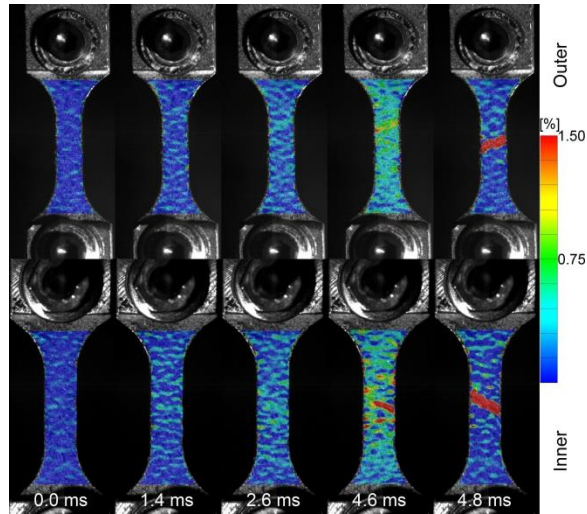


Figure 4.8 Strain fields on the outer (top) and inner surface of a coupon during a typical test. Color map shows strain along the vertical axis. Failure occurred between 4.6 and 4.8 ms.

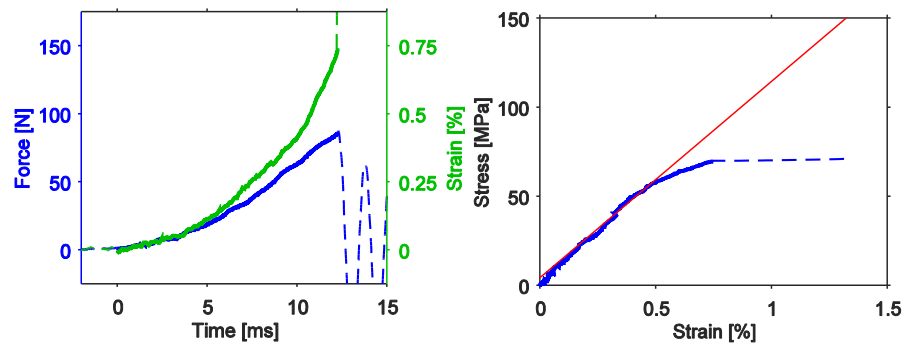


Figure 4.9 Typical force (blue) and strain (green) time histories (left) and corresponding engineering stress vs. engineering strain curves (right). Solid lines show data from commencement of loading to time of failure.

$$E = 18.61 \rho^{2.22}$$

$$\sigma_f = 109.54 \rho^{2.79}$$

ρ – Bone volume fraction

σ_f – Effective failure stress

E – Effective Young's modulus

Equation 4.1 Power law relationships.

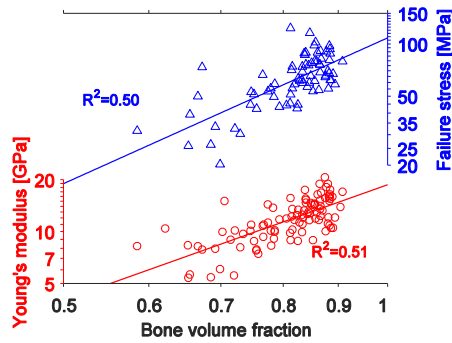


Figure 4.10 Effective Young's modulus and failure stress of calvarium cortical coupons as it varies with coupon bone volume fraction. Both y axes and the x axis are on logarithmic scales.

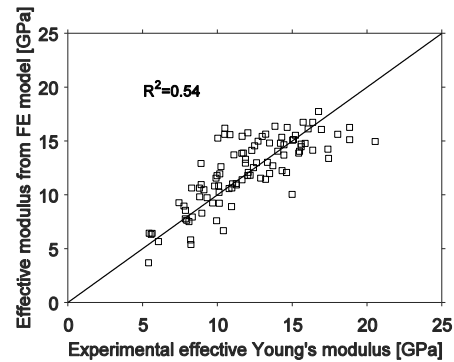


Figure 4.11 Effective structural modulus as predicted from implicit μ FE models vs. experimentally measured. A constant bone phase Young's modulus of 18.51 GPa was used.

4.3.2 Influence of bone microstructure – Implicit finite element model

The optimal value of bone phase modulus in the implicit FE models that yielded the experimentally determined effective modulus for each coupon has been summarized in Table 4.3. The predicted effective modulus using the average bone phase modulus of 18.51 GPa vs. the experimentally determined modulus for each coupon is shown in Figure 4.11. The coefficient of determination was improved from 51% to 54% with respect to the power law model.

4.3.3 Variance with subject and location on the calvarium

The average and standard deviation of effective Young's modulus, failure stress and failure strain at the different locations is shown in the contour plots in Figure 4.12. The variation of effective Young's modulus, failure stress and failure strain on the calvarium of nine individual subjects are shown in Figure A.8, Figure A.9 and Figure A.10, respectively (CT images of subject 1 did not include key anatomical landmarks and therefore its 2D projection could not be constructed). The Young's modulus of the bone phase at the osteon level as estimated from the empirical power law

model and implicit FE model are shown as average and standard deviation across nine subjects in Figure 4.13. These values for each individual subject are shown in Figure A.11 and Figure A.12.

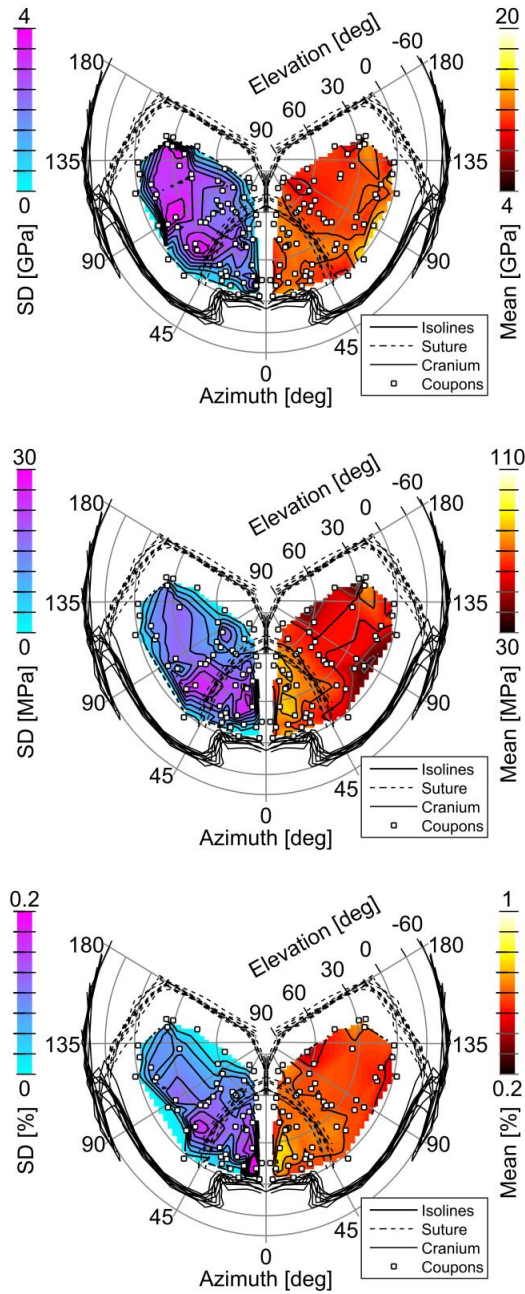


Figure 4.12 Effective structural Young's modulus (top), failure stress (middle) and failure strain (bottom) of the outer cortical layer. Contour map on right shows mean values across different subjects and on the left shows the standard deviations.

Table 4.2 Linear elastic material parameters for effective tensile response of human calvarium cortical bone from this study (shown in bold) and the literature.

	Percentiles					Average \pm SD
	Min	25 th	50 th	75 th	Max	
Elastic Modulus [GPa]						
<i>Current study (n=97)</i>	5.40	9.90	11.88	14.45	20.55	12.01 \pm 3.28
Robbins and Wood (1969) (n=50)						14.55
<i>Wood (1971) (n=123)</i>						16.00
Hubbard (1971) (n=8) *	7.79				15.31	9.72
Delille et al. (2007) (n=380) *	2.03				13.98	5.21
<i>Motherway et al. (2009) (n=18) *</i>						7.46 \pm 5.39
Auperrin et al. (2014) (n=167) *						5.00 \pm 3.12
<i>Peterson and Dechow (2002) (n=140) †</i>						21.00 \pm 3.8
Failure stress [MPa]						
<i>Current study (n=74)</i>	20.35	52.12	63.18	78.08	124.60	64.95 \pm 21.08
Evans and Lissner (1957) (n=15)	41.6				108.9	70.5
Robbins and Wood (1969) (n=50)						65.5
<i>Motherway et al. (2009) (n=18) *</i>						85.1 \pm 23.6
Failure strain [%]						
<i>Current study (n=74)</i>	0.34	0.48	0.58	0.65	1.09	0.59 \pm 0.15

Dynamic tests (nearest to strain rate 1 sec⁻¹) are shown in italics. Values derived indirectly from bending tests (*) and ultrasound tests (†) are also shown.

Table 4.3 Elastic modulus for bone phase at the length scale of osteons (in GPa).

	Percentile					Average \pm SD
	Min	25 th	50 th	75 th	Max	
Current study (n=97)	Human calvarium outer cortical layer (10 subjects)					
Power law model	11.52	16.27	19.04	20.96	32.48	19.00 \pm 3.91
Constant modulus FE model	12.04	15.94	18.39	20.02	28.95	18.51 \pm 3.46
Ascenzi and Bonucci (1967)	Human femoral shaft osteons (3 subjects)					
Tensile test; dry (n=7)						23.4 \pm 7.0
Tensile test; wet (n=12)						11.7 \pm 5.8
Rho et al., (1997) (n=12)	Human tibial cortex osteons (2 subjects)					
Nano-indentation						22.5 \pm 1.3
Rho et al., (1997) (n=6)	Human tibial cortex interstitial lamellae (2 subjects)					
Nano-indentation						25.8 \pm 0.7
Zysset et al. (1999) (n=1400)	Human (8 subjects)					
Nano-indentation	Femoral neck; osteonal					15.8 \pm 5.3
Nano-indentation	Femoral neck; interstitial					17.5 \pm 5.3
Nano-indentation	Femoral neck; trabecular					11.4 \pm 5.6
Nano-indentation	Femoral diaphysis; osteonal					19.1 \pm 5.4
Nano-indentation	Femoral diaphysis; interstitial					21.2 \pm 5.3

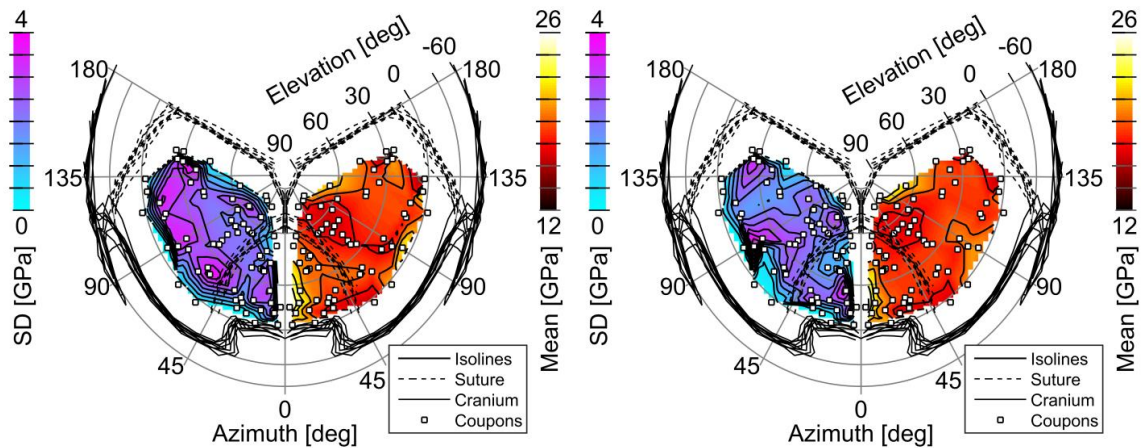


Figure 4.13 Young's modulus of calvarium cortical bone derived using empirical power law (left) and implicit FE models (right).

The mechanical properties of the coupons were normally distributed (Table A.25). One way ANOVA tests showed no significant variation of these properties with subject. The coupons were separated into two groups depending on whether it was harvested from the parietal bone or the frontal bone. One-way ANOVA within subject tests were then run for each measurement to compare these two groups taking into account between subject variations. The coupons were also divided into two groups, called superior and inferior, depending on whether they were harvested from the top or bottom of the calvarium (above or below 30° elevation with respect to the head coordinate system). The results of the ANOVA tests have been listed in Table A.26. The effective failure stress and strain differed between the frontal and parietal bones. Interestingly, the bone phase modulus, derived using the implicit FE models, was significantly different between the superior and inferior aspects of the calvarium, but not between the frontal and parietal bones.

Effective structural and bone phase mechanical properties for each coupon sample are tabulated in Table A.24.

4.4 Discussion

4.4.1 Effective properties of cortical coupons

The effective mechanical properties found in this study compare well with previously published studies where cortical layer coupons from the calvarium have been tested (Evans and Lissner, 1957; Robbins and Wood, 1969; Wood, 1971; summarized in Table 4.2). Elastic modulus derived from ultrasound pulse transmission techniques (Peterson and Dechow, 2002) have yielded numbers that are greater than values found through tensile testing. They are even greater than cortical bone phase modulus deduced in this study and found in several others. The bending response of composite bone beam samples from calvarium was adjusted using different strategies to estimate the stiffness of the cortical layers. Hubbard (1971) used a three layer sandwich structure approach, the thicknesses of which were determined through visual inspection. Delille et al. (2007) and Auperrin et al. (2014) used the ash percentage combined with a hollow beam assumption, and Motherway et al. (2009) used micro CT to determine mid-span second moments of area. The modulus estimated in all of these studies is less compared to the current study. This could be because bone from the cortical layers and the porous diploe have been treated identically.

4.4.2 Comparison to other studies of cortical coupons

Table 4.4 Effective mechanical properties from this study compared to other coupon tensile studies of human cortical bone

	Source	Strain rate [sec^{-1}]	Modulus [GPa]	Failure stress [MPa]
Current study	Calvarium	1.1	12.0 ± 3.3	65.0 ± 21.1
Kemper et al., (2005)	Rib	0.5	13.9 ± 3.7	124.3 ± 35.4
Subit et al. (2011)	Rib	1.7	13.5 ± 2.6	112.1 ± 24.5
Hansen et al. (2008)	Femur	1.0	16.5	120.0
Subit et al. (2013)	Femur	1.0	19.8 ± 2.2	123.7 ± 25.1
Subit et al. (2013)	Tibia	1.0	22.7 ± 0.9	167.4 ± 13.2

The effective Young's modulus of the cortical coupons is compared to those published by other authors for dynamic coupon tensile tests of cortical bone from the human body in Figure 4.5. A gradually increasing modulus and failure stress is observed as we travel lower in the body. The variance in both parameters is seen to decline. This observation is consistent with Wolff's proposal (Turner, 1992) that stress exerted on bone may influence its remodeling and architecture.

4.4.3 Properties of cortical bone at the micro scale

The fact that modeling the full micro-structure of cortical bone from the skull does not result in a large advantage in terms of predictive ability, as compared to using just porosity, reinforces Dempster's (1967) finding that the osteonal grain in this region is randomly oriented. It means that at a length scale larger than the coupon gage area (> 2.5 mm), modeling the skull cortical layers using an isotropic material is adequate.

The bone phase modulus deduced through BVF based power law model and through implicit FE models compares well with nano-indentation studies done by Rho et al. (1997) and Zysset et al. (1999) on cortical bone from tibia and femur (Table 4.3). Tensile tests conducted on single osteons from the human femoral shaft (Ascenzi and Bonucci, 1967) show that these values of bone phase modulus are closer to that of dry osteons. However, it should be noted that interstitial lamellae is stiffer than the osteons (Rho et al., 1997; Zysset et al., 1999). The variance in the data from this study is comparable to the nano-indentation studies and is less than the variance in Ascenzi and Bonucci's (1967) data.

The difference in the bone phase modulus, as calculated from micro FE, between the superior and inferior aspects of the calvarium may be caused by the in-vivo loading conditions of the skull. Due to gravity, the skull generally endures more loads in the inferior aspect as compared to the superior. This may be the reason the cortical bone in the inferior aspect is stiffer than that in the superior aspect (19.4 vs. 17.5 GPa respectively).

4.5 Conclusions

1. Bone microstructure near the cortical layer, as observable using μ CT at a resolution of 50 μ m, has small contribution to the variance in effective elastic modulus of the calvarium outer cortical layer.
2. Significant difference was found between frontal and parietal bone for effective failure stress and strain for the coupon tensile tests.
3. Bone phase modulus (18.51 ± 3.46 GPa) of the outer cortical layer varied significantly between the superior and inferior aspects of the calvarium.

5 Core compression tests

5.1 Objective

This study derives effective, isotropic, and homogenous elastic moduli of the porous diploe layer of the calvarium using compression tests on composite through-the-thickness cylindrical specimens (cores). These tests were conducted at strain-rates much lower than blast rates and the diploe layer properties found here are going to be used as quasi-static elastic modulus in its viscoelastic model. Cortical layer mechanical properties found in the coupon tensile study were used to isolate the properties of the diploe layer using the FE method. Concurrent μ CT study of the cortical test samples and the core samples ensured that the mechanical properties used for the cortical layers were representative and compatible with the layer thicknesses used. Within subject and between subject variations of the dynamic mechanical properties of the diploe has been reported.

5.2 Methodology

5.2.1 Specimen potting

After completion of μ CT and before testing, the skull cores were potted in a minimal amount of polyester resin (Bondo, 3M, Maplewood, Minnesota) in order to provide two flat parallel surfaces for mounting the specimen on the test rig. The mass of the cores was measured prior to potting using an electronic scale (resolution 0.01 g). The two part filler was mixed using syringes to produce consistent potting material. It was then applied to the inner and outer tables and put in a jig to ensure flat and parallel surfaces (Figure 5.1 top). The total potted thickness was measured using a digital Vernier caliper. Two typical potted skull core samples are shown in (Figure 5.1 bottom).



Figure 5.1 A skull core being potted (top) for mounting on the test device and two typical potted cores (bottom).

5.2.2 Dynamic compression test setup

The compression test setup (Figure 5.2) consists of the 8874 servo-hydraulic system (Instron, Norwood, Massachusetts) vertically pushing down on the potted core sample. Instrumentation consisted of a stationary piezo-resistive load-cell model 41 (Honeywell, Morristown, New Jersey) beneath the specimen and a linear potentiometer (Novotechnik T series, Novotechnik sensor oHG, Ostfildern, Germany) for sensing displacement. The component specifications are provided in Table 16. Data was recorded using a DEWE-2010 DAS (Dewetron GmbH, Wernau, Germany) at a sampling rate of 100 kHz.

The test fixture was all aluminum and consisted of a grooved specimen holder to prevent any accidental projectile due to slippage. The groove was larger than the core and the core specimen

were not restricted in the lateral directions during the tests. Also, no glue was used on the specimen boundaries during the compression tests, and the specimen was free to slip. The core specimens were loaded in the setup with the outer table facing the intruding Instron machine. A pre-load of 15 N was applied to ensure the loader was in contact with the core surface so that minimal inertial load was generated when the displacement was applied. A ramp displacement was then applied to the core outer table at a target rate of 15 mm/s. The target strain rate was 300 %/s. This choice was limited by the ability of the Instron to respond to a possible overload. To prevent any damage to the test equipment, the Instron control system was programmed to unload the setup when a force of 6.5 kN was reached.

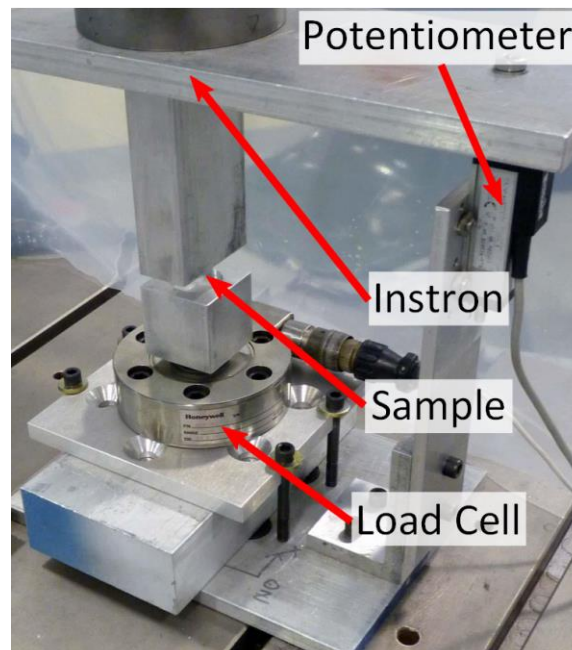


Figure 5.2 Compression test setup.

5.2.3 McElhaney's porous block model

To evaluate if the porosity of the diploe layer could be used to predict its mechanical modulus, the porous block model (PBM) was used. It was developed and used by McElhaney et al. (1970)

(Figure 5.3) to build a relationship between porosity, as it varies with depth through the thickness of the calvarium, and the effective Young's modulus of a skull core. It is based on the assumption that the material is composed of two homogenous phases, and one of them (the pore phase) does not lend any mechanical strength to the composite structure. Therefore, a linear relationship exists between porosity and modulus. Based on the observation that porosity is homogeneous on a plane tangential to the outer surface of the calvarium and that it varies only with depth, the through-the-thickness compression has been represented as the compression of a series of slabs with homogeneous porosity and thus, modulus. McElhaney et al. have used an assumed Gaussian through-the-thickness porosity distribution. The model parameter E_o (Equation 5.1) represents the actual stiffness of the bone phase. McElhaney et al. have observed that the value of E_o converges for calvarium core samples tested at quasi-static rates.

$$\frac{E_o}{E_r} = \int_0^1 \frac{dh}{(1 - \zeta(h))} \quad \text{Equation 5.1}$$

Where E_o – True Young's modulus of bone phase

E_r – Effective Young's modulus of calvarium in radial direction

h – Normalized through-the-thickness distance

$\zeta(h)$ – Porosity as a function of normalized through-the-thickness distance

In this study, the actual variation of porosity in the direction perpendicular to the skull outer surface has been determined from μ CT. Figure 5.4 shows the median and range of variation of porosity with depth, when averaged at a scale of 18.24 mm. The through-the-thickness distance has been normalized to the total thickness of the calvarium. Porosity variation specific to each sample has been used in Equation 5.1 in order to numerically find the actual stiffness of the bone

phase in order to see if porosity actually accounts for the variability in effective Young's modulus of the core samples even at dynamic loading rates.

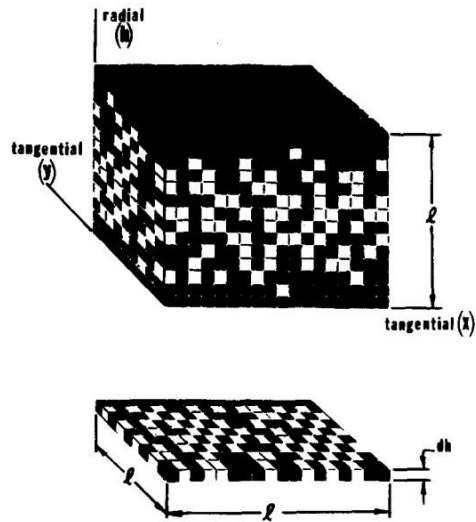


Figure 5.3 Porous block model used by (McElhaney et al., 1970).

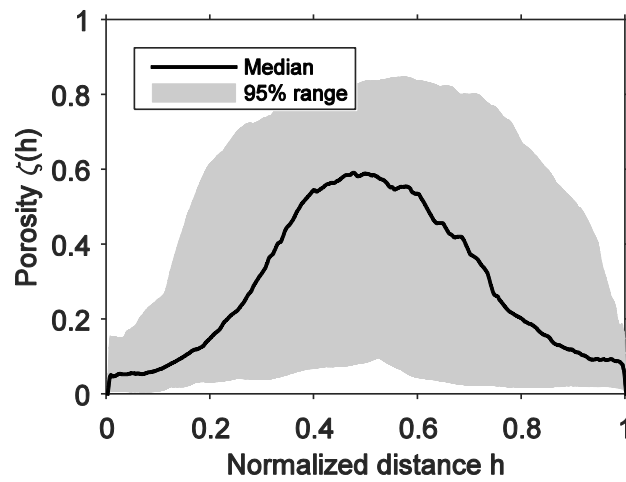


Figure 5.4 Median and 95% range of through-the-thickness variation of porosity in the calvarium.

In addition to finding the actual Young's modulus of the bone phase (using Equation 5.1), the PBM can also be used to determine the actual stress and strain of the bone phase as it varies with depth through the thickness. On the basis of the assumptions of the porous PBM, the stress

supported by the bone phase at any particular depth is inversely proportional to the bone volume fraction at that depth.

$$\sigma_o(h) = \frac{\sigma_r}{(1 - \zeta(h))} \quad \varepsilon_o(h) = \frac{\sigma_r}{E_o(1 - \zeta(h))} = \frac{\varepsilon_r E_r}{E_o(1 - \zeta(h))}$$

From Equation 5.1,

$$\varepsilon_o(h) = \frac{\varepsilon_r}{(1 - \zeta(h)) \int_0^1 \frac{dh}{(1 - \zeta(h))}}$$

$$\sigma_{o_{max}} = \frac{\sigma_r}{(1 - \zeta_{max})} \text{ and } \varepsilon_{o_{max}} = \frac{\varepsilon_r}{(1 - \zeta_{max}) \int_0^1 \frac{dh}{(1 - \zeta(h))}} \quad \text{Equation 5.2}$$

Where $\varepsilon_o(h)$ – Engineering strain of bone phase as a function of depth through the thickness

σ_r – Engineering stress in radial direction

ε_r – Effective engineering strain of calvarium in radial direction

$\sigma_{o_{max}}$ – Maximum theoretical stress occurring in the bone phase

$\varepsilon_{o_{max}}$ – Maximum theoretical strain occurring in the bone phase

ζ_{max} – Maximum porosity

Equation 5.2 has been used to determine the theoretical peak engineering stress and strain that occurs in the bone phase at failure.

5.2.4 Core simplified finite element model and optimization

Prior to testing, the specimens were scanned (using VivaCT, Scanco, Brüttisellen, Switzerland) at a resolution of 25 μm . Segmentation of the bone phase was done using a probabilistic approach.

Contiguous bone on the inner and outer surface of the cores was deemed as the cortical layers and their thicknesses were measured (more details in Section 3.2; median values of thicknesses as it

varies across the surface of the cores were used). As a result of the inhomogeneous nature of the specimens and the curvature of the interfaces between the different parts (the diploe layer, the cortical layers, and the potting layers) in the sample, the stress and strain field within each part is inhomogeneous. Therefore, these parts neither behave as springs in parallel nor as springs in series, but somewhere in between these extremes. This prohibited a straightforward analysis of the constitutive behavior of the diploe layer and an FE study was necessitated.

The FE mesh built from μ CT images included five parts – outer potting layer, outer cortical layer, diploe layer, inner cortical layer and the inner potting layer (from top to bottom in Figure 5.5 and Figure 5.6). The cortical layers in the FE models had constant thickness equal to the median value of thickness measured from μ CT for that particular core sample. The diploe layer occupied the entire volume between the two cortical layers. Since the objective was to derive effective modulus of the diploe layer, the individual trabeculae and pores were not modeled. Although the mesh resolution was 1 mm, the coordinates of the nodes at the interface of each part is within $\pm 30 \mu\text{m}$ of the actual interface. Each cortical layer had 442 hexahedral elements. The remaining parts included tetrahedral and pentahedral elements to capture the curvature of the interfaces while maintaining element quality. The FE models had approximately 4,000 elements in total.

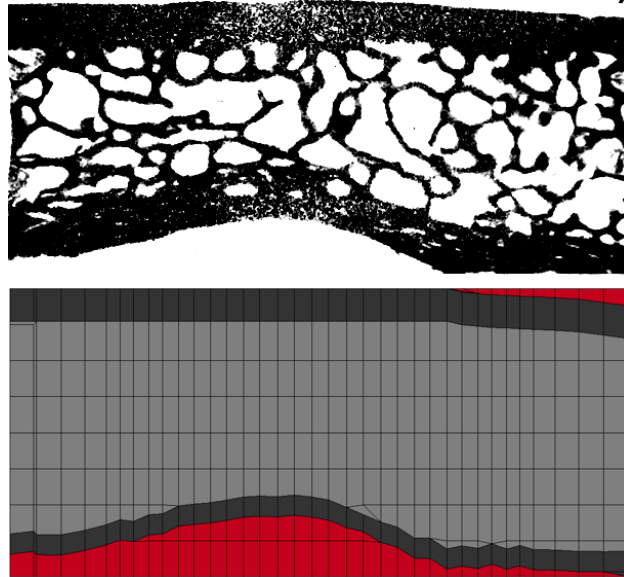


Figure 5.5 μ CT Cross-section image (top) and corresponding FE mesh. Red – potting, dark gray – cortical layers, light gray – diploe layer (bottom).

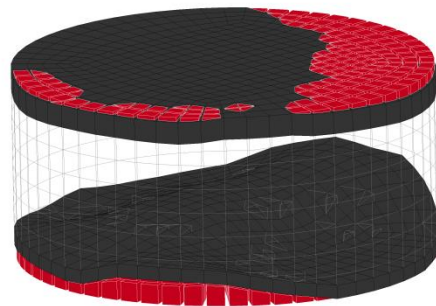


Figure 5.6 Three dimensional rendering of the FE mesh. Red – potting (elements have been shrunk for visibility), dark gray – cortical layers, light gray – diploe layer (shown as a wireframe).

5.2.5 Material properties and boundary conditions

Homogenous isotropic elastic materials were used for all the parts. Elastic modulus of the potting layers (364 MPa) was determined by conducting dynamic compression tests on a polyester core at similar strain rates and on the same test setup in which the potted samples were tested. Elastic

modulus of the outer cortical layer (18.51 ± 3.46 GPa) was taken from the coupon tensile study (Chapter 4). The modulus of the inner cortical layer was assumed to be the same as that of the outer layer. The bone phase modulus for each coupon on the left calvarium was used as the elastic modulus of the inner and outer cortical layers of the corresponding core from the right calvarium. Poisson's ratio for the cortical layers was taken from the literature ($\nu_{\text{cortical}} = 0.4$, Dong and Guo, 2004; Robbins and Wood, 1969). Simulations were run to assess the influence of strain and diploe layer modulus using the LSDYNA implicit solver (R7.1.1, LSTC, Livermore, CA).

The bottom node set was constrained in the vertical axis but were free to translate in the transverse axes. The top node set was displaced by a distance corresponding to 1% compressive strain. This value was approximately the higher limit of the linear stress vs. strain region in the dynamic compression experiments. The LSDYNA implicit solver was used to calculate the force required to produce this strain. The Newton Raphson method was used to iteratively obtain a value of diploe elastic modulus that yielded a structural force within 1 N of the observed experimental force. Force at 1% strain in the experiments was approximately 600 N. The value of diploe layer Poisson's ratio was obtained from the literature ($\nu_{\text{diploe}} = 0.2$, Dalstra et al., 1993; McElhaney et al., 1970).

5.3 Results



Figure 5.7 Calvarium core samples, belonging to subject 3, before (columns 1 and 3) and after (columns 2 and 4) testing. Failure cases have been shown by the red boxes.

5.3.1 Typical compression response

The test samples from a typical subject before and after testing are shown in Figure 5.7. A typical time history of the force and displacement for a failure case and the corresponding stress vs. strain curve is shown in Figure 5.8. At the beginning of the experiments, the displacement was seen to climb very fast compared to the force (Figure 5.8 top, A to B). This corresponds to the shallow non-linear stress vs. strain response (Figure 5.8 bottom, A to B). This nonlinear toe region was followed by a linear region (Figure 5.8, B to C). To facilitate comparison of stress vs. strain curves, the linear region was extrapolated to zero stress and the remaining strain (shown in Figure 5.8 bottom, G) was deducted. In effect, the stress strain curve was shifted left wards until the linear region intersected the origin. The trabecular diploe then failed as indicated by drop in force (Figure 5.8 D) and displacement increased at a higher rate. This was sometimes

accompanied by ejection of material from the trabecular region (Figure 5.7). The tables then came into contact with the trabecular debris and another linear domain set in (Figure 5.8 E to F). As the stress approached the set limit of 24 MPa, the core was unloaded. The sequence of events for the non-failure cases were the same except the stress limit was reached before any failure occurred.

Discounting the toe-region and the non-linearity near failure, the composite cores typically behaved as a linear elastic material. Engineering stress (force divided by sample un-deformed cross-sectional area) and engineering strain (displacement divided by sample un-deformed thickness) has been used in this paper because of the low strains involved (Peak strains – $7.68 \pm 2.35 \%$ and $6.67 \pm 1.75 \%$ in non-failure and failure cases respectively). The reported composite structural elastic modulus is the slope of the linear region in the stress vs. strain curve.

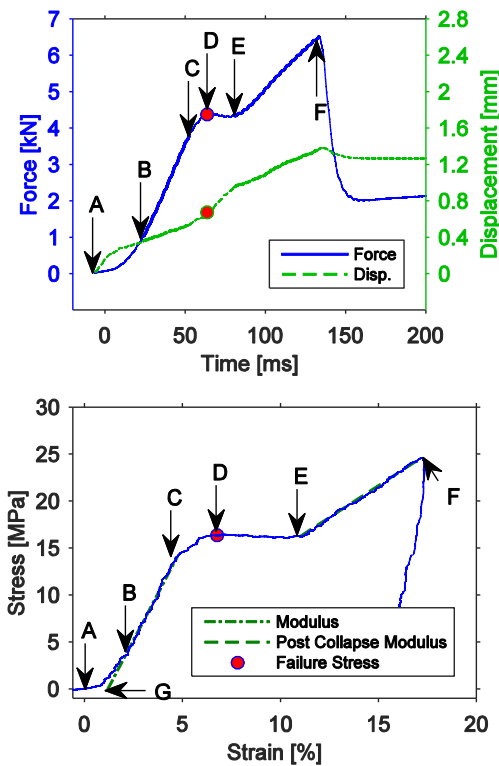


Figure 5.8 Typical force and displacement time histories in failure cases (top) and corresponding engineering stress vs. engineering strain curve (bottom).

5.3.2 Composite structural Young's modulus

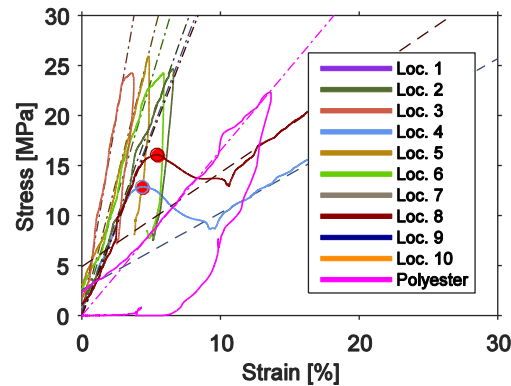


Figure 5.9 Engineering stress vs. engineering strain for samples belonging to a particular subject. The response of potting material (polyester) is also shown.

The results for 83 calvarium core samples are presented here. Fifteen samples were excluded from this study because of unusual size or shape or outlying mechanical response. Figure 5.9 combines the engineering stress vs. strain responses of the different samples from one particular subject. All the stress vs. strain plots combined by subject and by location, are shown in Figure A.13 and Figure A.14. The composite structural Young's modulus of all the core samples was 447.92 ± 134.18 MPa and ranged from 203.64 to 912.21 MPa (response for each sample tabulated in Table A.27). They were normally distributed in all of the subjects (Table A.28). One-way ANOVA tests showed that it varied significantly between subjects. No significant difference was found between composite structural elastic modulus of the frontal bone and parietal bone (one-way within subject ANOVA, $p > 0.05$ Table A.29). The average and standard deviation of composite structural Young's modulus at the different locations is shown in the contour map in Figure 5.10 (subject-wise distributions are shown in Figure A.15).

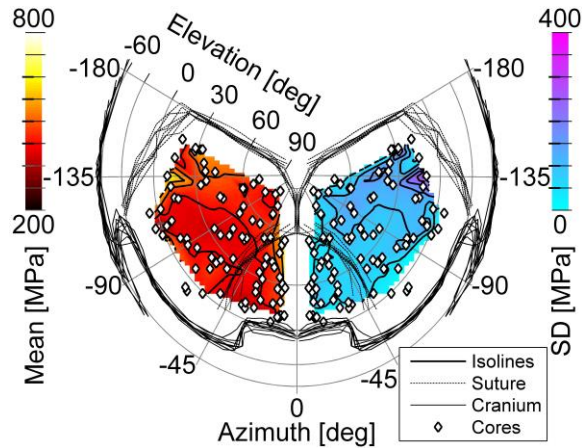


Figure 5.10 Composite structural Young's modulus in through-the-thickness compression. Contour map on left shows mean values across different subjects and on the right shows the standard deviations.

A total of 16 out of 83 core samples failed during the tests. Although this study was not designed to find failure characteristics of the cores, given the significant number of samples that failed, failure characteristics have been developed. The average effective failure stress in the failed specimens was 15.95 ± 4.03 MPa. Since all of the specimens did not fail, this number represents the average failure stress among the cores that were weak. Average porosity had a significant influence on effective failure stress ($R^2 = 0.33$). If average porosity is assumed to be the dominant factor in determining effective failure stress, the mean effective failure stress can be predicted on the basis of the linear regression model and distribution of average porosity. This yields an average effective failure stress of 20.26 ± 16.48 MPa. There was no correlation between effective strain and average porosity.

5.3.3 McElhaney's porous block model

Contrary to what was expected, the actual Young's modulus of the bone phase, computed using the PBM, had a larger variance than the effective modulus. It had an average value of 784.93 ± 297.30 MPa and ranged from 222.34 to 1872.32 MPa. The increase in variance of Young's modulus shows that the PBM cannot be used directly for dynamic loading. It is interesting to note

that upon accounting for porosity using the PBM, a modest correlation was developed between Young's modulus and average porosity, although the residual error actually increased. Bringing further dispute to the PBM, the variance in both failure stress and failure strain increased upon compensating for porosity, and the correlation between failure stress and average porosity was diminished.

5.3.4 Simplified finite element model

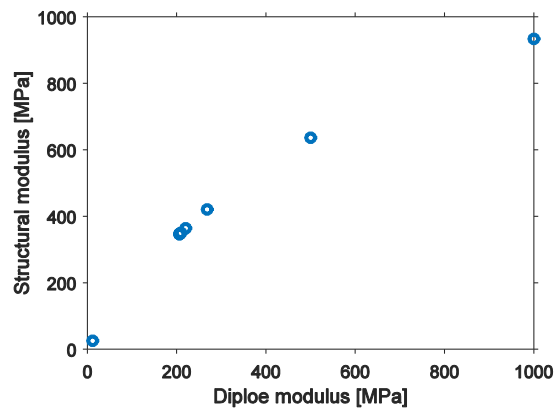


Figure 5.11 Typical relationship between diploe elastic modulus and structural modulus (force response normalized to strain and cross-section area) calculated using the simplified FE model (shown in circles).

To evaluate the influence of mesh size on the relationship between diploe modulus and structural response, simulations were run for five core samples with a finer mesh (0.5 mm). The resulting structural force response had a root mean square difference of less than 0.1% when compared to that of the 1 mm mesh.

A preliminary series of simulations showed that the structural response was linear with respect to strain, within reasonable limits. The structural response was monotonic, but non-linear with respect to diploe layer modulus. A typical curve is shown in Figure 5.10. The optimization was initialized with two initial seed values of diploe elastic modulus (500 and 1000 MPa). The

subsequent values were interpolated using the piecewise linear function from value of diploe elastic modulus and resulting structural modulus pairs that were previously simulated. The structural force response converged to within 1 N of the experimentally observed value typically within 10 iterations. A full preliminary simulation matrix is shown in Table 5.1.

Table 5.1 Simulation matrix – core simplified FE models run using LSDYNA implicit for identification of quasi-static modulus.

Number of cores	Mesh size [mm]	Strain [%]	Diploe layer elastic modulus [MPa]
Preliminary			
5	1.0	0.5, 1.0, 2.0, 5.0	500
5	1.0	1.0	100, 200, 500, 2000
Mesh sensitivity			
5	0.5, 1.0	1.0, 2.0	500
Final			
83	1.0	1.0	500, 1000, Newton Raphson iterations

The optimal diploe effective elastic modulus had an average value of 273 MPa and a standard deviation of 125 MPa (summarized statistics in Table 5.2 and values for each sample in Table A.27). They were normally distributed in a vast majority of the subjects (Table A.28). They varied significantly between subjects (one-way ANOVA test $p < 0.05$ Table A.29). To study the effect of anatomical location, the samples were divided into two groups, frontal or parietal, depending on the source bone and again into two groups, superior and inferior, depending on the elevation angle of its harvest location being greater or lesser than 30° . There was no significant difference between the diploe modulus of superior vs. inferior groups (One way within subjects ANOVA, $p > 0.05$). But the difference between frontal and parietal bones was significant (One

way within subjects ANOVA, $p < 0.05$). The optimal values of diploe modulus are shown in Figure 5.12 in terms of average across the subjects and standard deviation. Their statistical distribution is summarized in Table 5.2. Diploe modulus for each individual subject is shown in Figure A.16 (Reference anatomical landmarks were not captured in CT images of subject 1; therefore, corresponding 2D projections could not be built). Cross-section images from μ CT and the corresponding meshes for each core sample are shown in Section 14.4. The mechanical properties derived are also summarized.

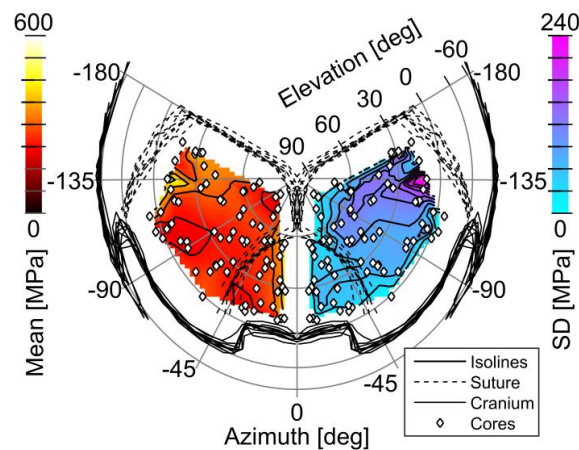


Figure 5.12 Effective elastic modulus of the diploe layer under compression in the normal direction. Contour map on left shows mean values across different subjects and on the right shows the standard deviations.

An explanation for the toe-region in the stress vs. strain response, other than being an actual characteristic of the response, may be the slightly imperfect alignment or roughness of the mounting faces of the cores. Hypothetically, the misalignment (estimated at $91.3 \pm 68 \mu\text{m}$ assuming the toe region is caused exclusively by misalignment) leads to a small area of contact, and hence, a softer response at the beginning of the experiment. This toe region would have resulted in a spurious non-uniform strain field with a peak magnitude of $1.37 \pm 1.1 \%$. Peak strain produced in the experiments was $9.93 \pm 5.44 \%$. Thus, the spurious non-uniform (in the direction transverse to the axis of compression) strain field may be considered negligible compared to the

peak strains produced in the experiments, and the assumption of uniform strain field inside the core may be considered valid.

Table 5.2 Linear elastic modulus for the effective response of porous bone under compression from this study (shown in bold) and the literature (in MPa).

	Percentiles					Average \pm SD
	Min	25 th	50 th	75 th	Max	
Human skull diploe layer						
<i>Present study (n=83)</i>	67.42	194.70	240.00	332.90	751.10	273.35 \pm 125.25
<i>Melvin et al. (1970)</i>						1379.00
From Other sources						
<i>Human tibial plateau (n=20)</i>					<i>Carter and Hayes (1977)</i>	81.2 \pm 76.4
Human lumbar spine (n=9)					Keaveny et al. (1997)	165 \pm 110
Vertebra (T10 – L5; n=30)					Morgan and Keaveny (2001)	344 \pm 148
Proximal tibia (n=15)					Odgaard and Linde (1991)	1091 \pm 634
Femoral neck (n=14)					Odgaard and Linde (1991)	3230 \pm 936
Dynamic tests are shown in italics. Wherever possible, dynamic properties have been chosen for a rate of 1 sec ⁻¹ .						

5.4 Discussion

5.4.1 Effective modulus of the cancellous diploe layer

The diploe elastic modulus found in this study is less compared to that reported by Melvin et al, who tested cuboidal specimens of fresh human diploe under compression between steel platens. They did not report the number of specimens or the statistical variance of the measured Young's moduli; therefore, it is difficult to interpret their results in the context of this study. However,

they did mention that in order to limit maximum compressive strain in high speed tests, a positive mechanical stop was used to limit ram travel. No other study was found that reported the elastic modulus of the diploe layer. It is true that there is a wide variation in the reported effective modulus of porous bone from other bones in the human body (Table 5.2). For instance, average values as different as 81 and 1091 MPa have been reported for the elastic modulus of porous trabecular bone from the proximal tibia (Carter and Hayes, 1977; Odgaard and Linde, 1991). The difficulty of directly testing porous bone is partially responsible for this large variance.

Measurement of strain from displacement of sample ends during compression tests may lead to significant underestimation of modulus (Odgaard and Linde, 1991). This can be overcome by strain measurement over a small segment of the sample using either strain gages or an optical instrument. End effects can also be overcome by potting porous bone samples inside end caps (Keaveny et al., 1997). Testing composite specimens, with the sandwich structure intact, mitigates this error.

The potting layer is necessitated by the curvature of the specimens. In addition to the interface between the potting layer and the cortical tables, the interface between the cortical tables and the diploe is curved. As a result of this curvature and the inhomogeneity of the diploe layer, the effect of the cortical layers and potting layers cannot be directly cancelled from the composite response, and finite element analysis is required. Perhaps due to the difficulty of distinction of the diploe layer from the cortical tables, despite several researchers having studied the composite response of the skull, even at dynamic rates (Halgrin et al., 2012; Motherway et al., 2009), none have tried to isolate the mechanical properties of the diploe. μ CT has helped in the delineation of the three layers by showing even the smallest of pores.

5.4.2 Current FE models

There is opportunity for improvement of the biofidelity of current head FE models. In contrast to the findings presented here, they use much higher values of diploe elastic modulus (Table 5.3). Consequently, they are stiffer in through-the-thickness compression. It is true that the presence of fluid in the diploe layer does result in strain-rate related stiffening and the effective modulus of the diploe layer is higher at higher strain rates.

Table 5.3 Diploe elastic modulus from this study (shown in bold) and diploe layer thickness compared to values used in current head FE models.

	Elastic modulus [MPa]	Diploe layer thickness
Current study	273	0.71 (average value)
Horgan and Gilchrist (2003)	1000	0.43
Panzer et al. (2012)	3257	0.40
Mao et al. (2013)	600	
Asgharpour et al. (2014)	4600	0.43

Wherever possible, dynamic mechanical properties have been chosen for a rate of 1 sec^{-1} .

Diploe layer thickness is expressed as a ratio to total thickness.

5.5 Conclusions

1. Porosity of the diploe layer had no significant influence on its effective elastic modulus.
2. Both composite through-the-thickness and effective diploe layer moduli varied significantly between subjects.
3. Effective Young's modulus of the diploe layer of the calvarium ($273 \pm 125 \text{ MPa}$) was found to vary between the frontal and parietal bones.

6 Core transmissibility tests

6.1 Objective

This study develops linear viscoelastic mechanical properties of the porous diploe layer of the calvarium using data from cyclic loading tests conducted on cylindrical samples from the human calvarium. The viscoelastic properties of the diploe layer were isolated from the combined response using the FE method. μ CT was utilized to build geometrically accurate FE mesh describing the shape of each layer in the sandwich structure of the test samples. Between subject and within subject variation of viscoelastic properties of the diploe layer have been reported.

6.2 Methodology

6.2.1 Transmissibility test setup



Figure 6.1 Transmissibility Test setup; Shaker and shaker-side instruments (left); Index table and table-side instruments (right); please note that an aluminum placeholder sample is installed in the image on right.

The transmissibility test setup (Figure 6.1) consisted of a piezo-electric reaction mass-type shaker (F7-1; Wilcoxon Research, Germantown, MD) exciting the test specimen against an index table. Test instrumentation included a piezo-electric load cell (DLC 101-50, Omega Engineering, Stamford, CT) and a piezo-electric accelerometer (8309, Brüel & Kjær, Nærum, Denmark) on

both sides of the core test specimen. All data were sampled at 2 MHz using a Synergy-CS data acquisition system (Hi-Techniques, Madison, WI). All the components of the test system (the shaker, instruments and test specimen) were mounted in the same horizontal axis with the core outer table facing the shaker. An index table was used to accommodate specimens of various thicknesses. Cyanoacrylate was used to glue the specimen to the test setup and it went into both compression and tension. The setup was installed on a vibration isolation table. A schematic of the test setup is shown in Figure 6.2.

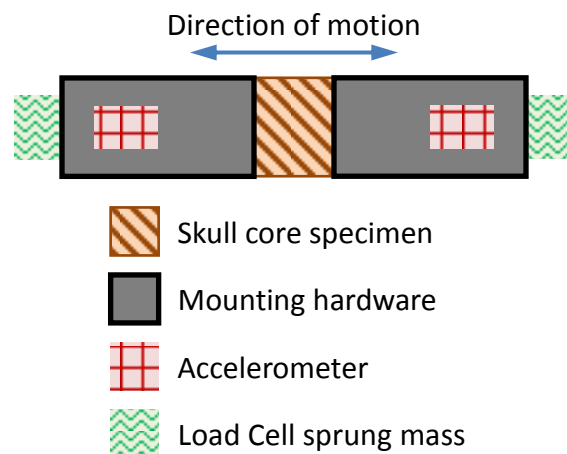


Figure 6.2 Schematic of test setup; skull core specimen sandwiched between two pseudo rigid transducers consisting of mounting hardware, accelerometer and load-cell sprung mass.

The transmissibility test control system was designed and run in LabVIEW (Figure 6.3). A Rigol DG 1022 arbitrary waveform generator was controlled through USB using the National Instruments Virtual Instrument Software Architecture (NI-VISA) to calibrate the shaker power amplifier. Excitation signal amplitudes depended on the frequency of excitation and were predetermined to control oscillation near resonance spots and ensure a nearly constant displacement magnitude. There was feedback from the waveform generator confirming generation and cessation of excitation voltage. The Synergy-CS data acquisition system,

controlled by LabVIEW over the Ethernet using transmission control protocol (TCP / IP), provided feedback indicating amplitude of oscillation, which was used to ascertain steady-state vibration. The system was programmed to deliver vibration at discreet frequencies ranging from 1 kHz to 20 kHz (evenly spaced in the logarithmic domain) and record steady state vibrations at each frequency. Steady-state was considered to have been established if the amplitude of force varied by less than 5% in the last quarter of the loading. Those frequencies, at which steady-state could not be achieved before sensor signals were saturated, were skipped.

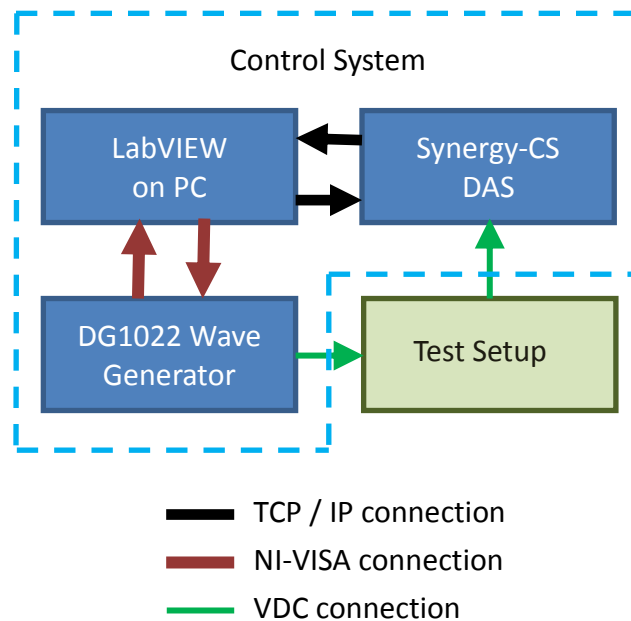


Figure 6.3 Schematic of the test control system; the controller (LABVIEW software in PC) communicates via TCP / IP with data acquisition system and via NI-VISA with the waveform generator.

In fact these tests were done on the cores before they were tested in the compression test setup. The strain amplitudes attained in the transmissibility tests were much smaller than the strains delivered in the compression tests and it was assumed that no permanent change occurred in the cores after they were tested in the transmissibility setup.

6.2.2 Viscoelastic material model for the diploe

The standard linear solid model was used to describe the constitutive behavior of the diploe layer. The time constant (β in Figure 6.4) was held constant so that the viscoelasticity could be compared across all samples. A time constant of 20 μs ($\beta=50$ kHz) was chosen to represent the gradual stiffening of the material over the course of the tested frequencies (1 – 20 kHz). The two other parameters E_∞ and E are referred to as the quasi-static modulus and the viscoelastic modulus, respectively. The value of Poisson's ratio was obtained from the literature ($\nu_{\text{diploe}} = 0.2$, Dalstra et al., 1993; McElhaney et al., 1970).

The viscoelastic properties derived in this study are designed for use in high strain rate scenarios such as impact and explosive blast. Therefore, relatively low-rate dynamic compression response of the diploe layer, derived in Chapter 5, was used as the quasi-static component of the diploe linear viscoelastic model.

6.2.3 Experimental and FE model boundary conditions

In the test setup, the potted skull cores are fixed to the mounting hardware on both inner and outer surfaces, and the circumference of the cylindrical specimen is traction free. Thus, the inner and outer tables move only longitudinally and there is no transverse (radial) motion at the two boundaries. However, it is probable that there is transverse motion of the core material at other locations within the core, especially near the traction-free boundary. Although this effect could have been avoided by careful selection of sample size, the core diameter was constrained by the size of the pores in the diploe. A minimum diameter of cores was required for valid continuum assumption. Also, due to the curvature of the skull, cores could not be over a certain maximum diameter in order to avoid requirement of excessive potting. These factors precluded the exploitation of the diameter to length ratio of the core samples towards problem simplification.

There is also the possibility of the pore contents to flow out of the diploe without any resistance even though material drip was not noted during testing.

Cyclic compression-tension loading tests were done on the cores and the steady-state force and displacement boundary conditions ($F(t)$, $u(t)$ and, $u'(t)$ in Figure 6.4) were recorded at discrete frequencies of loading ranging from 1 to 20 kHz. Since the test setup had to accommodate samples of varying sizes, there was unwanted compliance resulting in significant displacement at the blocked end ($u'(t)$ in Figure 6.4). This displacement has been recorded in the tests and applied in the FE models used in this study. As a consequence of this displacement, at certain frequencies, much of the force response could be attributed to specimen inertia. This effect was especially pronounced at large frequencies of loading. These displacement boundary conditions were used as input conditions for the FE models used in this study. The force boundary condition was the optimization objective.

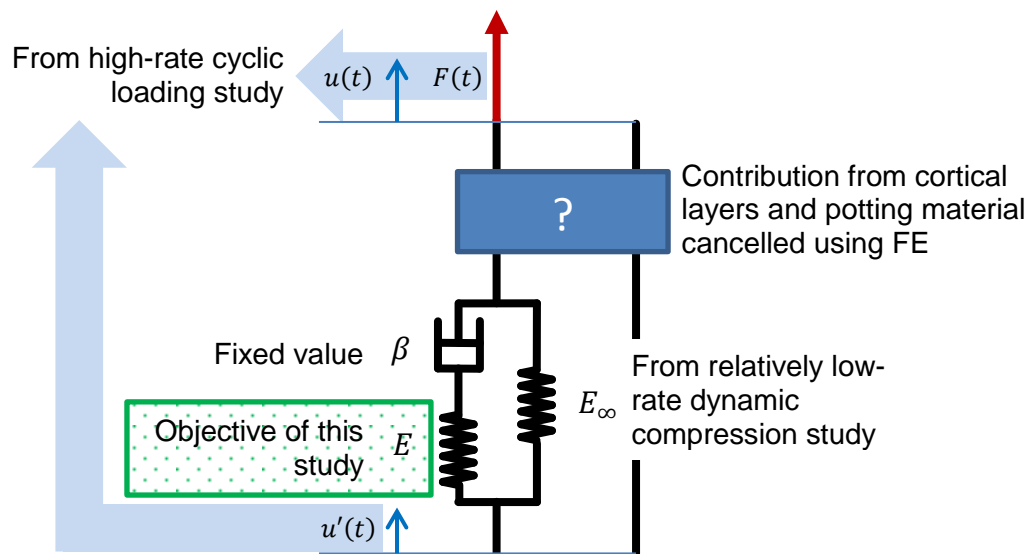


Figure 6.4 Illustration of methodology used for obtaining viscoelastic properties of the diploe layer of the calvarium. The diploe material is represented by the standard linear solid element with three parameters.

The same FE meshes that were used in chapter 5 were used in this study. As mentioned in chapter 5, the linear elastic material model was used to describe the behavior of the cortical layers. The cortical layers have been assumed to have no strain-rate related effects in this study, and the entire through-the-thickness composite viscoelasticity has been accommodated in the viscoelasticity of the diploe layer. The FE model exhibits correct effective viscoelasticity despite the cortical layers having no viscoelasticity.

A cylindrical core sample with dimensions similar to the potted skull cores was constructed with only potting material. This polyester core was tested using the same low-rate dynamic compression and cyclic loading protocols in order to estimate its viscoelastic material properties for application in the FE models used in this study. As mentioned in chapter 5, low-rate dynamic modulus of the potting material was obtained in the same manner in which the low-rate properties of the core samples were found, and its viscoelastic component was determined using the same methodology described here.

The nodes in the top and bottom boundaries of the samples were constrained in both axes perpendicular to the cylinder axis and their motion along the axis of the cylinder (amplitude, frequency and phase) was prescribed according to experimental observations. The FE model was solved using the LS DYNA (R7.1.1, LSTC, Livermore, CA) explicit solver. The diploe layer viscoelastic modulus was optimized to match the resulting force amplitude at steady-state and the experimental force amplitude. The optimization was done using the Newton Raphson method to obtain a least square fit of the force spectrum.

Steady-state in the simulations was ascertained using an approach similar to that used in the experiments. If the averaged force amplitude in the last quarter of loading was less than 5% different from that in the third quarter, steady-state was said to have been achieved. Simulations

were run for an initial 24 cycles of loading and the number of cycles was doubled every time steady-state was not reached.

6.2.4 Inertia

Mass densities of the different parts in the model have a large contribution to the force spectrum, particularly at frequencies where the acceleration amplitude is large. The mass of the polyester core was directly measured and the density of potting material (1.17 g/cm^3) was determined via division by volume of the core. The density of the cortical and diploe layers was not so straightforward. The densities of the two cortical layers were assumed to be equal. This density was obtained from the regression coefficient of the skull core sample mass, measured before potting, expressed as a bi-linear function of the combined volume of the cortical layers and the volume of the diploe layer. The regression coefficient corresponding to the combined volume of the cortical layers (2.37 g/cm^3) was used as the mass density of both cortical layers in the FE models of all the cores. The mass of the cortical layers of each core was then deducted from their measured total mass and the remaining mass was divided by the volume of the diploe layer to obtain diploe layer density for that particular core ($1.48 \pm 0.15 \text{ g/cm}^3$).

6.3 Results

6.3.1 Data from cyclic loading tests

The excitation level for the frequency sweep was adjusted so that a constant displacement and thus constant strain was delivered over the entire frequency range. The displacements at both ends of the sample were captured using accelerometers with large bandwidth. The displaced end of the sample was called the shaker-side and the blocked end was called the table-side. A typical set of results from cyclic loading tests is shown in Figure 6.5. The magnitudes of the signals are shown in the left and the phases are shown in the right. The magnitude of acceleration on the

shaker-side was increased with frequency (blue triangles; Figure 6.5 left) in order to maintain displacement amplitude. The force response (black circles; Figure 6.5 left) was observed to climb with increasing frequency despite maintenance of a steady strain level (approximately 100 μ strain). This is a combined effect of viscoelastic stiffening and sample inertia. The phases of the different signals show two important phenomena. At the low frequency end, the force (black circles; Figure 6.5 right) is out of phase with acceleration, as if a massless spring was being excited. But as the frequency of oscillation increases, a phase transition occurs in the force (near 3 kHz in Figure 6.5 right) due to dominance of sample inertia with increasing acceleration levels. The second note-worthy phenomenon is the phase transition of table-side acceleration (red triangles; Figure 6.5 right). At the low frequency end, the table-side acceleration is in phase with the input shaker-side acceleration. But it becomes out of phase (near 7 kHz Figure 6.5 right) in the super-resonance frequency domain as the mode of vibration changes. The table-side acceleration is nearly negligible at the low frequency end but is significant near the resonance frequency. All of these effects are observable in the FE simulations.

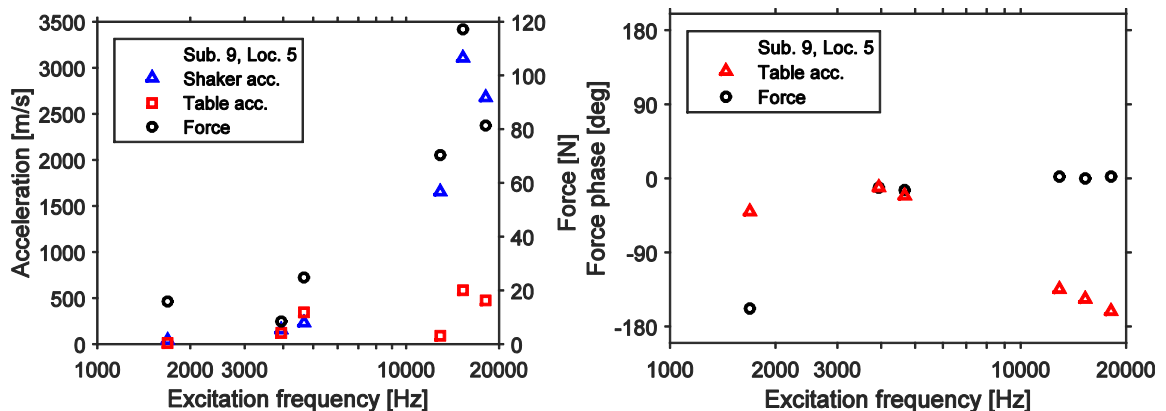


Figure 6.5 Typical results from cyclic loading tests. Magnitudes are plotted on the left and phases on the right.

Horizontal axes are on a logarithmic scale.

6.3.2 Mesh sensitivity and viscoelasticity parameter optimization

To evaluate the influence of mesh size on the relationship between diploe viscoelastic modulus and the force spectrum, simulations were run for five core samples with a finer mesh (0.5 mm). The resulting force spectrum had an RMS difference of less than 0.5% when compared to that of the 1 mm mesh. The Newton Raphson optimization was initialized with two seed values (6.0 and 7.5 GPa) and the force amplitude averaged across the spectrum converged to within 5% of the experimentally observed average typically within 5 iterations. The initial seed values were chosen on the basis of the stiffening of the dynamic composite response over the frequency range of excitation (1 to 10 GPa in Figure 6.6). However, much of the stiffening was found to originate from the inertia of the test samples rather than viscoelasticity of the diploe layer and the viscoelastic modulus converged to lower values during optimization. A detailed simulation matrix is shown in Table 6.1. A typical set of results of optimization is shown in Figure 6.6.

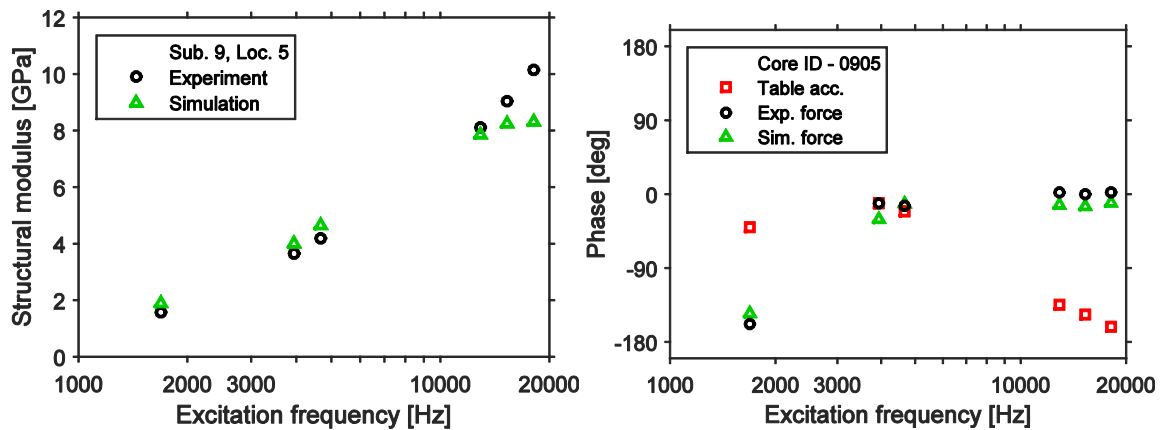


Figure 6.6 Typical set of results showing force response (normalized to cross-section area and magnitude of strain) from simulation with optimized viscoelastic modulus (triangles) compared against the experimental results (circles). Magnitudes are plotted on the left and phases on the right.

Table 6.1 Simulation matrix – core simplified FE models run using LSDYNA explicit for identification of viscoelastic parameters.

Number of cores	Mesh size	Frequency [kHz]	Diploe viscoelastic modulus [GPa]
Mesh sensitivity			
5	0.5, 1.0 mm	~ 10	6.0
Final			
81	1.0 mm	Typically 6 levels	6.0, 7.5, Newton Raphson iterations

6.3.3 Viscoelastic modulus

The optimized standard linear solid model parameters of potting material and the diploe layer are shown in Table 6.2 (viscoelastic moduli for each sample tabulated in Table A.30). Its variation across the calvarium in terms of average and standard deviation is shown in Figure 6.7. The force and acceleration magnitude and phase spectra for each core are shown in Sections 14.6.1 and 14.6.3 respectively. Section 14.6.2 shows the experimental and optimized simulation spectra of apparent dynamic modulus. The phase spectra of optimized simulations are also shown in Section 14.6.3.

Table 6.2 Optimized standard linear solid model parameters. (± 1 S.D. are shown)

Standard linear solid model	ρ [g/cm ³]	E_{∞} [MPa]	$E_{20\mu s}$ [MPa]	β [Hz]
Potting material	1.17	364	5576	50,000
Diploe layer (n=81)	1.48 ± 0.15	274 ± 126	884 ± 374	50,000

6.4 Discussion

6.4.1 Rationale for use of low-rate dynamic properties as quasi-static properties and choice of viscoelastic time constant

The dynamic modulus of the diploe layer was calculated from stress vs. strain time histories spanning an average of $67 \text{ ms} \pm 19 \text{ ms}$. The slope of stress vs. time for a linear viscoelastic material follows the same trend as the relaxation function (Lakes, 2009). A viscoelastic unit with a decay constant as slow as 500 Hz would subside to 5% of its contribution within a tenth of this time range. Therefore, for the experiments conducted at a frequency range of 1 to 20 kHz, these properties may be treated as quasi-static. Absence of viscoelastic units below this frequency range was shown by the low frequency cyclic loading tests.

As determined using the FE models, the quasi-static modulus sufficiently explained the dynamic force response at the frequencies in which cyclic loading tests were done. A gradually increasing modulus was found in all cases. There was no indication of a peak in the complex modulus in the frequency range tested. A time constant ($\beta=50 \text{ kHz}$) exceeding the range of test frequency was chosen on this basis. To date, a peak in material loss tangent for human bone has not been discovered. Note that Sasaki et al. (1993) found a peak in $\tan\delta$ at approximately 10^{-4} Hz for bovine cortical bone from stress relaxation data. The material loss tangent, which signifies the proportion of energy lost during cyclic loading and is a function of frequency, is addressed further in Section 6.4.4.

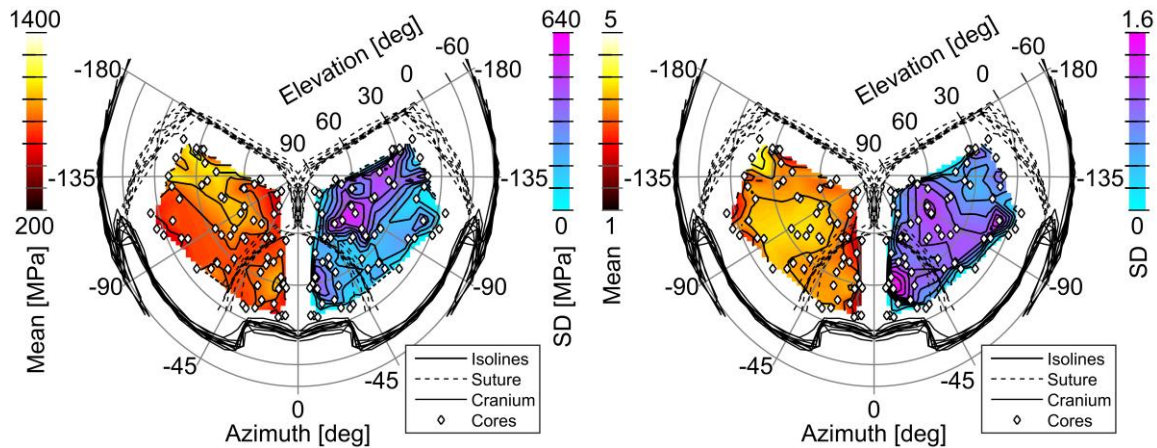


Figure 6.7 Viscoelastic modulus (left: absolute; right: fractional, relative to quasi-static modulus) of the cancellous diploe layer. Average values across nine subjects are shown on the contour map on the left and the standard deviations are shown on the right.

6.4.2 Comparison to other modes of testing, and need for finite element modeling

Derivation of viscoelastic properties from constant strain-rate experiments requires accurate knowledge of the stress history as the relationship of stress with strain is non-linear for a viscoelastic material (Lakes, 2009). Cortical bone from the skull has been tested at under dynamic strain rates and the effect of strain-rate on its effective modulus has been reported (Robbins and Wood, 1969). Johnson et al. (2010) have used time-history data from these tests to determine viscoelastic properties of cortical bone. Viscoelastic properties of human cortical bone from other sources were also derived from creep (Park and Lakes, 1986) and step relaxation experiments (Lakes et al., 1979; Sasaki et al., 1993). These experiments are unsuitable for evaluation of viscoelasticity associated with a small time constant because of the finite rise-time of the desired step input (Lakes, 2009). Nonetheless, both of these approaches involve fitting the relaxation function to the experimental data (directly for the step tests and through the Boltzmann superposition integral for ramp tests). Yet another method is quantification of either damping of resonant vibration (Lakes, 1982), or attenuation of sound waves propagating through the material

(Adler and Cook, 1975). These methods are used for characterization at higher frequencies and are susceptible to spurious energy loss or damping at the transducers.

The frequency dependent complex modulus can be directly obtained through observation of the relationship between steady-state stress and strain through cyclic loading. Decay constants and corresponding moduli for a time-domain model (such as a Prony series description) can be obtained through this approach without any curve fitting. Viscoelasticity of small, homogenous and geometrically uniform cortical bone samples has been characterized in this mode over a broad range of frequency using a torsional pendulum (Garner et al., 1999). But, as in this case, when composite samples are used, the calculation of stress and strain in the sample is not straightforward. The stiffness and viscoelasticity of the diploe layer has been found to vary greatly between fixed and free end conditions (Dong et al., 2004; Keaveny et al., 1997). The use of through-the-thickness composite samples was chosen to ensure a natural boundary condition for the diploe layer. Therefore, the tested core samples were inhomogeneous and included the potting layers, the cortical layers and, the diploe layer, which within itself was inhomogeneous. The diploe layer was treated as a continuum and its effective mechanical properties were evaluated in this study, and the FE method was used to decouple the mechanical response of the different layers in the core samples. Because of the inhomogeneity of the diploe layer (trabecular size ~ 0.5 mm and pore size ~ 2 mm), the continuum assumption necessitated the use of large samples (18 mm dia.) in this study. Interestingly, it was found that a significant part of the force response was the contribution of material inertia, especially at the higher frequency when the accelerations were large.

6.4.3 Dependence on location

Shapiro-Wilk normality tests showed that both absolute values of viscoelastic moduli and the fractional values were distributed normally in nine of ten subjects (Table A.31). Although the

viscoelastic modulus (both absolute and fractional values) of the calvarium diploe layer varied significantly between subjects, there was no correlation with subject age or any of the anthropometric measurements (one-way ANOVA tests, Table A.32). One-way within subjects ANOVA tests indicated that the fractional viscoelasticity of the diploe layer was different for the frontal and parietal bones. The fractional values of viscoelastic modulus relative to the quasi-static modulus varied between the frontal and parietal bones (one-way within subject ANOVA; $p=0.01$) but did not vary between the superior and inferior aspects of the calvarium. The absolute values of the viscoelastic modulus did not vary between the frontal and parietal bones or between the superior and inferior aspects of the calvarium (one-way within subject ANOVA; $p>0.05$). The variation of diploe layer viscoelastic modulus across the calvaria of nine individual subjects is shown in Figure A.17 and Figure A.18 in terms of absolute and fractional values respectively.

6.4.4 Material loss tangent – $\tan\delta$

There is very limited number of studies in the literature about the viscoelastic response of bone tissue at the frequency range reported in this paper. In previous papers, viscoelasticity is mostly reported in terms of the material loss tangent ($\tan\delta$). Figure 6.8 compares values of $\tan\delta$ derived from the standard linear solid parameters optimized in this paper with the only data for bone available at the same frequency range (Garner et al., 1999). Considering the greater number of samples in this study, the loss tangent of porous diploe layer is about ten times that of tibial cortical bone. The only previous study, where viscoelasticity of porous bone was directly measured (bovine tibial cancellous bone, Dong et al., 2004), reported $\tan\delta$ values ranging from 0.05 to 0.3 at frequencies ranging from 1 to 20 Hz, which, compared to $\tan\delta$ for cortical bone measured at similar frequencies ((Garner et al., 1999); (Lakes et al., 1979)), represents a similar ten-fold change.

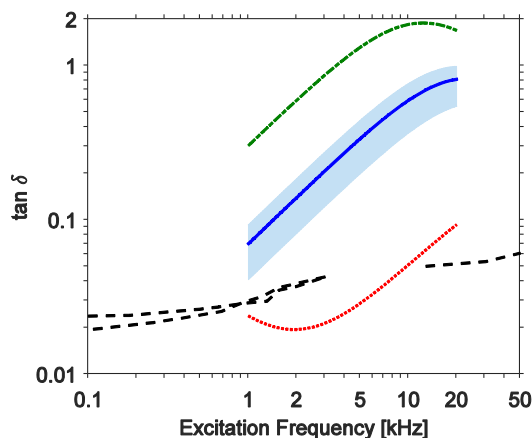


Figure 6.8 Variation of material loss tangent ($\tan\delta$) of the cancellous diploe layer (solid line – average values; shaded area – ± 1 S.D) compared to loss tangent of polyester potting material (broken line), loss tangent of cortical bone from human tibia (Garner et al., 1999, dashed line) and , two term Prony series (Johnson et al., 2010) fit to human calvarium cortical bone dynamic tensile tests (Wood, 1971), (dotted line).

Due to the lack of accurate data, an elastic material was used for the cortical layers in the FE models used in this study. While the viscoelastic material loss of cortical bone from the calvarium has been estimated to be significantly less (Johnson et al., 2010), using a viscoelastic cortical layer could lead to a small reduction in the estimates of diploe layer viscoelastic modulus.

Material loss tangent of polyester potting material, as found from cyclic loading tests done on core composed of only polyester, is greater compared to the calvarium diploe layer (Figure 6.8). Although rheometric tests on polymers are rarely done at such high frequencies, dynamic mechanical analysis done on polyester have exhibited loss tangents of up to 2 at a frequency of 100 Hz (Takeshita et al., 2012).

6.4.5 Comparison to in vivo blast loading

The peak strain in the tests ranged from 4.5 to 130 μ strain and peak stress ranged from 15 to 614 kPa. These peak stresses are somewhat less than the peak blast over pressures reported in the literature (500 – 1500 kPa, Chafi et al., 2009). In-vivo, the cores are surrounded by the rest of the

skull and transverse behavior (Poisson's ratio) is important. This information cannot be deduced from this test series as the lateral deformation of the samples was not observed. There is also the possibility of the pore contents to flow out of the diploe without any resistance even though material drip was not noted during testing. Therefore, the extent of stiffening could be significantly different in-vivo than what was seen in these tests.

6.5 Conclusions

- 1 The diploe layer stiffens around fourfold over a decade of frequency (1 to 10 kHz).
- 2 Viscoelastic material loss tangent of the diploe layer of the calvarium is more than an order of magnitude greater compared to cortical bone in the 10 to 50 kHz range.
- 3 The fractional viscoelastic modulus (3.3 ± 1.2) varies between the frontal and parietal bones.

7 Simplified plane-strain finite element model of the calvarium

7.1 Objective

I hypothesize that the variations of viscoelastic response of the diploe layer and that of its thicknesses significantly alters the boundary conditions, and therefore the response, of the brain caused by blast exposure of the head. This hypothesis was tested using a simplified version of the plane-strain blast FE model developed by Panzer et al. (2012). The objective of this task was to quantify the difference in few hypothetical stress and strain based injury criteria of brain tissue, caused by the between subjects variation of geometric and mechanical properties of the calvarium. The effect of absence of viscoelasticity in the calvarium was also analyzed.

7.2 Methodology

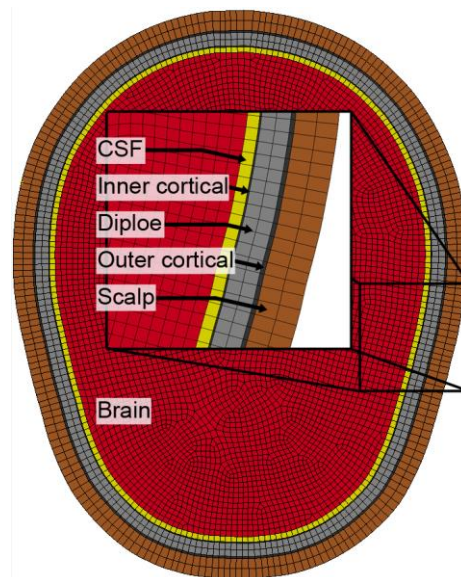


Figure 7.1 Simplified Lagrangian mesh of the skull brain system used in free-field blast simulation from Panzer et al. (2012). Blast impact occurs from the anterior aspect (bottom of this image).

7.2.1 Plane strain model

A simplified version of the plane-strain model developed by Panzer et al. (2012) was used in this study. In summary, the model simulates a free-field blast case using the arbitrary Lagrangian Eulerian (ALE) explicit solver in LS DYNA (R7.1.1, LSTC, Livermore, CA). The simplified model uses the same Eulerian mesh that simulates the propagation of the blast shockwave in the air surrounding the head, but uses a simplified Lagrangian mesh instead of the detailed mesh of the head used by Panzer et al. (2012). The simplified Lagrangian mesh (shown in Figure 7.1) consisted of six parts: the brain, a 2 mm thick cerebrospinal fluid (CSF) layer, the diploe and two cortical layers of the calvarium, and a 7 mm thick layer representing the scalp. A cross-section of the cranium 24 mm superior to the nasion and parallel to the Frankfort plane was used as the shape of the simplified skull. This shape represents the average cranial shape of the nine subjects that were studied (Section 3.3.1). The mesh consisted of a single layer of 6,484 hexahedral elements (2 mm characteristic length).

Material properties of grey matter (Panzer et al., 2012) were used for the entire brain. Mechanical properties for the cerebrospinal fluid layer and the scalp were also taken from Panzer et al. (2012). The deviatoric responses of the brain and the scalp were modeled as linear viscoelastic (Table 7.1), while dynamic viscosity and mass density of water was applied to the CSF layer. The volumetric responses of the brain, scalp and CSF were modeled using the Mie-Gruneisen equations of state using parameters of water ($C = 1,484$ m/s, $S_1 = 1.979$, and $\gamma_0 = 0.110$). The densities of these materials can be found in Table 7.1. The air was modeled using the ideal gas law ($\gamma = 1.4$) with initial standard atmospheric conditions ($P_0 = 101.32$ kPa, $\rho_0 = 1.23$ g/mm³).

The different simulation cases (Table 7.2) used the median and ± 1 standard deviation values of those properties of the calvarium which were found to vary significantly between subjects, viz. the thicknesses of the outer cortical layer, the cancellous diploe layer, and the inner cortical layer,

and the viscoelastic properties, including both quasi-static and relaxation components, of the diploe layer. These simulations were used to assess the influence of variation of properties of the calvarium on brain deformation. Simulations were also run using two other sets of model parameters for comparison. Case DEM Q (Table 7.2) used an elastic material model with the median quasi-static modulus of the diploe layer used as its' elastic Young's modulus. Case DEM I also used an elastic material, but the median combined quasi-static and viscoelastic modulus, representing the instantaneous response was used as the Young's modulus. These models were used to study effect of diploe layer viscoelasticity on the frequency spectrum of pressure inside the brain. Furthermore, the median case was run without the CSF and the scalp, and with the brain directly attached to the inside of the skull (Case NCNS, Table 7.2), to show the importance, or lack thereof, of variation in properties of the calvarium with respect to the presence or absence of the scalp and CSF layers. All the cases were compared to the median case which used the median value of all parameters studied. Mass density of the cortical layers and the diploe layer were fixed and were determined as explained in Section 6.2.4. Since the mass density found from the core samples did not correlate with layer thickness or mechanical properties, the median values were used ($\rho_{\text{cortical}} = 2.374 \text{ g/cm}^3$, $\rho_{\text{diploe}} = 1.475 \text{ g/cm}^3$). Poisson's ratio for both layers was taken from the literature ($\nu_{\text{diploe}} = 0.4$, Dong and Guo, 2004; Robbins and Wood, 1969; $\nu_{\text{diploe}} = 0.2$, Dalstra et al., 1993; McElhaney et al., 1970). All simulations were run for 10 ms. A real world blast overpressure time history, with a free-field peak overpressure of 250 kPa (shown in Figure 7.2, Shridharani et al., 2012) was used as the input free-field condition.

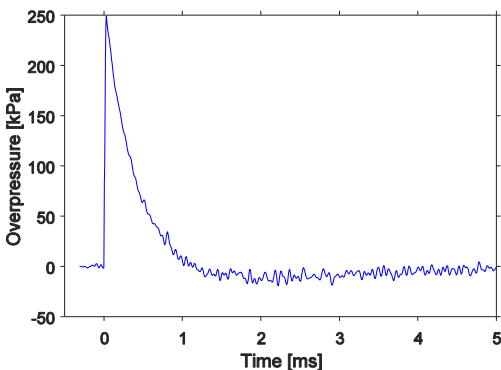


Figure 7.2 Blast overpressure time-history used in the simplified plane-strain simulations.

7.2.2 Brain tissue injury criteria

Research related to brain injury mechanisms has been discussed in Section 1.10. Few hypothetical indicators of brain tissue injury, that were observed (Antona-Makoshi et al., 2015, 2012; Margulies et al., 1990; Takhounts et al., 2003) to correlate with brain injury in animal studies are listed in Table 1.2. Panzer et al. (2012) have observed that stress in the brain, even in case of severe blast exposure, is less than previously established threshold for cell death under static loading and have suggested that the thresholds may be dependent on strain rate.

In the FE model used here, only in-plane strains exist in the brain tissue because of the plane-strain assumption. Also, the two principal strains in this plane are interrelated as a result of the near incompressibility of brain tissue. Thus there is only one independent strain invariant, and maximum shear strain was chosen as the strain based injury criteria (Table 7.3). This is not the case for stress as normal stresses may exist in the vertical direction. Pressure and Von-Mises stress, which represent dilatational and deviatoric components of stress, were also investigated using the plane strain model (Table 7.3). Since brain injury may be dependent on strain rate, maximum shear strain-rate was analyzed as another hypothetical injury criterion.

Table 7.1 Linear viscoelastic materials used for the scalp and the brain in the simplified plane strain model.

Brain	$\rho = 1.06 \text{ g/cm}^3$	$K = 2.19 \text{ GPa}$
	Shear modulus G_i [kPa]	Decay constant β_i [Hz]
	41.22	0.00
	19.90	5.30
	40.40	200.00
	100.50	4,350.00
	808.70	100,000.00
Scalp	$\rho = 1.13 \text{ g/cm}^3$	$K = 2.19 \text{ GPa}$
	Shear modulus G_i [kPa]	Decay constant β_i [Hz]
	1,197.60	0.00
	296.40	5.30
	333.20	200.00
	29.70	4,350.00

Table 7.2 Layer thickness and material parameters used in plane-strain free-field blast simulation cases.

Case	Layer thicknesses [mm]			Material properties		
	Outer	Diploe	Inner	Cortical modulus	Diploe modulus	
				[GPa]	Quasi-static E_{∞} [MPa]	Fractional viscoelastic $E_{20\mu s}/E_{\infty}$
Median	● 0.81	● 3.59	● 0.46	● 18.4	● 240	● 3.52
OCT -	▼ 0.59	● 3.59	● 0.46	● 18.4	● 240	● 3.52
OCT +	▲ 1.06	● 3.59	● 0.46	● 18.4	● 240	● 3.52
DT -	● 0.81	▼ 1.99	● 0.46	● 18.4	● 240	● 3.52
DT +	● 0.81	▲ 5.55	● 0.46	● 18.4	● 240	● 3.52
ICT -	● 0.81	● 3.59	▼ 0.36	● 18.4	● 240	● 3.52
ICT +	● 0.81	● 3.59	▲ 0.73	● 18.4	● 240	● 3.52
DQM -	● 0.81	● 3.59	● 0.46	● 18.4	▼ 179	● 3.52
DQM +	● 0.81	● 3.59	● 0.46	● 18.4	▲ 360	● 3.52
DVM -	● 0.81	● 3.59	● 0.46	● 18.4	● 240	▼ 1.90
DVM +	● 0.81	● 3.59	● 0.46	● 18.4	● 240	▲ 4.56
NCNS	Identical to Case 01 except without CSF and scalp					
DEM Q	● 0.81	● 3.59	● 0.46	● 18.4	240	0
DEM I	● 0.81	● 3.59	● 0.46	● 18.4	1,085	0

▼ – 16th, ● – 50th, ▲ – 84th percentile values; OCT – Outer cortical thickness; DT –

Diploe thickness; ICT – Inner cortical thickness; DQM – Diploe quasi-static

modulus; DVM – Diploe viscoelastic modulus; NCNS – No CSF no scalp; DEM Q –

Diploe elastic modulus quasi-static DEM I – Diploe elastic modulus instantaneous

Table 7.3 Brain deformation metrics tested as hypothetical brain injury criteria.

Strain based

- 1 Maximum shear strain
- 2 Maximum shear strain rate

Stress based

- 3 Pressure
 - 4 Von Mises stress
-

The peak values of these deformation metrics for all elements in the brain were extracted from the time histories of element stress-strain data gathered at 100 kHz from the explicit simulations.

Numerical differentiation was used to calculate the strain rate tensor from the strain tensor (Lai et al., 2012). Because of the three-dimensional stress state, the eigenvalues of the stress tensor were computed using the Jacobi iteration method. The brain deformation metrics were calculated using the following formulae.

$$\text{Strain tensor (plane strain)} \begin{bmatrix} \varepsilon_{xx} & \varepsilon_{xy} & 0 \\ \varepsilon_{xy} & \varepsilon_{yy} & 0 \\ 0 & 0 & 0 \end{bmatrix} \rightarrow \begin{bmatrix} \varepsilon_1 & 0 & 0 \\ 0 & 0 & 0 \\ 0 & 0 & \varepsilon_3 \end{bmatrix} \quad \varepsilon_{1,3} = \frac{\varepsilon_{xx} + \varepsilon_{yy}}{2} \pm \sqrt{\left(\frac{\varepsilon_{xx} - \varepsilon_{yy}}{2}\right)^2 + \varepsilon_{xy}^2}$$

$$\begin{bmatrix} \varepsilon_{xx} & \varepsilon_{xy} & 0 \\ \varepsilon_{xy} & \varepsilon_{yy} & 0 \\ 0 & 0 & 0 \end{bmatrix} \xrightarrow{\text{numerical differentiation}} \begin{bmatrix} \dot{\varepsilon}_{xx} & \dot{\varepsilon}_{xy} & 0 \\ \dot{\varepsilon}_{xy} & \dot{\varepsilon}_{yy} & 0 \\ 0 & 0 & 0 \end{bmatrix} \quad \text{Strain-rate tensor}$$

$$\text{Strain-rate tensor} \begin{bmatrix} \dot{\varepsilon}_{xx} & \dot{\varepsilon}_{xy} & 0 \\ \dot{\varepsilon}_{xy} & \dot{\varepsilon}_{yy} & 0 \\ 0 & 0 & 0 \end{bmatrix} \rightarrow \begin{bmatrix} \dot{\varepsilon}_1 & 0 & 0 \\ 0 & 0 & 0 \\ 0 & 0 & \dot{\varepsilon}_3 \end{bmatrix} \quad \dot{\varepsilon}_{1,3} = \frac{\dot{\varepsilon}_{xx} + \dot{\varepsilon}_{yy}}{2} \pm \sqrt{\left(\frac{\dot{\varepsilon}_{xx} - \dot{\varepsilon}_{yy}}{2}\right)^2 + \dot{\varepsilon}_{xy}^2}$$

$$\text{Stress tensor} \begin{bmatrix} \sigma_{xx} & \sigma_{xy} & \sigma_{zx} \\ \sigma_{xy} & \sigma_{yy} & \sigma_{yz} \\ \sigma_{zx} & \sigma_{yz} & \sigma_{zz} \end{bmatrix} \xrightarrow{\text{Jacobi iteration}} \begin{bmatrix} \sigma_1 & 0 & 0 \\ 0 & \sigma_2 & 0 \\ 0 & 0 & \sigma_3 \end{bmatrix}$$

$$\text{Maximum shear strain } \varepsilon_{max} = \frac{\varepsilon_1 - \varepsilon_3}{2}$$

Equation 7.1

$$\text{Maximum shear strain-rate } \dot{\varepsilon}_{max} = \frac{\dot{\varepsilon}_1 - \dot{\varepsilon}_3}{2}$$

$$\text{Pressure } p = -\frac{\sigma_1 + \sigma_2 + \sigma_3}{3}$$

$$\text{Von Mises stress } \sigma_v = \sqrt{\frac{(\sigma_1 - \sigma_2)^2 + (\sigma_2 - \sigma_3)^2 + (\sigma_3 - \sigma_1)^2}{2}}$$

7.3 Results

7.3.1 Eulerian air mesh response

Figure 7.3 shows the pressure in the Eulerian air mesh at a point adjacent to the blast impact location on the head (reflected pressure, green line) and at another point equally downstream from the blast inlet, but far away from the head (simulation free-field pressure, red line) compared to the target air pressure time history. The peak in the simulated free-field pressure was quite accurate at 343.7 kPa and remained constant across all the simulation cases. The propagation of the blast shock wave in the Eulerian air mesh is shown in Section 14.7.1.

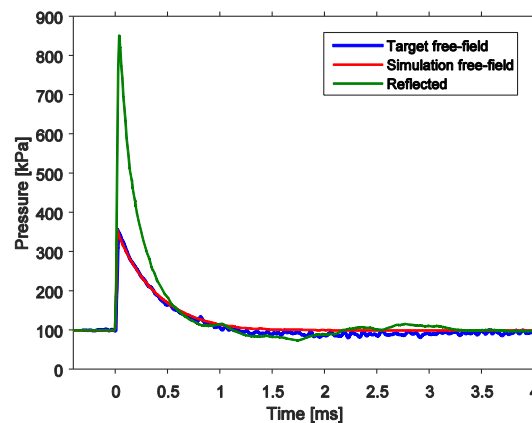


Figure 7.3 Free field and reflected pressure at blast impact location, compared to target pressure time history.

7.3.2 Time history of brain deformation

Upon impact, the pressure rises first at the frontal region, and subsequently at the center, lateral and occipital aspects, showing the progression of the shockwave towards the rear of the head. In the return stroke, peak pressure occurs first at the occiput and center (Figure 7.4 left). What is interesting to note is that the peak amplitude of pressure at the different locations get closer to each other with each reflection inside the cranium (Figure 7.4 right) before eventually becoming equal.

In addition to this oscillating response of pressure (peak C ~ 7 kHz in Figure 7.5 left), corresponding to the reflection of the stress wave back and forth in the cranium, two more lower frequency modes exist (peaks A and B in Figure 7.5 left). These are caused by coupling of the brain with the bending of the calvarium (Figure 7.5 right). Initially ($t < 2$ ms) the bending of the calvarium is a superposition of two modes (200 and 400 Hz). Figure 7.6 shows the low frequency mode shape of the skull which is sustained till the end of simulation.

The Von Mises stress (Figure 7.7) and maximum shear strain (Figure 7.8) and maximum shear strain rate (Figure 7.9) being associated with the compliant shear response of the brain tissue does not exhibit the high frequency response seen for pressure (~ 7 kHz). In contrast to pressure, which exhibits an intense transient response, the other metrics exhibit a response which gradually subsides in the 10 ms simulation time. The frequency content of these metrics lie below 1 kHz with the frontal region experiencing greater frequency compared to the occiput.

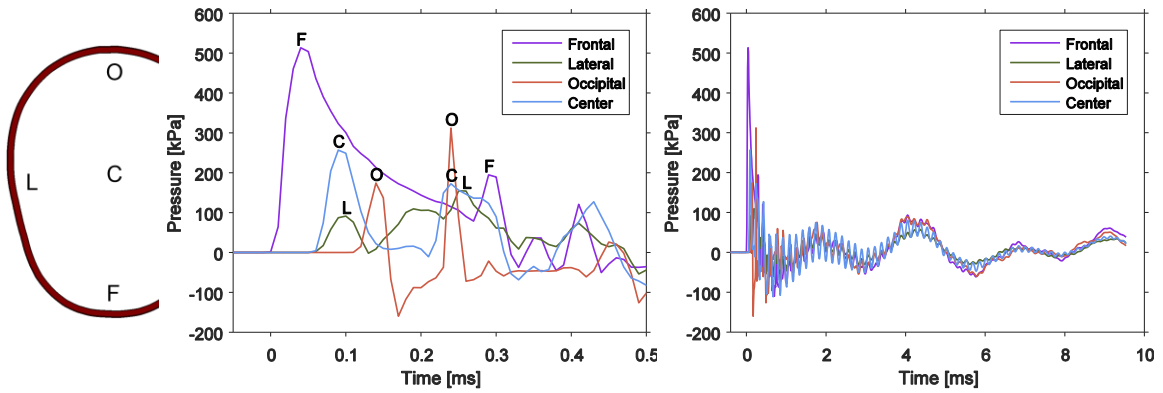


Figure 7.4 Pressure at different locations inside the brain (blast impact occurs in the frontal side), showing transient response (left; letters at the peaks indicate the location) and long term response (right).

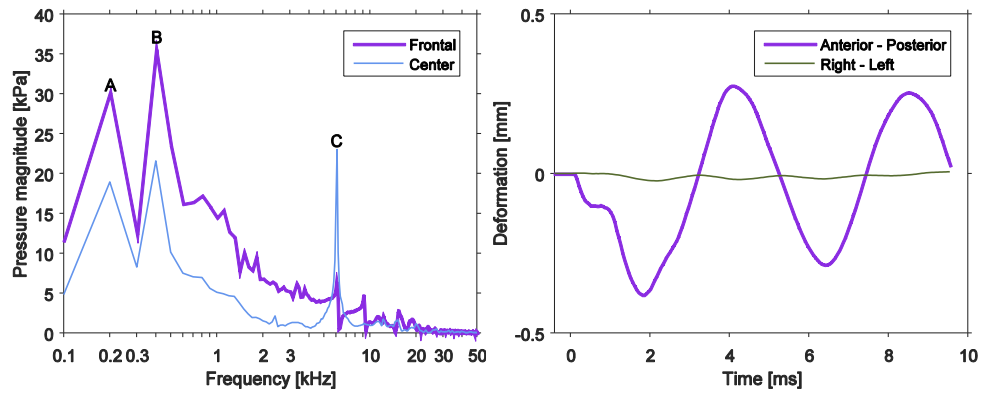


Figure 7.5 Frequency spectrum of pressure at frontal and central brain (left). Deformation of the skull anterior to posterior and right to left directions.

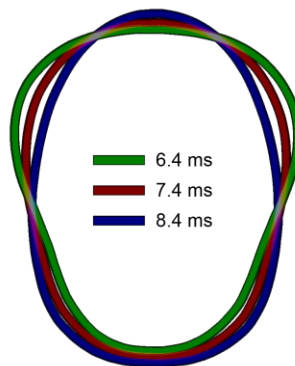


Figure 7.6 Bending mode of the skull (displacement amplified by a factor of 40).

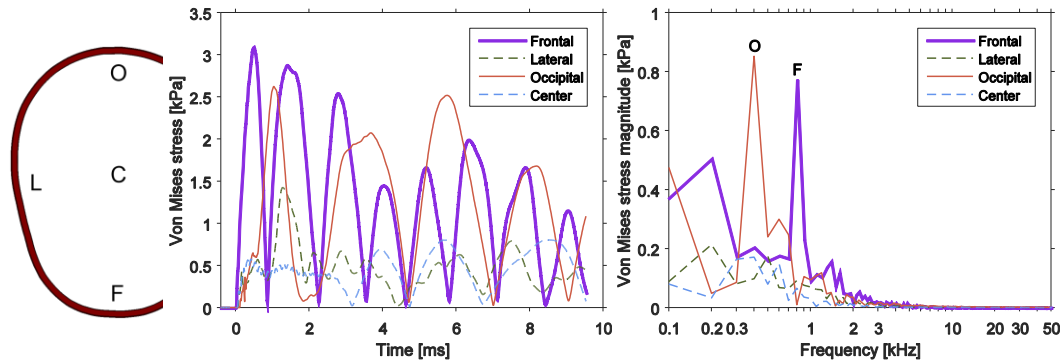


Figure 7.7 Von Mises stress at different locations inside the brain (left), and corresponding frequency spectra (right; letters at the peaks indicate the location).

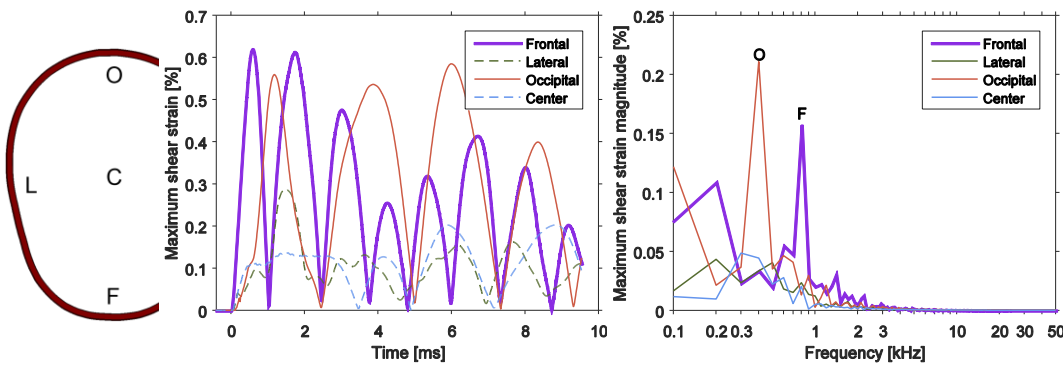


Figure 7.8 Maximum shear strain at different locations inside the brain (left), and corresponding frequency spectra (right; letters at the peaks indicate the location).

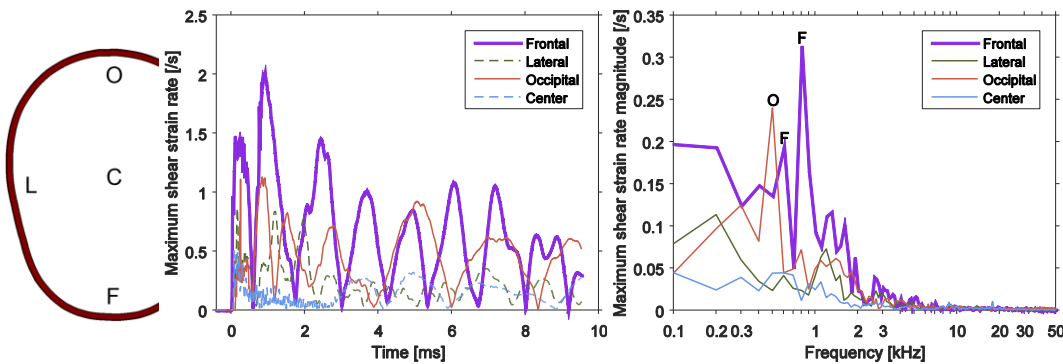


Figure 7.9 Maximum shear strain rate at different locations inside the brain (left), and corresponding frequency spectra (right; letters at the peaks indicate the location).

7.3.3 Peak brain deformation

The peak deformation that each element of the brain attains in the 10 ms of simulation was determined and plotted (Figure 7.10). The spatial distributions of peak deformations in each simulation case have been tabulated in Section 14.7.2. The peak deformation metrics across the brain (Table 7.3) were used as outcome variables in a linear model. Values of 0, -1 and 1 were used for median, -1 S.D. and +1 S.D. cases for each parameter that were varied, were used as predictor variables (Table 7.4).

$$y_i = \beta_{i0} + \sum_{j=1}^6 \beta_{ij} x_j$$

y_i – Brain deformation metrics

$$x_j = \begin{cases} 1 & -1 \text{ S.D.} \\ 0 & - \text{Median value of } j^{\text{th}} \text{ factor} \\ -1 & -1 \text{ S.D.} \end{cases}$$

β_{ij} – Coefficient indicating the change in i^{th} metric as a result of ± 1 S.D. change in j^{th} factor

β_{i0} – Intercept for i^{th} brain deformation metric

Table 7.4 Predictor variables used in linear model for each simulation case.

Case	Factors (i=1 to 6)					
	OCT	DT	ICT	DQM	DVM	NCNS
Median	0	0	0	0	0	0
OCT -	-1	0	0	0	0	0
OCT +	1	0	0	0	0	0
DT -	0	-1	0	0	0	0
DT +	0	1	0	0	0	0
ICT -	0	0	-1	0	0	0
ICT +	0	0	1	0	0	0
DQM -	0	0	0	-1	0	0
DQM +	0	0	0	1	0	0
DVM -	0	0	0	0	-1	0
DVM +	0	0	0	0	1	0
NCNS	0	0	0	0	0	1

OCT – Outer cortical thickness; DT – Diploe thickness; ICT – Inner cortical thickness; DQM – Diploe quasi-static modulus; DVM – Diploe viscoelastic modulus; NCNS – No CSF and no scalp

The linear model statistics are tabulated in Table 7.5 and Table 7.6. These results show that all of the properties of the calvarium that were varied had significant influence on all of deformation metrics that were investigated ($p < 0.05$), except the diploe layer quasi-static modulus, which had no significant effect on the maximum shear strain rate.

Table 7.5 Statistics of linear model fit to the simulation data to predict stress based deformation metrics.

Linear model for pressure [kPa]				Linear model for Von Mises stress [kPa]			
Factor	Coefficient	S.E.	p	Factor	Coefficient	S.E.	p
Intercept	236.011	0.423	0.000	Intercept	1.827	0.003	0.000
OCT	-5.752	0.992	0.000	OCT	-0.122	0.006	0.000
DT	7.155	0.992	0.000	DT	-0.660	0.006	0.000
ICT	-3.344	0.992	0.001	ICT	-0.150	0.006	0.000
DQM	-2.860	0.992	0.004	DQM	-0.061	0.006	0.000
DVM	-5.151	0.992	0.000	DVM	-0.040	0.006	0.000
NCNS	4.151	1.433	0.004	NCNS	0.216	0.009	0.000

OCT – Outer cortical thickness; DT – Diploe thickness; ICT – Inner cortical thickness; DQM – Diploe quasi-static modulus; DVM – Diploe viscoelastic modulus; NCNS – No CSF and no scalp

The effect size, indicated by the magnitude of the coefficients relative to the intercept value (Table 7.7), show that ± 1 S.D. variation in all the layer thicknesses led to more than 5% change in Von Mises stress and maximum shear strain. The effect of variation of all the mechanical properties however led to less than 5% change in all the deformation metrics. The difference in all of the metrics, except strain rate, as a result of variation in diploe layer thickness is greater than the difference caused by complete absence of the scalp and the CSF layer.

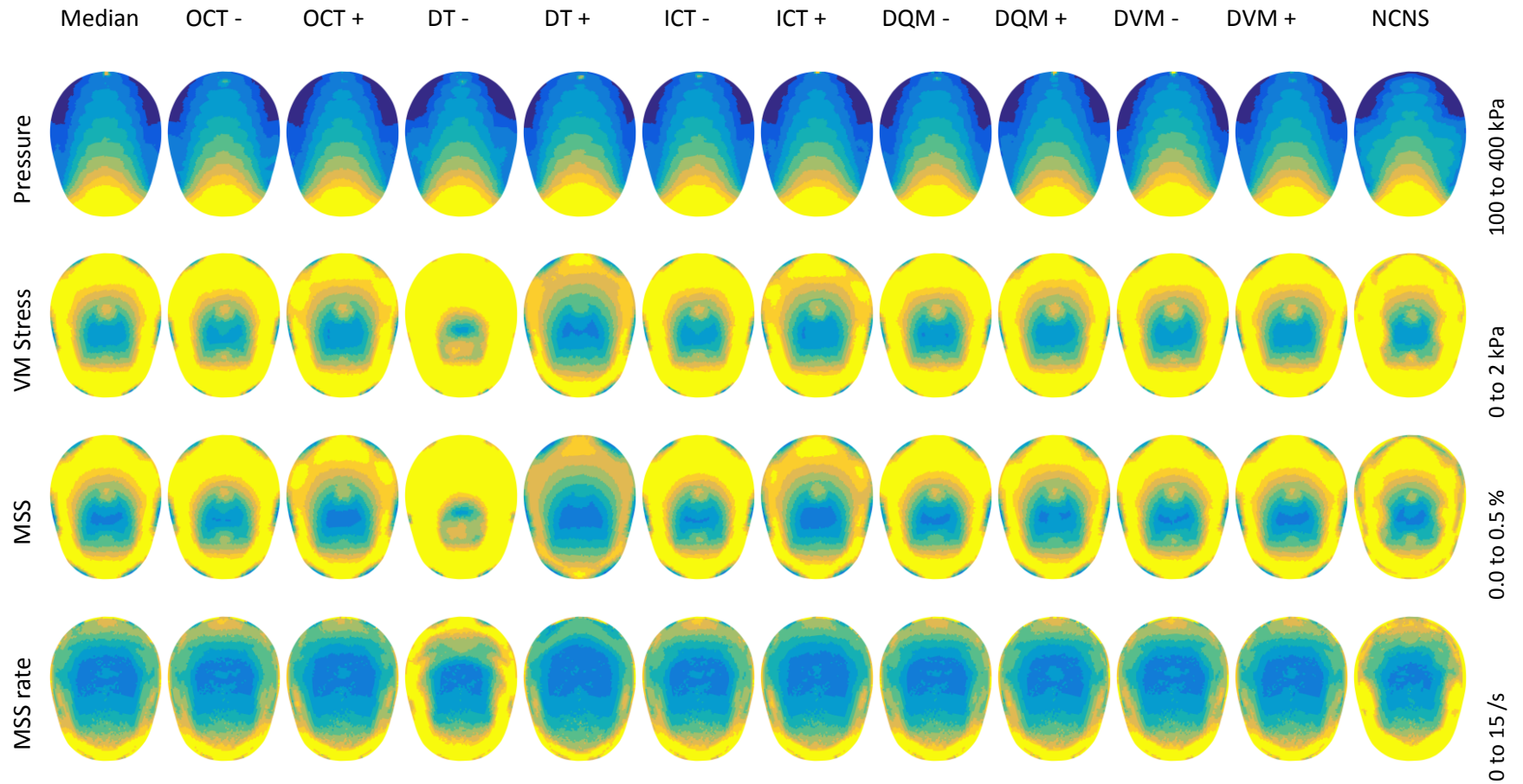


Figure 7.10 Peak deformation metrics (from top to bottom) across the brain for the different simulation cases (from left to right). MSS – maximum shear strain; VM – Von Mises. Color scale limits are shown on right. OCT – Outer cortical thickness; DT – Diploe thickness; ICT – Inner cortical thickness; DQM – Diploe quasi-static modulus; DVM – Diploe viscoelastic modulus; NCNS – No CSF no scalp.

Table 7.6 Statistics of linear model fit to the simulation data to predict strain based deformation metrics.

Linear model for maximum shear strain [%]				Linear model for maximum shear strain rate [1/s]			
Factor	Coefficient	S.E.	p	Factor	Coefficient	S.E.	p
Intercept	0.417	0.001	0.000	Intercept	8.394	0.017	0.000
OCT	-0.037	0.001	0.000	OCT	-0.240	0.041	0.000
DT	-0.174	0.001	0.000	DT	-1.744	0.041	0.000
ICT	-0.045	0.001	0.000	ICT	-0.296	0.041	0.000
DQM	-0.020	0.001	0.000	DQM	-0.071	0.041	0.083
DVM	-0.009	0.001	0.000	DVM	-0.222	0.041	0.000
NCNS	0.015	0.002	0.000	NCNS	3.719	0.059	0.000

OCT – Outer cortical thickness; DT – Diploe thickness; ICT – Inner cortical thickness; DQM – Diploe quasi-static modulus; DVM – Diploe viscoelastic modulus; NCNS – No CSF and no scalp

7.3.4 Influence of viscoelasticity – spectral analysis

Spectrogram of the pressure in the brain at the frontal boundary for the DEM Q, DEM I and Median cases are shown in Figure 7.11 left. Attenuation of the high-frequency energy content is clear in this region of the brain and almost all stress content above 10 kHz at the frontal boundary is attenuated by the viscoelastic skull after 1 ms. However, there is almost no difference caused by viscoelasticity of the diploe layer on the frequency spectrum of stress in the interior of the brain (Figure 7.11 right).

Table 7.7 Linear model coefficients expressed as percentage of intercept.

	Pressure	Von Mises stress	Maximum shear strain	Maximum shear strain rate
Intercept	236.011 kPa	1.827 kPa	0.417 %	8.394 /s
Outer cortical thickness	2.44%	6.70%	8.86%	2.86%
Diploe thickness	3.03%	36.14%	41.68%	20.78%
Inner cortical thickness	1.42%	8.22%	10.71%	3.52%
Diploe quasi-static modulus	1.21%	3.34%	4.72%	0.84%
Diploe viscoelastic modulus	2.18%	2.21%	2.07%	2.64%
No CSF no scalp	1.76%	11.83%	3.49%	44.30%

Changes greater than 5% are shown in bold.

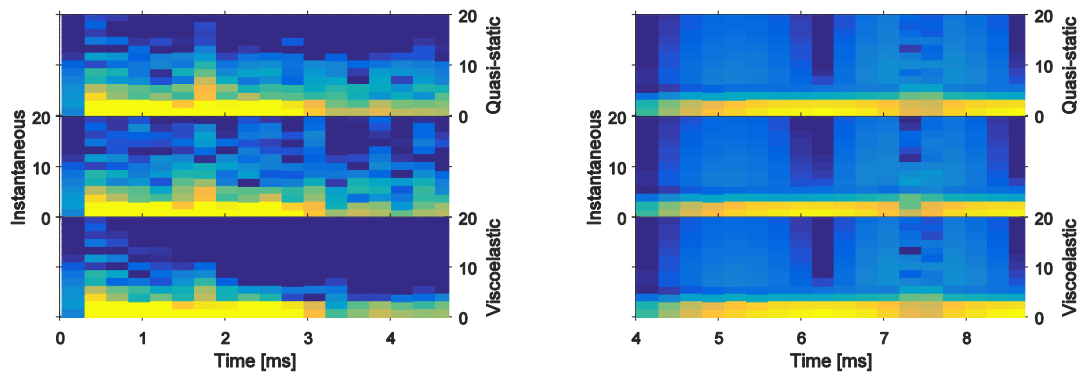


Figure 7.11 Spectrograms of pressure in the frontal (left) and central (right) brain. From top to bottom cases

DEM Q, DEM I and Median.

7.4 Discussion

Table 7.8 Case wise peak reflected overpressure and maximum peak brain pressure in kPa.

Case	Reflected	Peak brain	Case	Reflected	Peak brain
Median	853.52	525.42	ICT +	866.00	518.89
OCT -	843.98	534.46	DQM -	853.56	531.00
OCT +	866.46	519.28	DQM +	853.60	526.77
DT -	867.99	544.87	DVM -	853.43	541.92
DT +	636.34	541.99	DVM +	853.57	524.47
ICT -	849.72	529.67	NCNS	791.93	584.93

OCT – Outer cortical thickness; DT – Diploe thickness; ICT – Inner cortical thickness;

DQM – Diploe quasi-static modulus; DVM – Diploe viscoelastic modulus; NCNS – No

CSF and no scalp

The reflected overpressure (Figure 7.3, Table 7.8) was 853.5 kPa for the median case (Case 1) and it did not change for the cases where the mechanical properties of the calvarium were changed. However, it increased substantially for the thicker cortical tables (Case 3 and Case 7) and vice versa. Interestingly, this effect was opposite for the diploe layer thickness, where the greater thickness (Case 5) resulted in a substantially reduced reflected overpressure. The reflected peak overpressure was also reduced in the absence of the scalp and CSF.

The difference in reflected pressure is a result of change in cross-section area exposed to blast and mechanical properties. The volume of the brain and CSF was constant for each simulation case, therefore, change in layer thicknesses resulted in the change of cross-section. The reflected pressure is more representative of the load applied to the head; therefore, this change in reflected

pressure could be responsible for some of the variation in brain deformation outcome. The peak reflected pressure did not correlate with the maximum peak brain pressure (Table 7.8).

The effect of variation of mechanical properties on brain deformation was substantially less as compared to that of the layer thicknesses. Therefore, blast brain injury researchers should consider between subjects variation in layer thicknesses in their design and analysis. Variations in mechanical properties and modeling the viscoelastic response of the calvarium are relatively less important.

7.4.1 Bending stiffness

The bending stiffness of the integrated calvarium model presented in this chapter is softer compared to current FE models of the head that use different materials for the layers of the calvarium sandwich structure (Table 7.9). Experimental data from bending tests done on beam samples from the human calvarium is also shown in the same table. For comparison, the stiffness values have been normalized to beam width to account for differences in test specimen geometry.

Hubbard (1971) has reported the product of Young's modulus and second moment of area from regression analysis of their bending data. These values have been adjusted for different beam widths using Equation 7.2. Motherway et al. (2009) and Auperrin et al. (2014) have assumed that the bone in the porous diploe layer and the cortical tables have the same Young's modulus. The effect of porosity in the diploe layer has been accounted for using the second moment of area.

The stiffness under pure bending has been derived from the reported Young's modulus and second moments of area using Equation 7.2. The bending stiffness of the current head FE models have been calculated from the specified Young's modulus of the layers using Equation 7.3. While Asgharpour et al. (2014) have used constant values of layer thicknesses, Horgan and Gilchrist (2003) and Panzer et al. (2012) have specified fixed ratios of layer thicknesses. Values of total

thickness have been taken from Section 3.3.2 in this dissertation for estimation of stiffness in these cases. In the models where viscoelastic properties have been used for any of the layers, the quasi-static components have been used to calculate the quasi-static bending stiffness and the instantaneous responses were used to compute the dynamic bending stiffness.

$$\frac{M}{w\kappa} = \frac{E_{eff}I_{eff}}{w} \quad \text{Equation 7.2}$$

$$\frac{M}{w\kappa} = \int E(y)y^2 dy \quad \text{Equation 7.3}$$

M – Bending moment [Nm]

w – Beam width [m]

κ – Curvature [m⁻¹]

E_{eff} – Effective Young's modulus under single material assumption

I_{eff} – Effective second moment of area

y – Distance from neutral axis [m]

E(y) – Young's modulus as a function of distance from neutral axis [Pa]

The average value of stiffness under pure bending of the integrated calvarium model presented in this chapter is less than those of the other head FE models analyzed. While the quasi-static bending stiffness of the models published by Horgan and Gilchrist (2003) and Panzer et al. (2012) are very close to the bending studies done by Hubbard (1971) and Motherway et al. (2009), much softer responses have been reported by Auperrin et al. (2014), who tested a much larger sample of beams.

The variance of measurements made by Motherway et al. (2009) and Auperrin et al. (2014) could not be established because the second moment of area of each test specimen was not reported.

Since Asgharpour et al. (2014) have specified fixed values for both layer thicknesses and

mechanical properties, the resulting bending stiffness has no variance across the calvarium. This variation in case of the other head FE models arises from the variance in total thickness of the calvarium observed in this study (Section 3.3.2). Concurrent analysis of mechanical properties and layer thicknesses in the same samples is a valuable strength of this study, which results in a smaller variance of bending stiffness of the calvarium as compared to the other head FE models. This is a result of the paired values of layer thicknesses and mechanical properties used.

Table 7.9 Average values of stiffness under pure bending of the calvarium from the literature.

Three point beam bending test on samples (Equation 7.2)		$\frac{M}{\omega K}$
Hubbard (1971)	8 parietal beams; 4 embalmed calvaria	240 ± 147
<i>Motherway et al. (2009)</i>	<i>60 frontal and parietal beams; 8 fresh calvaria</i>	<i>346</i>
Auperrin et al. (2014)	357 frontal and parietal beams; 21 fresh calvaria	96
Current head FE models (Equation 7.3)		$\frac{M}{\omega K}$
Horgan and Gilchrist (2003)	Values of total thicknesses of calvarium taken from this study (n=85 Section 3.3.2), fixed individual layer thickness	209 ± 177
Panzer et al. (2012)	ratios and mechanical properties	183 ± 156 <i>256 ± 217</i>
Asgharpour et al. (2014)	Fixed layer thicknesses and mechanical properties	405
This study	Paired values of layer thickness and material properties	156 ± 114
	(n=85)	<i>169 ± 124</i>

Bending stiffness is normalized to width of samples ($M/\omega K$, units are Nm). Italics indicate dynamic stiffness.

7.5 Conclusions

- 1 Compared to mechanical properties, layer thicknesses have more influence on the peak deformation in the majority of the brain.
- 2 Change in deformation caused by variations in layer thicknesses, particularly the diploe layer thickness, is comparable to that caused by the presence or absence of the CSF and scalp.
- 3 The viscoelastic diploe layer attenuates the high frequency content of stress in regions near the blast impact site after 2 ms after impact.

8 Hypotheses

8.1 Variance with subject

For assessment of inter-subject variability of the properties found in this study, all measurements were grouped by subject.

The values of the layer thicknesses did not match any parametric distribution and the non-parametric Wilcoxon rank sum test was used to determine if data from two subjects were significantly different. All combinations of subjects ($10C2 = 45$) were tested. While the magnitude of difference was more than 10% in majority of the cases for all measurements, it was found that only the absolute values of diploe layer thicknesses varied significantly in more than 90% of the subject pairs (Table 3.3).

8.1.1 H0 – Layer thicknesses do not vary between subjects

Wilcoxon rank sum	Outcome, significance, effect-size in case of rejection (H0 rejection threshold 90%, % cases with $p < 0.05$, median % absolute difference)	
	Absolute	Ratio to total thickness
Outer cortical thickness	Not rejected, 73.3, 15.0	Not rejected, 77.8, 20.9
Inner cortical thickness	Not rejected, 73.3, 22.0	Not rejected, 88.9, 42.3
Diploe thickness *	Rejected, 91.1, 33.8	Not rejected, 86.7, 10.5

The mechanical properties were found to vary normally and they were tested for inter-subject variation using the one-way ANOVA test. Both effective structural and bone phase cortical layer properties did not vary significantly with subjects (Table A.26, Table A.29, and Table A.32). While both composite through-the-thickness quasi-static modulus and effective diploe layer properties (quasi-static and viscoelastic modulus) varied significantly between subjects.

8.1.2 H0 – Mechanical properties do not vary between subjects

One-way ANOVA	Outcome, significance, effect-size in case of rejection (H0 rejection threshold p-value 0.05, p-value, eta squared %)
Cortical quasi-static modulus	Not rejected, 0.572
Diploe quasi-static modulus *	Rejected, 0.000, 38.2
Diploe viscoelastic modulus *	Rejected, 0.000, 63.8
Diploe fractional viscoelasticity *	Rejected, 0.018, 26.0

8.2 Variance with location

For investigation of difference in measurements with location on the calvarium, all measurements were separated into two groups, first on the basis of whether the sample source was the frontal or the parietal bone, and second whether the sample was harvested from the superior or inferior aspect of the calvarium.

Since the thickness measurements were not distributed normally, the grouping (explained in previous paragraph) was done separately for each subject and tested using the non-parametric Wilcoxon rank sum test. The thicknesses were grouped by location for each subject and tested (Table 3.4).

8.2.1 H0 – Layer thicknesses do not vary with location on the calvarium

Wilcoxon rank sum	Outcome, significance, effect-size in case of rejection (H0 rejection threshold 90%, peak % unanimous cases with $p < 0.05$, median % difference)	
	Absolute	Ratio to total thickness
Parietal vs. frontal		
Outer cortical thickness	Not rejected, 50	Not rejected, 60
Inner cortical thickness	Not rejected, 30	Not rejected, 40
Diploe thickness	Not rejected, 80	Not rejected, 40
Inferior vs. superior		
Outer cortical thickness	Not rejected, 40	Not rejected, 80
Inner cortical thickness	Not rejected, 30	Not rejected, 60
Diploe thickness	Not rejected, 70	Not rejected, 70

The mechanical properties were normally distributed and their difference with location was tested using the one-way within subjects ANOVA (Table A.29 and Table A.32). The effective structural failure properties (both stress and strain) of the outer cortical layer of the calvarium were found to be different for the frontal and parietal bones. Similarly, the diploe layer quasi-static modulus and fractional viscoelasticity were also significantly different between the frontal and parietal bones. On the other hand, the cortical layer bone phase modulus (as derived using micro FE) was significantly larger in the inferior aspect of the calvarium as compared to the superior.

8.2.2 H0 – Mechanical properties do not vary with location on the calvarium

One-way within subjects ANOVA	Outcome, significance, effect-size in case of rejection (H0 rejection threshold p-value 0.05, p-value, eta squared %)
Parietal vs. frontal	
Cortical quasi-static modulus	Not rejected, 0.187
Diploe quasi-static modulus *	Rejected, 0.022, 21.0
Diploe viscoelastic modulus	Not rejected, 0.970
Diploe fractional viscoelasticity *	Rejected, 0.042, 11.4
Inferior vs. superior	
Cortical quasi-static modulus *	Rejected, 0.029, 27.6
Diploe quasi-static modulus	Not rejected, 0.114
Diploe viscoelastic modulus	Not rejected, 0.853
Diploe fractional viscoelasticity	Not rejected, 0.588

8.3 Influence on blast brain injury

The influence of the inter-subject variation of the measured parameters on blast brain injury was investigated using a plane-strain FE model. Simulations were run using the median and ± 1 standard deviation values of each parameter in conjunction with the median values of the rest. A few hypothetical brain tissue injury criteria were calculated for each simulation case. A linear model was used to assess the significance of difference. It was found that nearly all variations produced significant effect on all the deformation metrics studied. But only the variation of layer thicknesses caused greater than 5% difference in Von Mises stress and maximum principal strain.

The effect of variation viscoelastic properties was much smaller compared to the influence of variation in layer thicknesses and absence or presence of the CSF and scalp.

8.3.1 H0 – Brain deformation do not vary as a result of between subjects variation of calvarium geometry and viscoelastic properties

Linear model	Effect-size in case of rejection at $\alpha=0.05$ (in engineering units)			
	Pressure [kPa]	Von Mises stress [kPa]	Maximum shear strain [%]	Maximum shear strain rate [/s]
Outer cortical thickness	-5.752	-0.122	-0.037	-0.240
Diploe thickness	7.155	-0.660	-0.174	-1.744
Inner cortical thickness	-3.344	-0.150	-0.045	-0.296
Diploe quasi-static modulus	-2.860	-0.061	-0.020	
Diploe fractional viscoelasticity	-5.151	-0.040	-0.009	-0.222

9 Limitations

9.1 Effect of fluid content in the diploe layer

Since the diploe contains interconnected pores filled with fluids, removal of the cylindrical cores from the calvarium could significantly change the mechanics of fluid flow relative to the in-vivo case. This study does not attempt to study the fluid mechanics of the diploe layer and merely treats it as a viscoelastic solid continuum. Therefore, the properties obtained here may be significantly different from the in-vivo case.

9.2 Distinction of layers of the calvarium

Compared to other methods of segmentation (Buie et al., 2007), the method of distinction of the three layers of the calvarium developed in this dissertation may appear sensitive to the smallest intra-cortical pores in the bone. But the values reported are median measurements in 2.5 by 2.5 mm areas in addition to 100 Monte Carlo iterations. Thus the influence of the small pores at the scale of μ CT resolution is mitigated to a large extent. Reporting the median value is akin to the blurring of the μ CT images in the direction tangential to the skull (Lillie et al., 2015).

9.3 Isotropy of the cortical and diploe layers

Isotropy was assumed for the micro-scale (50 μ m) mechanical behavior of cortical layers of the calvarium. Although human cortical bone from the long bones is known to be anisotropic from studies of histology and mechanical response (Carando et al., 1989; Fan et al., 2002; Turner et al., 1995), anisotropy is not observed in studies of skull cortical bone (Dempster, 1967; McElhaney et al., 1970). Nonetheless, observation of osteonal anisotropy in the coupons was not possible at the imaging resolution (50 μ m) used.

While there is evidence that the diploe layer of the human calvarium is transversely isotropic, at least under shear (McElhaney et al., 1970), assumption of full isotropy of the diploe layer is a limitation of this dissertation. The composite samples were tested under compression and tension in only the direction normal to the skull and therefore the anisotropy could not be analyzed.

However, through visual inspection of μ CT images of the composite core samples (Section 14.4), no organized material arrangement was apparent and the trabeculae appeared randomly oriented.

It is currently understood that trabecular bone remodeling occurs as a result of the stress imposed on the bone, and there is evidence of alignment of trabeculae to directions of loading in the human vertebrae (Pal et al., 1988). In contrast to the vertebra or the long bones of the human

body, except at the points of muscular attachment (temporalis muscle at the lateral boundary of the frontal and inferior boundary of the parietal bones) the skull bears much less loads. This was another factor that encouraged the assumption of isotropy.

For complete description of an isotropic material, it is essential to outline its transverse behavior and Poisson's ratio. The deformation of the gage area in the direction perpendicular to tension in the coupon tensile tests could not be sensed with sufficient signal to noise ratio using the digital image stereo-correlation technique because of the limited length of the gage area in the lateral direction as compared to the direction of loading (2.5 vs. 6 mm respectively). As a result, the transverse deformation behavior coupled to the tension could not be characterized. The deformation of the composite cores in the transverse directions was not sensed in the dynamic compression and cyclic transmissibility tests. The force response in the micro FE models of the coupon tensile tests was insensitive to the Poisson's ratio and a value of 0.40 was used (Dong and Guo, 2004; Robbins and Wood, 1969). The Poisson's ratio of the diploe layer was assumed to be 0.20 (Dalstra et al., 1993; McElhaney et al., 1970). The lack of this information means that the shear response cannot be predicted for both the cortical and diploe layers using data from this study.

9.4 Assumption of linear viscoelasticity

It was assumed that the viscoelastic behavior scaled linearly with magnitude of strain or stress. Increase in $\tan\delta$ with increasing strain has been observed in case of the soft tissues of the human body (Funk et al., 1999; Toms et al., 2002; Woo et al., 1980) and hard materials like copper and manganese alloys (Laddha and Aken, 1995; Ritchie and Pan, 1992). Although this behavior cannot be captured using a linear viscoelastic material, difference in strain magnitude could explain to some extent the relatively large material loss tangent found in this study compared to cortical bone studies (Garner et al., 1999).

10 Contributions

10.1 Methodology for layer thickness estimation

A probabilistic and threshold-independent segmentation was used in this dissertation. It was used to address the uncertainty in partial volume effects. The apparent density corresponding to 50% probability of segmentation was 730 mg HA/cm³ at an average and the median apparent density of the mode corresponding to bone for each core was 989 mg HA/cm³ at an average. A methodology for determination of the layer thicknesses at length scales of interest was developed. A Monte Carlo study using the probabilistic segmentation showed that this method is not sensitive to partial volume effects in case of μ CT of the calvarium. The outer cortical layer was shown to be thicker than the inner.

10.2 Methodology for determination of viscoelasticity in bone

A test setup was designed that utilized a piezoelectric shaker to apply linear vibration and lightweight and rigid transducer pairs were used to monitor the boundary conditions on a cylindrical sample. A concurrent μ CT study was used to develop geometrically accurate FE models of the composite test specimens. The displacement boundary conditions as recorded in the experiments were used as inputs to these FE models and the viscoelastic properties of a particular component was identified through optimization with the objective of matching the force at the boundary.

In contrary to previous studies in the literature (Garner et al., 1999), larger samples of variable size have been used to have a valid continuum assumption and a sizeable part of the force response was found to be attributable to sample inertia.

10.3 Influence of cortical bone microstructure on its structural response

Correlation (Power law regression, $R^2 = 0.51$) was found between the porosity of cortical coupon samples and their effective mechanical modulus. The fact that micro FE models provided only a small improvement in the predictability of effective composite modulus of cortical bone from the calvarium (linear regression, $R^2 = 0.54$) indicates the lack of arrangement and organization of pores immediately adjacent to the cortical layers in the calvarium. The use of micro FE models was still deemed successful because it reduced the variation in the estimated material property to 19% (compared to 27% for the effective structural modulus and 21% for the prediction from BVF based power law model).

10.4 Dependence on location

Because of the large sample size for the geometric study (median measurements at 2,850 regions in the 94 skull core samples) and the skewed distribution of these measurements, the non-parametric Wilcoxon rank sum test was used to determine the statistical significance of differences. The layer thicknesses and the diploe layer bone volume fraction were found to vary between the frontal and parietal bones of each subject, but there was no common trend.

The mechanical properties on the other hand were tested using one-way within subject ANOVA which controls for between subject differences. The cortical layer bone phase Young's modulus as derived from the micro FE models varied between the superior and inferior aspects of the skull while the diploe layer effective quasi-static modulus and fractional viscoelasticity were different for the frontal and parietal bones.

10.5 Analysis of mechanical properties and microstructure of same samples

There is no other study in the literature which has reported the mechanical properties, microstructure, and layer thicknesses in same samples of bone from the human calvarium. As a

result of this combined approach, the Young's modulus of cortical bone of the calvarium found in this study has smaller variance as compared to other studies of calvarium cortical bone samples. The paired values of layer thicknesses and mechanical properties of the cortical and diploe layers yielded bending stiffness values which varied less than models that used constant mechanical properties because of the same reason.

10.6 Integrated model of the calvarium

The geometry presented by this dissertation in terms of average and variance, of 3D shape and layer thicknesses, observed in the ten subjects, can be directly used to obtain the three dimensional mesh for use in an FE model of the calvarium. The influence of the variation of this geometry in the brain response can be studied by future researchers.

Material properties of the three layers are provided in this dissertation as average values and variances across the calvarium. Despite the assumptions of isotropy and linear elasticity, this represents a valuable dataset for use by future researchers. The head FE modeler can apply these mechanical properties to the mesh built in the previous step or even to their existing mesh.

10.7 Impact of variation of properties of the calvarium on brain deformation

A simplified plane-strain version of this model has been used to demonstrate the difference made by a viscoelastic calvarium on the deformation of the brain caused by a blast. The effects of variation of layer thicknesses and mechanical properties were also analyzed. It was found that layer thicknesses had substantial influence on the Von Mises stress and maximum shear strain. The mechanical properties on the other hand did not have a substantial effect.

10.8 Summary

1. A new method of probabilistic segmentation of bone that does not require the assumption of any threshold value is presented. This technique allows the use of Monte Carlo methods to quantify any error in segmentation introduced by partial volume effects and noise. Variance in results due to probabilistic segmentation is found to be very small.
2. Detection of small pores in the calvarium, which was previously impossible, was enabled by μ CT and the thicknesses of the cortical tables were determined to be actually much less than the existing values in the literature.
3. The diploe layer thickness varied significantly between subjects (median value of 1.25 mm or 33.8%).
4. The outer cortical layer was found to be significantly thicker than the inner cortical layer (median ratio is 1.68).
5. Although there were significant differences in layer thicknesses across the calvarium, there was no common trend in this difference, except for diploe layer thickness which was greater for frontal bone in eight out of the ten subjects.
6. Diploe layer bone volume fraction was significantly greater in the inferior aspect of the calvarium in nine out of ten subjects.
7. Bone microstructure near the cortical layer, as observable using μ CT at a resolution of 50 μ m, has small contribution to the variance in effective elastic modulus of the calvarium outer cortical layer.
8. Significant difference found between frontal and parietal bone for effective failure stress and strain for the coupon tensile tests.

9. Bone phase modulus (18.51 ± 3.46 GPa) of the outer cortical layer varied significantly between the superior and inferior aspects of the calvarium.
10. Porosity of the diploe layer had no significant influence on its effective elastic modulus.
11. Both composite through-the-thickness and effective diploe layer moduli varied significantly between subjects.
12. Effective Young's modulus of the diploe layer of the calvarium (273 ± 125 MPa) was found to vary between the frontal and parietal bones.
13. The diploe layer stiffens around fourfold over a decade of frequency (1 to 10 kHz).
14. Viscoelastic material loss tangent of the diploe layer of the calvarium is more than an order of magnitude greater compared to cortical bone in the 10 to 50 kHz range.
15. The fractional viscoelastic modulus (3.3 ± 1.2) varies between the frontal and parietal bones.
16. Based on the ten calvaria studied, an average morphology of the cranial vault (and its variance) has been presented. A map of layer thicknesses and mechanical parameters in the sampled area on the calvarium (and its variance) has also been shown.
17. The results have been shown on a 2D Alber's conic projection of the cranial vault. These can be directly used in any FE model of the calvarium through identification of the cranial landmarks and reverse mapping.
18. Compared to mechanical properties, layer thicknesses have more influence on the peak deformation in the majority of the brain.

19. Change in deformation caused by variations in layer thicknesses, particularly the diploe layer thickness, is comparable to that caused by the presence or absence of the CSF and scalp.
20. The viscoelastic diploe layer attenuates the high frequency content of stress in regions near the blast impact site after 2 ms after impact.

11 Future work

11.1 Detailed blast-brain FE study

Blast researchers are the intended audience of the data presented in this dissertation. Although a simplified model of the skull brain system is used in this dissertation to highlight the impact of viscoelasticity of the calvarium on the deformation of the brain caused by blast, a far more extensive study is required. More detailed models of the head and brain are available and they can be augmented with the statistical information obtained in this study to predict more accurately a complete spectrum of outcomes rather than a unique deterministic outcome caused by a particular blast wave.

The investigation of the effects of location dependency of layer thicknesses and mechanical properties may yield valuable information regarding blast brain injury and result in effective counter-measure design. However, this requires a 3D FE model of the cranium.

11.2 Micro scale properties of trabecular bone

The μ CT imaging of the composite core samples could be used to build high resolution micro FE models. These models can be used to estimate the properties of trabecular bone at the micro scale and test the hypothesis of relatively greater variance in the elastic properties of the trabecular

bone. Micro FE models of the diploe layer were built at a resolution of 50 μm . These models had approximately 12 million elements each (Figure 11.1) and solving it using the LSDYNA implicit solver required an extremely large memory and nearly 3 hours per sample per iteration. A more complex model with fluid structure interaction can be used to study the properties of the pore contents.

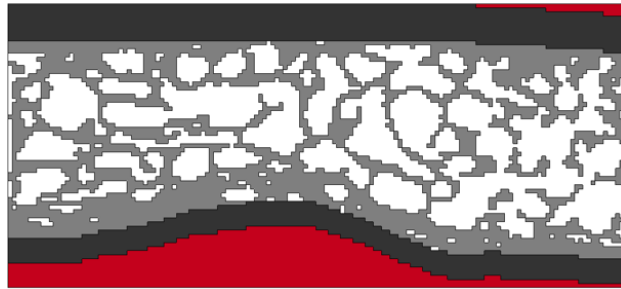


Figure 11.1 A cross-section view of a micro FE model of a composite core specimen.

12 Conclusion

This dissertation investigates the shape, geometry, and microstructure of the human calvarium and develops a viscoelastic model to predict its high-strain rate mechanical behavior in through-the-thickness deformation mode. Because of the distinction of the three layers the integrated model additionally exhibits accurate bending response. The statistical variation of these measurements between and within subjects has been investigated. This information is essential for simulation of blast exposure of the human head. Methodologies have been developed for objective distinction of the three layers of the calvarium and, testing the viscoelastic response of composite specimens in the frequency range of 1 to 20 kHz. A simplified FE model was used to highlight the importance of the variation of parameters obtained in this study.

13 References

- Abel, J.M., Gennarelli, T.A., Segawa, H., 1978. Incidence and severity of cerebral concussion in the rhesus monkey following sagittal plane angular acceleration.
- Ackerman, M.J., 1998. The Visible Human Project. *Proc. IEEE* 86, 504–511.
doi:10.1109/5.662875
- Adeloye, A., Kattan, K.R., Silverman, F.N., 1975. Thickness of the normal skull in the American blacks and whites. *Am. J. Phys. Anthropol.* 43, 23–30. doi:10.1002/ajpa.1330430105
- Adler, L., Cook, K. V, 1975. Ultrasonic parameters of freshly frozen dog tibia. *J. Acoust. Soc. Am.* 58.
- Antona-Makoshi, J., Davidsson, J., Ejima, S., Ono, K., 2012. Reanalysis of monkey head concussion experiment data using a novel monkey finite element model to develop brain tissue injury reference values, in: *Proceedings of the International Research Council on the Biomechanics of Injury Conference*. pp. 441–454.
- Antona-Makoshi, J., Davidsson, J., Ejima, S., Ono, K., Brodin, K., Anata, K., 2013. Correlation of global head and brain tissue injury criteria to experimental concussion derived from monkey head trauma experiments, in: *IRCOBI Conference*. pp. 509–522.
- Antona-Makoshi, J., Eliasson, E., Davidsson, J., Ejima, S., Ono, K., 2015. Effect of Aging on Brain Injury Prediction in Rotational Head Trauma—A Parameter Study with a Rat Finite Element Model. *Traffic Inj. Prev.* 16, S91–S99. doi:10.1080/15389588.2015.1021416
- Anzelmo, M., Ventrice, F., Barbeito-Andrés, J., Pucciarelli, H.M., Sardi, M.L., 2015. Ontogenetic changes in cranial vault thickness in a modern sample of *Homo sapiens*. *Am. J. Hum. Biol.*

27, 475–485. doi:10.1002/ajhb.22673

Ascenzi, A., Bonucci, E., 1967. The tensile properties of single osteons. *Anat. Rec.* 158, 375–386.

doi:10.1002/ar.1091580403

Asgharpour, Z., Baumgartner, D., Willinger, R., Graw, M., Peldschus, S., 2014. The validation and application of a finite element human head model for frontal skull fracture analysis. *J. Mech. Behav. Biomed. Mater.* 33, 16–23. doi:10.1016/j.jmbbm.2013.02.010

Auperrin, A., Delille, R., Lesueur, D., Bruyère, K., Masson, C., Drazétic, P., 2014. Geometrical and material parameters to assess the macroscopic mechanical behaviour of fresh cranial bone samples. *J. Biomech.* 47, 1180–5. doi:10.1016/j.jbiomech.2013.10.060

Baer, M.J., Harris, J.E., 1969. A commentary on the growth of the human brain and skull. *Am. J. Phys. Anthropol.* 30, 39–44. doi:10.1002/ajpa.1330300105

Bain, A.C., Meaney, D.F., 2000. Tissue-Level Thresholds for Axonal Damage in an Experimental Model of Central Nervous System White Matter Injury. *J. Biomech. Eng.* 122, 615–622.

Bandak, F.A., Eppinger, R.H., 1994. Three-dimensional finite element analysis of the human brain under combined rotational and translational accelerations. *Proc. Stapp Car Crash Conf.* 38, 145–163.

Baral, P., Koirala, S., Gupta, M.K., 2014. Calvarial thickness of Nepalese skulls-computerised tomographic (CT) study. *Anat. Physiol. Curr. Res.* 2014.

Barber, T.W., Brockway, J.A., Moffatt, C.A., 1969. Static compression testing of specimens from an embalmed human skull. *Tex. Rep. Biol. Med.* 28, 497–508.

Benninghoff, A., 1925. Spaltlinien am Knochen, eine Methode zur Ermittlung der Architektur

- platter knochen. *Verh Anat Ges* 34, 189–206.
- Bilukha, O.O., Brennan, M., Anderson, M., 2008. The Lasting Legacy of War: Epidemiology of Injuries from Landmines and Unexploded Ordnance in Afghanistan, 2002–2006. *Prehosp. Disaster Med.* 23, 493–499. doi:10.1017/S1049023X00006300
- Black, J., Korostoff, E., 1973. Dynamic mechanical properties of viable human cortical bone. *J. Biomech.* 6, 435–438. doi:10.1016/0021-9290(73)90001-8
- Blumbers, P.C., Scott, G., Vis, J.I.M.M., Wainwright, H., Simpson, D.A., McLean, A.J., 1995. Topography of Axonal Injury as Defined by Amyloid Precursor Protein and the Sector Scoring Method in Mild and Severe Closed Head Injury. *J. Neurotrauma* 12, 565–572. doi:10.1089/neu.1995.12.565
- Boothroyd, B., 1964. THE PROBLEM OF DEMINERALISATION IN THIN SECTIONS OF FULLY CALCIFIED BONE. *J. Cell Biol.* 20, 165–173. doi:10.1083/jcb.20.1.165
- Boruah, S., Subit, D.L., Crandall, J.R., Salzar, R.S., Shender, B.S., Paskoff, G., 2014. A lumped-mass model to simulate through-the-thickness transmission of vibration in the adult human skull. *Proc. IRCOBI Conf.*
- Brown, S., Bailey, D.L., Willowson, K., Baldock, C., 2008. Investigation of the relationship between linear attenuation coefficients and CT Hounsfield units using radionuclides for SPECT. *Appl. Radiat. Isot.* 66, 1206–12. doi:10.1016/j.apradiso.2008.01.002
- Buechner, P.M., Lakes, R.S., Swan, C., Brand, R.A., 2001. A Broadband Viscoelastic Spectroscopic Study of Bovine Bone: Implications for Fluid Flow. *Ann. Biomed. Eng.* 29, 719–728. doi:10.1114/1.1385813

- Buie, H.R., Campbell, G.M., Klinck, R.J., MacNeil, J.A., Boyd, S.K., 2007. Automatic segmentation of cortical and trabecular compartments based on a dual threshold technique for in vivo micro-CT bone analysis. *Bone* 41, 505–15. doi:10.1016/j.bone.2007.07.007
- Carando, S., Barbos, M.P., Ascenzi, A., Boyde, A., 1989. Orientation of collagen in human tibial and fibular shaft and possible correlation with mechanical properties. *Bone* 10, 139–142. doi:10.1016/8756-3282(89)90012-4
- Carter, D.R., Hayes, W.C., 1977. The compressive behavior of bone as a two-phase porous structure. *J. Bone Jt. Surg.* 59, 954–962.
- CARTER, D.R., SPENGLER, D.A.N.M., 1978. Mechanical Properties and Composition of Cortical Bone. *Clin. Orthop. Relat. Res.* 135.
- Cernak, I., Noble-Haeusslein, L.J., 2010. Traumatic Brain Injury: An Overview of Pathobiology with Emphasis on Military Populations. *J. Cereb. Blood Flow Metab.* 30, 255–266. doi:10.1038/jcbfm.2009.203
- Chafi, M.S., Ganpule, S., Gu, Li., Chandra, N., 2011. DYNAMIC RESPONSE OF BRAIN SUBJECTED TO BLAST LOADINGS: INFLUENCE OF FREQUENCY RANGES. *Int. J. Appl. Mech.* 03, 803–823. doi:10.1142/S175882511100124X
- Chafi, M.S., Karami, G., Ziejewski, M., 2009. Biomechanical Assessment of Brain Dynamic Responses Due to Blast Pressure Waves. *Ann. Biomed. Eng.* 38, 490–504. doi:10.1007/s10439-009-9813-z
- Chafi, M.S., Karami, G., Ziejewski, M., 2009. Numerical analysis of blast-induced wave propagation using FSI and ALE multi-material formulations. *Int. J. Impact Eng.* 36, 1269–1275. doi:10.1016/j.ijimpeng.2009.03.007

- Chandra, N., Ganpule, S., Kleinschmit, N.N., Feng, R., Holmberg, A.D., Sundaramurthy, A., Selvan, V., Alai, A., 2012. Evolution of blast wave profiles in simulated air blasts: experiment and computational modeling. *Shock Waves* 22, 403–415. doi:10.1007/s00193-012-0399-2
- Chen, Y., Huang, W., 2011. Non-impact, blast-induced mild TBI and PTSD: Concepts and caveats. *Brain Inj.* 25, 641–650. doi:10.3109/02699052.2011.580313
- Collins, D.L., Zijdenbos, A.P., Kollokian, V., Sled, J.G., Kabani, N.J., Holmes, C.J., Evans, A.C., 1998. Design and construction of a realistic digital brain phantom. *IEEE Trans. Med. Imaging* 17, 463–468. doi:10.1109/42.712135
- Cooper, G.J., 1996. Protection of the Lung from Blast Overpressure by Thoracic Stress Wave Decouplers. *J. Trauma Acute Care Surg.* 40.
- Cooper, G.J., Townend, D.J., Cater, S.R., Pearce, B.P., 1991. The role of stress waves in thoracic visceral injury from blast loading: Modification of stress transmission by foams and high-density materials. *J. Biomech.* 24, 273–285. doi:10.1016/0021-9290(91)90346-O
- Cripps, N.P.J., Cooper, G.J., 1996. The Influence of Personal Blast Protection on the Distribution and Severity of Primary Blast Gut Injury. *J. Trauma Acute Care Surg.* 40.
- Crowninshield, R.D., Pope, M.H., 1974. The response of compact bone in tension at various strain rates. *Ann. Biomed. Eng.* 2, 217–225.
- Currey, J.D., 1988. The effect of porosity and mineral content on the Young's modulus of elasticity of compact bone. *J. Biomech.* 21, 131–139. doi:10.1016/0021-9290(88)90006-1
- Dalstra, M., Huiskes, R., Odgaard, A., van Erning, L., 1993. Mechanical and textural properties

- of pelvic trabecular bone. *J. Biomech.* 26, 523–535. doi:10.1016/0021-9290(93)90014-6
- Davenport, N.D., Lim, K.O., Armstrong, M.T., Sponheim, S.R., 2012. Diffuse and spatially variable white matter disruptions are associated with blast-related mild traumatic brain injury. *Neuroimage* 59, 2017–24. doi:10.1016/j.neuroimage.2011.10.050
- de Souza Fernandes, A.C., Neto, A.I.T., de Freitas, A.C., de Moraes, M., 2011. Dimensional analysis of the parietal bone in areas of surgical interest and relationship between parietal thickness and cephalic index. *J. Oral Maxillofac. Surg.* 69, 2930–5. doi:10.1016/j.joms.2011.02.026
- Deck, C., Willinger, R., 2008. Improved head injury criteria based on head FE model. *Int. J. Crashworthiness* 13, 667–678. doi:10.1080/13588260802411523
- Deligianni, D.D., Maris, A., Missirlis, Y.F., 1994. Stress relaxation behaviour of trabecular bone specimens. *J. Biomech.* 27, 1469–1476. doi:10.1016/0021-9290(94)90196-1
- Delille, R., Lesueur, D., Potier, P., Drazetic, P., Markiewicz, E., 2007. Experimental study of the bone behaviour of the human skull bone for the development of a physical head model. *Int. J. Crashworthiness* 12, 101–108. doi:10.1080/13588260701433081
- Dempster, W.T., 1967. Correlation of types of cortical grain structure with architectural features of the human skull. *Am. J. Anat.* 120, 7–31. doi:10.1002/aja.1001200103
- Denny-Brown, D., Russell, W.R., 1940. Experimental cerebral concussion. *J. Physiol.* 99, 153. doi:10.1113/jphysiol.1940.sp003887
- Dong, X.N., Guo, X.E., 2004. The dependence of transversely isotropic elasticity of human femoral cortical bone on porosity. *J. Biomech.* 37, 1281–7.

doi:10.1016/j.jbiomech.2003.12.011

Dong, X.N., Yeni, Y.N., Les, C.M., Fyhrie, D.P., 2004. Effects of end boundary conditions and specimen geometry on the viscoelastic properties of cancellous bone measured by dynamic mechanical analysis. *J. Biomed. Mater. Res. Part A* 68A, 573–583.

doi:10.1002/jbm.a.20108

Elahi, M.M., Lessard, M.L., Hakim, S., Watkin, K., Sampalis, J., 1997. Ultrasound in the Assessment of Cranial Bone Thickness. *J. Craniofac. Surg.* 8.

Elder, G.A., Cristian, A., 2009. Blast-related mild traumatic brain injury: mechanisms of injury and impact on clinical care. *Mt. Sinai J. Med. A J. Transl. Pers. Med.* 76, 111–118.

doi:10.1002/msj.20098

Elkin, B.S., Morrison III, B., 2007. Region-specific tolerance criteria for the living brain. *Stapp Car Crash J.* 51, 127.

Evans, F.G., Lissner, H.R., 1957. Tensile and compressive strength of human parietal bone. *J. Appl. Physiol.* 10, 493–497.

Fan, Z., Swadener, J.G., Rho, J.Y., Roy, M.E., Pharr, G.M., 2002. Anisotropic properties of human tibial cortical bone as measured by nanoindentation. *J. Orthop. Res.* 20, 806–810.

doi:10.1016/S0736-0266(01)00186-3

Faul, M., Xu, L., Wald, M.M., Coronado, V.G., 2010. Traumatic brain injury in the United States. Atlanta, GA Centers Dis. Control Prev. Natl. Cent. Inj. Prev. Control.

Fischer, H., 2010. US Military casualty statistics: operation new dawn, operation Iraqi freedom, and operation enduring freedom.

- Frasca, P., Harper, R., Katz, J.L., 1981. Strain and frequency dependence of shear storage modulus for human single osteons and cortical bone microsamples—Size and hydration effects. *J. Biomech.* 14, 679–690. doi:10.1016/0021-9290(81)90050-6
- Funk, J.R., Hall, G.W., Crandall, J.R., Pilkey, W.D., 1999. Linear and Quasi-Linear Viscoelastic Characterization of Ankle Ligaments. *J. Biomech. Eng.* 122, 15–22.
- Gadd, C.W., 1966. Use of Weighted-impulse Criterion for Estimating Injury Hazard: Proceedings of the Tenth Stapp Car Crash Conference. Society of Automotive Engineers. Inc., New York.
- Galbraith, J.A., Thibault, L.E., Matteson, D.R., 1993. Mechanical and Electrical Responses of the Squid Giant Axon to Simple Elongation. *J. Biomech. Eng.* 115, 13–22.
- Ganpule, S., Alai, A., Plougonven, E., Chandra, N., 2012. Mechanics of blast loading on the head models in the study of traumatic brain injury using experimental and computational approaches. *Biomech. Model. Mechanobiol.* 12, 511–531. doi:10.1007/s10237-012-0421-8
- Garner, E., Lakes, R., Lee, T., Swan, C., Brand, R., 1999. Viscoelastic Dissipation in Compact Bone: Implications for Stress-Induced Fluid Flow in Bone. *J. Biomech. Eng.* 122, 166–172.
- Gayzik, F.S., Moreno, D.P., Geer, C.P., Wuertzer, S.D., Martin, R.S., Stitzel, J.D., 2011. Development of a Full Body CAD Dataset for Computational Modeling: A Multi-modality Approach. *Ann. Biomed. Eng.* 39, 2568–2583. doi:10.1007/s10439-011-0359-5
- Gennarelli, T.A., Thibault, L.E., Adams, J.H., Graham, D.I., Thompson, C.J., Marcincin, R.P., 1982. Diffuse axonal injury and traumatic coma in the primate. *Ann. Neurol.* 12, 564–574. doi:10.1002/ana.410120611

- Ghajar, J., 2000. Traumatic brain injury. *Lancet* (London, England) 356, 923–9.
doi:10.1016/S0140-6736(00)02689-1
- Gilchrist, M.D., O'Donoghue, D., Horgan, T.J., 2001. A two-dimensional analysis of the biomechanics of frontal and occipital head impact injuries. *Int. J. Crashworthiness* 6, 253–262. doi:10.1533/cras.2001.0176
- Gordon, C.C., Churchill, T., Clauser, C.E., Bradtmiller, B., McConville, J.T., 1989. Anthropometric survey of US army personnel: methods and summary statistics 1988.
- Got, C., Patel, A., Fayon, A., Tarriere, C., Walfisch, G., 1978. Results of experimental head impacts on cadavers: the various data obtained and their relations to some measured physical parameters, in: *Proceedings: Stapp Car Crash Conference*. pp. 57–99.
- Gould, S.J., 1993. *American polygeny and craniometry before Darwin*. Bloomington.
- Gray, H., 1918. *Anatomy of the human body*. Lea & Febiger.
- Gross, A.G., 1958. A New Theory on the Dynamics of Brain Concussion and Brain Injury. *J. Neurosurg.* 15, 548–561. doi:10.3171/jns.1958.15.5.0548
- Gurdjian, E.S., Hodgson, V.R., Thomas, L.M., Patrick, L.M., 1968. Significance of Relative Movements of Scalp, Skull, and Intracranial Contents During Impact Injury of the Head. *J. Neurosurg.* 29, 70–72. doi:10.3171/jns.1968.29.1.0070
- Gurdjian, E.S., Lissner, H.R., 1961. Photoelastic Confirmation of the Presence of Shear Strains at the Craniospinal Junction in Closed Head Injury. *J. Neurosurg.* 18, 58–60.
doi:10.3171/jns.1961.18.1.0058
- Gurdjian, E.S., Lissner, H.R., Webster, J.E., Latimer, F.R., Haddad, B.F., 1954. Studies on

Experimental Concussion: Relation of Physiologic Effect to Time Duration of Intracranial Pressure Increase at Impact. *Neurology* 4, 674. doi:10.1212/WNL.4.9.674

Gurdjian, E.S., Roberts, V.L., Thomas, L.M., 1966. TOLERANCE CURVES OF ACCELERATION AND INTRACRANIAL PRESSURE AND PROTECTIVE INDEX IN EXPERIMENTAL HEAD INJURY. *J. Trauma Acute Care Surg.* 6.

Haggare, J., Rönning, O., 1995. Growth of the cranial vault: Influence of intracranial and extracranial pressures. *Acta Odontol. Scand.* 53, 192–195.
doi:10.3109/00016359509005971

Halgrin, J., Shiri, S., Marechal, C., Haugou, G., Bresson, F., Colard, T., 2012. Experimental and numerical characterisation of the mechanical behaviour of the cranial bone. *Comput. Methods Biomech. Biomed. Engin.* 15, 313–315. doi:10.1080/10255842.2012.713719

Haller, J.S., 1970. The species problem: nineteenth-century concepts of racial inferiority in the origin of man controversy. *Am. Anthropol.* 72, 1319–1329.

Hansen, U., Zioupos, P., Simpson, R., Currey, J.D., Hynd, D., 2008. The Effect of Strain Rate on the Mechanical Properties of Human Cortical Bone. *J. Biomech. Eng.* 130, 11011.

Hardy, W.N., Foster, C.D., Mason, M.J., Yang, K.H., King, A.I., Tashman, S., 2001. Investigation of Head Injury Mechanisms Using Neutral Density Technology and High-Speed Biplanar X-ray. *Stapp Car Crash J.* 45, 337—368.

Hatipoglu, H.G., Ozcan, H.N., Hatipoglu, U.S., Yuksel, E., 2008. Age, sex and body mass index in relation to calvarial diploe thickness and craniometric data on MRI. *Forensic Sci. Int.* 182, 46–51. doi:10.1016/j.forsciint.2008.09.014

- Hayes, W.C., Snyder, B., 1981. Toward a quantitative formulation of Wolff's law in trabecular bone. *Mech. Prop. bone* 45, 43–68.
- Hodgson, V.R., Brinn, J., Thomas, L.M., Greenberg, S.W., 1970. Fracture behavior of the skull frontal bone against cylindrical surfaces.
- Hoge, C.W., McGurk, D., Thomas, J.L., Cox, A.L., Engel, C.C., Castro, C.A., 2008. Mild Traumatic Brain Injury in U.S. Soldiers Returning from Iraq. *N. Engl. J. Med.* 358, 453–463. doi:10.1056/NEJMoa072972
- Holbourn, A.H.S., 1943. Mechanics of head injuries. *Lancet* 242, 438–441.
- Horgan, T.J., Gilchrist, M.D., 2003. The creation of three-dimensional finite element models for simulating head impact biomechanics. *Int. J. Crashworthiness* 8, 353–366.
- Howells, W.W., 1973. CRANIAL VARIATION IN MAN. A STUDY BY MULTIVARIATE ANALYSIS OF PATTERNS OF DIFFERENCE. AMONG RECENT HUMAN POPULATIONS. *Pap. PEABODY MUSEUM Archaeol. Ethnol.* 1–259.
- Hubbard, R.P., 1971. Flexure of layered cranial bone. *J. Biomech.* 4, 251–263.
- Huxley, T.H., 1867. On two widely contrasted forms of the human cranium. *J. Anat. Physiol.* 1, 60.
- Hwang, K., Hollinger, J.O., Chung, R.S., Lee, S.I.I., 2000. Histomorphometry of Parietal Bones Versus Age and Race. *J. Craniofac. Surg.* 11.
- Hwang, K., Kim, J.H., Baik, S.H., 1997. Thickness Map of Parietal Bone in Korean Adults. *J. Craniofac. Surg.* 8.
- Ishida, H., Dodo, Y., 1990. Cranial Thickness of Modern and Neolithic Populations in Japan.

Hum. Biol. 62, 389–401.

Jenkinson, A.F., 1955. The frequency distribution of the annual maximum (or minimum) values of meteorological elements. *Q. J. R. Meteorol. Soc.* 81, 158–171.

doi:10.1002/qj.49708134804

Johnson, T.P.M., Socrate, S., Boyce, M.C., 2010. A viscoelastic, viscoplastic model of cortical bone valid at low and high strain rates. *Acta Biomater.* 6, 4073–80.

doi:10.1016/j.actbio.2010.04.017

Jorge, R.E., Acion, L., White, T., Tordesillas-Gutierrez, D., Pierson, R., Crespo-Facorro, B., Magnotta, V.A., 2012. White matter abnormalities in veterans with mild traumatic brain injury. *Am. J. Psychiatry* 169, 1284–1291.

Jung, Y.-S., Kim, H.-J., Choi, S.-W., Kang, J.-W., Cha, I.-H., 2003. Regional thickness of parietal bone in Korean adults. *Int. J. Oral Maxillofac. Surg.* 32, 638–41.

doi:10.1054/ijom.2002.0415

Keaveny, T.M., Morgan, E.F., Niebur, G.L., Yeh, O.C., 2001. Biomechanics of Trabecular Bone. *Annu. Rev. Biomed. Eng.* 3, 307–333. doi:10.1146/annurev.bioeng.3.1.307

Keaveny, T.M., Pinilla, T.P., Crawford, R.P., Kopperdahl, D.L., Lou, A., 1997. Systematic and random errors in compression testing of trabecular bone. *J. Orthop. Res.* 15, 101–110.

doi:10.1002/jor.1100150115

Keith, A., 1910. Description of a New Craniometer and of Certain Age Changes in the Anthropoid Skull. *J. Anat. Physiol.* 44, 251–270.

Kemper, A.R., McNally, C., Kennedy, E.A., Manoogian, S.J., al, et, 2005. Material Properties of

- Human Rib Cortical Bone from Dynamic Tension Coupon Testing. *Stapp Car Crash J.* 49, 199–230.
- Kimpara, H., Iwamoto, M., 2011. Mild Traumatic Brain Injury Predictors Based on Angular Accelerations During Impacts. *Ann. Biomed. Eng.* 40, 114–126. doi:10.1007/s10439-011-0414-2
- King, A.I., Yang, K.H., Zhang, L., Hardy, W., Viano, D.C., 2003. Is head injury caused by linear or angular acceleration, in: *IRCOBI Conference*. pp. 1–12.
- Kleiven, S., 2006. Evaluation of head injury criteria using a finite element model validated against experiments on localized brain motion, intracerebral acceleration, and intracranial pressure. *Int. J. Crashworthiness* 11, 65–79. doi:10.1533/ijcr.2005.0384
- Kosif, R., Sirmatel, O., Canan, A., 2013. Morphometric measurements of the cranium in congenital bilateral blind males and females. *Bosn. J. Basic Med. Sci.* 13, 237–241.
- Krogman, W., 1951. Craniometry and cephalometry as research tools in growth of head and face1. *Am. J. Orthod.* 37, 406–414. doi:10.1016/0002-9416(51)90190-X
- Kushner, A., 1940. EVALUATION OF WOLFF'S LAW OF BONE FORMATION. *J. Bone Jt. Surg.* 22, 589–596.
- Laddha, S., Aken, D.C., 1995. On the application of magnetomechanical models to explain damping in an antiferromagnetic copper-manganese alloy. *Metall. Mater. Trans. A* 26, 957–964. doi:10.1007/BF02649092
- Lai, W.M., Rubin, D., Krempl, E., 2012. Kinematics of a continuum, in: *Introduction to Continuum Mechanics*. p. 98,108.

- Lakes, R.S., 2009. Viscoelastic materials. Cambridge University Press.
- Lakes, R.S., 1982. Dynamical Study of Couple Stress Effects in Human Compact Bone. *J. Biomech. Eng.* 104, 6–11.
- Lakes, R.S., Katz, J.L., Sternstein, S.S., 1979. Viscoelastic properties of wet cortical bone—I. Torsional and biaxial studies. *J. Biomech.* 12, 657–678. doi:10.1016/0021-9290(79)90016-2
- Lanyon, L.E., 1974. EXPERIMENTAL SUPPORT FOR THE TRAJECTORIAL THEORY OF BONE STRUCTURE. *Bone Joint J.* 56-B, 160–166.
- Laplaca, M.C., Lee, V.M.-Y., Thibault, L.E., 1997. An In Vitro Model of Traumatic Neuronal Injury: Loading Rate-Dependent Changes in Acute Cytosolic Calcium and Lactate Dehydrogenase Release. *J. Neurotrauma* 14, 355–368. doi:10.1089/neu.1997.14.355
- Le Lorc'h-Bukiet, I., Tulasne, J.-F., Llorens, A., Lesclous, P., 2005. Parietal bone as graft material for maxillary sinus floor elevation: structure and remodeling of the donor and of recipient sites. *Clin. Oral Implants Res.* 16, 244–249. doi:10.1111/j.1600-0501.2004.01102.x
- Lee, C., Loyd, A.M., Nightingale, R., Myers, B.S., Damon, A., Bass, C.R., 2014. Three-Dimensional Adult Male Head and Skull Contours. *Traffic Inj. Prev.* 15, 402–406. doi:10.1080/15389588.2013.822492
- Lewis, J.L., Goldsmith, W., 1975. The dynamic fracture and prefracture response of compact bone by split Hopkinson bar methods. *J. Biomech.* 8, 27–40. doi:10.1016/0021-9290(75)90040-8
- Lillie, E.M., Urban, J.E., Weaver, A.A., Powers, A.K., Stitzel, J.D., 2015. Estimation of skull

- table thickness with clinical CT and validation with microCT. *J. Anat.* 226, 73–80.
doi:10.1111/joa.12259
- Linde, F., Nørgaard, P., Hvid, I., Odgaard, A., Søballe, K., 1991. Mechanical properties of trabecular bone. Dependency on strain rate. *J. Biomech.* 24, 803–809. doi:10.1016/0021-9290(91)90305-7
- Ling, G., Bandak, F., Armonda, R., Grant, G., Ecklund, J., 2009. Explosive Blast Neurotrauma. *J. Neurotrauma* 26, 815–825. doi:10.1089/neu.2007.0484
- Lissner, H.R., Lebow, M., Evans, F.G., 1960. Experimental studies on the relation between acceleration and intracranial pressure changes in man. *Surg. Gynecol. Obstet.* 111, 329—338.
- Lubbock, P., Goldsmith, W., 1980. Experimental cavitation studies in a model head-neck system. *J. Biomech.* 13, 1041–1052. doi:10.1016/0021-9290(80)90048-2
- Lynnerup, N., 2016. Cranial thickness in relation to age, sex and general body build in a Danish forensic sample. *Forensic Sci. Int.* 117, 45–51. doi:10.1016/S0379-0738(00)00447-3
- Lynnerup, N., Astrup, J.G., Sejrsen, B., others, 2005. Thickness of the human cranial diploe in relation to age, sex and general body build. *Head Face Med* 1, 1–7.
- Mac Donald, C.L., Johnson, A.M., Cooper, D., Nelson, E.C., Werner, N.J., Shimony, J.S., Snyder, A.Z., Raichle, M.E., Witherow, J.R., Fang, R., Flaherty, S.F., Brody, D.L., 2011. Detection of Blast-Related Traumatic Brain Injury in U.S. Military Personnel. *N. Engl. J. Med.* 364, 2091–2100. doi:10.1056/NEJMoa1008069
- Magnuson, J., Leonessa, F., Ling, G.S.F., 2012. Neuropathology of Explosive Blast Traumatic

- Brain Injury. *Curr. Neurol. Neurosci. Rep.* 12, 570–579. doi:10.1007/s11910-012-0303-6
- Mano, J.F., 2005. Viscoelastic properties of bone: Mechanical spectroscopy studies on a chicken model. *Mater. Sci. Eng. C* 25, 145–152. doi:10.1016/j.msec.2005.01.017
- Mao, H., Zhang, L., Jiang, B., Genthikatti, V. V., Jin, X., Zhu, F., Makwana, R., Gill, A., Jandir, G., Singh, A., Yang, K.H., 2013. Development of a Finite Element Human Head Model Partially Validated With Thirty Five Experimental Cases. *J. Biomech. Eng.* 135, 111002.
- Margulies, S.S., Thibault, L.E., Gennarelli, T.A., 1990. Physical model simulations of brain injury in the primate. *J. Biomech.* 23, 823–836. doi:10.1016/0021-9290(90)90029-3
- McCalden, R.W., McGeough, J.A., Barker, M.B., Court-Brown, C.M., 1993. Age-related changes in the tensile properties of cortical bone. The relative importance of changes in porosity, mineralization, and microstructure. *J. Bone Jt. Surg.* 75, 1193–1205.
- McElhaney, J.H., 1966. Dynamic response of bone and muscle tissue. *J. Appl. Physiol.* 21, 1231–1236.
- McElhaney, J.H., Fogle, J.L., Melvin, J.W., Haynes, R.R., Roberts, V.L., Alem, N.M., 1970. Mechanical properties of cranial bone. *J. Biomech.* 3, 495–511. doi:10.1016/0021-9290(70)90059-X
- Meaney, D.F., Smith, D., Ross, D.T., Gennarelli, T.A., 1993. Diffuse axonal injury in the miniature pig: biomechanical development and injury threshold. *ASME Appl. Mech. Div.* 169, 169.
- Melvin, J.W., McElhaney, J.H., Roberts, V.L., 1970. Development of a mechanical model of the human head-determination of tissue properties and synthetic substitute materials.

- Moore, D.F., Jérusalem, A., Nyein, M., Noels, L., Jaffee, M.S., Radovitzky, R.A., 2009. Computational biology - modeling of primary blast effects on the central nervous system. *Neuroimage* 47 Suppl 2, T10–20. doi:10.1016/j.neuroimage.2009.02.019
- Moreira-Gonzalez, A., Papay, F.E., Zins, J.E., 2006. Calvarial Thickness and Its Relation to Cranial Bone Harvest. *Plast. Reconstr. Surg.* 117.
- Morgan, E.F., Keaveny, T.M., 2001. Dependence of yield strain of human trabecular bone on anatomic site. *J. Biomech.* 34, 569–577. doi:10.1016/S0021-9290(01)00011-2
- Morrison III, B., Cater, H.L., Wang, C.C.B., Thomas, F.C., others, 2003. A tissue level tolerance criterion for living brain developed with an in vitro model of traumatic mechanical loading. *Stapp Car Crash J.* 47, 93.
- Moss, W.C., King, M.J., Blackman, E.G., 2009. Skull Flexure from Blast Waves: A Mechanism for Brain Injury with Implications for Helmet Design. *Phys. Rev. Lett.* 103, 108702.
- Motherway, J.A., Verschueren, P., Van der Perre, G., Vander Sloten, J., Gilchrist, M.D., 2009. The mechanical properties of cranial bone: the effect of loading rate and cranial sampling position. *J. Biomech.* 42, 2129–35. doi:10.1016/j.jbiomech.2009.05.030
- Murray, C.J., Lopez, A.D., 1996. Global health statistics: a compendium of incidence prevalence and mortality estimates for over 200 conditions.
- Myers, B.S., McElhaney, J.H., Doherty, B.J., 1991. The viscoelastic responses of the human cervical spine in torsion: Experimental limitations of quasi-linear theory, and a method for reducing these effects. *J. Biomech.* 24, 811–817. doi:10.1016/0021-9290(91)90306-8
- Nahum, A.M., Gatts, J.D., Gadd, C.W., Danforth, J., 1968. Impact tolerance of the skull and face.

- Nahum, A.M., Smith, R., Ward, C.C., 1977. Intracranial pressure dynamics during head impact.
- Nahum, A.M., Smith, R.W., 1976. Experimental model for closed head impact injury. Proc. Stapp Car Crash Conf. 20, 785–814.
- Newman, J.A., Shewchenko, N., Welbourne, E., 2000. A proposed new biomechanical head injury assessment function - the maximum power index. Stapp Car Crash J. 44, 215—247.
- Nusholtz, G.S., Lux, P., Kaiker, P., Janicki, M.A., 1984. Head impact response - skull deformation and angular accelerations. Proc. Stapp Car Crash Conf. 28, 41–74.
- Nyein, M.K., Jason, A.M., Yu, L., Pita, C.M., Joannopoulos, J.D., Moore, D.F., Radovitzky, R.A., 2010. In silico investigation of intracranial blast mitigation with relevance to military traumatic brain injury. Proc. Natl. Acad. Sci. 107, 20703–20708.
doi:10.1073/pnas.1014786107
- Odgaard, A., Linde, F., 1991. The underestimation of Young's modulus in compressive testing of cancellous bone specimens. J. Biomech. 24, 691–698. doi:10.1016/0021-9290(91)90333-I
- Oyen, O.J., Walker, A., 1977. Stereometric craniometry. Am. J. Phys. Anthropol. 46, 177–182.
doi:10.1002/ajpa.1330460123
- Pal, G.P., Cosio, L., Routal, R. V., 1988. Trajectory architecture of the trabecular bone between the body and the neural arch in human vertebrae. Anat. Rec. 222, 418–425.
doi:10.1002/ar.1092220414
- Panzer, M.B., Myers, B.S., Bass, C.R., 2013. Mesh considerations for finite element blast modelling in biomechanics. Comput. Methods Biomech. Biomed. Engin. 16, 612–621.
doi:10.1080/10255842.2011.629615

- Panzer, M.B., Myers, B.S., Capehart, B.P., Bass, C.R., 2012. Development of a Finite Element Model for Blast Brain Injury and the Effects of CSF Cavitation. *Ann. Biomed. Eng.* 40, 1530–1544. doi:10.1007/s10439-012-0519-2
- Park, H.C., Lakes, R.S., 1986. Cosserat micromechanics of human bone: Strain redistribution by a hydration sensitive constituent. *J. Biomech.* 19, 385–397. doi:10.1016/0021-9290(86)90015-1
- Pensler, J., McCarthy, J.G., 1985. The Calvarial Donor Site: An Anatomic Study in Cadavers. *Plast. Reconstr. Surg.* 75.
- Peterson, J., Dechow, P.C., 2003. Material properties of the human cranial vault and zygoma. *Anat. Rec. Part A Discov. Mol. Cell. Evol. Biol.* 274A, 785–797. doi:10.1002/ar.a.10096
- Peterson, J., Dechow, P.C., 2002. Material properties of the inner and outer cortical tables of the human parietal bone. *Anat. Rec.* 268, 7–15. doi:10.1002/ar.10131
- Pham, D.L., Xu, C., Prince, J.L., 2000. Current Methods in Medical Image Segmentation. *Annu. Rev. Biomed. Eng.* 2, 315–337. doi:10.1146/annurev.bioeng.2.1.315
- Povlishock, J.T., Christman, C.W., 1995. The Pathobiology of Traumatically Induced Axonal Injury in Animals and Humans: A Review of Current Thoughts. *J. Neurotrauma* 12, 555–564. doi:10.1089/neu.1995.12.555
- Quaglioni, V., Russa, V. La, Corneo, S., 2009. Nonlinear stress relaxation of trabecular bone. *Mech. Res. Commun.* 36, 275–283. doi:10.1016/j.mechrescom.2008.10.012
- Rafaels, K.A., “Dale” Bass, C.R., Panzer, M.B., Salzar, R.S., Woods, W.A., Feldman, S.H., Walilko, T., Kent, R.W., Capehart, B.P., Foster, J.B., Derkunt, B., Toman, A., 2012. Brain

- injury risk from primary blast. *J. Trauma Acute Care Surg.* 73.
- Rahmoun, J., Auperrin, A., Delille, R., Naceur, H., Drazetic, P., 2014. Characterization and micromechanical modeling of the human cranial bone elastic properties. *Mech. Res. Commun.* 60, 7–14. doi:10.1016/j.mechrescom.2014.04.001
- Relethford, J.H., 2010. Population-specific deviations of global human craniometric variation from a neutral model. *Am. J. Phys. Anthropol.* 142, 105–111. doi:10.1002/ajpa.21207
- Rho, J.-Y., Tsui, T.Y., Pharr, G.M., 1997. Elastic properties of human cortical and trabecular lamellar bone measured by nanoindentation. *Biomaterials* 18, 1325–1330. doi:10.1016/S0142-9612(97)00073-2
- Ritchie, I.G., Pan, Z.L., 1992. Characterization of the damping properties of high-damping alloys, in: *M 3 D: Mechanics and Mechanisms of Material Damping*. ASTM International.
- Robbins, D.H., Wood, J.L., 1969. Determination of mechanical properties of the bones of the skull. *Exp. Mech.* 9, 236–240.
- Roche, A.F., 1953. Increase in cranial thickness during growth. *Hum. Biol.* 25, 81.
- Ross, M.D., Lee, K.A., Castle, W.M., 1976. Skull thickness of Black and White races. *S. Afr. Med. J.* 50, 635—638.
- Rowson, S., Duma, S.M., 2013. Brain Injury Prediction: Assessing the Combined Probability of Concussion Using Linear and Rotational Head Acceleration. *Ann. Biomed. Eng.* 41, 873–882. doi:10.1007/s10439-012-0731-0
- Ruan, J., Prasad, P., 2001. The effects of skull thickness variations on human head dynamic impact responses. *Stapp Car Crash J.* 45, 395–414.

- Sabancıoğulları, V., Koşar, M.İ., Salk, I., Erdil, F.H., Oztoprak, I., Cimen, M., 2012. Diploe thickness and cranial dimensions in males and females in mid-Anatolian population: an MRI study. *Forensic Sci. Int.* 219, 289.e1–7. doi:10.1016/j.forsciint.2011.11.033
- Sabancıoğulları, V., Salk, I., Cimen, M., 2013. The relationship between total calvarial thickness and diploe in the elderly. *Int. J. Morphol* 31, 38–44.
- Sasaki, N., Nakayama, Y., Yoshikawa, M., Enyo, A., 1993. Stress relaxation function of bone and bone collagen. *J. Biomech.* 26, 1369–1376. doi:10.1016/0021-9290(93)90088-V
- Schaller, R., Barrault, S., Zysset, P., 2004. Mechanical spectroscopy of bovine compact bone. *Mater. Sci. Eng. A* 370, 569–574. doi:10.1016/j.msea.2003.08.107
- Schueler, F., Zimmer, G., Min, J.-X., Mattern, R., 1994. Assessment of mechanical properties of the human skull-cap through basic biomechanical tests and quantitative computed tomography (QCT), in: *Proceedings of the International Research Council on the Biomechanics of Injury Conference*. pp. 23–37.
- Shepherd, T.N., Zhang, J., Ovaert, T.C., Roeder, R.K., Niebur, G.L., 2011. Direct comparison of nanoindentation and macroscopic measurements of bone viscoelasticity. *J. Mech. Behav. Biomed. Mater.* 4, 2055–62. doi:10.1016/j.jmbbm.2011.07.004
- Shridharani, J.K., Wood, G.W., Panzer, M.B., Capehart, B.P., Nyein, M.K., Radovitzky, R.A., Bass, C.R., 2012. Porcine head response to blast.
- Singh, D., Cronin, D.S., Haladuick, T.N., 2014. Head and brain response to blast using sagittal and transverse finite element models. *Int. j. numer. method. biomed. eng.* 30, 470–489. doi:10.1002/cnm.2612

- Snyder, J.P., 1987. Map projections--A working manual. US Government Printing Office.
- Spitzer, V.M., Whitlock, D.G., 1998. The visible human dataset: The anatomical platform for human simulation. *Anat. Rec.* 253, 49–57. doi:10.1002/(SICI)1097-0185(199804)253:2<49::AID-AR8>3.0.CO;2-9
- Stålhammar, D., 1975a. EXPERIMENTAL BRAIN DAMAGE FROM FLUID PRESSURES DUE TO IMPACT ACCELERATION. 2. Pathophysiological Observations. *Acta Neurol. Scand.* 52, 27–37. doi:10.1111/j.1600-0404.1975.tb02825.x
- Stålhammar, D., 1975b. EXPERIMENTAL BRAIN DAMAGE FROM FLUID PRESSURES DUE TO IMPACT ACCELERATION. 1. Design of Experimental Procedure. *Acta Neurol. Scand.* 52, 7–26. doi:10.1111/j.1600-0404.1975.tb02824.x
- Stålhammar, D., Olsson, Y., 1975. EXPERIMENTAL BRAIN DAMAGE FROM FLUID PRESSURES DUE TO IMPACT ACCELERATION. 3. Morphological Observations. *Acta Neurol. Scand.* 52, 38–55. doi:10.1111/j.1600-0404.1975.tb02826.x
- Stalnaker, R.L., Alem, N.M., Benson, J.B., 1977a. Validation studies for head impact injury model.
- Stalnaker, R.L., Melvin, J.W., Nusholtz, G.S., Alem, N.M., Benson, J.B., 1977b. Head impact response.
- Strich, S., 1961. Shearing of nerve fibres as a cause of brain damage due to head injury: a pathological study of twenty cases. *Lancet* 278, 443–448.
- Subit, D., ARREGUI-DALMASES, C., SALAZAR, R., Crandall, J., 2013. Pediatric, Adult and Elderly Bone Material Properties, in: 2013 IRCOBI Conference Proceedings, Paper IRC-13-

87.

Subit, D., de Dios, E. del P., Valazquez-Ameijide, J., Arregui-Dalmases, C., Crandall, J., 2011.

Tensile material properties of human rib cortical bone under quasi-static and dynamic failure loading and influence of the bone microstructure on failure characteristics. arXiv Prepr. arXiv1108.0390.

Suh, C.-C., Yang, W.-J., McElhaney, J.H., 1972. Rarefaction of liquids in a spherical shell due to local radial loads with application to brain damage.

Sullivan, W.G., Smith, A.A., 1989. The Split Calvarial Graft Donor Site in the Elderly: A Study in Cadavers. *Plast. Reconstr. Surg.* 84.

Summers, C.R., Ivins, B., Schwab, K.A., 2009. Traumatic brain injury in the United States: an epidemiologic overview. *Mt. Sinai J. Med. A J. Transl. Pers. Med.* 76, 105–110.
doi:10.1002/msj.20100

Takeshita, Y., Sawada, T., Handa, T., Watanuki, Y., Kudo, T., 2012. Influence of air-cooling time on physical properties of thermoplastic polyester powder coatings. *Prog. Org. Coatings* 75, 584–589. doi:10.1016/j.porgcoat.2012.07.003

Takhounts, E.G., Craig, M.J., Moorhouse, K., McFadden, J., Hasija, V., 2013. Development of brain injury criteria (BrIC). *Stapp Car Crash J.* 57, 243.

Takhounts, E.G., Eppinger, R.H., Campbell, J.Q., Tannous, R.E., others, 2003. On the development of the SIMon finite element head model. *Stapp Car Crash J.* 47, 107.

Takhounts, E.G., Hasija, V., Ridella, S.A., Rowson, S., Duma, S.M., 2011. Kinematic rotational brain injury criterion (BRIC), in: *Proceedings of the 22nd Enhanced Safety of Vehicles*

Conference. Paper.

Takhounts, E.G., Ridella, S.A., Hasija, V., Tannous, R.E., Campbell, J.Q., Malone, D., Danelson, K., Stitzel, J., Rowson, S., Duma, S., 2008. Investigation of traumatic brain injuries using the next generation of simulated injury monitor (SIMon) finite element head model. *Stapp Car Crash J.* 52, 1.

Taylor, P.A., Ford, C.C., 2009. Simulation of Blast-Induced Early-Time Intracranial Wave Physics leading to Traumatic Brain Injury. *J. Biomech. Eng.* 131, 61007.

Todd, T.W., 1924. Thickness of the male white cranium. *Anat. Rec.* 27, 245–256.
doi:10.1002/ar.1090270504

Toms, S.R., Dakin, G.J., Lemons, J.E., Eberhardt, A.W., 2002. Quasi-linear viscoelastic behavior of the human periodontal ligament. *J. Biomech.* 35, 1411–1415. doi:10.1016/S0021-9290(02)00166-5

Torimitsu, S., Nishida, Y., Takano, T., Koizumi, Y., Hayakawa, M., Yajima, D., Inokuchi, G., Makino, Y., Motomura, A., Chiba, F., Iwase, H., 2014. Effects of the freezing and thawing process on biomechanical properties of the human skull. *Leg. Med. (Tokyo)*. 16, 102–5.
doi:10.1016/j.legalmed.2013.11.005

Torres-Lagares, D., Tulasne, J.-F., Pouget, C., Llorens, A., Saffar, J.-L., Lesclous, P., 2010. Structure and remodelling of the human parietal bone: an age and gender histomorphometric study. *J. Craniomaxillofac. Surg.* 38, 325–30. doi:10.1016/j.jcms.2009.07.012

Tretbar, S.H., Plinkert, P.K., Federspil, P.A., 2009. Accuracy of Ultrasound Measurements for Skull Bone Thickness Using Coded Signals. *IEEE Trans. Biomed. Eng.* 56, 733–740.
doi:10.1109/TBME.2008.2011058

- Turner, C.H., 1992. On Wolff's law of trabecular architecture. *J. Biomech.* 25, 1–9.
doi:10.1016/0021-9290(92)90240-2
- Turner, C.H., Chandran, A., Pidaparti, R.M.V., 1995. The anisotropy of osteonal bone and its ultrastructural implications. *Bone* 17, 85–89. doi:10.1016/8756-3282(95)00148-7
- Unterberg, A.W., Stover, J., Kress, B., Kiening, K.L., 2004. Edema and brain trauma. *Neuroscience* 129, 1021–9. doi:10.1016/j.neuroscience.2004.06.046
- Versace, J., 1971. A review of the severity index.
- White, T.D., Asfaw, B., DeGusta, D., Gilbert, H., Richards, G.D., Suwa, G., Clark Howell, F., 2003. Pleistocene *Homo sapiens* from Middle Awash, Ethiopia. *Nature* 423, 742–747.
- Wolff, J., 1893. Das gesetz der transformation der knochen. *DMW-Deutsche Medizinische Wochenschrift* 19, 1222–1224.
- Woo, S.L.-Y., Simon, B.R., Kuei, S.C., Akeson, W.H., 1980. Quasi-Linear Viscoelastic Properties of Normal Articular Cartilage. *J. Biomech. Eng.* 102, 85–90.
- Wood, J.L., 1971. Dynamic response of human cranial bone. *J. Biomech.* 4, 1–12.
doi:10.1016/0021-9290(71)90010-8
- Yamashita, J., Furman, B.R., Rawls, H.R., Wang, X., Agrawal, C.M., 2001. The use of dynamic mechanical analysis to assess the viscoelastic properties of human cortical bone. *J. Biomed. Mater. Res.* 58, 47–53. doi:10.1002/1097-4636(2001)58:1<47::AID-JBM70>3.0.CO;2-U
- Zasler, N.D., Katz, D.I., Zafonte, R.D., Arciniegas, D.B., 2012. “ Brain Injury Medicine, ”: Principles and Practice. Demos Medical Publishing.
- Zysset, P.K., Edward Guo, X., Edward Hoffler, C., Moore, K.E., Goldstein, S.A., 1999. Elastic

modulus and hardness of cortical and trabecular bone lamellae measured by nanoindentation in the human femur. *J. Biomech.* 32, 1005–1012. doi:10.1016/S0021-9290(99)00111-6

14 Appendix

14.1 Tables

Table A.1 Summary of trabecular diploe or skull composite mechanical studies.				
Study	Number and type		Strain Rate and	
	of specimens	Size	mode	Findings
Evans and Lissner, 1957	23 cuboidal wet embalmed composite parietal bone	n/a	Quasi-static; compressive; normal to skull	Diploe compressive strength [11.7 25.1 39.8] MPa
	70 cuboidal fresh composite calvarium	5 x 5 mm	Quasi-static; compressive; normal to skull	Composite elastic modulus [0.070 1.390 3.654] GPa Diploe compressive strength [5.3 36.5 108.2] MPa
Robbins and Wood, 1969	370 cylindrical embalmed composite calvarium	9.5 mm dia.	Quasi-static; shear; normal to skull	Diploe shear strength 13.1 MPa
Barber et al., 1969	243 cylindrical embalmed composite calvarium	8 mm dia	Quasi-static; compression; normal to skull	Composite elastic modulus Frontal <0.112 0.545 0.978> GPa Parietal <0.068 0.718 1.368> GPa Occipital <0.215 0.738 1.260> GPa Diploe elastic strength Frontal <15.8 50.7 85.6> MPa Parietal <37.3 75.6 113.9> MPa Occipital <31.8 80.3 128.8> MPa

Table A.1 Summary of trabecular diploe or skull composite mechanical studies continued...

Study	Number and type		Strain Rate and mode	Findings
	of specimens	Size		
Melvin et al., 1970	unknown number of cuboidal fresh diploe from calvarium	3.81 x 3.81 mm	unknown rate; compressive; normal to skull	Diploe compressive modulus 1.38 GPa Diploe compressive strength [9.0 41.4 219.9] MPa
	unknown number of cylindrical embalmed composite calvarium	9.5 mm dia.	unknown rate; shear; normal to skull	Diploe shear strength 20.7 MPa
McElhaney et al., 1970	237 cuboidal embalmed composite calvarium	6.35 x 5.08 mm	Quasi-static; compressive; normal to skull	Composite elastic modulus <0.97 2.41 3.86> GPa Diploe compressive strength <38.6 73.8 108.9> MPa Poisson's ratio <0.11 0.19 0.27>
	210 cuboidal embalmed composite calvarium	6.35 x 5.08 mm	Quasi-static; compressive; tangential to skull	Composite elastic modulus <2.55 5.59 8.62> GPa Composite compressive strength <60.7 96.5 132.4> MPa Poisson's ratio <0.11 0.22 0.33>

Table A.1 Summary of trabecular diploe or skull composite mechanical studies continued...

Study	Number and type		Strain Rate and	
	of specimens	Size	mode	Findings
McElhaney et al., 1970	348 cylindrical embalmed composite calvarium	6.86 mm dia.	Quasi-static; shear; normal to skull	Diploe shear strength <17.9 21.3 24.8> MPa Diploe anisotropy ratio <1.3 2.5 3.7>
	90 cylindrical embalmed composite calvarium	6.86 mm dia.	Quasi-static; torsion; normal to skull	Diploe shear modulus <0.41 1.38 2.34> GPa Diploe shear strength <16.6 22.1 27.6> MPa
Hubbard, 1971	8 cuboidal embalmed parietal bone specimens	50.8 x 10.9 mm	Quasi-static; bending; tangential to skull	Effective diploe shear modulus [112 341 550] MPa
Schueler et al., 1994	81 cuboidal fresh parietal bone specimens	10 x 10 mm	Quasi-static; compression; normal to skull	Composite elastic modulus <0.169 0.314 0.459> GPa [0.056 0.753] GPa
Halgrin et al., 2012	17 cylindrical fresh composite parietal bone specimens	9 mm dia.	Dynamic; compression; normal to skull	Composite elastic modulus 0.576 GPa

Table A.2 Summary of skull cortical layer mechanical studies.

Study	Number and type		Strain Rate and		Findings
	of specimens	Size	mode		
Evans and Lissner, 1957	15 cuboidal wet embalmed composite parietal bone	n/a	Quasi-static; tensile; tangential to skull		Cortical tensile strength [41.6 070.5 108.9] MPa
	100 cuboidal wet embalmed composite parietal bone	n/a	Quasi-static; compressive; tangential to skull		Cortical compressive strength [31.0 152.2 329.6] MPa
Robbins and Wood, 1969	50 fresh cortical coupons from calvarium	1.29 mm ² cross- section	Quasi-static; tensile; tangential to skull		Cortical elastic modulus 14.55 GPa Cortical tensile strength 65.5 MPa
Melvin et al., 1970	unknown number of fresh cortical coupons from calvarium	1.27 x 1.27 mm cross- section; 2.54 mm gage	0.01 to 100 s ⁻¹ ; tensile; tangential to skull		Cortical elastic modulus from 12.41 to 19.99 GPa with rate
Wood, 1971	120 fresh cortical coupons from calvarium	1.52 x 1.07 mm cross- section; 2.54 mm gage	0.005 to 150 s ⁻¹ ; tensile; tangential to skull		Cortical elastic modulus from 10.34 to 22.06 GPa with rate; Linear regression with rate 16.00 + 1.93 log $\dot{\epsilon}$ GPa

Table A.2 Summary of skull cortical layer mechanical studies continued...

Study	Number and type		Strain Rate and		Findings
	of specimens	Size	mode		
Hubbard, 1971	8 cuboidal embalmed parietal bone specimens	50.8 x 10.9 mm	Quasi-static; bending; tangential to skull		Effective cortical modulus
					[7.79 9.72 15.31] GPa
					Effective cortical shear modulus
					[149 459 745] MPa
Peterson and Dechow, 2002	140 fresh cortical cylindrical parietal bone specimens	5 mm dia.	2.25 MHz normal and transverse ultrasound; tangential to skull		Cortical elastic modulus
					<17.2 21.0 24.8> GPa
					Cortical shear modulus
					<0.9 6.8 12.7> GPa
Delille et al., 2007	380 cuboidal embalmed composite calvarium	60 x 14 mm	Quasi-static; bending; tangential to skull		Effective cortical modulus
					[2.03 5.21 13.98] GPa

Table A.2 Summary of skull cortical layer mechanical studies continued...				
Study	Number and type		Strain Rate and	
	of specimens	Size	mode	Findings
				Effective cortical modulus
	18 cuboidal fresh	60 x 10	20 s ⁻¹ ; bending;	<2.07 7.46 12.85> GPa
	composite calvarium	mm	tangential to skull	Effective cortical strength
				<61.6 85.1 108.7> MPa
				Effective cortical modulus
Motherway et al., 2009	20 cuboidal fresh	60 x 10	30 s ⁻¹ ; bending;	<1.39 10.77 20.15> GPa
	composite calvarium	mm	tangential to skull	Effective cortical strength
				<59.4 86.4 113.5> MPa
				Effective cortical modulus
	22 cuboidal fresh	60 x 10	100 s ⁻¹ ; bending;	<5.25 15.54 25.83> GPa
	composite calvarium	mm	tangential to skull	Effective cortical strength
				<81.0 127.8 174.7> MPa

Table A.3 Summary of current head FE models.

Study	Geometry	Layer materials /		
		thicknesses	Skull material	mesh size
Gilchrist et al., 2001	2D mesh from sagittal slice	Single material	Elastic; fit to (Nahum et al., 1977)	1 mm
Horgan and Gilchrist, 2003	3D mesh from spline contour interpolation from (Ackerman, 1998)	Diploe uniform 50% of total thickness	Elastic	5.2 mm
Takhounts et al., 2008	3D mesh from CT study of single male with head size close to 50 th percentile	Single material	Rigid	NA
Moore et al., 2009	3D mesh from (Collins et al., 1998)	Single material	Elastic +eos	2.9 mm
Moss et al., 2009	3D mesh of a hollow elastic ellipsoid	Single material	Viscoelastic (Wood, 1971)	NA
Taylor and Ford, 2009	3D mesh from (Collins et al., 1998)	Single material	Elastic (CARTER and SPENGLER, 1978)	1 mm
Nyein et al., 2010	3D mesh from (Collins et al., 1998)	Single material	Elastic +eos	2.9 mm

Table A.3 Summary of current head FE models continued...

Study	Geometry	Layer materials /		
		thicknesses	Skull material	mesh size
	3D mesh from spline			
Chafi et al., 2009	contour interpolation from (Ackerman, 1998)	Single material	Elastic	5.2 mm
	2D mesh; axial; from (Ackerman, 1998)	Diploe uniform 40% of total thickness	bulk-Elastic (McElhaney et al., 1970); shear- Viscoelastic (McElhaney, 1966)	1.5 mm
Panzer et al., 2012	scaled to 50th percentile male (Gordon et al., 1989)	(Lynnerup et al., 2005)		
	3D mesh from (Gayzik et al., 2011)	Diploe 40% of total thickness (Lynnerup et al., 2005)	Elastic (McElhaney et al., 1970)	1.5 mm
Asgharpour et al., 2014	3D mesh from CMM study of adult male skull	Diploe 40% of total thickness	Elastic (McElhaney et al., 1970)	10 mm
	2D mesh; axial and sagittal; from (Ackerman, 1998)	Single material	Elastic	1 mm

Table A.4 Summary of head / brain injury studies.

Study	Metric	Assumed Cause	Basis	link to tissue level
Versace, 1971	Linear acceleration time-history	Pressure	Sensory deficit from impact and air blast tests on dogs.	Cadaver head drop tests with pressure monitoring.
Bain and Meaney, 2000	Strain	Strain	Morphological injury and electrophysiological impairment after dynamic stretch tests on optic nerve of guinea pig.	NA
Newman et al., 2000	Power	NA	Football player injury reconstruction with HIII ATD and empirical injury model with rate of change in kinetic energy as predictor	NA

Shaded studies do investigate tissue level mechanics and are purely empirical

Table A.4 Summary of head / brain injury studies continued...

Study	Metric	Cause	Basis	link to tissue level
Takhounts et al., 2003, 2008, 2013	CSDM, DDM, RMDM	Strain - DAI; Cavitation - Contusion; Relative motion - subdural hematoma	Metrics for three brain injury mechanisms evaluated for animal experiments. Good correlation with HIC15 in frontal and side impact cases observed.	FE model
Morrison III et al., 2003; Elkin and Morrison III, 2007	Strain, strain rate and time post injury	Strain	Cell death from fluorescent dye photography after equibiaxial stretch tests on rat cortex and hippocampus slice cultures.	NA
Rafaels et al., 2012	External pressure and duration	NA	Pathological parameters, sensory deficit and histology after blast exposure of ferrets	NA

Shaded studies do investigate tissue level mechanics and are purely empirical

Table A.4 Summary of head / brain injury studies continued...

Study	Metric	Assumed		link to tissue level
		Cause	Basis	
Kimpara and Iwamoto, 2011	Rotational acceleration time-history and CSDM	Strain	Concussive and non-concussive football head impacts with 6DOF acceleration data	FE model of the human head
Rowson and Duma, 2013	Peak linear and angular acceleration	NA	Concussive and non-concussive football head impacts with 6DOF acceleration data	
Antona-Makoshi et al., 2013	Maximum principal strain	Strain	Sensory deficit and clinical measurements after impact tests on macaques	FE models of macaque head

Shaded studies do investigate tissue level mechanics and are purely empirical

Table A.5 Format of sample unique identification numbers

aabb	Core ID
aabbcc	Coupon ID
aa	Subject number
bb	Location number *
cc	Repetition number

* Location IDs are roughly arranged anterior to posterior
of the calvarium

14.2 Radiographic imaging

14.2.1 Distribution of measurements over the calvarium of each subject

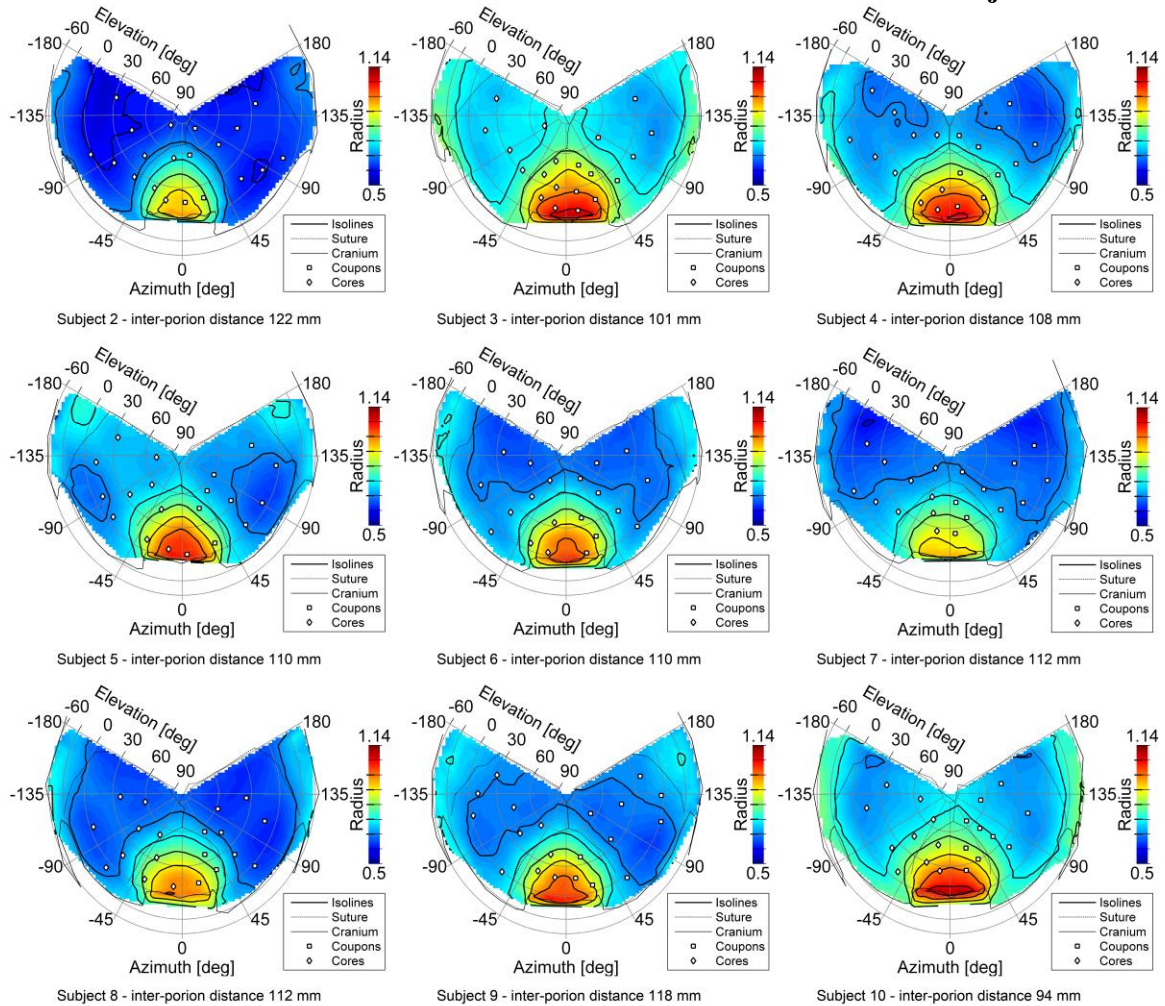


Figure A.1 Individual Cranial vault outer shapes

Notes: The harvest locations (Cores: diamonds, coupons: squares) marked on a 2 dimension Alber's projection of the skull showing extent of the sandwich layer in each of the nine cranial vaults (solid lines), the coronal, sagittal and lambdoid sutures (dotted lines), contour: Normalized distance to skull outer surface from origin (radius). These distances have been normalized to the inter-porion distance (listed beneath each plot).

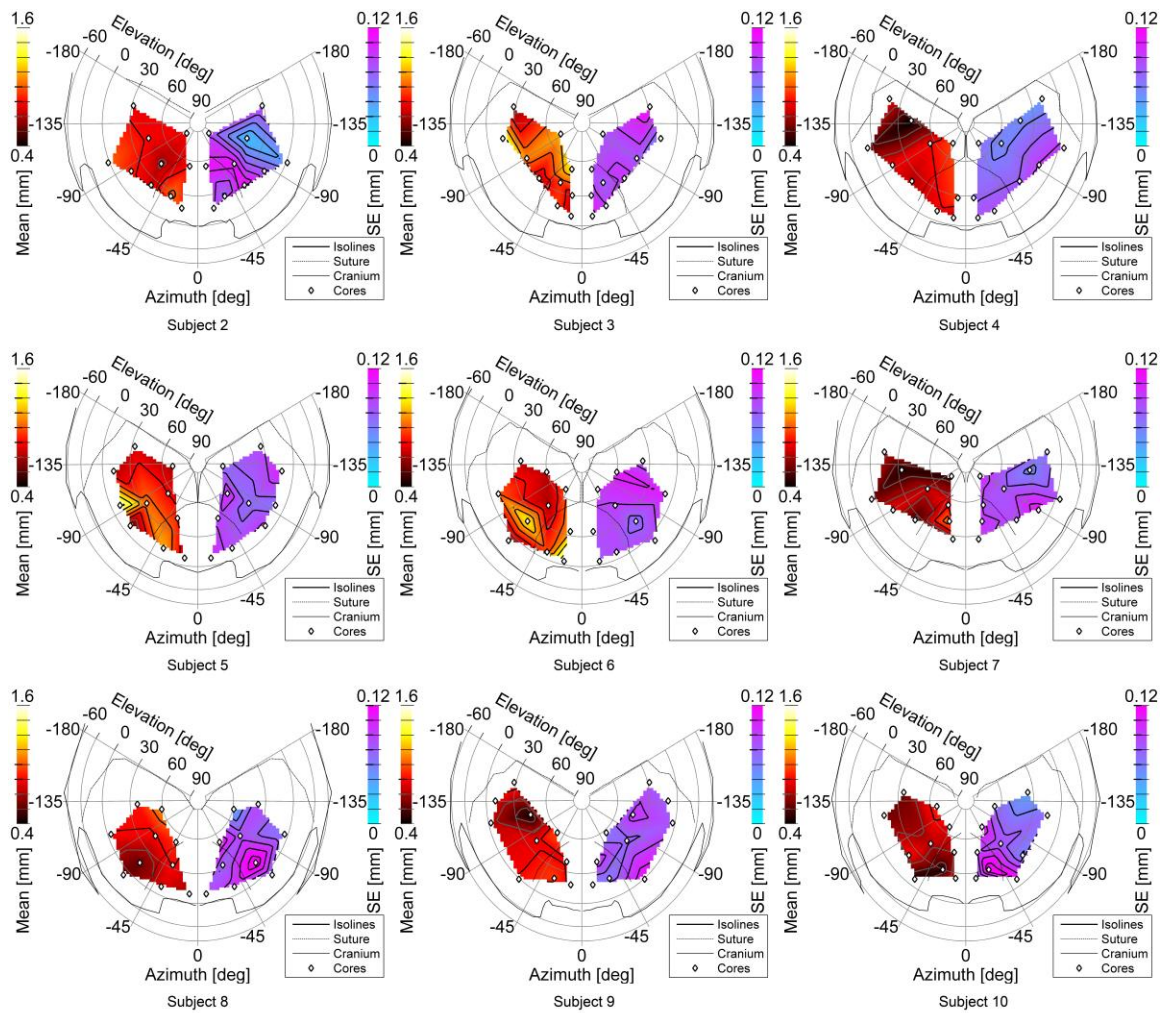


Figure A.2 Individual outer cortical layer thickness; left: average; right: standard error.

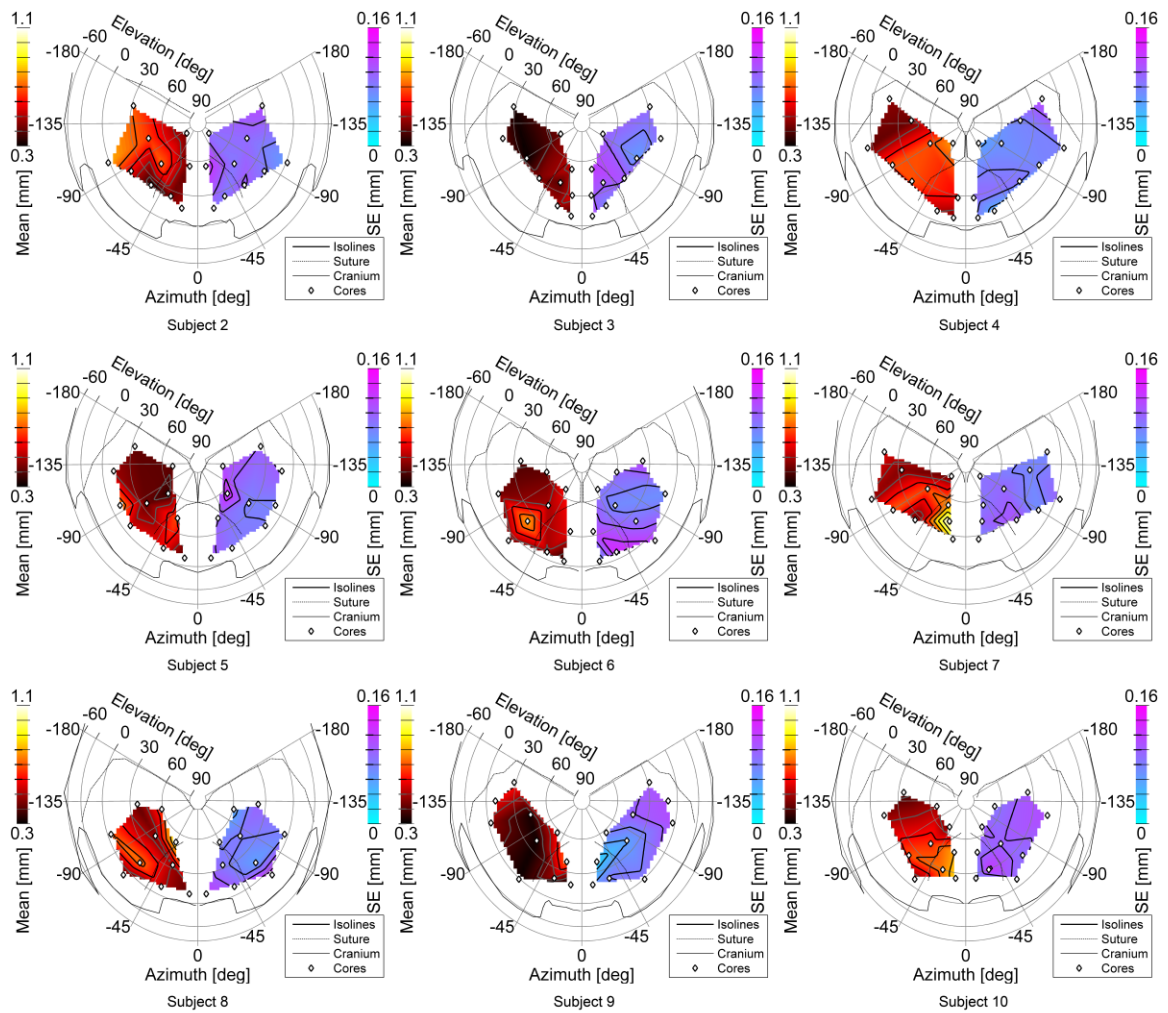


Figure A.3 Individual inner cortical layer thickness; left: average; right: standard error.

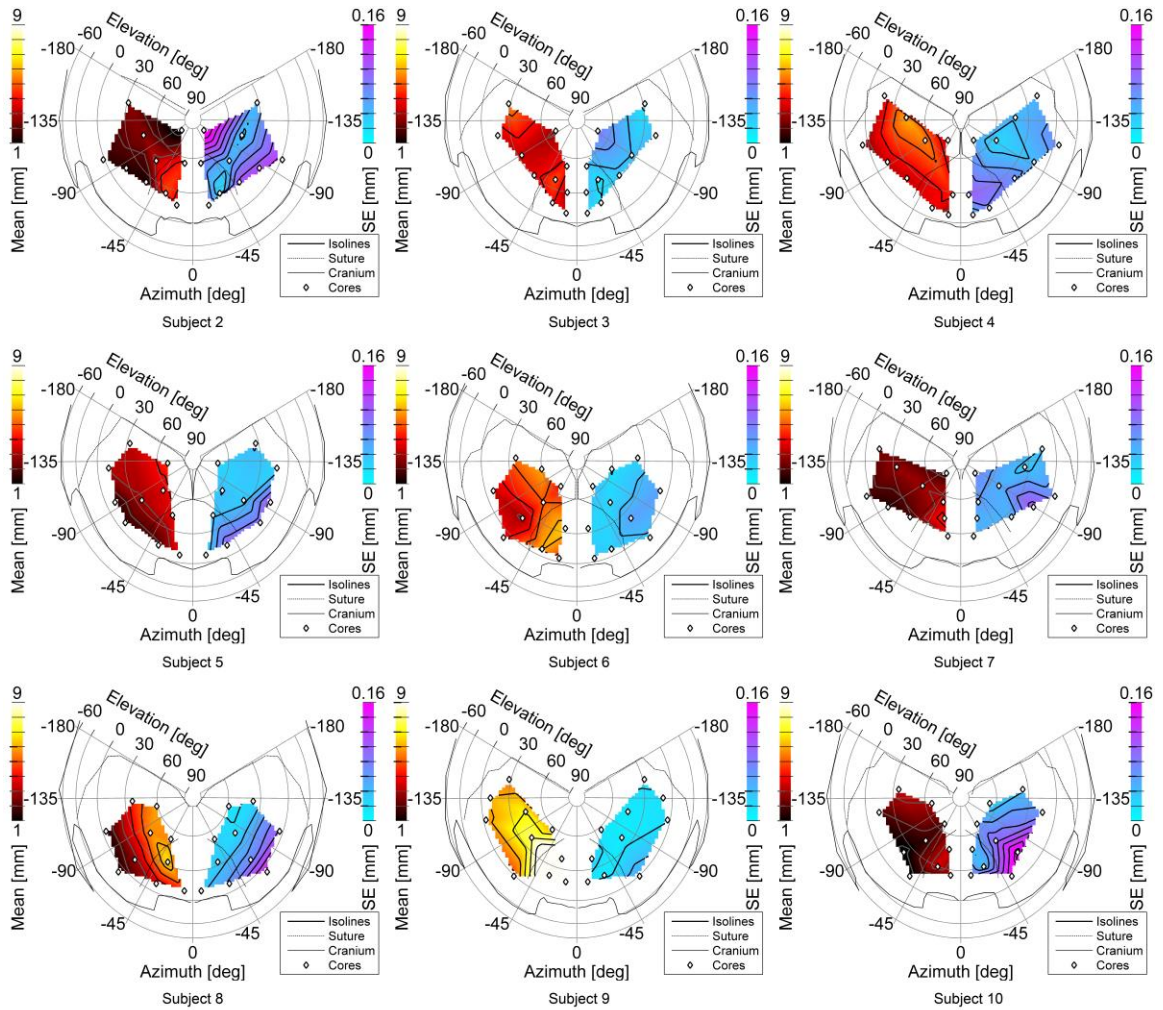


Figure A.4 Individual cancellous layer thickness; left: average; right: standard error.

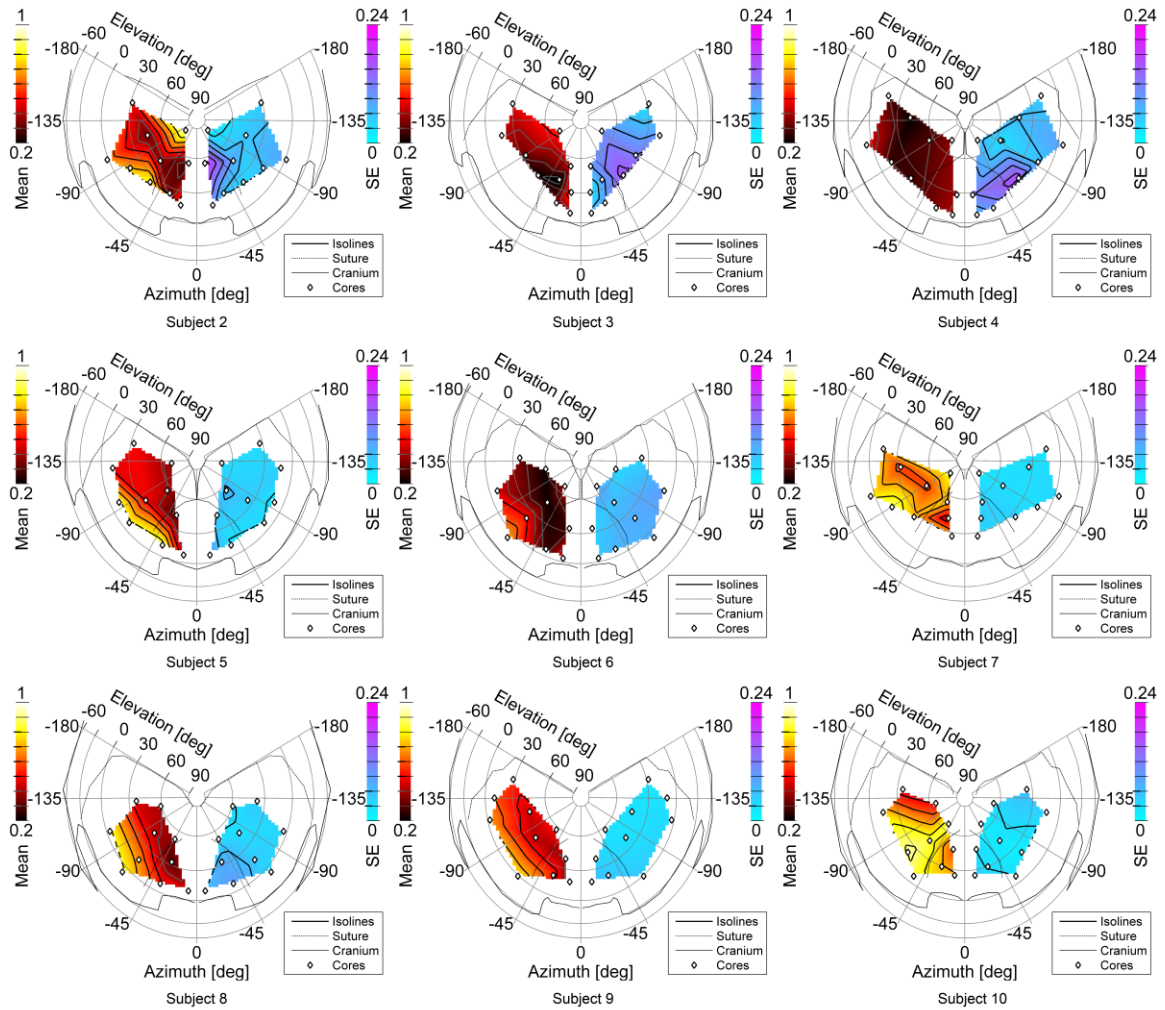


Figure A.5 Individual cancellous layer bone volume fraction; left: average; right: standard error.

14.2.2 Tabulated results

Table A.6 List of core samples and their harvest locations.

ID	Azimuth	Elevation	Radius	Frontal	Superior
	[deg]	[deg]	[mm]		
0102				Yes	No
0103				Yes	Yes
0104				No	Yes
0105				No	Yes
0106				No	No
0108				Yes	No
0201	-17.25	16.71	110.08	Yes	No
0202	-32.61	24.68	97.81	Yes	No
0203	-17.10	55.26	88.99	Yes	Yes
0204	-73.23	79.69	74.58	No	Yes
0205	-66.11	44.50	78.18	No	Yes
0206	-58.70	23.55	78.25	No	No
0208	-101.78	-1.50	70.65	No	No
0209	-111.16	45.88	69.75	No	Yes
0210	-156.51	31.55	66.58	No	Yes

Table A.6 List of core samples and their harvest locations continued...

ID	Azimuth	Elevation	Radius	Frontal	Superior
	[deg]	[deg]	[mm]		
0301	-10.57	9.73	104.81	Yes	No
0302	-26.44	16.79	98.61	Yes	No
0303	-12.21	29.89	95.60	Yes	No
0304	-19.57	52.39	84.06	Yes	Yes
0305	-31.74	38.24	86.34	Yes	Yes
0306	-59.58	31.03	75.49	No	Yes
0307	-89.14	33.67	72.29	No	Yes
0308	-119.92	17.20	70.88	No	No
0310	-154.39	28.19	71.69	No	No
0402	-29.10	10.36	101.76	Yes	No
0403	-9.69	27.85	101.54	Yes	No
0404	-51.41	71.82	74.16	No	Yes
0405	-93.24	55.83	71.87	No	Yes
0406	-67.52	21.40	77.69	No	No
0407	-93.32	14.23	71.90	No	No
0408	-115.46	-6.67	73.51	No	No
0409	-139.01	42.85	71.33	No	Yes
0410	-160.34	18.17	69.27	No	No

Table A.6 List of core samples and their harvest locations continued...

ID	Azimuth [deg]	Elevation [deg]	Radius [mm]	Frontal	Superior
0501	-12.94	8.23	112.93	Yes	No
0502	-35.58	11.48	96.51	Yes	No
0503	-32.81	42.73	88.90	Yes	Yes
0504	-70.47	55.68	76.93	No	Yes
0505	-81.68	34.86	78.07	No	Yes
0506	-74.58	8.03	73.58	No	No
0507	-95.69	10.16	70.34	No	No
0508	-128.56	12.82	74.91	No	No
0509	-127.38	69.66	75.99	No	Yes
0510	-157.14	32.99	76.25	No	Yes
0602	-34.55	7.62	93.36	Yes	No
0603	-15.52	33.83	96.48	Yes	Yes
0604	-50.84	66.49	73.15	No	Yes
0605	-61.42	45.93	74.20	No	Yes
0606	-68.48	21.61	76.12	No	No
0608	-107.71	8.80	72.45	No	No
0609	-116.65	59.97	69.13	No	Yes

Table A.6 List of core samples and their harvest locations continued...

ID	Azimuth	Elevation	Radius	Frontal	Superior
	[deg]	[deg]	[mm]		
0701	-15.70	26.53	98.78	Yes	No
0702	-25.59	41.48	89.90	Yes	Yes
0703	-36.84	54.14	80.50	Yes	Yes
0704	-76.33	75.98	72.60	No	Yes
0705	-88.20	51.86	73.00	No	Yes
0706	-66.48	25.07	80.15	No	No
0707	-89.39	12.72	74.01	No	No
0708	-106.48	-5.24	71.85	No	No
0709	-127.62	33.43	70.63	No	Yes
0710	-147.09	15.36	67.66	No	No
0801	-8.44	9.98	107.62	Yes	No
0802	-37.17	9.04	92.19	Yes	No
0803	-34.16	33.00	92.97	Yes	Yes
0804	-44.41	52.27	79.60	No	Yes
0805	-78.70	43.63	73.95	No	Yes
0806	-67.99	15.67	74.35	No	No
0808	-105.76	3.97	69.53	No	No
0809	-116.47	59.03	70.29	No	Yes
0810	-130.89	37.14	71.44	No	Yes

ID	Azimuth	Elevation	Radius	Frontal	Superior
	[deg]	[deg]	[mm]		
0904	-59.23	57.47	79.70	No	Yes
0905	-76.01	39.05	77.69	No	Yes
0906	-61.43	-0.93	81.79	No	No
0907	-116.17	2.85	76.60	No	No
0908	-135.28	10.69	78.12	No	No
0909	-113.91	44.43	76.51	No	Yes
0910	-156.64	28.19	77.66	No	No
1001	-12.07	25.00	92.81	Yes	No
1002	-29.76	29.71	84.00	Yes	No
1004	-20.37	47.55	79.26	Yes	Yes
1005	-62.11	44.11	70.51	No	Yes
1008	-121.22	14.60	62.39	No	No
1009	-119.66	65.77	66.33	No	Yes
1010	-146.19	35.30	63.61	No	Yes

Table A.7 List of core samples and their microstructural parameters.

ID	Potted	Un-potted	Layer thicknesses [mm]			
	thickness [mm]		mass [g]	Outer	Diploe	Inner
0102	7.64	1.77	0.50	2.00	0.19	0.681
0103	9.84	3.03	0.87	4.94	0.45	0.236
0104	8.75	2.69	0.84	5.18	0.41	0.170
0105	6.96	2.07	0.52	2.45	0.35	0.751
0106	8.07	2.27	0.64	3.79	0.25	0.604
0108	7.09	2.32	0.42	4.31	0.23	0.209
0201	7.18	2.64	0.89	3.96	0.50	0.569
0202	8.00	2.84	1.09	4.80	0.39	0.308
0203	7.77	2.87	0.95	4.65	0.41	0.188
0204	5.43	1.44	0.79	0.34	0.44	0.962
0205	6.30	2.15	0.64	3.42	0.67	0.308
0206	5.30	1.44	0.80	1.39	0.38	0.847
0208	5.62	1.80	0.99	1.35	0.75	0.714
0209	5.52	1.85	0.83	2.49	0.67	0.293
0210	5.53	2.03	0.83	2.45	0.75	0.498

Table A.7 List of core samples and their microstructural parameters continued...

ID	Potted	Un-potted mass [g]	Layer thicknesses [mm]			
	thickness [mm]		Outer	Diploe	Inner	Diploe BVF
0301	7.56	2.42	0.69	3.59	0.32	0.375
0302	6.18	2.56	0.99	4.15	0.48	0.344
0303	5.85	2.24	0.86	3.02	0.53	0.583
0304	7.84	3.02	1.27	4.14	0.56	0.365
0305	7.91	2.88	0.97	4.95	0.37	0.146
0306	6.68	2.37	0.76	3.84	0.39	0.204
0307	7.14	2.34	1.07	3.39	0.30	0.327
0308	7.24	2.59	1.45	3.33	0.40	0.453
0310	6.26	3.04	0.61	5.59	0.32	0.477
0402	7.86	3.14	0.83	3.94	0.49	0.300
0403	9.06	3.30	1.06	4.81	0.63	0.320
0404	6.92	2.33	1.04	3.21	0.76	0.324
0405	8.50	2.96	0.83	5.47	0.71	0.296
0406	6.51	2.28	0.72	3.54	0.73	0.194
0407	6.60	2.44	0.95	3.44	0.72	0.251
0408	5.95	2.02	0.56	2.73	0.39	0.425
0409	8.67	2.96	0.39	6.40	0.44	0.200
0410	6.80	2.63	0.88	3.76	0.45	0.293

Table A.7 List of core samples and their microstructural parameters continued...

ID	Potted	Un-potted	Layer thicknesses [mm]			
	thickness [mm]		mass [g]	Outer	Diploe	Inner
0501	6.67	2.55	0.69	3.97	0.35	0.402
0502	5.17	2.03	1.15	1.99	0.58	0.864
0503	6.58	2.65	0.98	3.69	0.64	0.271
0504	6.44	2.30	0.81	3.55	0.30	0.432
0505	5.46	2.33	1.09	2.93	0.39	0.500
0506	4.25	1.66	0.47	1.46	0.55	0.829
0507	4.83	2.11	1.74	1.21	0.79	0.837
0508	6.00	2.28	0.69	3.16	0.47	0.465
0509	7.48	2.69	0.66	4.30	0.41	0.367
0510	5.86	2.26	0.86	3.32	0.39	0.503
0602	9.28	3.47	0.90	6.16	0.46	0.227
0603	9.25	3.64	1.28	6.46	0.52	0.288
0604	7.27	2.78	1.07	4.25	0.62	0.370
0605	7.47	2.78	0.63	4.98	0.51	0.212
0606	7.09	2.70	1.47	2.81	0.88	0.578
0608	6.30	2.43	1.04	3.46	0.44	0.501
0609	8.33	3.08	0.83	5.88	0.44	0.211

Table A.7 List of core samples and their microstructural parameters continued...

ID	Potted	Un-potted	Layer thicknesses [mm]			
	thickness [mm]		mass [g]	Outer	Diploe	Inner
0701	7.75	2.80	0.63	3.50	0.95	0.716
0702	8.01	3.53	1.16	4.51	1.18	0.450
0703	6.56	2.63	0.78	3.38	0.76	0.776
0704	6.05	1.75	0.44	1.76	0.41	0.804
0705	6.64	2.17	0.76	2.84	0.68	0.577
0706	4.98	1.75	0.51	1.95	0.40	0.747
0707	5.08	1.73	0.80	1.20	0.74	0.939
0708	5.75	1.67	0.60	1.83	0.43	0.809
0709	5.42	2.00	0.46	2.79	0.45	0.574
0710	5.47	2.06	0.73	2.26	0.58	0.706
0801	7.78	2.90	0.73	4.71	0.45	0.443
0802	7.84	2.46	0.75	3.68	0.55	0.464
0803	9.62	3.47	0.88	6.98	0.53	0.280
0804	8.84	3.37	0.93	5.41	0.96	0.351
0805	9.14	3.24	0.83	5.68	0.50	0.419
0806	5.71	2.17	0.54	1.51	0.32	0.829
0808	4.67	1.58	0.84	1.16	0.76	0.879

Table A.7 List of core samples and their microstructural parameters continued...

ID	Potted	Un-potted mass [g]	Layer thicknesses [mm]				Diploe BVF
	thickness [mm]		Outer	Diploe	Inner		
0809	9.86	3.73	1.15	5.85	0.70	0.405	
0810	7.06	2.72	0.89	4.28	0.40	0.446	
0904	10.46	3.71	1.09	6.11	0.61	0.492	
0905	7.90	2.89	0.80	7.93	0.29	0.405	
0906	9.11	3.18	0.79	4.88	0.31	0.848	
0907	9.16	3.61	0.78	5.82	0.46	0.686	
0908	9.14	3.75	0.79	6.09	0.55	0.604	
0909	9.45	3.51	0.45	7.08	0.34	0.448	
0910	8.32	3.37	0.96	5.28	0.58	0.529	
1001	6.01	2.31	0.83	2.45	0.90	0.767	
1002	6.57	2.56	0.40	3.65	0.74	0.714	
1004	10.61	3.95	0.68	3.32	0.87	0.589	
1005	4.60	1.69	0.77	1.68	0.72	0.844	
1008	4.69	1.61	0.58	2.10	0.45	0.752	
1009	6.18	2.29	1.02	2.98	0.56	0.501	
1010	6.93	2.31	0.60	3.46	0.36	0.432	

14.2.3 Statistical test results

Table A.8 Results of normality tests (p-values from Shapiro-Wilk test) of layer thicknesses and diploe layer

BVF measurements for each subject.

Sub	Absolute thicknesses			Diploe BVF	Ratio to total thickness		
	Outer	Diploe	Inner		Outer	Diploe	Inner
1	* 0.000	* 0.049	* 0.000	* 0.000	* 0.000	* 0.000	* 0.000
2	0.109	* 0.000	* 0.000	* 0.000	* 0.000	* 0.000	* 0.000
3	* 0.000	* 0.037	* 0.000	* 0.005	* 0.000	* 0.000	* 0.000
4	* 0.000	* 0.001	* 0.002	* 0.000	* 0.000	* 0.000	* 0.000
5	* 0.000	* 0.000	* 0.000	* 0.000	* 0.000	* 0.000	* 0.000
6	* 0.000	* 0.004	* 0.000	* 0.000	* 0.000	* 0.000	* 0.000
7	* 0.000	* 0.000	* 0.000	* 0.000	* 0.000	* 0.000	* 0.001
8	* 0.011	* 0.000	* 0.000	* 0.000	* 0.000	* 0.000	* 0.000
9	* 0.001	* 0.000	* 0.000	* 0.000	* 0.000	* 0.000	* 0.000
10	* 0.018	* 0.000	* 0.000	* 0.000	* 0.000	* 0.000	* 0.000

Significant values ($\alpha=0.05$) are shown in bold and marked with an asterisk.

Table A.9 Significance (p-values from non-parametric Wilcoxon rank sum test) of difference in layer thickness and diploe layer bone volume fraction measurements between frontal and parietal bones.

Sub.	Cortical layer thickness				Diploe layer	
	Parietal vs. frontal		Inner vs. Outer		Parietal vs. frontal	
	Outer	Inner	Parietal	Frontal	Thickness	Volume fraction
1	* 0.036	0.401	* 0.000	* 0.000	0.067	0.312
2	* 0.002	* 0.000	* 0.000	* 0.000	* 0.000	* 0.000
3	0.075	* 0.006	* 0.000	* 0.000	* 0.024	0.455
4	* 0.027	* 0.005	* 0.000	* 0.000	* 0.014	* 0.000
5	0.124	0.086	* 0.000	* 0.000	* 0.010	* 0.008
6	* 0.000	0.063	* 0.000	* 0.000	* 0.000	0.103
7	* 0.000	* 0.000	* 0.002	0.221	* 0.000	* 0.000
8	0.447	* 0.000	* 0.000	* 0.000	* 0.000	* 0.000
9	0.066	0.304	* 0.000	* 0.000	* 0.000	* 0.000
10	0.427	* 0.000	* 0.000	* 0.003	* 0.000	* 0.000

Significant values ($\alpha=0.05$) are shown in bold and marked with an asterisk.

Table A.10 Difference in median values of layer thickness (mm) and diploe layer bone volume fraction between the frontal and parietal bones.

Sub.	Cortical layer thickness [mm]				Diploe layer	
	Parietal vs. frontal		Inner vs. Outer		Parietal vs. frontal	
	Outer	Inner	Parietal	Frontal	Thickness [mm]	Volume fraction
1	* -0.09	-0.03	* -0.33	* -0.40	-0.89	0.08
2	* -0.15	* 0.17	* -0.21	* -0.53	* -2.34	* 0.20
3	0.13	* -0.09	* -0.66	* -0.46	* -0.27	0.06
4	* -0.10	* 0.10	* -0.14	* -0.34	* 0.69	* -0.05
5	-0.19	-0.04	* -0.34	* -0.48	* -0.44	* 0.13
6	* -0.45	0.09	* -0.31	* -0.85	* -1.55	0.03
7	* -0.28	* -0.42	* -0.06	0.08	* -1.59	* 0.08
8	0.02	* 0.11	* -0.19	* -0.29	* -0.58	* 0.12
9	-0.07	-0.06	* -0.37	* -0.38	* -6.47	* 0.15
10	0.02	* -0.37	* -0.19	* 0.20	* -1.30	* 0.15

Significant values ($\alpha=0.05$) are marked with an asterisk and shown in bold.

Table A.11 Significance (p-values from non-parametric Wilcoxon rank sum test) of difference in layer thickness and diploe layer bone volume fraction measurements between the superior and inferior aspects of the calvarium.

Sub.	Cortical layer thickness				Diploe layer	
	Inferior vs. Superior		Inner vs. Outer		Superior vs. Inferior	
	Outer	Inner	Inferior	Superior	Thickness	Volume fraction
1	* 0.001	* 0.000	* 0.000	* 0.000	0.389	0.262
2	* 0.001	* 0.017	* 0.000	* 0.000	0.702	* 0.000
3	* 0.002	0.618	* 0.000	* 0.000	0.982	* 0.000
4	0.248	* 0.004	* 0.000	* 0.049	* 0.000	* 0.004
5	0.564	* 0.002	* 0.000	* 0.000	* 0.000	* 0.000
6	* 0.000	0.591	* 0.000	* 0.000	* 0.000	* 0.000
7	0.387	0.275	0.120	0.344	* 0.000	* 0.000
8	* 0.000	0.610	* 0.000	* 0.000	* 0.000	* 0.000
9	* 0.024	0.168	* 0.000	* 0.000	* 0.000	* 0.000
10	* 0.001	* 0.032	0.995	* 0.000	* 0.000	* 0.000

Significant values ($\alpha=0.05$) are marked with an asterisk and shown in bold.

Table A.12 Difference in median values of layer thickness (mm) and diploe layer bone volume fraction between the superior and inferior aspects of the calvarium.

Sub.	Cortical layer thickness [mm]				Diploe layer	
	Inferior vs. Superior		Inner vs. Outer		Superior vs. Inferior	
	Outer	Inner	Inferior	Superior	Thickness [mm]	Volume fraction
1	* -0.22	* -0.16	* -0.35	* -0.41	0.35	0.09
2	* 0.16	* -0.12	* -0.52	* -0.24	0.54	* 0.23
3	* -0.21	0.02	* -0.44	* -0.68	-0.14	* 0.18
4	0.10	* -0.10	* -0.27	* -0.07	* -2.00	* 0.02
5	-0.05	* 0.10	* -0.29	* -0.43	* -1.13	* 0.33
6	* 0.18	-0.05	* -0.62	* -0.38	* -1.38	* 0.22
7	0.00	0.00	-0.06	-0.06	* -0.88	* 0.17
8	* -0.25	0.01	* -0.12	* -0.37	* -3.16	* 0.29
9	* 0.10	-0.07	* -0.43	* -0.27	* -1.51	* 0.16
10	* -0.09	* 0.12	0.01	* -0.20	* -1.06	* 0.20

Significant values ($\alpha=0.05$) are marked with an asterisk and shown in bold.

Table A.13 Significance (p-values from non-parametric Wilcoxon rank sum test) of difference in ratios of layer thicknesses to total thickness between parietal and frontal bones and the superior and inferior aspects of the calvarium.

Sub.	Parietal vs. frontal			Inferior vs. superior		
	Outer	Diploe	Inner	Outer	Diploe	Inner
1	0.218	0.488	0.843	0.112	* 0.001	* 0.000
2	* 0.000	* 0.000	* 0.000	* 0.016	0.730	* 0.040
3	* 0.004	0.154	* 0.047	* 0.005	0.082	0.721
4	* 0.003	0.112	0.379	* 0.000	* 0.000	* 0.007
5	0.901	0.828	0.916	* 0.000	* 0.000	* 0.000
6	0.198	0.514	* 0.000	* 0.000	* 0.000	* 0.045
7	* 0.001	0.135	0.429	* 0.001	* 0.000	* 0.002
8	* 0.000	* 0.000	* 0.000	* 0.000	* 0.000	* 0.000
9	* 0.000	* 0.000	* 0.000	* 0.001	* 0.004	0.624
10	* 0.000	* 0.000	0.913	* 0.015	* 0.000	* 0.000

Significant values ($\alpha=0.05$) are marked with an asterisk and shown in bold.

Table A.14 Difference in median values of ratios of layer thicknesses to total thickness between parietal and frontal bones and the superior and inferior aspects of the calvarium.

Sub.	Parietal vs. frontal			Inferior vs. superior		
	Outer	Diploe	Inner	Outer	Diploe	Inner
1	-0.022	0.009	-0.001	-0.019	* 0.044	* -0.025
2	* 0.061	* -0.165	* 0.101	* 0.020	0.009	* -0.034
3	* 0.032	-0.018	* -0.015	* -0.027	0.023	0.003
4	* -0.030	0.013	0.009	* 0.068	* -0.082	* 0.021
5	0.000	-0.012	-0.003	* 0.045	* -0.106	* 0.046
6	-0.013	-0.001	* 0.032	* 0.037	* -0.054	* 0.004
7	* 0.026	-0.011	-0.012	* 0.033	* -0.064	* 0.029
8	* 0.034	* -0.060	* 0.035	* 0.047	* -0.110	* 0.065
9	* 0.042	* -0.065	* 0.019	* 0.016	* -0.026	0.001
10	* 0.093	* -0.078	-0.019	* 0.045	* -0.124	* 0.101

Significant values ($\alpha=0.05$) are marked with an asterisk and shown in bold.

Table A.15 Significance (top right half, p-values from non-parametric Wilcoxon rank sum test) of difference and, difference in median values (bottom left half in mm) of outer cortical layer thicknesses between subjects.

Sub.	2	3	4	5	6	7	8	9	10	Sub.
	* 0.000	* 0.000	* 0.017	* 0.000	* 0.000	0.479	* 0.003	* 0.001	0.843	1
		0.065	* 0.000	0.637	0.097	* 0.000	* 0.004	* 0.004	* 0.000	2
9	-0.110 *		* 0.000	* 0.049	0.931	* 0.000	* 0.000	* 0.000	* 0.000	3
8	-0.115 *	-0.004		* 0.001	* 0.000	* 0.000	0.268	0.220	* 0.002	4
7	0.032	0.142 *	0.147 *		* 0.050	* 0.000	* 0.032	0.057	* 0.000	5
6	-0.261 *	-0.151 *	-0.147 *	-0.293 *		* 0.000	* 0.000	* 0.000	* 0.000	6
5	-0.176 *	-0.066	-0.061 *	-0.208 *	0.085 *		* 0.000	* 0.000	0.508	7
4	-0.077 *	0.034	0.038	-0.109 *	0.184 *	0.099 *		0.856	* 0.000	8
3	-0.265 *	-0.155 *	-0.150 *	-0.297 *	-0.004	-0.089 *	-0.188 *		* 0.000	9
2	-0.215 *	-0.104 *	-0.100 *	-0.246 *	0.047	-0.039	-0.138 *	0.050		
1	-0.007	0.103 *	0.108 *	-0.039	0.254 *	0.169 *	0.070 *	0.258 *	0.207 *	
Sub.	10	9	8	7	6	5	4	3	2	Sub.

Significant values ($\alpha=0.05$) are marked with an asterisk and shown in bold.

Table A.16 Significance (top right half, p-values from non-parametric Wilcoxon rank sum test) of difference and, difference in median values (bottom left half in mm) of diploe layer thicknesses between subjects.

Sub.	2	3	4	5	6	7	8	9	10	Sub.
	* 0.000	0.714	0.884	* 0.000	* 0.000	* 0.000	* 0.030	* 0.000	* 0.000	1
		* 0.000	* 0.000	0.947	* 0.000	* 0.000	* 0.000	* 0.000	* 0.000	2
9	-4.133 *		0.565	* 0.000	* 0.000	* 0.000	* 0.001	* 0.000	* 0.000	3
8	-2.043 *	2.090 *		* 0.000	* 0.000	* 0.000	* 0.019	* 0.000	* 0.000	4
7	0.080 *	4.213 *	2.123 *		* 0.000	* 0.000	* 0.000	* 0.000	* 0.000	5
6	-2.361 *	1.772 *	-0.318 *	-2.441 *		* 0.000	* 0.000	* 0.000	* 0.000	6
5	-0.688 *	3.445 *	1.355 *	-0.768 *	1.673 *		* 0.000	* 0.000	* 0.029	7
4	-1.252 *	2.881 *	0.791 *	-1.332 *	1.109 *	-0.564 *		* 0.000	* 0.000	8
3	-1.333 *	2.799 *	0.710 *	-1.414 *	1.028 *	-0.646 *	-0.081		* 0.000	9
2	-0.459 *	3.674 *	1.584 *	-0.539 *	1.902 *	0.229	0.793 *	0.874 *		
1	-1.375 *	2.758 *	0.668 *	-1.455 *	0.986 *	-0.687 *	-0.123	-0.041	-0.916 *	
Sub.	10	9	8	7	6	5	4	3	2	Sub.

Significant values ($\alpha=0.05$) are marked with an asterisk and shown in bold.

Table A.17 Significance (top right half, p-values from non-parametric Wilcoxon rank sum test) of difference and, difference in median values (bottom left half in mm) of inner cortical layer thicknesses between subjects.

Sub.	2	3	4	5	6	7	8	9	10	Sub.
	* 0.000	* 0.000	* 0.000	* 0.000	* 0.000	* 0.000	* 0.000	* 0.000	* 0.000	1
		* 0.000	0.306	* 0.019	* 0.009	* 0.009	* 0.712	* 0.000	* 0.000	2
9	0.149 *		* 0.000	* 0.000	* 0.000	* 0.000	* 0.000	0.088	* 0.000	3
8	0.000	-0.150 *		* 0.000	* 0.000	0.052	0.592	* 0.000	0.811	4
7	-0.025	-0.174 *	-0.025 *		0.802	* 0.000	* 0.004	0.053	* 0.001	5
6	0.107 *	-0.042	0.108 *	0.132 *		* 0.000	* 0.002	0.083	* 0.001	6
5	0.092 *	-0.057	0.092 *	0.117 *	-0.016		* 0.016	* 0.000	0.102	7
4	0.007	-0.142 *	0.008	0.032	-0.100 *	-0.084 *		* 0.000	0.419	8
3	0.180 *	0.031	0.181 *	0.205 *	0.073 *	0.088 *	0.173 *		* 0.000	9
2	0.042 *	-0.107 *	0.042 *	0.067 *	-0.065 *	-0.050 *	0.035	-0.138 *		
1	0.249 *	0.100 *	0.250 *	0.274 *	0.142 *	0.158 *	0.242 *	0.069 *	0.207 *	
Sub.	10	9	8	7	6	5	4	3	2	Sub.

Significant values ($\alpha=0.05$) are marked with an asterisk and shown in bold.

Table A.18 Significance (top right half, p-values from non-parametric Wilcoxon rank sum test) of difference and, difference in median values (bottom left half) of diploe layer BVF between subjects.

Sub.	2	3	4	5	6	7	8	9	10	Sub.
	* 0.009	0.286	* 0.027	* 0.000	0.502	* 0.000	* 0.000	* 0.000	* 0.000	1
		* 0.002	* 0.000	* 0.000	* 0.000	* 0.000	* 0.000	* 0.000	* 0.000	2
9	0.248 *		* 0.000	* 0.000	0.270	* 0.000	* 0.000	* 0.000	* 0.000	3
8	0.295 *	0.047		* 0.000	* 0.031	* 0.000	* 0.000	* 0.000	* 0.000	4
7	0.045 *	-0.202 *	-0.249 *		* 0.000	* 0.000	0.263	0.695	* 0.000	5
6	0.433 *	0.186 *	0.139 *	0.388 *		* 0.000	* 0.000	* 0.000	* 0.000	6
5	0.271 *	0.024	-0.023	0.226 *	-0.162 *		* 0.000	* 0.000	* 0.027	7
4	0.454 *	0.206 *	0.159 *	0.408 *	0.020 *	0.182 *		0.075	* 0.000	8
3	0.363 *	0.116 *	0.069 *	0.318 *	-0.070	0.092 *	-0.090 *		* 0.000	9
2	0.373 *	0.125 *	0.078 *	0.328 *	-0.061 *	0.102 *	-0.081 *	0.010 *		
1	0.379 *	0.132 *	0.085 *	0.334 *	-0.054	0.108 *	-0.074 *	0.016	0.006 *	
Sub.	10	9	8	7	6	5	4	3	2	Sub.

Significant values ($\alpha=0.05$) are marked with an asterisk and shown in bold.

Table A.19 Significance (top right half, p-values from non-parametric Wilcoxon rank sum test) of difference and, difference in median values (bottom left half) of ratios of outer cortical layer thickness to total thickness between subjects.

Sub.	2	3	4	5	6	7	8	9	10	Sub.
	* 0.000	* 0.000	0.368	* 0.000	0.535	* 0.000	0.234	* 0.000	* 0.000	1
		* 0.003	* 0.000	0.293	* 0.000	* 0.000	* 0.000	* 0.000	0.400	2
9	0.102 *		* 0.000	* 0.043	* 0.000	0.496	* 0.000	* 0.000	* 0.000	3
8	0.039 *	-0.062 *		* 0.000	0.567	* 0.001	0.926	* 0.000	* 0.000	4
7	0.021 *	-0.081 *	-0.019 *		* 0.000	* 0.009	* 0.000	* 0.000	0.794	5
6	0.042 *	-0.060 *	0.003	0.021 *		* 0.000	0.438	* 0.000	* 0.000	6
5	-0.006	-0.108 *	-0.046 *	-0.027 *	-0.048 *		* 0.001	* 0.000	* 0.005	7
4	0.033 *	-0.069 *	-0.007	0.012 *	-0.010	0.039 *		* 0.000	* 0.000	8
3	0.005 *	-0.097 *	-0.034 *	-0.016	-0.037 *	0.011 *	-0.027 *		* 0.000	9
2	0.013	-0.115 *	-0.052 *	-0.034 *	-0.055 *	-0.007	-0.045 *	-0.018 *		
1	0.057 *	-0.046 *	0.017	0.036 *	0.014	0.063 *	0.024	0.051 *	0.069 *	
Sub.	10	9	8	7	6	5	4	3	2	Sub.

Significant values ($\alpha=0.05$) are marked with an asterisk and shown in bold.

Table A.20 Significance (top right half, p-values from non-parametric Wilcoxon rank sum test) of difference and, difference in median values (bottom left half in mm) of ratios of diploe layer thicknesses to total thickness between subjects.

Sub.	2	3	4	5	6	7	8	9	10	Sub.
	* 0.000	* 0.031	* 0.000	* 0.000	* 0.037	* 0.000	* 0.000	* 0.000	* 0.000	1
		* 0.000	* 0.006	* 0.011	* 0.000	* 0.000	* 0.002	* 0.000	* 0.000	2
9	0.116 *		* 0.000	* 0.000	0.958	* 0.000	* 0.000	* 0.000	* 0.000	3
8	0.068 *	-0.048 *		0.797	* 0.000	* 0.000	0.204	* 0.000	* 0.000	4
7	0.007	-0.108 *	-0.061 *		* 0.000	* 0.000	0.494	* 0.000	* 0.000	5
6	0.089 *	-0.026 *	0.021 *	0.082 *		* 0.000	* 0.000	* 0.000	* 0.000	6
5	0.061 *	-0.055 *	-0.007	0.054 *	-0.028 *		* 0.000	* 0.000	0.260	7
4	0.055 *	-0.060 *	-0.013	0.048 *	-0.034 *	-0.006		* 0.000	* 0.000	8
3	0.092 *	-0.023 *	0.024 *	0.085 *	0.003	0.031 *	0.037 *		* 0.000	9
2	0.045 *	-0.071 *	-0.023 *	0.037 *	-0.045 *	-0.016 *	-0.010 *	-0.047 *		
1	0.099	-0.016	0.031	0.092	0.010	0.038	0.044	0.007 *	0.055 *	
Sub.	10	9	8	7	6	5	4	3	2	Sub.

Significant values ($\alpha=0.05$) are marked with an asterisk and shown in bold.

Table A.21 Significance (top right half, p-values from non-parametric Wilcoxon rank sum test) of difference and, difference in median values (bottom left half in mm) of ratios of inner cortical layer thickness to total thickness between subjects.

Sub.	2	3	4	5	6	7	8	9	10	Sub.
	* 0.000	* 0.000	* 0.017	* 0.000	* 0.000	0.479	* 0.003	* 0.001	0.843	1
		0.065	* 0.000	0.637	0.097	* 0.000	* 0.004	* 0.004	* 0.000	2
9	-0.110 *		* 0.000	* 0.049	0.931	* 0.000	* 0.000	* 0.000	* 0.000	3
8	-0.115 *	-0.004		* 0.001	* 0.000	* 0.000	0.268	0.220	* 0.002	4
7	0.032	0.142 *	0.147 *		* 0.050	* 0.000	* 0.032	0.057	* 0.000	5
6	-0.261 *	-0.151 *	-0.147 *	-0.293 *		* 0.000	* 0.000	* 0.000	* 0.000	6
5	-0.176 *	-0.066	-0.061 *	-0.208 *	0.085 *		* 0.000	* 0.000	0.508	7
4	-0.077 *	0.034	0.038	-0.109 *	0.184 *	0.099 *		0.856	* 0.000	8
3	-0.265 *	-0.155 *	-0.150 *	-0.297 *	-0.004	-0.089 *	-0.188 *		* 0.000	9
2	-0.215 *	-0.104 *	-0.100 *	-0.246 *	0.047	-0.039	-0.138 *	0.050		
1	-0.007	0.103 *	0.108 *	-0.039	0.254 *	0.169 *	0.070 *	0.258 *	0.207 *	
Sub.	10	9	8	7	6	5	4	3	2	Sub.

Significant values ($\alpha=0.05$) are marked with an asterisk and shown in bold.

14.3 Coupon tensile testing

14.3.1 Experimental data

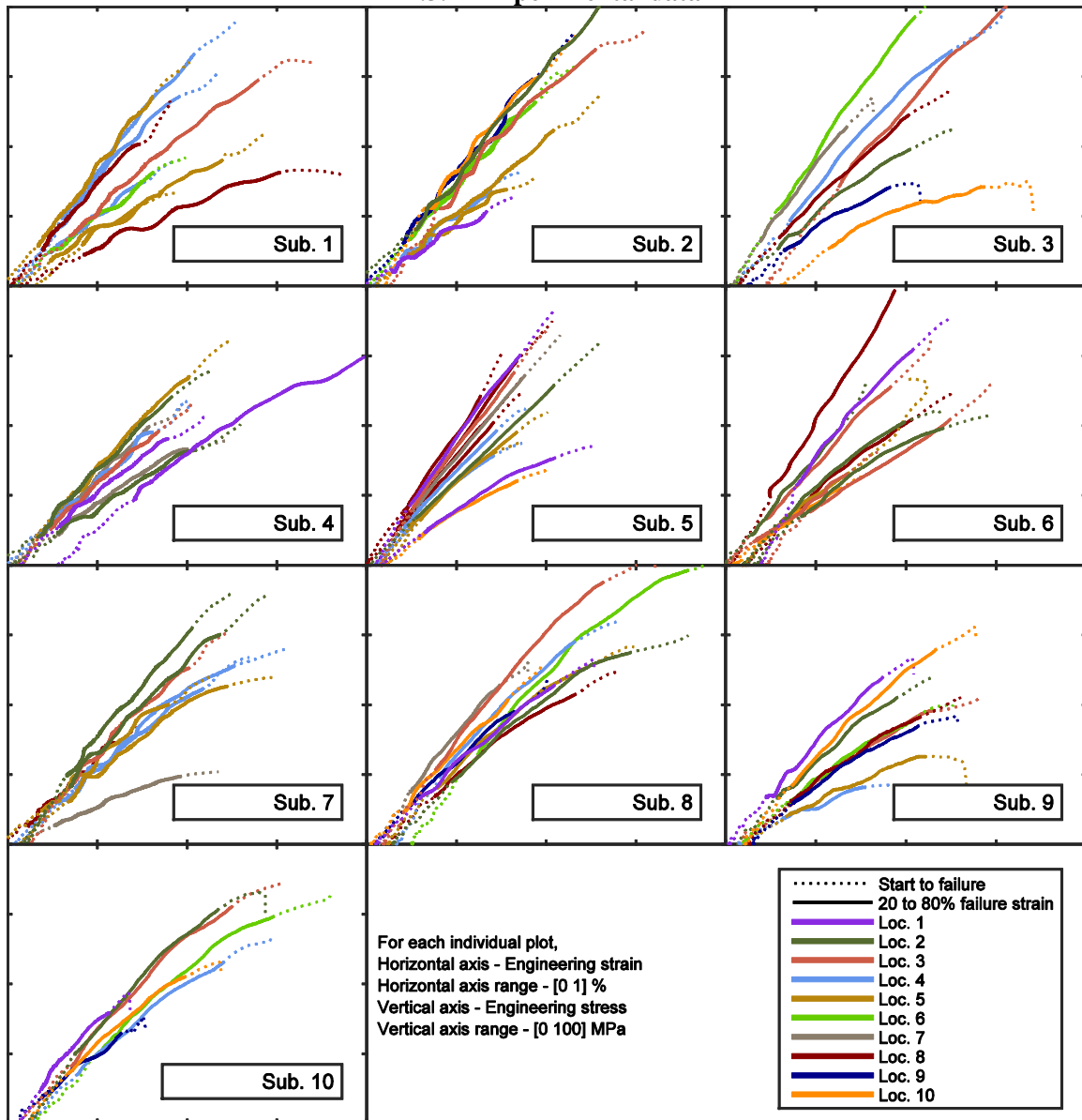


Figure A.6 Engineering stress vs. strain for coupon tensile tests combined by subject.

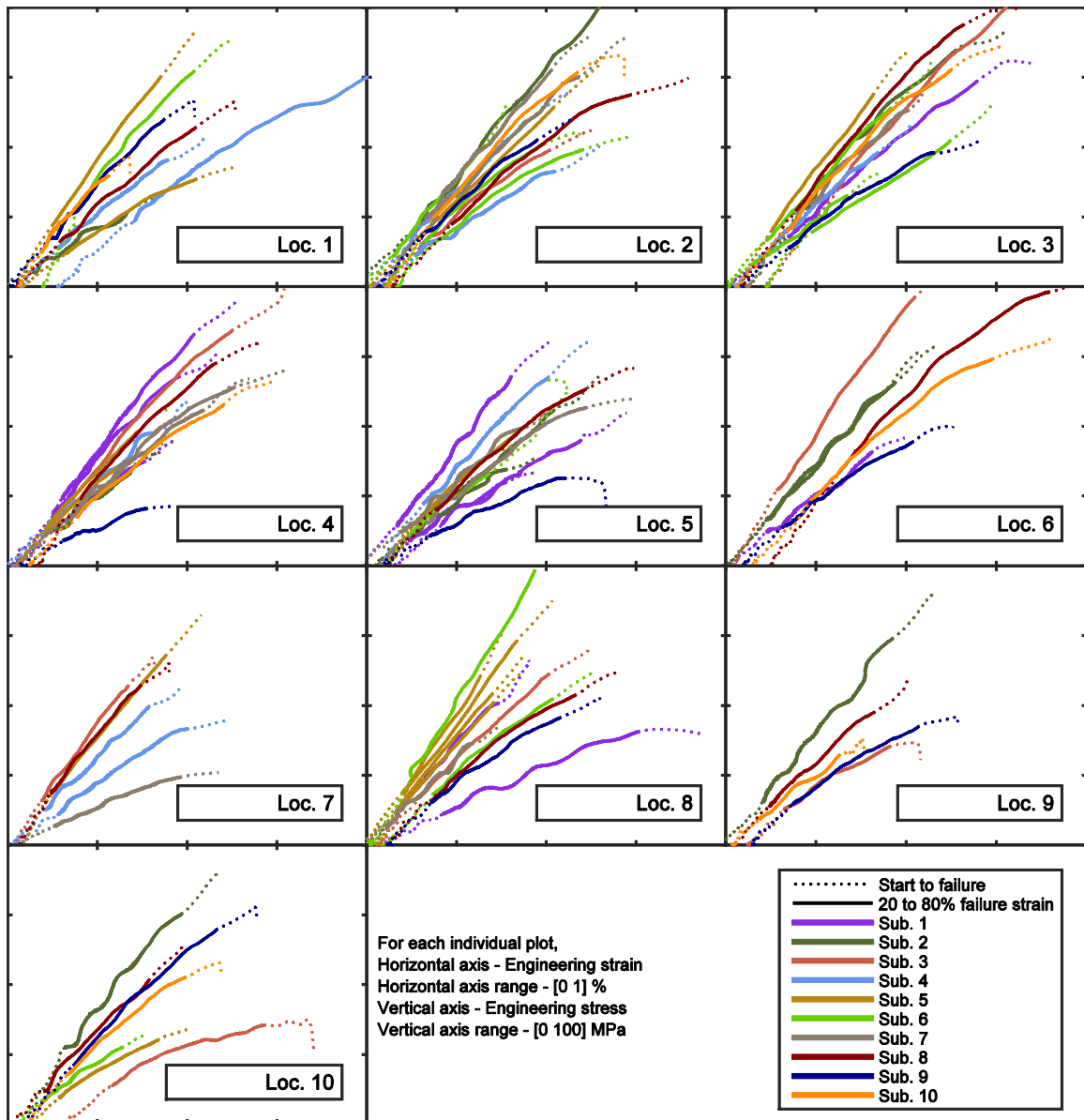


Figure A.7 Engineering stress vs. strain for coupon tensile tests combined by location.

14.3.2 Tabulated results

Table A.22 List of coupon samples and their harvest locations.

ID	Azimuth	Elevation	Radius	Frontal	Superior
	[deg]	[deg]	[mm]		
010301				Yes	Yes
010401				No	Yes
010402				No	Yes
010403				No	Yes
010501				No	No
010502				No	No
010503				No	No
010601				No	No
010801				No	No
010802				No	No
020101	3.20	16.02	112.37	Yes	No
020201	23.00	17.60	104.79	Yes	No
020301	16.79	57.80	86.12	Yes	Yes
020401	67.90	76.42	74.67	No	Yes
020501	78.66	51.43	74.25	No	Yes
020502	78.66	51.43	74.25	No	Yes
020601	66.74	14.35	71.27	No	No

Table A.22 List of coupon samples and their harvest locations continued...

ID	Azimuth	Elevation	Radius	Frontal	Superior
	[deg]	[deg]	[mm]		
020602	66.74	14.35	71.27	No	No
020901	115.79	42.05	72.58	No	Yes
021001	147.89	25.41	73.24	No	No
030201	30.10	13.61	98.70	Yes	No
030301	12.04	25.85	98.88	Yes	No
030401	21.90	48.60	87.80	Yes	Yes
030601	59.21	18.60	77.68	No	No
030701	89.32	21.37	70.44	No	No
030801	118.29	11.82	68.15	No	No
030901	84.37	58.06	72.35	No	Yes
031001	154.25	28.73	68.54	No	No
040101	7.26	11.71	111.70	Yes	No
040102	7.26	11.71	111.70	Yes	No
040201	34.71	13.46	99.92	Yes	No
040202	34.71	13.46	99.92	Yes	No
040301	15.42	42.36	92.28	Yes	Yes
040401	37.01	73.21	75.35	No	Yes

Table A.22 List of coupon samples and their harvest locations continued...

ID	Azimuth	Elevation	Radius	Frontal	Superior
	[deg]	[deg]	[mm]		
040501	64.44	55.49	75.29	No	Yes
040701	82.37	18.66	74.90	No	No
040702	82.37	18.66	74.90	No	No
050101	4.52	3.64	113.82	Yes	No
050102	4.52	3.64	113.82	Yes	No
050201	32.21	8.88	96.11	Yes	No
050301	28.11	44.78	84.50	Yes	Yes
050401	54.49	54.91	75.72	No	Yes
050402	54.49	54.91	75.72	No	Yes
050501	72.86	33.93	73.95	No	Yes
050502	72.86	33.93	73.95	No	Yes
050701	90.87	6.38	67.27	No	No
050801	126.22	3.73	69.05	No	No
050802	126.22	3.73	69.05	No	No
050803	126.22	3.73	69.05	No	No
050804	126.22	3.73	69.05	No	No
051001	146.61	29.30	74.39	No	No

ID	Azimuth	Elevation	Radius	Frontal	Superior
	[deg]	[deg]	[mm]		
060101	18.69	2.85	106.52	Yes	No
060201	31.98	16.46	96.74	Yes	No
060202	31.98	16.46	96.74	Yes	No
060203	31.98	16.46	96.74	Yes	No
060301	21.52	37.19	92.71	Yes	Yes
060302	21.52	37.19	92.71	Yes	Yes
060303	21.52	37.19	92.71	Yes	Yes
060501	62.77	49.44	75.01	No	Yes
060801	110.65	14.30	71.40	No	No
060802	110.65	14.30	71.40	No	No
061001	140.83	38.24	70.05	No	Yes
070201	23.69	37.67	89.43	Yes	Yes
070202	23.69	37.67	89.43	Yes	Yes
070301	11.13	52.62	85.19	Yes	Yes
070401	57.47	74.89	74.04	No	Yes
070402	57.47	74.89	74.04	No	Yes

ID	Azimuth	Elevation	Radius	Frontal	Superior
	[deg]	[deg]	[mm]		
070501	69.82	51.21	73.87	No	Yes
070502	69.82	51.21	73.87	No	Yes
070701	87.98	13.61	72.92	No	No
070801	115.02	-2.74	71.32	No	No
080101	16.57	12.32	105.12	Yes	No
080201	38.18	19.16	90.93	Yes	No
080301	32.20	36.55	87.68	Yes	Yes
080401	47.66	54.33	76.63	No	Yes
080501	69.88	44.29	72.25	No	Yes
080601	63.40	20.96	73.37	No	No
080701	70.08	-2.97	68.59	No	No
080801	108.82	12.35	67.63	No	No
080901	101.54	58.10	67.42	No	Yes
081001	129.57	34.78	68.25	No	Yes
090101	10.22	18.20	113.07	Yes	No
090201	25.46	7.70	105.08	Yes	No
090301	20.04	36.82	96.56	Yes	Yes

Table A.22 List of coupon samples and their harvest locations continued...

ID	Azimuth	Elevation	Radius	Frontal	Superior
	[deg]	[deg]	[mm]		
090401	77.82	64.80	75.12	No	Yes
090501	68.92	36.48	76.09	No	Yes
090601	56.17	-3.62	78.95	No	No
090801	133.65	2.97	79.32	No	No
090901	119.73	42.22	76.73	No	Yes
091001	154.11	23.70	77.61	No	No
100101	18.68	24.39	91.59	Yes	No
100201	36.31	30.68	81.34	Yes	Yes
100301	25.54	44.03	79.76	Yes	Yes
100401	47.87	64.99	70.73	No	Yes
100601	69.56	39.39	69.36	No	Yes
100901	117.32	64.71	66.24	No	Yes
101001	150.65	46.39	63.96	No	Yes

**Table A.23 Repetitions at same location and failure outside gage-area status
for each coupon sample.**

ID	Repetition		Broke outside gage area
	Same depth	Different depth	
010301	No	No	Yes
010401	No	No	No
010402	Yes	No	No
010403	No	Yes	No
010501	No	No	No
010502	No	Yes	Yes
010503	Yes	No	No
010601	No	No	No
010801	No	No	No
010802	Yes	No	No
020101	No	No	No
020201	No	No	No
020301	No	No	No
020401	No	No	Yes
020501	No	No	No
020502	Yes	No	Yes
020601	No	No	No
020602	Yes	No	No

Table A.23 Repetitions at same location and failure outside gage-area status for each coupon sample continued...

ID	Repetition		Broke outside gage area
	Same depth	Different depth	
020901	No	No	Yes
021001	No	No	No
030201	No	No	No
030301	No	No	No
030401	No	No	No
030601	No	No	Yes
030701	No	No	No
030801	No	No	No
030901	No	No	No
031001	No	No	No
040101	No	No	No
040102	Yes	No	Yes
040201	No	No	No
040202	Yes	No	No
040301	No	No	No
040401	No	No	No
040501	No	No	Yes

Table A.23 Repetitions at same location and failure outside gage-area status for each coupon sample continued...

ID	Repetition		Broke outside gage area
	Same depth	Different depth	
040701	No	No	No
040702	Yes	No	No
050101	No	No	No
050102	Yes	No	No
050201	No	No	Yes
050301	No	No	No
050401	No	No	No
050402	Yes	No	No
050501	No	No	No
050502	Yes	No	No
050701	No	No	Yes
050801	No	No	No
050802	No	Yes	No
050803	Yes	No	No
050804	No	Yes	No
051001	No	No	Yes

Table A.23 Repetitions at same location and failure outside gage-area status for each coupon sample continued...

ID	Repetition		Broke outside gage area
	Same depth	Different depth	
060101	No	No	No
060201	No	No	No
060202	No	Yes	No
060203	Yes	No	No
060301	No	No	Yes
060302	Yes	No	No
060303	No	Yes	Yes
060501	No	No	Yes
060801	No	No	Yes
060802	Yes	No	No
061001	No	No	Yes
070201	No	No	No
070202	Yes	No	No
070301	No	No	No
070401	No	No	No
070402	Yes	No	No

Table A.23 Repetitions at same location and failure outside gage-area status for each coupon sample continued...

ID	Repetition		Broke outside gage area
	Same depth	Different depth	
070501	No	No	No
070502	Yes	No	No
070701	No	No	No
070801	No	No	No
080101	No	No	No
080201	No	No	No
080301	No	No	No
080401	No	No	No
080501	No	No	No
080601	No	No	No
080701	No	No	Yes
080801	No	No	No
080901	No	No	No
081001	No	No	No
090101	No	No	Yes
090201	No	No	No

Table A.23 Repetitions at same location and failure outside gage-area status for each coupon sample continued...

ID	Repetition		Broke outside gage area
	Same depth	Different depth	
090301	No	No	No
090401	No	No	Yes
090501	No	No	No
090601	No	No	No
090801	No	No	No
090901	No	No	Yes
091001	No	No	No
100101	No	No	Yes
100201	No	No	Yes
100301	No	No	Yes
100401	No	No	No
100601	No	No	No
100901	No	No	No
101001	No	No	No

Table A.24 List of coupon samples and their mechanical properties.

ID	Bone volume fraction	Structural	Failure	Bone phase modulus [GPa]		
		modulus [GPa]	Stress [MPa]	Strain [%]	from power	
					law model	from implicit FE model
010301	0.767	10.97	80.36	0.857	19.72	19.13
010401	0.865	15.09	76.67	0.578	20.79	18.51
010402	0.884	16.37	94.35	0.602	21.52	18.17
010403	0.746	10.08	45.05	0.443	19.30	17.27
010501	0.908	16.96	80.08	0.528	20.99	19.59
010502	0.755	7.76	54.77	0.645	14.47	16.09
010503	0.692	7.94	33.54	0.443	17.98	19.31
010601	0.812	9.81	45.83	0.476	15.57	16.84
010801	0.655	5.64	39.50	0.901	14.39	16.29
010802	0.848	14.62	66.12	0.440	21.05	22.48
020101	0.585	8.23	31.79	0.432	26.95	28.37
020201	0.813	15.60	124.58	0.868	24.71	19.69
020301	0.866	14.03	92.05	0.708	19.28	18.54
020401	0.702	9.94	40.76	0.407	21.75	24.31
020501	0.890	10.49	67.98	0.624	13.59	12.04
020502	0.767	9.31	38.78	0.440	16.77	17.76

Table A.24 List of coupon samples and their mechanical properties continued...

ID	Bone volume fraction	Structural	Failure	Bone phase modulus [GPa]		
		modulus [GPa]	Stress [MPa]	Strain [%]	from power	from implicit
					law model	FE model
020601	0.850	14.30	78.46	0.577	20.50	17.30
020602	0.840	14.67	76.82	0.538	21.60	16.75
020901	0.882	16.07	91.02	0.592	21.21	18.50
021001	0.861	16.37	90.15	0.540	22.81	21.49
030201	0.779	10.11	55.93	0.603	17.59	18.35
030301	0.847	12.72	117.11	1.004	18.38	15.76
030401	0.855	14.22	99.14	0.741	20.12	17.84
030601	0.880	18.85	114.68	0.628	25.01	23.13
030701	0.885	17.44	62.53	0.395	22.88	24.19
030801	0.814	12.19	71.41	0.586	19.21	19.14
030901	0.730	8.09	30.54	0.483	16.27	19.99
031001	0.685	5.43	26.44	0.702	12.56	15.68
040101	0.673	7.85	74.24	1.092	18.90	18.77
040102	0.621	10.40	53.39	0.503	29.83	28.95
040201	0.866	13.49	69.31	0.611	18.57	20.92
040202	0.666	8.21	50.33	0.638	20.17	26.22

Table A.24 List of coupon samples and their mechanical properties continued...

ID	Bone volume fraction	Structural	Failure	Bone phase modulus [GPa]		
		modulus [GPa]	Stress [MPa]	Strain [%]	from power	from implicit
					law model	FE model
040301	0.819	11.64	59.05	0.484	18.10	18.97
040401	0.881	12.06	55.81	0.514	15.96	18.53
040501	0.904	13.85	80.89	0.576	17.31	15.71
040701	0.825	8.81	45.06	0.596	13.48	16.66
040702	0.842	12.62	57.06	0.478	18.45	18.04
050101	0.877	18.05	91.44	0.499	24.12	21.45
050102	0.756	7.86	42.61	0.592	14.63	17.06
050201	0.866	12.30	80.09	0.635	16.90	16.16
050301	0.868	16.77	83.07	0.465	22.97	17.55
050401	0.793	11.73	43.76	0.413	19.58	15.68
050402	0.816	13.49	55.95	0.420	21.18	16.90
050501	0.863	11.65	54.71	0.446	16.14	14.02
050502	0.806	11.88	44.63	0.391	19.18	16.59
050701	0.839	15.49	82.36	0.498	22.83	20.47
050801	0.856	14.45	61.82	0.411	20.41	19.58
050802	0.838	17.39	87.34	0.519	25.73	22.67

Table A.24 List of coupon samples and their mechanical properties continued...

ID	Bone volume fraction	Structural	Failure		Bone phase modulus [GPa]	
		modulus [GPa]	Stress [MPa]	Strain [%]	from power law model	from implicit FE model
050803	0.883	15.73	68.49	0.441	20.75	17.45
050804	0.865	18.84	76.93	0.341	26.00	21.51
051001	0.758	7.43	34.35	0.455	13.71	14.88
060101	0.885	15.44	88.96	0.527	20.26	20.65
060201	0.875	15.60	64.90	0.396	20.96	20.02
060202	0.747	10.94	53.36	0.546	20.88	22.81
060203	0.853	8.90	53.83	0.655	12.68	12.80
060301	0.780	8.28	65.54	0.636	14.37	14.45
060302	0.856	14.45	80.42	0.572	20.40	18.31
060303	0.734	9.68	40.49	0.429	19.19	19.45
060501	0.785	9.97	66.10	0.365	17.03	15.72
060801	0.875	20.55	127.62	0.572	27.66	25.51
060802	0.886	10.48	62.54	0.555	13.71	12.47
061001	0.715	8.96	32.03	0.368	18.84	20.05
070201	0.837	13.22	89.16	0.681	19.63	21.46
070202	0.840	15.22	90.09	0.573	22.42	18.19

Table A.24 List of coupon samples and their mechanical properties continued...

ID	Bone volume fraction	Structural	Failure	Bone phase modulus [GPa]		
		modulus [GPa]	Stress [MPa]	Strain [%]	from power	
					law model	from implicit FE model
070301	0.845	12.99	75.99	0.548	18.88	15.64
070401	0.766	10.78	66.95	0.656	19.48	18.90
070402	0.834	11.01	69.91	0.740	16.48	18.55
070501	0.834	12.03	60.20	0.586	17.97	18.94
070502	0.786	10.16	59.39	0.730	17.33	15.77
070701	0.653	5.40	25.99	0.570	13.87	27.19
070801	0.824	12.41	42.89	0.400	19.04	18.39
080101	0.828	11.27	62.01	0.617	17.11	19.17
080201	0.816	10.24	74.83	0.824	16.08	15.07
080301	0.883	15.03	98.63	0.764	19.80	18.51
080401	0.859	12.89	80.08	0.614	18.03	20.72
080501	0.880	11.10	70.67	0.688	14.73	15.03
080601	0.857	11.88	103.32	0.962	16.71	17.04
080701	0.889	15.87	62.11	0.413	20.61	19.94
080801	0.833	9.90	62.49	0.649	14.85	15.92
080901	0.894	12.04	59.06	0.480	15.44	14.17
081001	0.826	13.34	63.82	0.479	20.37	19.03

Table A.24 List of coupon samples and their mechanical properties continued...

ID	Bone volume fraction	Structural	Failure	Bone phase modulus [GPa]		
		modulus [GPa]	Stress [MPa]	Strain [%]	from power	from implicit
					law model	FE model
090101	0.774	14.32	60.92	0.532	25.26	21.72
090201	0.846	11.63	60.30	0.547	16.85	15.59
090301	0.751	8.80	51.71	0.663	16.57	15.37
090401	0.720	5.56	20.97	0.431	11.52	16.31
090501	0.699	6.05	20.35	0.624	13.39	14.49
090601	0.784	9.09	49.95	0.581	15.58	16.12
090801	0.813	8.91	51.57	0.591	14.11	15.11
090901	0.652	8.32	43.00	0.572	21.44	19.46
091001	0.833	12.49	74.64	0.654	18.71	15.94
100101	0.706	15.00	39.71	0.311	32.48	27.72
100201	0.783	13.71	74.95	0.660	23.59	20.04
100301	0.870	13.22	85.37	0.742	18.01	15.70
100401	0.876	10.02	66.24	0.675	13.44	12.19
100601	0.883	10.83	81.53	0.820	14.26	12.90
100901	0.721	10.13	32.71	0.364	20.89	20.39
101001	0.774	11.25	53.72	0.538	19.83	18.92

14.3.3 Statistical test results

Table A.25 Results of normality tests (p-values from Shapiro-Wilk test) of mechanical properties of the calvarium cortical layer for each subject.

Sub	Effective structural properties			BVF	Bone phase modulus	
	Modulus	Failure stress	Failure strain		Power law	FE
1	0.419	0.503	* 0.042	0.769	0.589	0.399
2	0.119	0.479	0.389	* 0.025	0.893	0.601
3	0.958	0.413	0.659	0.367	0.985	0.444
4	0.366	0.582	* 0.001	0.085	* 0.017	0.064
5	0.521	0.284	0.517	0.064	0.739	0.387
6	0.051	0.228	0.197	0.058	0.361	0.689
7	0.257	0.658	0.470	* 0.002	0.872	* 0.032
8	0.567	* 0.027	0.840	0.226	0.237	0.428
9	0.636	0.335	0.521	0.857	0.716	* 0.014
10	0.327	0.523	0.512	0.186	0.448	0.543

Significant values ($\alpha=0.05$) are shown in bold and marked with an asterisk.

Table A.26 Results of one-way ANOVA tests of mechanical properties of the calvarium cortical layer.

Dependent variable	DF	SS	MS	F	p	ges	
Main effect – Subject							
Effective modulus	9	127.3	14.1	1.356	0.221	0.123	
Effective failure stress	9	4801	533	1.067	0.395	0.099	
Effective failure strain	9	0.327	0.036	1.808	0.078	0.158	
Bone modulus BVF	9	140.3	15.6	1.023	0.428	0.096	
Bone modulus FE	9	93.2	10.4	0.851	0.572	0.081	
Dependent variable	DFn	DFd	SSn	SSd	F	p	ges
Main effect – is frontal, random effect – Subject							
Effective modulus	1	9	2.2	16.5	1.192	0.303	0.058
Effective failure stress	1	9	855	648	11.871	* 0.007	0.323
Effective failure strain	1	9	0.056	0.047	10.583	* 0.010	0.289
Bone modulus BVF	1	9	25.1	36.2	6.240	* 0.034	0.270
Bone modulus FE	1	9	7.8	34.6	2.039	0.187	0.127
Main effect – is superior, random effect – Subject							
Effective modulus	1	9	1.9	34.1	0.510	0.493	0.029
Effective failure stress	1	9	9	2046	0.038	0.850	0.002
Effective failure strain	1	9	0.000	0.083	0.053	0.823	0.003
Bone modulus BVF	1	9	22.8	104.6	1.961	0.195	0.097
Bone modulus FE	1	9	37.3	50.0	6.718	* 0.029	0.276
Significant values ($\alpha=0.05$) are shown in bold and marked with an asterisk.							

14.3.4 Distribution of cortical layer mechanical properties over the calvarium of each subject

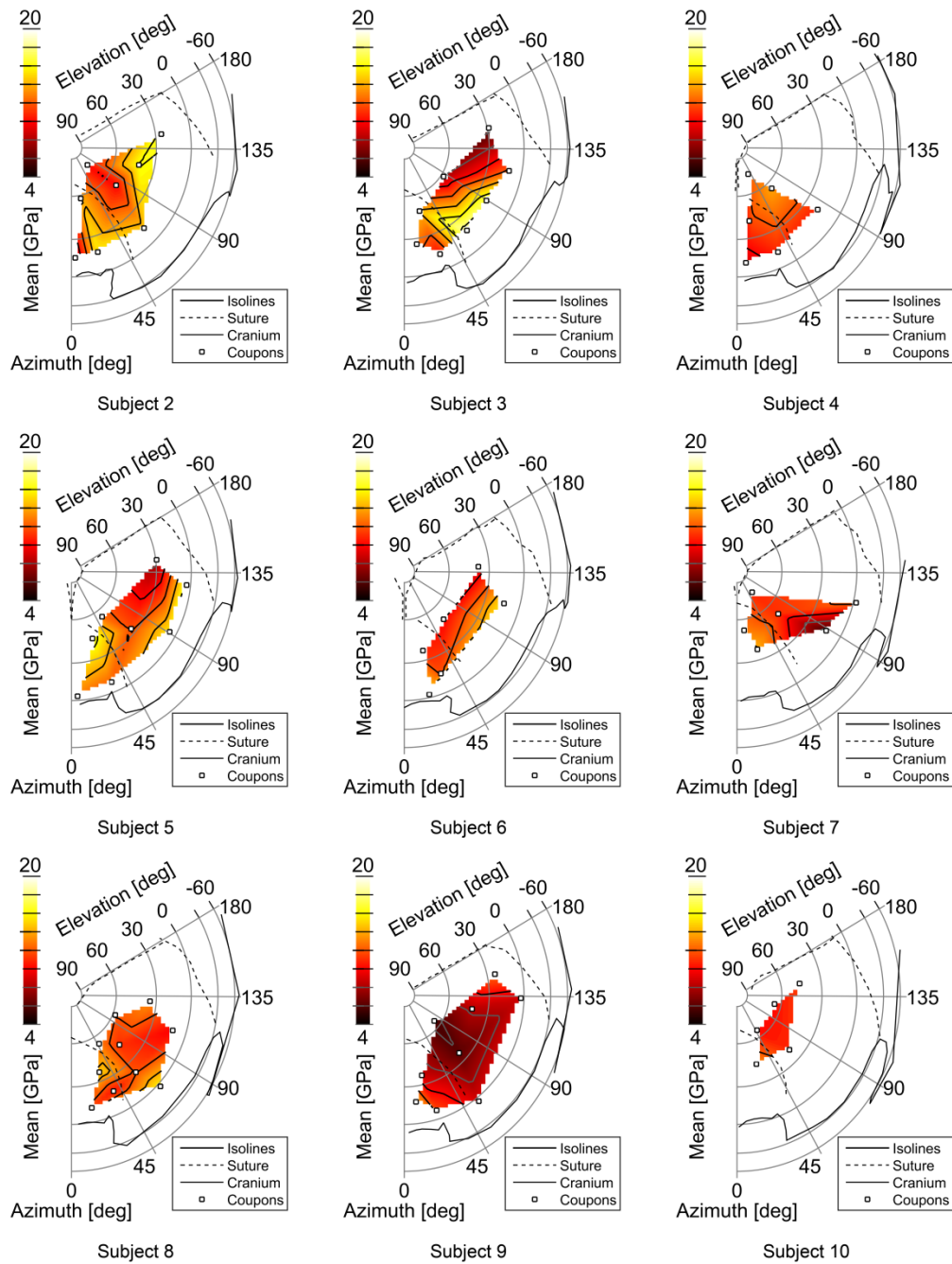


Figure A.8 Effective structural Young's modulus of cortical coupons.

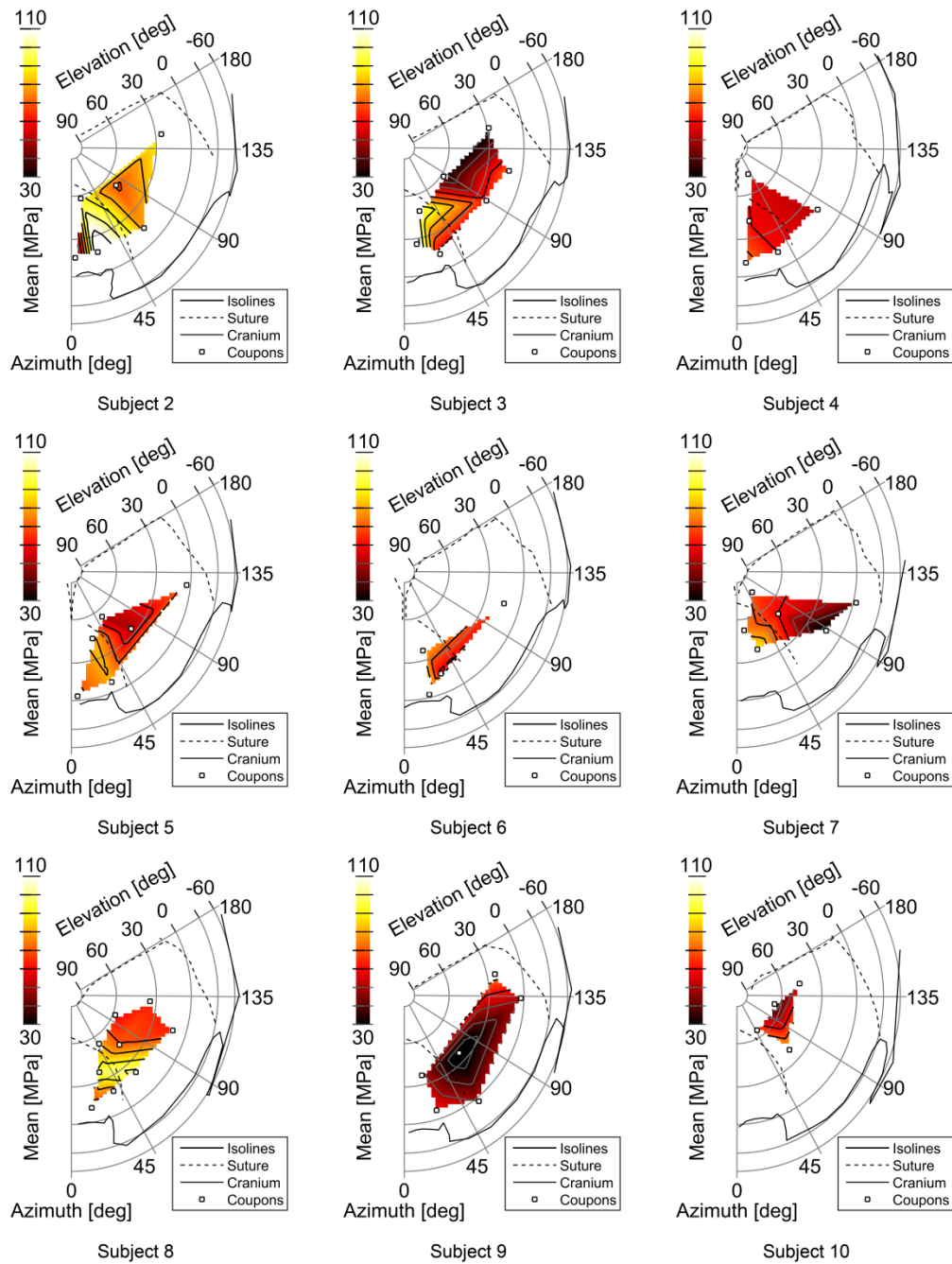


Figure A.9 Effective structural failure stress of cortical coupons.

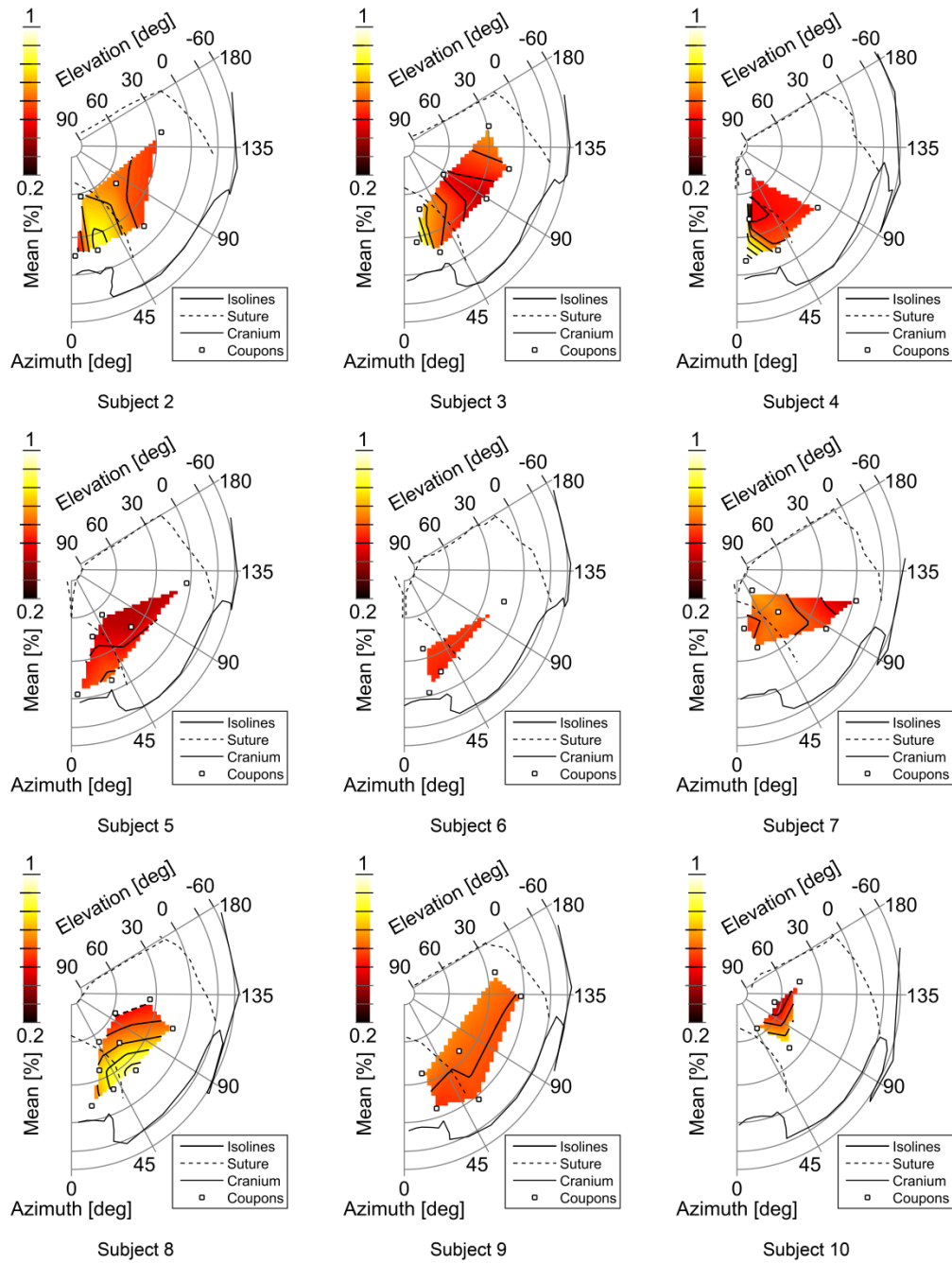


Figure A.10 Effective structural failure strain of cortical coupons.

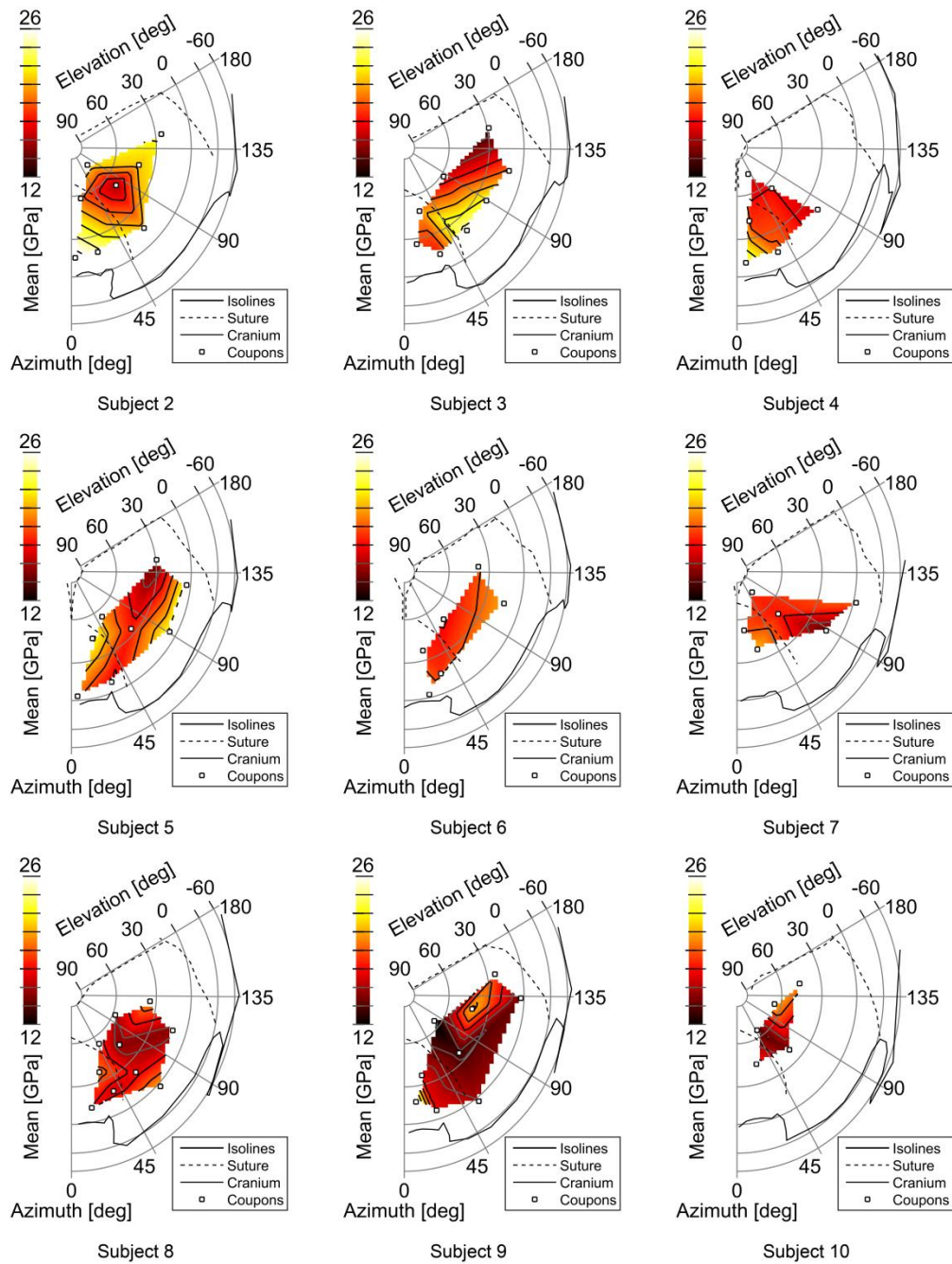


Figure A.11 Cortical bone phase Young's modulus, as derived from BVF based power law model.

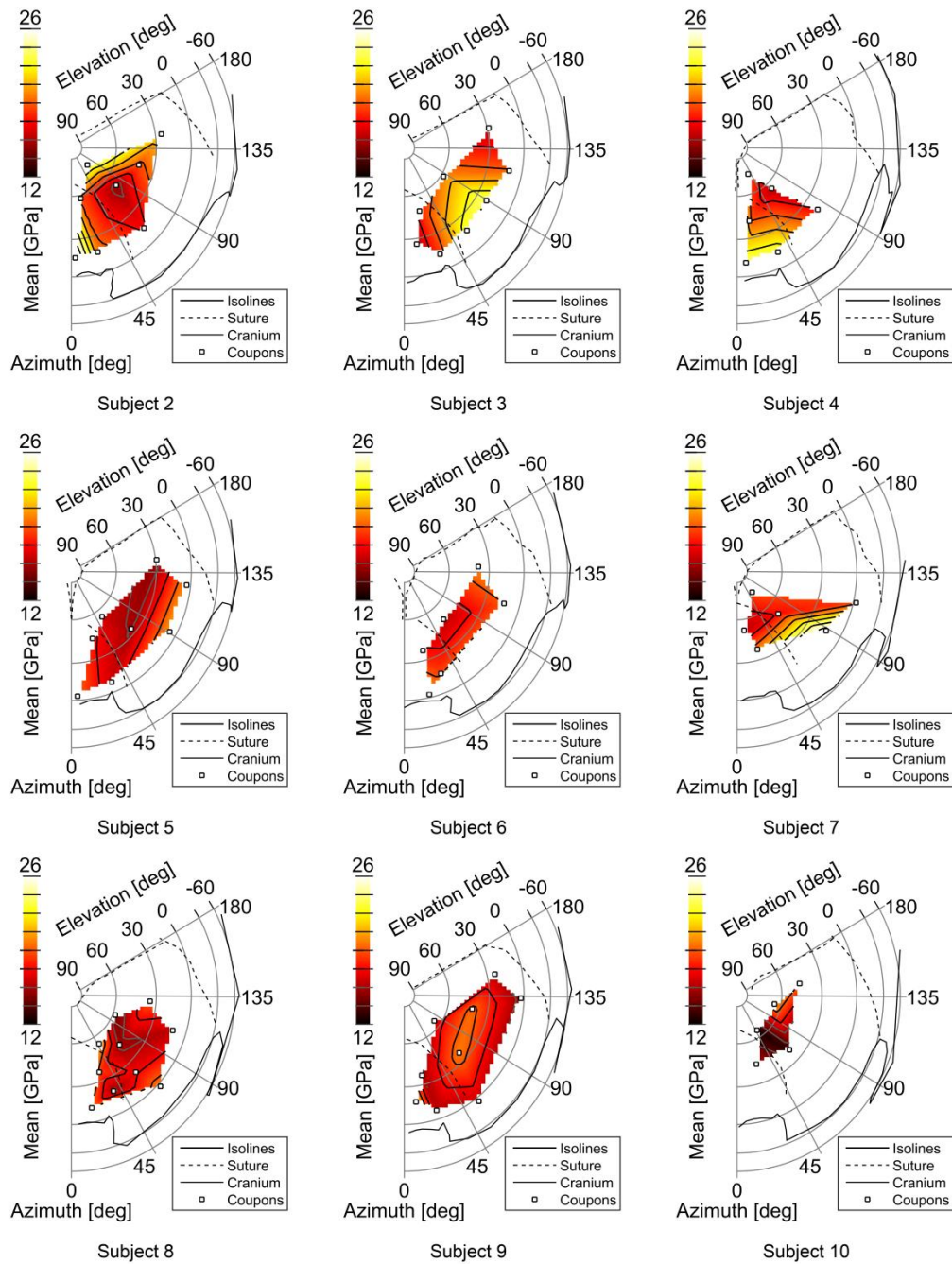
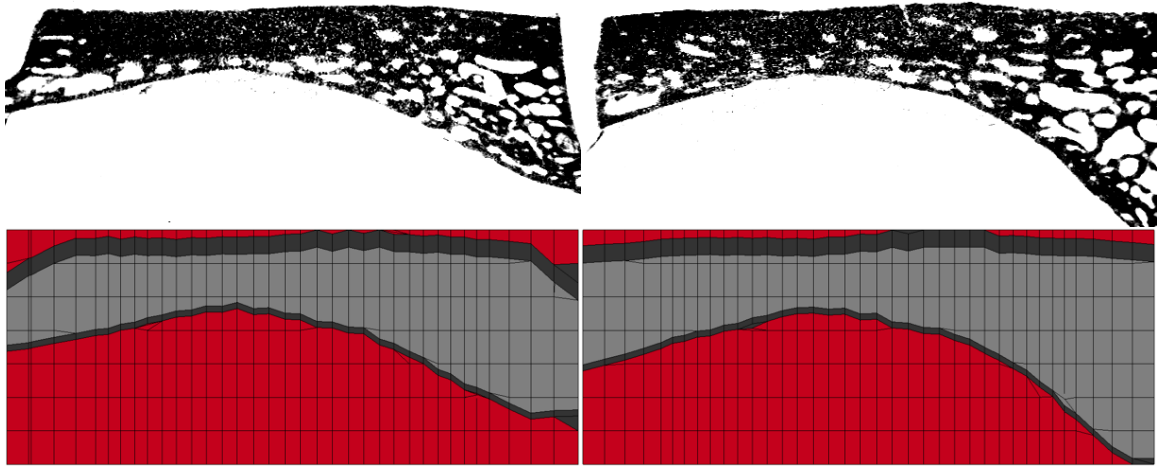


Figure A.12 Cortical bone phase Young's modulus, as derived from implicit micro FE models.

14.4 Micro computed tomography cross-sections of the core and coupon samples, and their mechanical properties

This section contains the μ CT cross-section images of the cylindrical core samples along two orthogonal planes perpendicular to the surface of the skull (black – bone, white – pore). These planes are not aligned to any particular direction on the calvarium. Cross-sections of the corresponding simplified FE mesh is also shown (Red – potting, dark gray – cortical layers, light gray – diploe layer). The corresponding mechanical properties and diploe layer bone volume fraction are tabulated.

Also shown for each core sample are μ CT cross-section images of the gage area of cortical coupons that have been obtained from a symmetric location from the same calvarium (black – bone, white – pore). The mechanical properties of the coupons are also tabulated. Few core samples do not have a corresponding coupon sample that was successfully tested. The Young's modulus used for the cortical layers in the simplified FE models in these cases is the global average value of 18.51 GPa.



ID – Source

0102 – Frontal

Trabecular bone volume fraction

0.641

Effective quasi-static modulus [MPa]

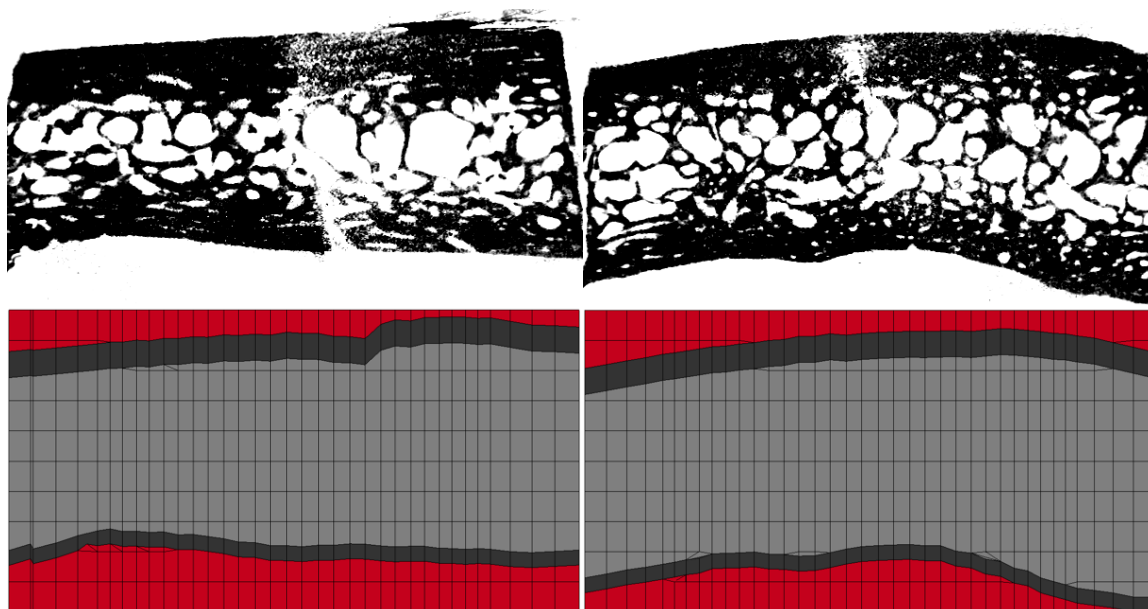
387.001

Diploe quasi-static modulus [MPa]

222.054

Diploe viscoelastic modulus [MPa @ 50 kHz]

817.754



ID – Source

0103 – Frontal

Trabecular bone volume fraction

0.239

Effective quasi-static modulus [MPa]

797.583

Diploe quasi-static modulus [MPa]

698.945

Diploe viscoelastic modulus [MPa @ 50 kHz]

1033.073



010301

Bone volume fraction

0.767

Effective modulus [GPa]

10.965

Effective failure stress [MPa]

80.360

Effective failure strain [%]

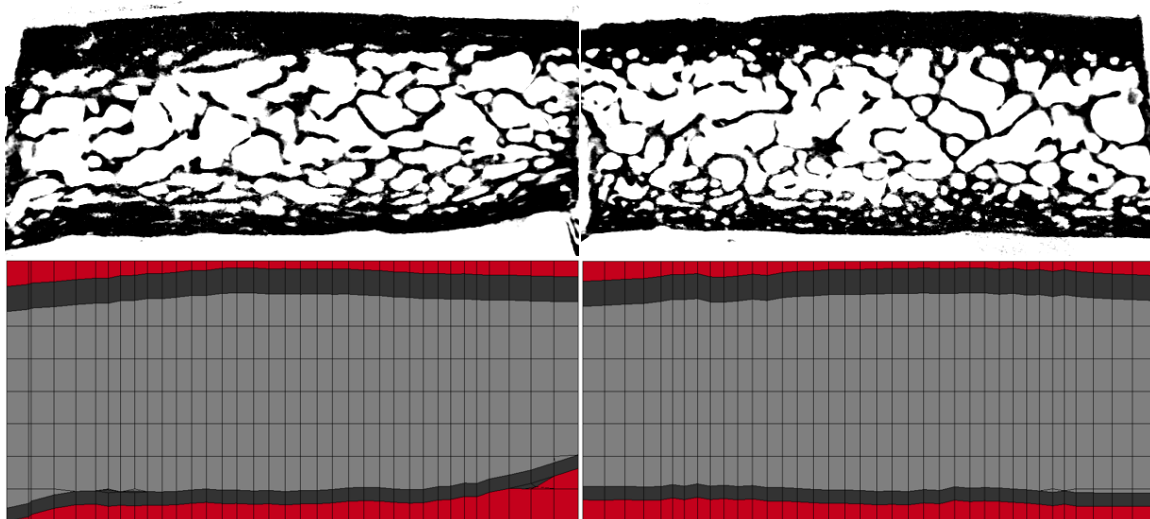
0.857

Bone modulus from BVF [GPa]

19.721

Bone modulus from μ FE [GPa]

19.134



ID – Source

0104 – Parietal

Trabecular bone volume fraction

0.175

Effective quasi-static modulus [MPa]

365.223

Diploe quasi-static modulus [MPa]

239.998

Diploe viscoelastic modulus [MPa @ 50 kHz]

1020.971



010401

010402 Same depth

010403 Different depth

Bone volume fraction

0.865

0.884

0.746

Effective modulus [GPa]

15.086

16.374

10.080

Effective failure stress [MPa]

76.673

94.346

45.046

Effective failure strain [%]

0.578

0.602

0.443

Bone modulus from BVF [GPa]

20.788

21.516

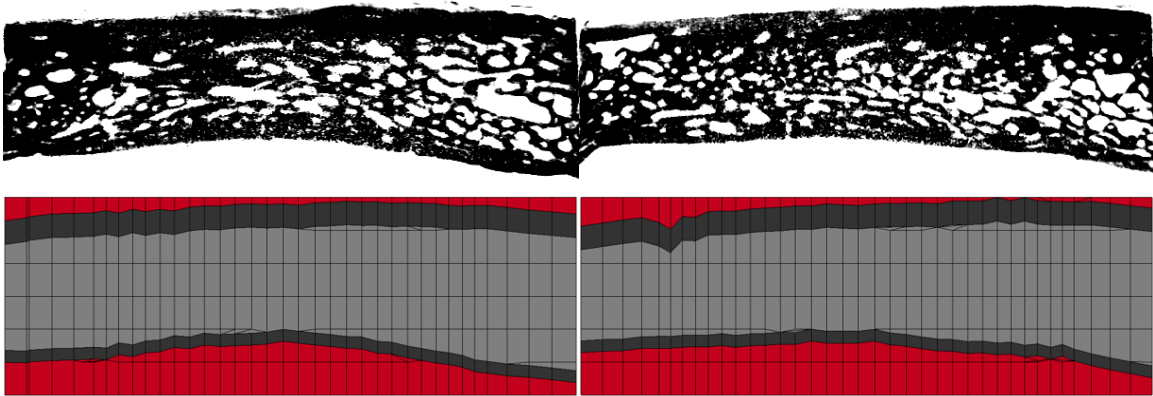
19.303

Bone modulus from μ FE [GPa]

18.511

18.172

17.274



ID – Source

0105 – Parietal

Trabecular bone volume fraction

0.577

Effective quasi-static modulus [MPa]

543.571

Diploe quasi-static modulus [MPa]

336.984

Diploe viscoelastic modulus [MPa @ 50 kHz]

877.515



010501

010502 Different depth 010503 Same depth

Bone volume fraction

0.908

0.755

0.692

Effective modulus [GPa]

16.956

7.763

7.945

Effective failure stress [MPa]

80.084

54.765

33.539

Effective failure strain [%]

0.528

0.645

0.443

Bone modulus from BVF [GPa]

20.993

14.467

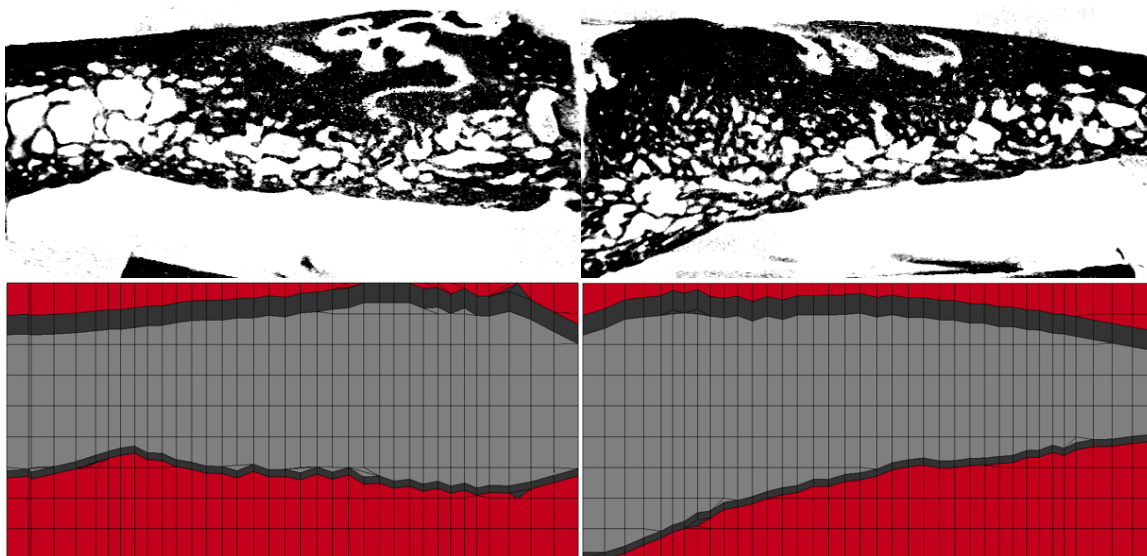
17.978

Bone modulus from μ FE [GPa]

19.588

16.092

19.312



ID – Source

0106 – Parietal

Trabecular bone volume fraction

0.540

Effective quasi-static modulus [MPa]

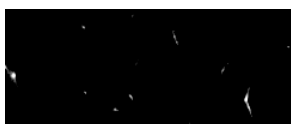
470.035

Diploe quasi-static modulus [MPa]

338.483

Diploe viscoelastic modulus [MPa @ 50 kHz]

1129.253



010601

Bone volume fraction

0.812

Effective modulus [GPa]

9.810

Effective failure stress [MPa]

45.827

Effective failure strain [%]

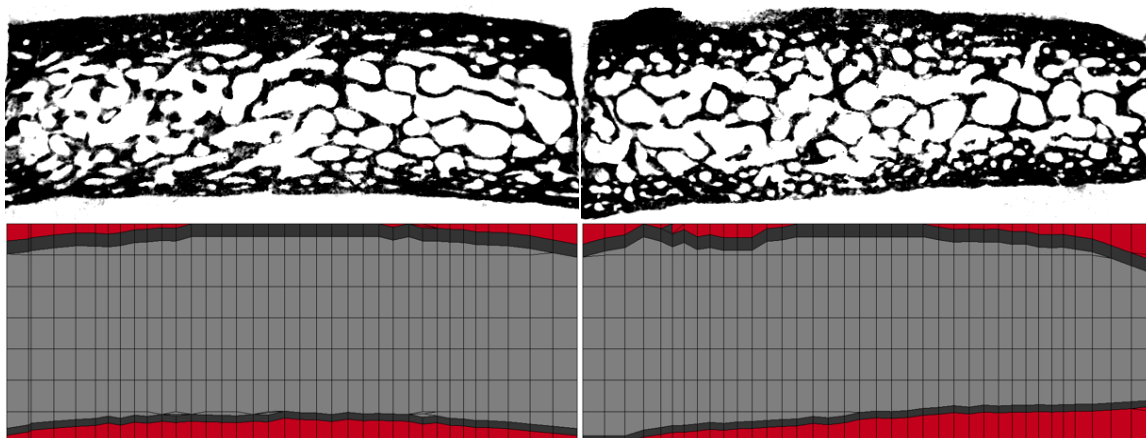
0.476

Bone modulus from BVF [GPa]

15.570

Bone modulus from μ FE [GPa]

16.837



ID – Source

0108 – Parietal

Trabecular bone volume fraction

0.213

Effective quasi-static modulus [MPa]

357.860

Diploe quasi-static modulus [MPa]

251.271

Diploe viscoelastic modulus [MPa @ 50 kHz]

1153.474



010801

010802 Same depth

Bone volume fraction

0.655

0.848

Effective modulus [GPa]

5.637

14.623

Effective failure stress [MPa]

39.502

66.122

Effective failure strain [%]

0.901

0.440

Bone modulus from BVF [GPa]

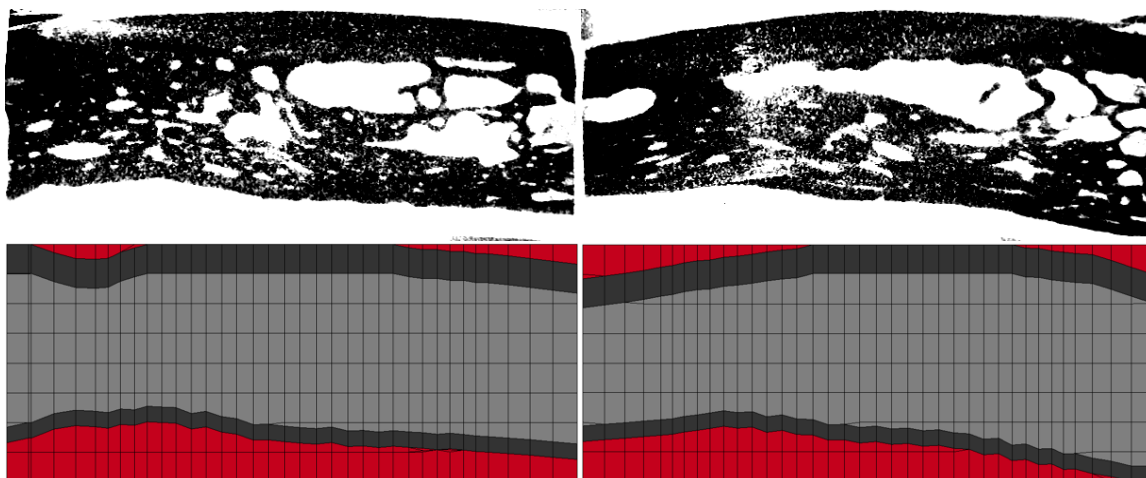
14.386

21.048

Bone modulus from μ FE [GPa]

16.292

22.482



ID – Source

0201 – Frontal

Trabecular bone volume fraction

0.577

Effective quasi-static modulus [MPa]

438.420

Diploe quasi-static modulus [MPa]

261.395

Diploe viscoelastic modulus [MPa @ 50 kHz]

727.769



020101

Bone volume fraction

0.585

Effective modulus [GPa]

8.226

Effective failure stress [MPa]

31.786

Effective failure strain [%]

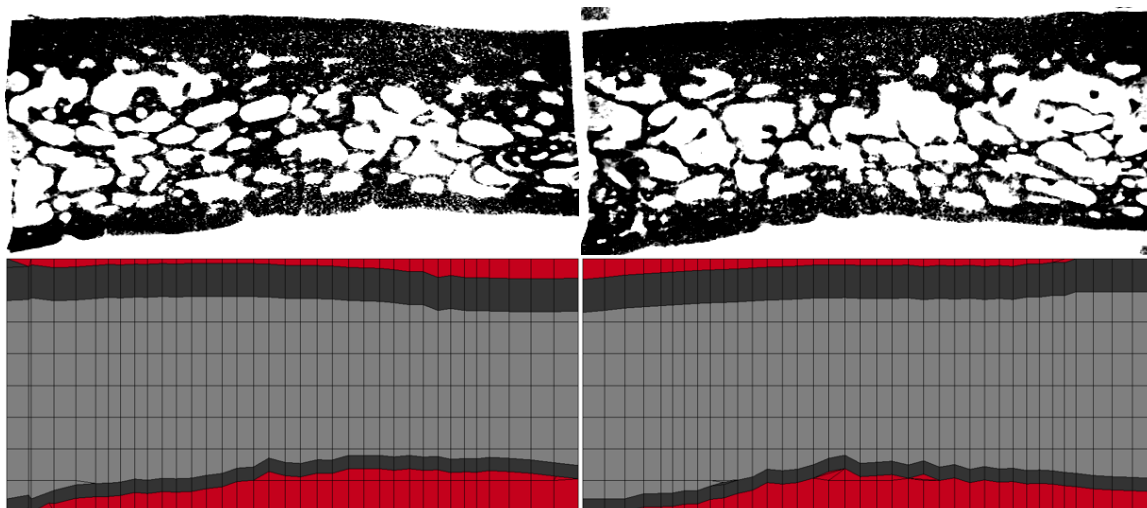
0.432

Bone modulus from BVF [GPa]

26.954

Bone modulus from μ FE [GPa]

28.365



ID – Source

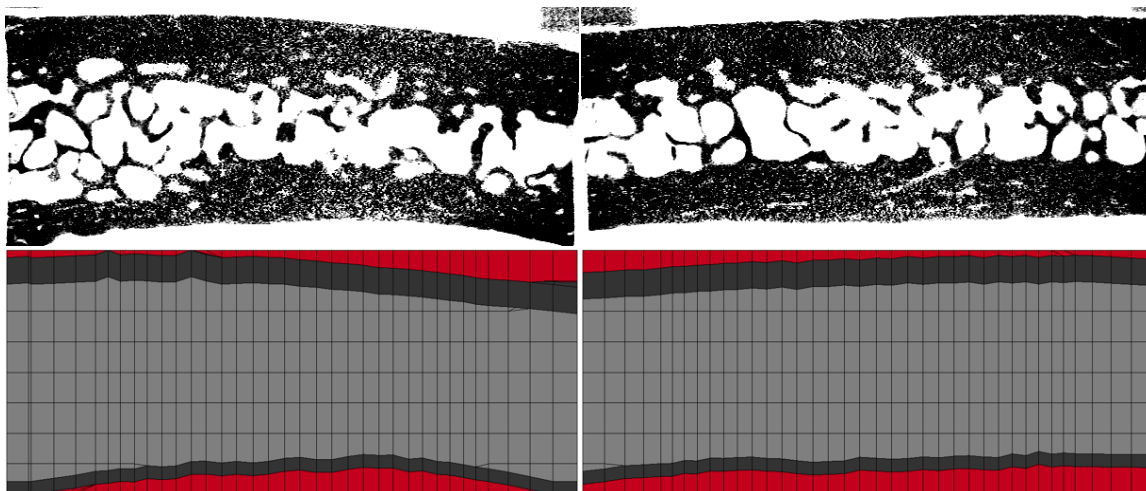
0202 – Frontal

Trabecular bone volume fraction	0.324
Effective quasi-static modulus [MPa]	360.210
Diploe quasi-static modulus [MPa]	222.559
Diploe viscoelastic modulus [MPa @ 50 kHz]	815.830



020201

Bone volume fraction	0.813
Effective modulus [GPa]	15.599
Effective failure stress [MPa]	124.581
Effective failure strain [%]	0.868
Bone modulus from BVF [GPa]	24.709
Bone modulus from μ FE [GPa]	19.688



ID – Source

0203 – Frontal

Trabecular bone volume fraction

0.266

Effective quasi-static modulus [MPa]

640.542

Diploe quasi-static modulus [MPa]

449.862

Diploe viscoelastic modulus [MPa @ 50 kHz]

779.682



020301

Bone volume fraction

0.866

Effective modulus [GPa]

14.033

Effective failure stress [MPa]

92.047

Effective failure strain [%]

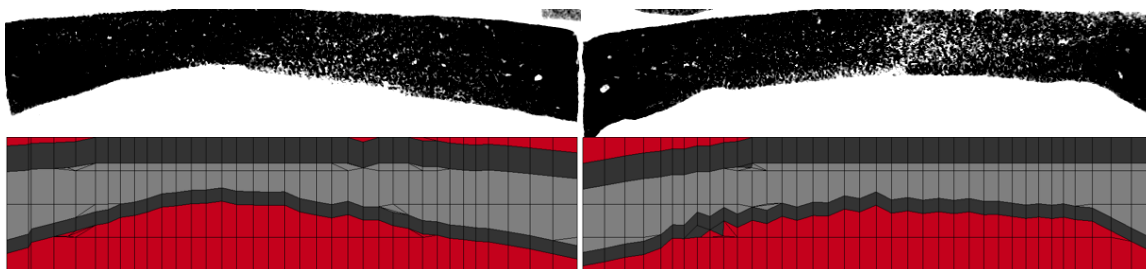
0.708

Bone modulus from BVF [GPa]

19.281

Bone modulus from μ FE [GPa]

18.544



ID – Source

0204 – Parietal

Trabecular bone volume fraction

0.944

Effective quasi-static modulus [MPa]

485.353

Diploe quasi-static modulus [MPa]

196.021

Diploe viscoelastic modulus [MPa @ 50 kHz]

532.593



020401

Bone volume fraction

0.702

Effective modulus [GPa]

9.943

Effective failure stress [MPa]

40.756

Effective failure strain [%]

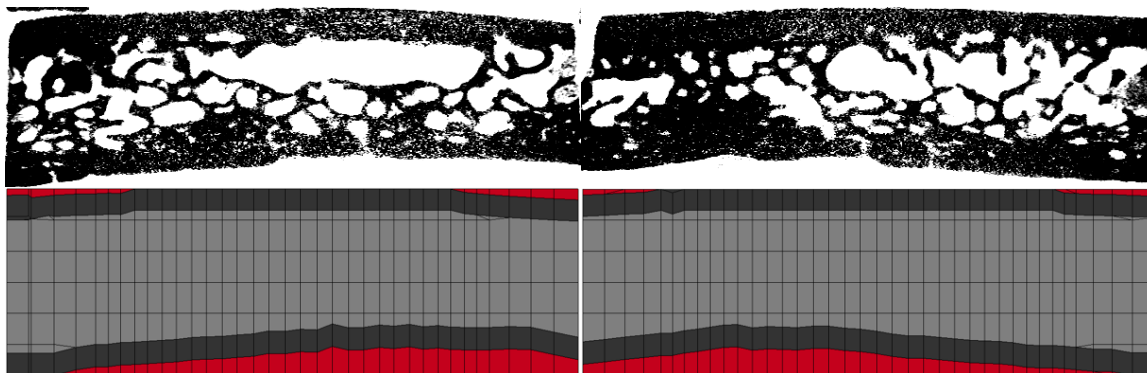
0.407

Bone modulus from BVF [GPa]

21.746

Bone modulus from μ FE [GPa]

24.315



ID – Source

0205 – Parietal

Trabecular bone volume fraction

0.352

Effective quasi-static modulus [MPa]

327.410

Diploe quasi-static modulus [MPa]

178.743

Diploe viscoelastic modulus [MPa @ 50 kHz]

715.235



020501

020502 Same depth

Bone volume fraction

0.890

0.767

Effective modulus [GPa]

10.495

9.305

Effective failure stress [MPa]

67.976

38.785

Effective failure strain [%]

0.624

0.440

Bone modulus from BVF [GPa]

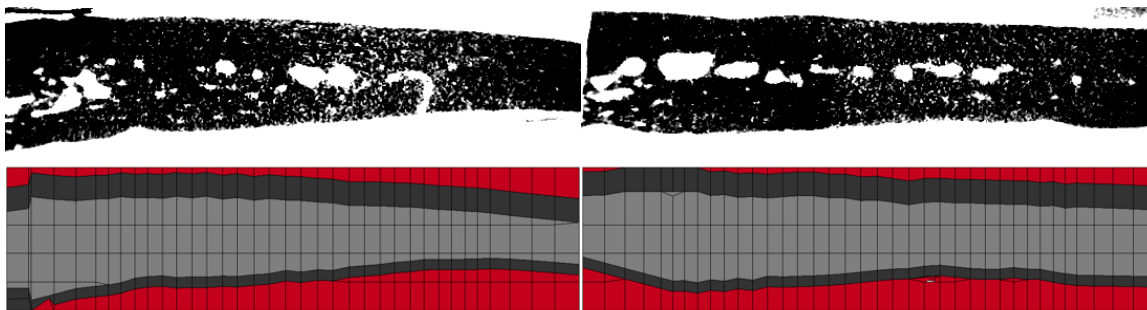
13.587

16.768

Bone modulus from μ FE [GPa]

12.036

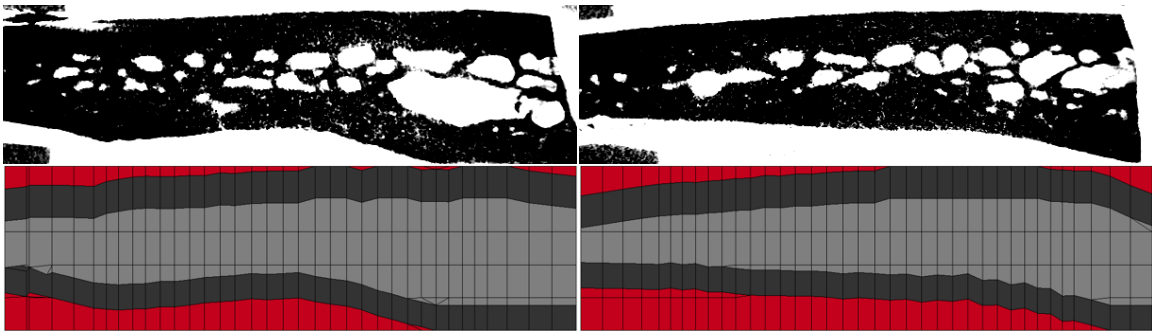
17.756



ID – Source	0206 – Parietal
Trabecular bone volume fraction	0.818
Effective quasi-static modulus [MPa]	501.365
Diploe quasi-static modulus [MPa]	247.884
Diploe viscoelastic modulus [MPa @ 50 kHz]	561.644



	020601	020602 Same depth
Bone volume fraction	0.850	0.840
Effective modulus [GPa]	14.305	14.665
Effective failure stress [MPa]	78.458	76.819
Effective failure strain [%]	0.577	0.538
Bone modulus from BVF [GPa]	20.503	21.601
Bone modulus from μ FE [GPa]	17.303	16.746



ID – Source

0208 – Parietal

Trabecular bone volume fraction

0.650

Effective quasi-static modulus [MPa]

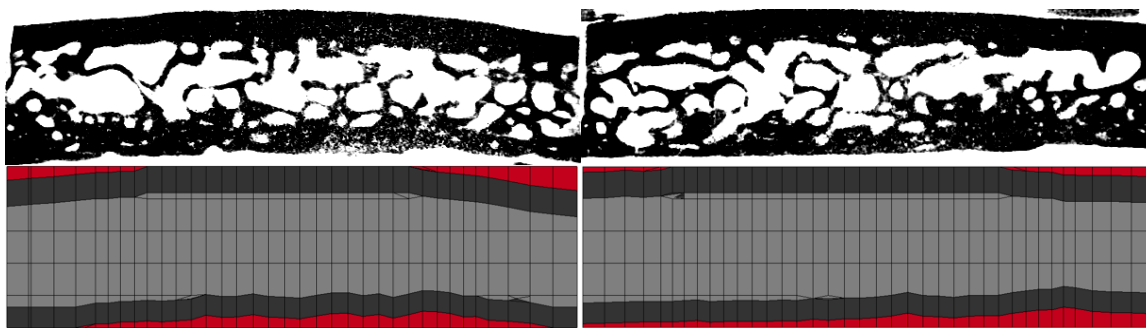
541.270

Diploe quasi-static modulus [MPa]

226.405

Diploe viscoelastic modulus [MPa @ 50 kHz]

581.661



ID – Source

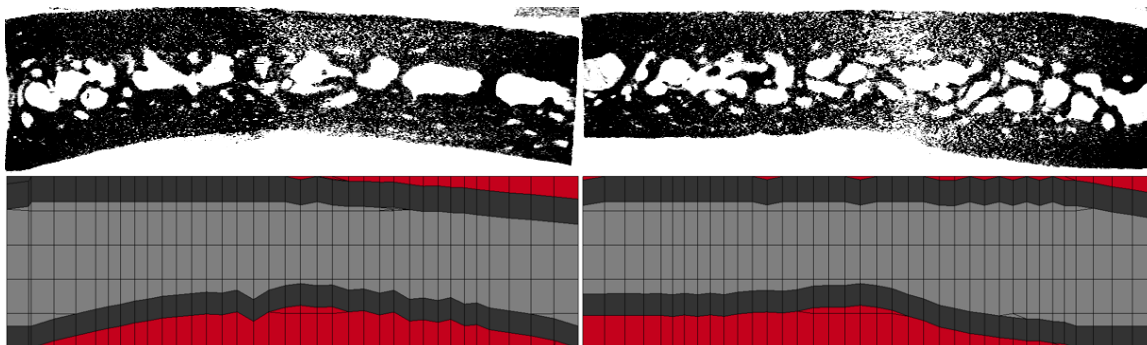
0209 – Parietal

Trabecular bone volume fraction	0.316
Effective quasi-static modulus [MPa]	384.293
Diploe quasi-static modulus [MPa]	192.002
Diploe viscoelastic modulus [MPa @ 50 kHz]	868.723



020901

Bone volume fraction	0.882
Effective modulus [GPa]	16.069
Effective failure stress [MPa]	91.024
Effective failure strain [%]	0.592
Bone modulus from BVF [GPa]	21.208
Bone modulus from μ FE [GPa]	18.502



ID – Source

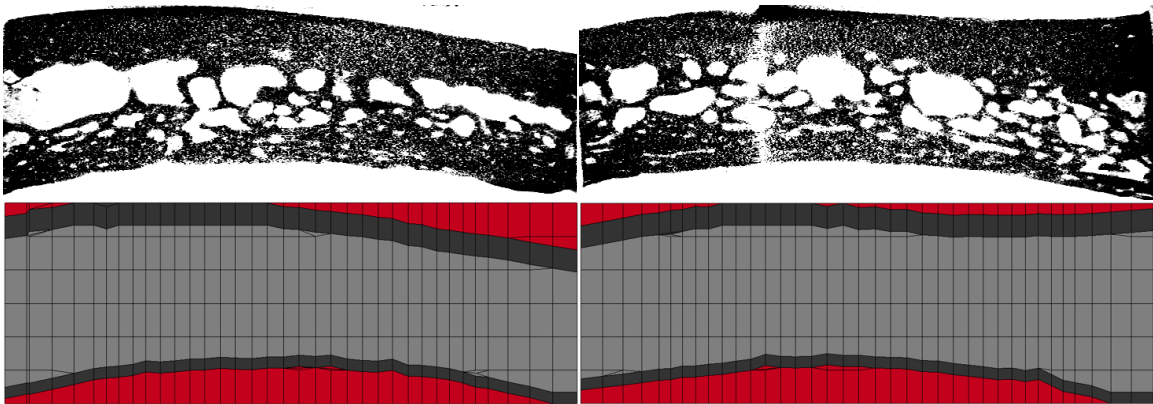
0210 – Parietal

Trabecular bone volume fraction	0.471
Effective quasi-static modulus [MPa]	615.747
Diploe quasi-static modulus [MPa]	335.509
Diploe viscoelastic modulus [MPa @ 50 kHz]	764.844



021001

Bone volume fraction	0.861
Effective modulus [GPa]	16.373
Effective failure stress [MPa]	90.148
Effective failure strain [%]	0.540
Bone modulus from BVF [GPa]	22.814
Bone modulus from μ FE [GPa]	21.494



ID – Source

0301 – Parietal

Trabecular bone volume fraction

0.367

Effective quasi-static modulus [MPa]

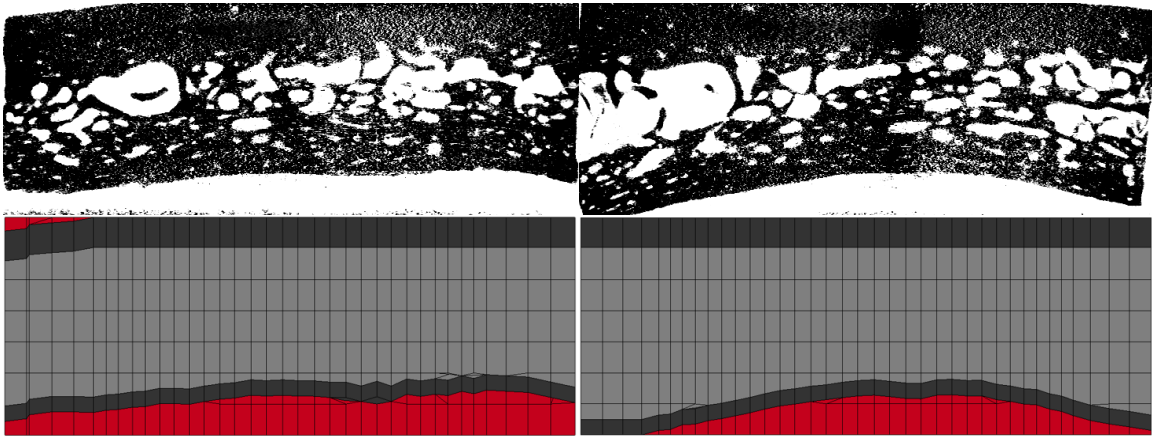
632.548

Diploe quasi-static modulus [MPa]

431.265

Diploe viscoelastic modulus [MPa @ 50 kHz]

670.937



ID – Source

0302 – Parietal

Trabecular bone volume fraction

0.346

Effective quasi-static modulus [MPa]

428.642

Diploe quasi-static modulus [MPa]

258.538

Diploe viscoelastic modulus [MPa @ 50 kHz]

1265.62



030201

Bone volume fraction

0.779

Effective modulus [GPa]

10.111

Effective failure stress [MPa]

55.927

Effective failure strain [%]

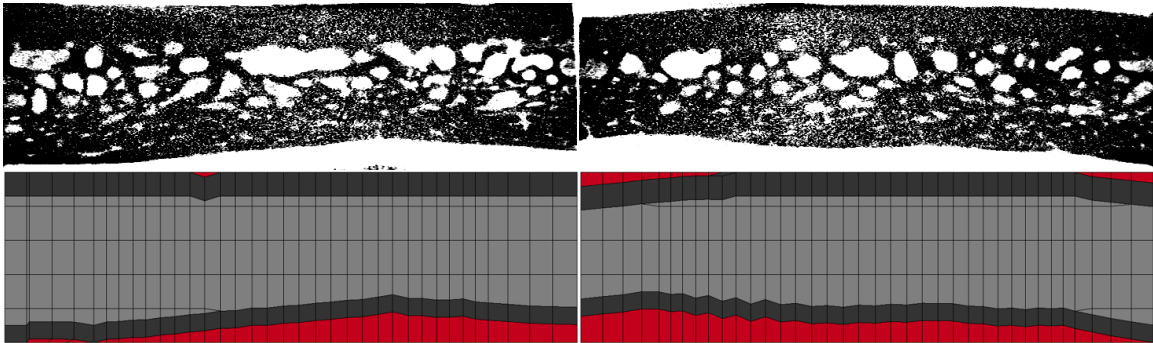
0.603

Bone modulus from BVF [GPa]

17.587

Bone modulus from μ FE [GPa]

18.353



ID – Source

0303 – Frontal

Trabecular bone volume fraction

0.574

Effective quasi-static modulus [MPa]

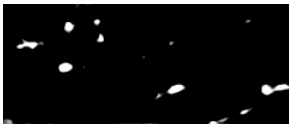
535.153

Diploe quasi-static modulus [MPa]

304.388

Diploe viscoelastic modulus [MPa @ 50 kHz]

838.114



030301

Bone volume fraction

0.847

Effective modulus [GPa]

12.716

Effective failure stress [MPa]

117.114

Effective failure strain [%]

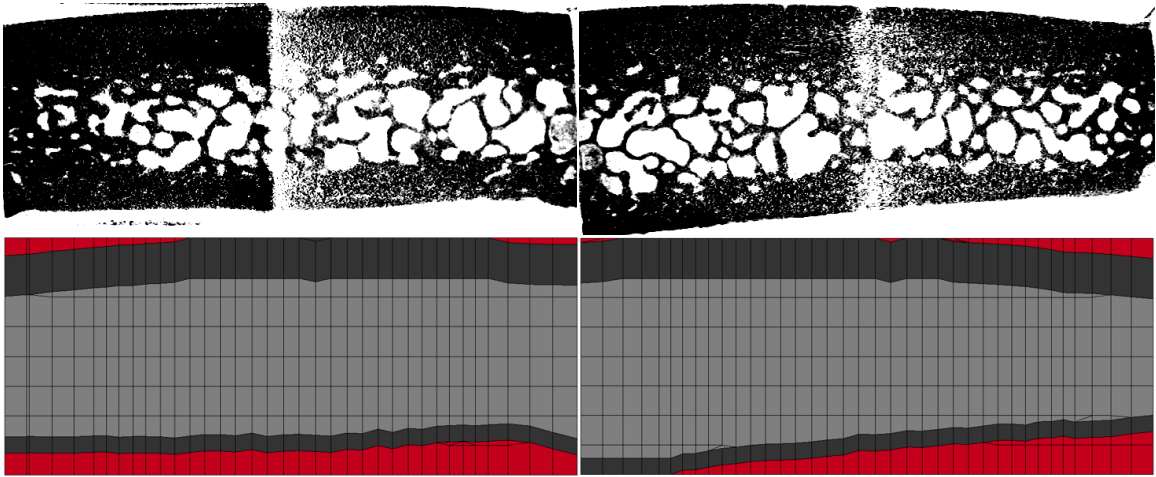
1.004

Bone modulus from BVF [GPa]

18.376

Bone modulus from μ FE [GPa]

15.759



ID – Source

0304 – Frontal

Trabecular bone volume fraction

0.406

Effective quasi-static modulus [MPa]

522.550

Diploe quasi-static modulus [MPa]

304.494

Diploe viscoelastic modulus [MPa @ 50 kHz]

na



030401

Bone volume fraction

0.855

Effective modulus [GPa]

14.218

Effective failure stress [MPa]

99.136

Effective failure strain [%]

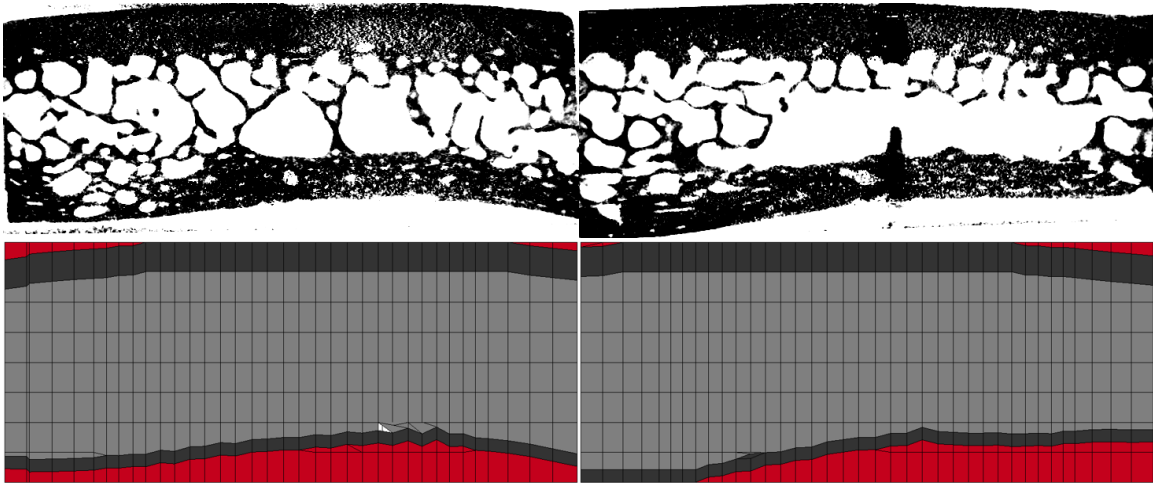
0.741

Bone modulus from BVF [GPa]

20.118

Bone modulus from μ FE [GPa]

17.844



ID – Source

0305 – Frontal

Trabecular bone volume fraction

0.157

Effective quasi-static modulus [MPa]

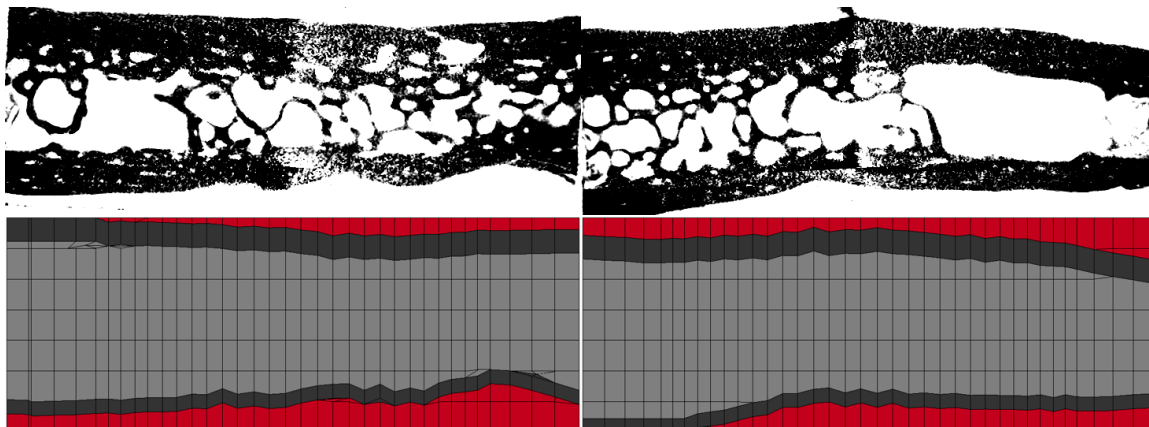
321.448

Diploe quasi-static modulus [MPa]

200.701

Diploe viscoelastic modulus [MPa @ 50 kHz]

842.559



ID – Source

0306 – Parietal

Trabecular bone volume fraction

0.201

Effective quasi-static modulus [MPa]

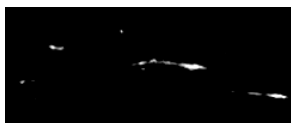
392.643

Diploe quasi-static modulus [MPa]

232.508

Diploe viscoelastic modulus [MPa @ 50 kHz]

737.975



030601

Bone volume fraction

0.880

Effective modulus [GPa]

18.845

Effective failure stress [MPa]

114.681

Effective failure strain [%]

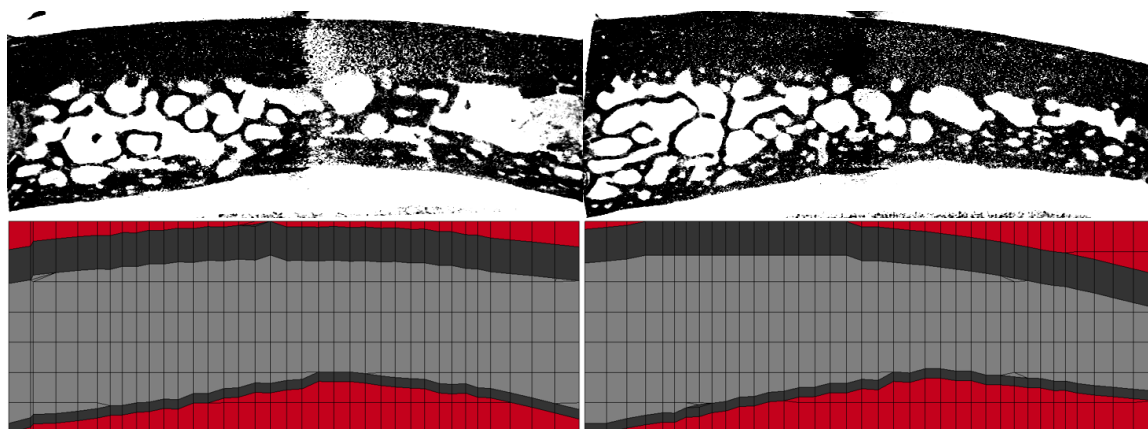
0.628

Bone modulus from BVF [GPa]

25.006

Bone modulus from μ FE [GPa]

23.134



ID – Source

0307 – Parietal

Trabecular bone volume fraction

0.331

Effective quasi-static modulus [MPa]

335.876

Diploe quasi-static modulus [MPa]

180.544

Diploe viscoelastic modulus [MPa @ 50 kHz]

663.854



030701

Bone volume fraction

0.885

Effective modulus [GPa]

17.436

Effective failure stress [MPa]

62.531

Effective failure strain [%]

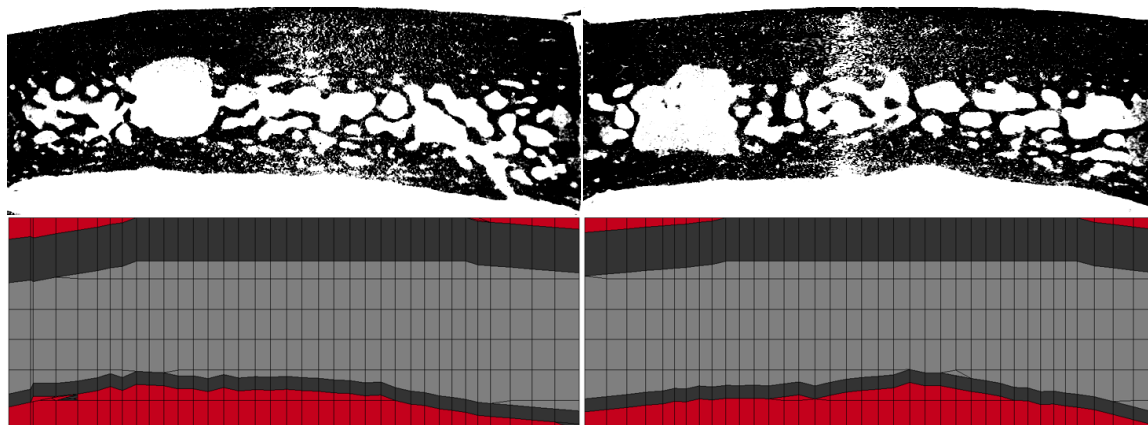
0.395

Bone modulus from BVF [GPa]

22.882

Bone modulus from μ FE [GPa]

24.187



ID – Source

0308 – Parietal

Trabecular bone volume fraction

0.405

Effective quasi-static modulus [MPa]

346.655

Diploe quasi-static modulus [MPa]

176.044

Diploe viscoelastic modulus [MPa @ 50 kHz]

699.363



030801

Bone volume fraction

0.814

Effective modulus [GPa]

12.191

Effective failure stress [MPa]

71.415

Effective failure strain [%]

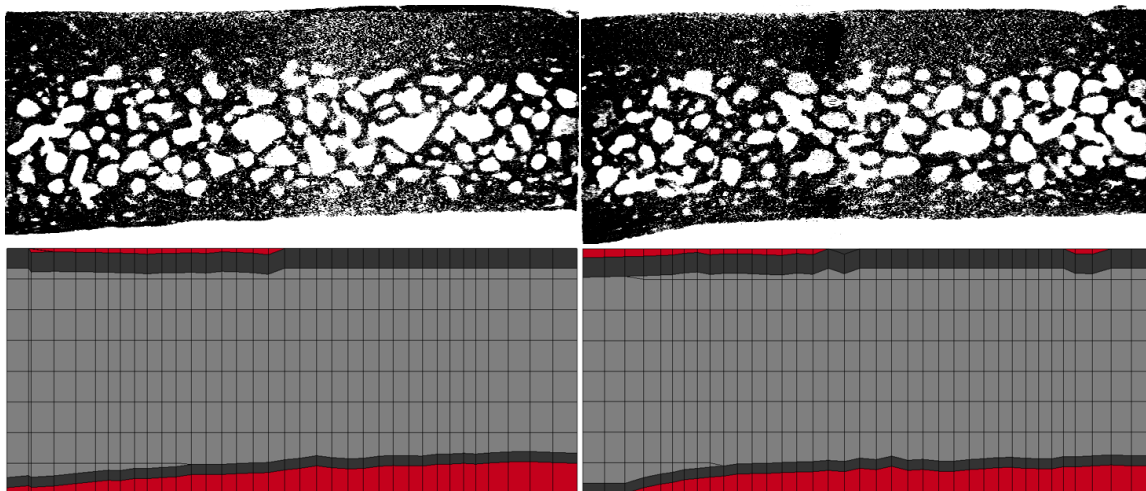
0.586

Bone modulus from BVF [GPa]

19.208

Bone modulus from μ FE [GPa]

19.144



ID – Source

0310 – Parietal

Trabecular bone volume fraction

0.468

Effective quasi-static modulus [MPa]

556.378

Diploe quasi-static modulus [MPa]

406.088

Diploe viscoelastic modulus [MPa @ 50 kHz]

935.819



031001

Bone volume fraction

0.685

Effective modulus [GPa]

5.433

Effective failure stress [MPa]

26.442

Effective failure strain [%]

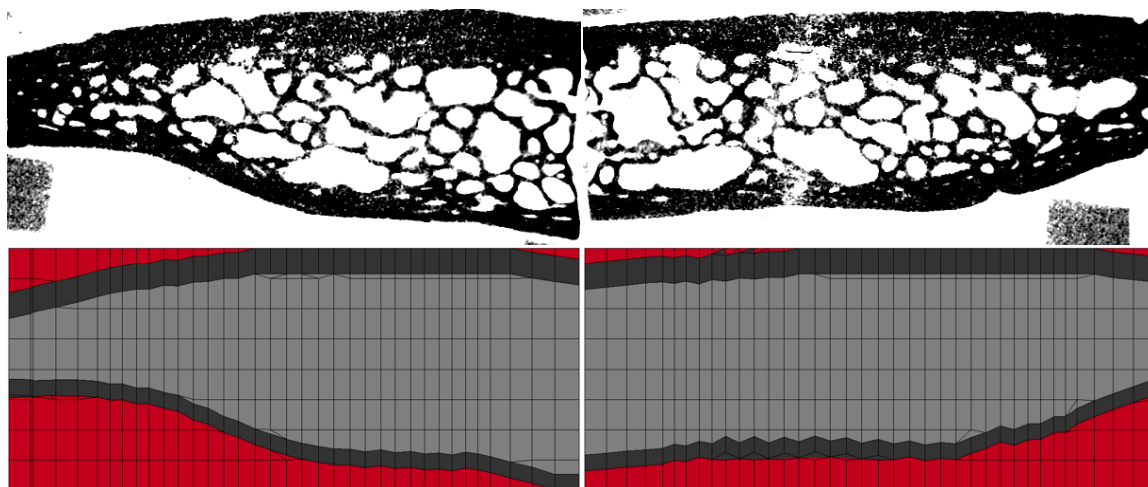
0.702

Bone modulus from BVF [GPa]

12.555

Bone modulus from μ FE [GPa]

15.677



ID – Source

0402 – Parietal

Trabecular bone volume fraction

0.345

Effective quasi-static modulus [MPa]

379.116

Diploe quasi-static modulus [MPa]

220.758

Diploe viscoelastic modulus [MPa @ 50 kHz]

821.874



040201

040202 Same depth

Bone volume fraction

0.866

0.666

Effective modulus [GPa]

13.492

8.210

Effective failure stress [MPa]

69.308

50.330

Effective failure strain [%]

0.611

0.638

Bone modulus from BVF [GPa]

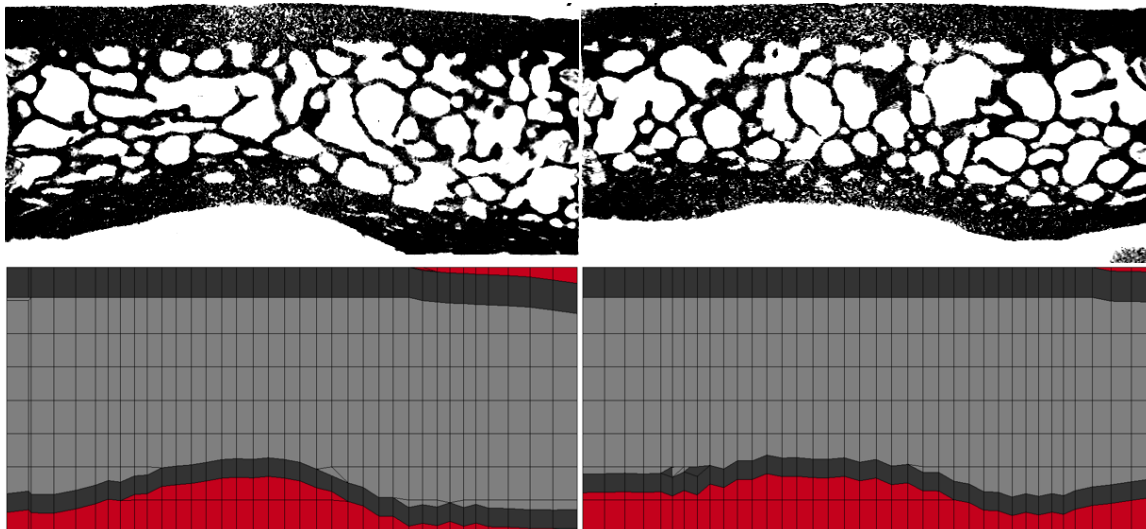
18.572

20.175

Bone modulus from μ FE [GPa]

20.918

26.215



ID – Source

0403 – Parietal

Trabecular bone volume fraction

0.388

Effective quasi-static modulus [MPa]

615.034

Diploe quasi-static modulus [MPa]

421.264

Diploe viscoelastic modulus [MPa @ 50 kHz]

605.981



040301

Bone volume fraction

0.819

Effective modulus [GPa]

11.645

Effective failure stress [MPa]

59.048

Effective failure strain [%]

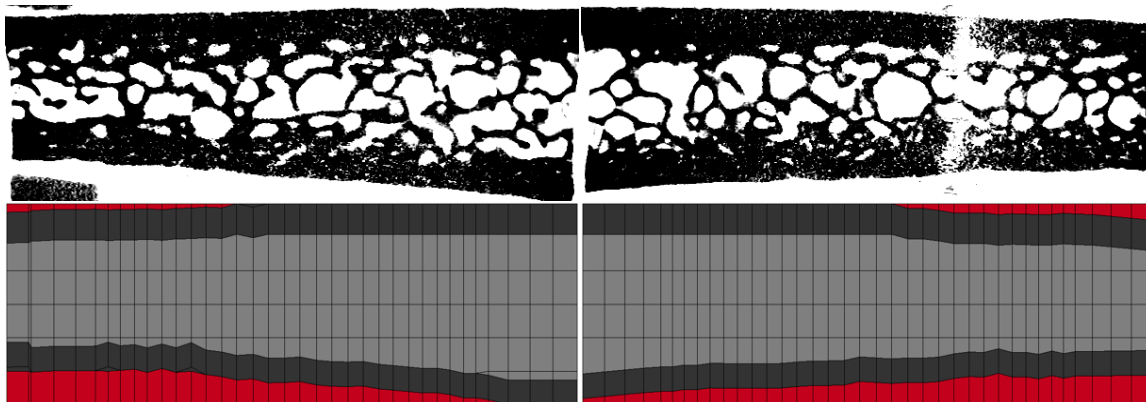
0.484

Bone modulus from BVF [GPa]

18.100

Bone modulus from μ FE [GPa]

18.966



ID – Source

0404 – Frontal

Trabecular bone volume fraction

0.358

Effective quasi-static modulus [MPa]

402.286

Diploe quasi-static modulus [MPa]

205.906

Diploe viscoelastic modulus [MPa @ 50 kHz]

617.026



040401

Bone volume fraction

0.881

Effective modulus [GPa]

12.059

Effective failure stress [MPa]

55.808

Effective failure strain [%]

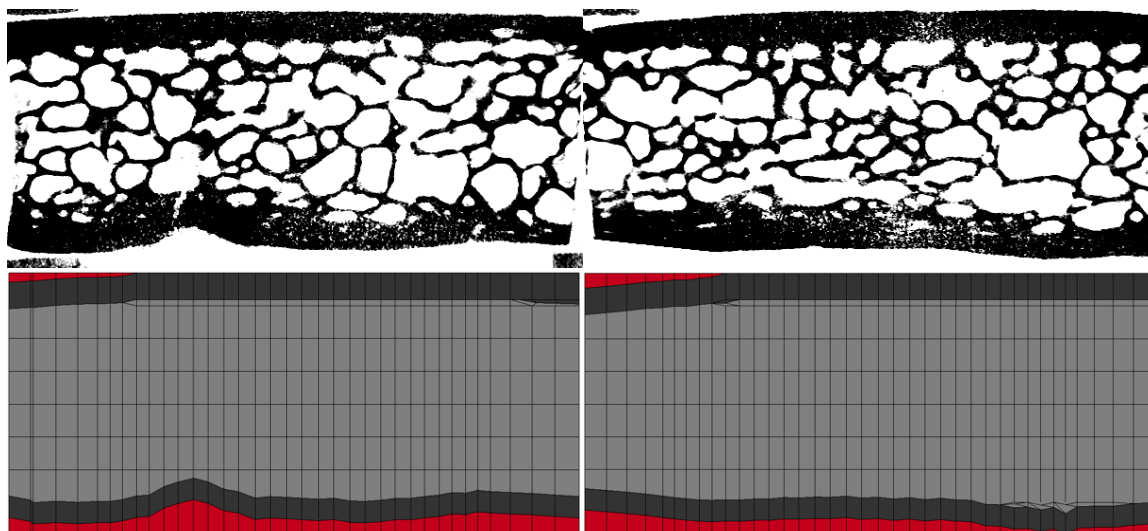
0.514

Bone modulus from BVF [GPa]

15.961

Bone modulus from μ FE [GPa]

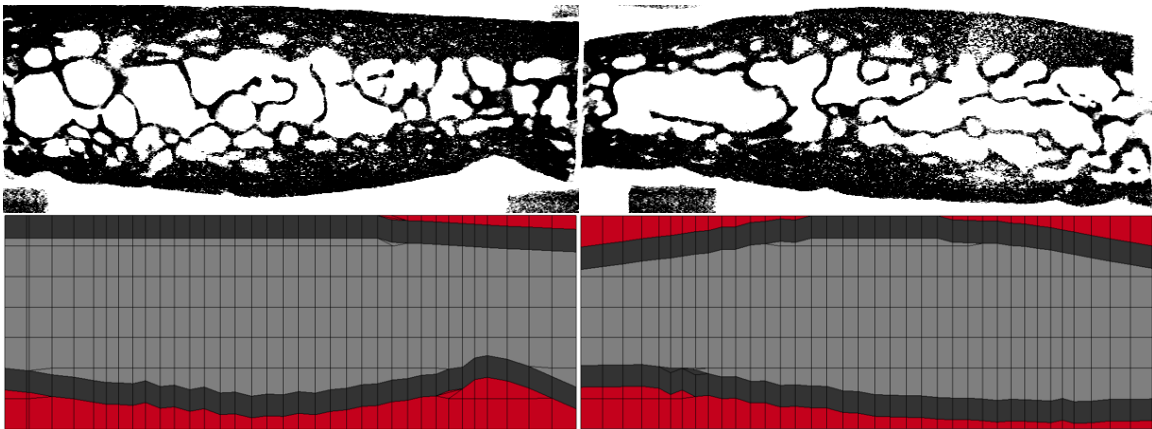
18.531



ID – Source	0405 – Frontal
Trabecular bone volume fraction	0.296
Effective quasi-static modulus [MPa]	265.256
Diploe quasi-static modulus [MPa]	168.195
Diploe viscoelastic modulus [MPa @ 50 kHz]	951.418



040501	
Bone volume fraction	0.904
Effective modulus [GPa]	13.847
Effective failure stress [MPa]	80.886
Effective failure strain [%]	0.576
Bone modulus from BVF [GPa]	17.306
Bone modulus from μ FE [GPa]	15.706



ID – Source

0406 – Frontal

Trabecular bone volume fraction

0.265

Effective quasi-static modulus [MPa]

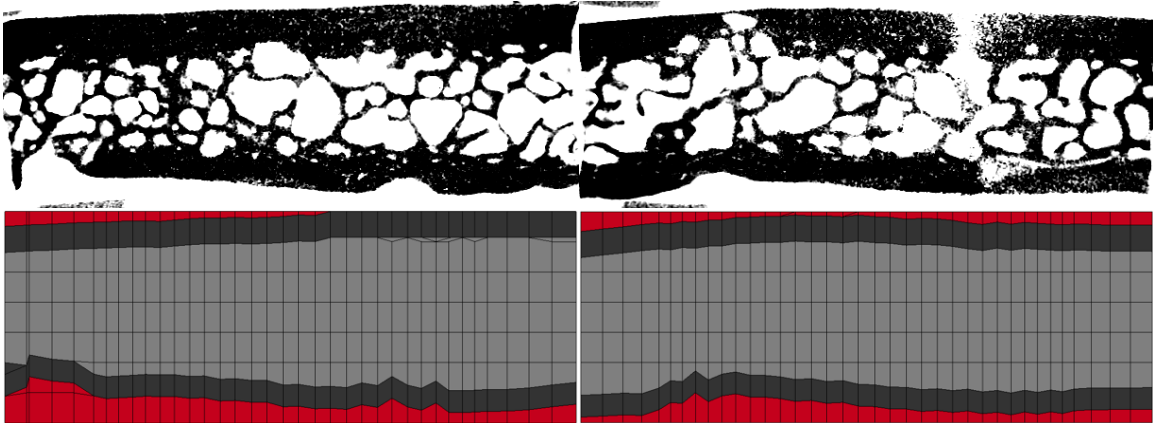
407.823

Diploe quasi-static modulus [MPa]

229.659

Diploe viscoelastic modulus [MPa @ 50 kHz]

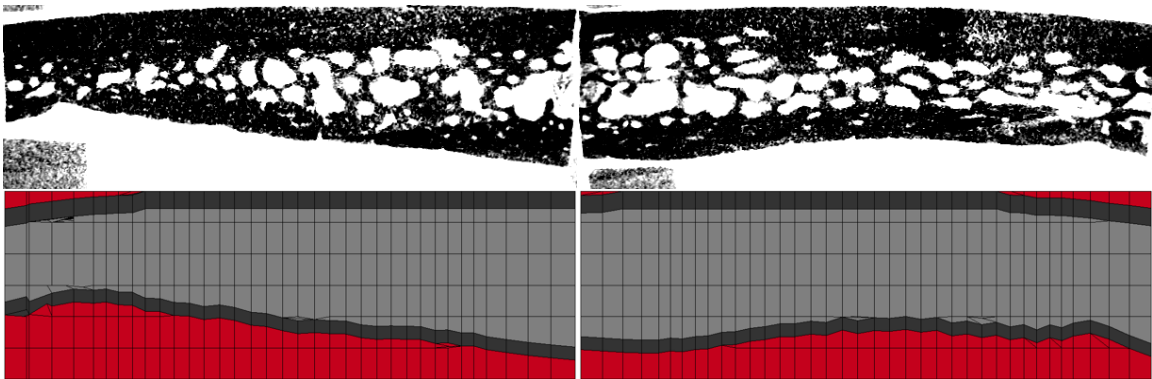
653.116



ID – Source	0407 – Parietal
Trabecular bone volume fraction	0.259
Effective quasi-static modulus [MPa]	363.953
Diploe quasi-static modulus [MPa]	199.461
Diploe viscoelastic modulus [MPa @ 50 kHz]	736.012



	040701	040702 Same depth
Bone volume fraction	0.825	0.842
Effective modulus [GPa]	8.812	12.616
Effective failure stress [MPa]	45.064	57.056
Effective failure strain [%]	0.596	0.478
Bone modulus from BVF [GPa]	13.478	18.448
Bone modulus from μ FE [GPa]	16.664	18.041



ID – Source

0408 – Parietal

Trabecular bone volume fraction

0.474

Effective quasi-static modulus [MPa]

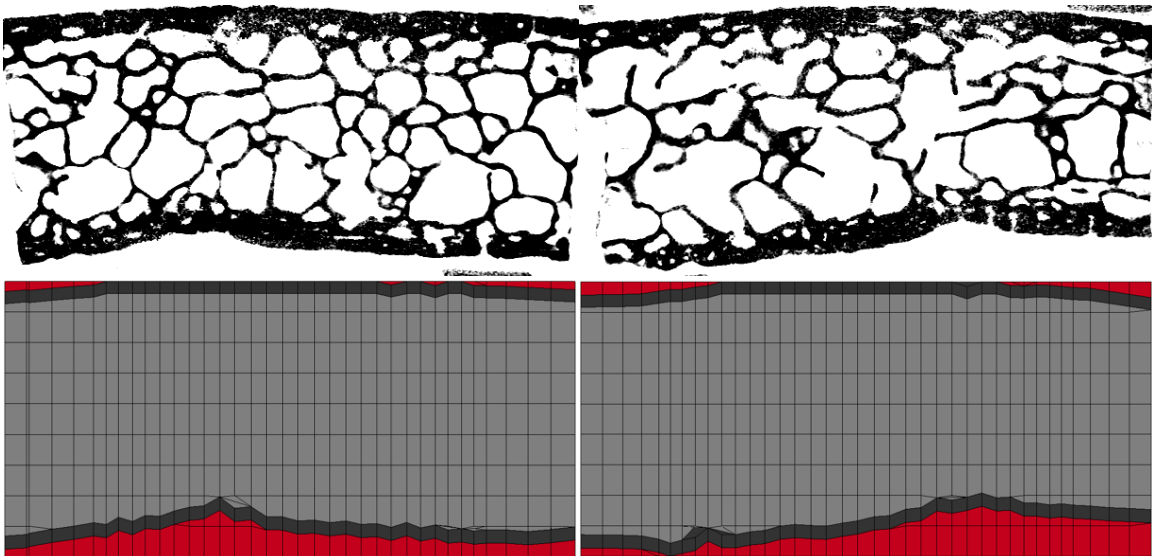
555.800

Diploe quasi-static modulus [MPa]

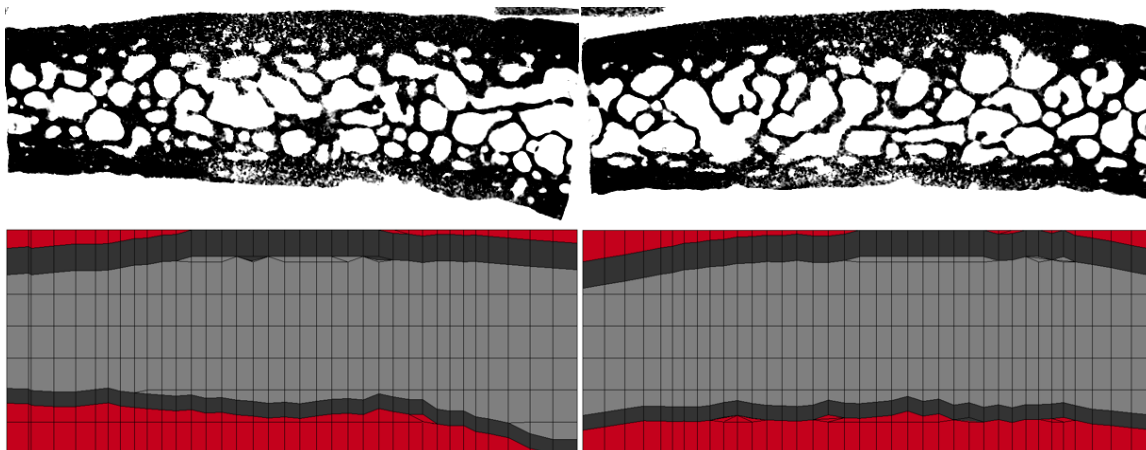
359.673

Diploe viscoelastic modulus [MPa @ 50 kHz]

646.088



ID – Source	0409 – Parietal
Trabecular bone volume fraction	0.206
Effective quasi-static modulus [MPa]	281.324
Diploe quasi-static modulus [MPa]	204.970
Diploe viscoelastic modulus [MPa @ 50 kHz]	762.850



ID – Source

0410 – Parietal

Trabecular bone volume fraction

0.305

Effective quasi-static modulus [MPa]

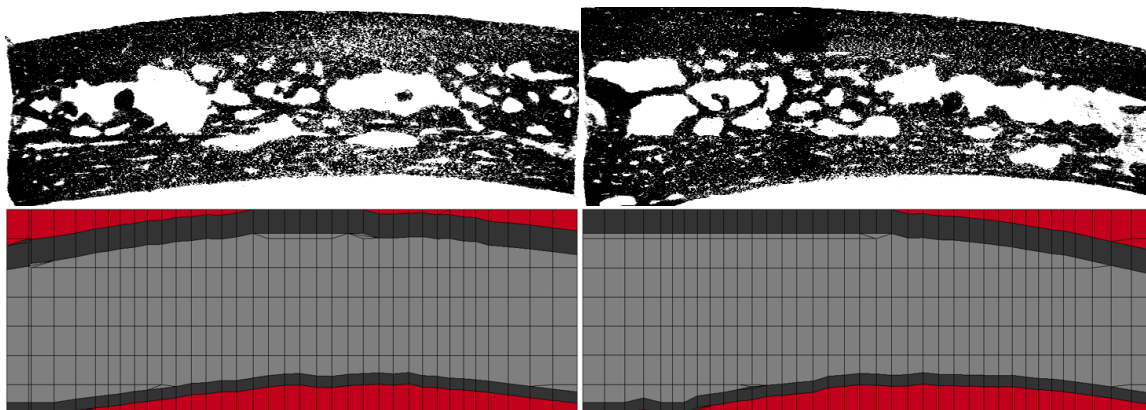
341.299

Diploe quasi-static modulus [MPa]

193.425

Diploe viscoelastic modulus [MPa @ 50 kHz]

943.939



ID – Source

0501 – Parietal

Trabecular bone volume fraction

0.414

Effective quasi-static modulus [MPa]

351.625

Diploe quasi-static modulus [MPa]

214.132

Diploe viscoelastic modulus [MPa @ 50 kHz]

538.887



050101

050102 Same depth

Bone volume fraction

0.877

0.756

Effective modulus [GPa]

18.045

7.863

Effective failure stress [MPa]

91.436

42.605

Effective failure strain [%]

0.499

0.592

Bone modulus from BVF [GPa]

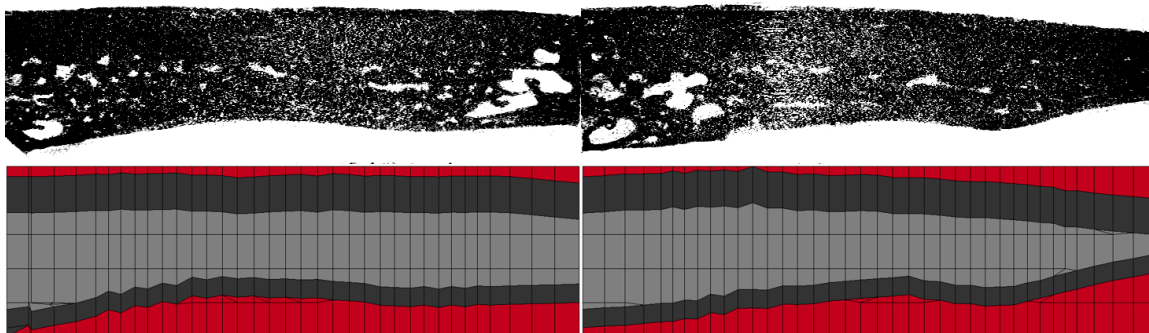
24.121

14.627

Bone modulus from μ FE [GPa]

21.446

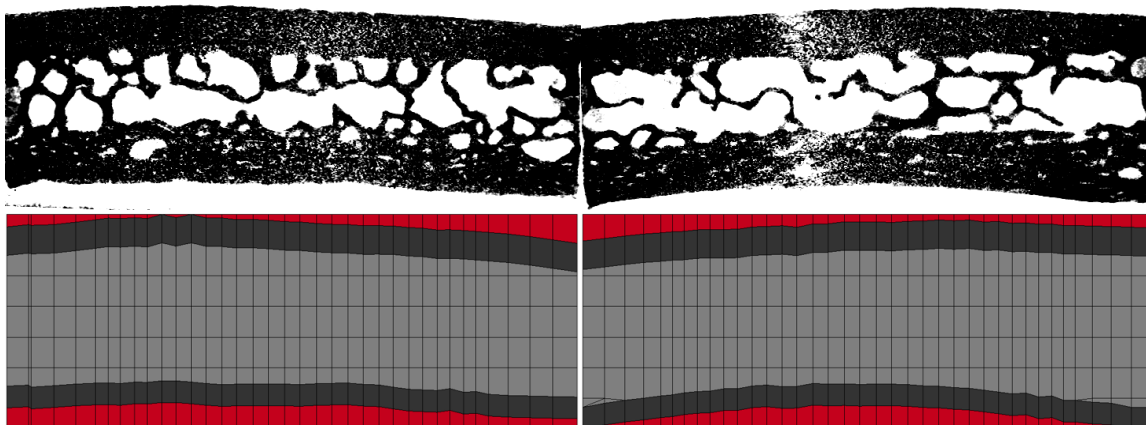
17.059



ID – Source	0502 – Parietal
Trabecular bone volume fraction	0.856
Effective quasi-static modulus [MPa]	390.684
Diploe quasi-static modulus [MPa]	157.472
Diploe viscoelastic modulus [MPa @ 50 kHz]	na



050201	
Bone volume fraction	0.866
Effective modulus [GPa]	12.297
Effective failure stress [MPa]	80.087
Effective failure strain [%]	0.635
Bone modulus from BVF [GPa]	16.898
Bone modulus from μ FE [GPa]	16.156



ID – Source

0503 – Parietal

Trabecular bone volume fraction

0.273

Effective quasi-static modulus [MPa]

367.111

Diploe quasi-static modulus [MPa]

201.527

Diploe viscoelastic modulus [MPa @ 50 kHz]

709.161



050301

Bone volume fraction

0.868

Effective modulus [GPa]

16.766

Effective failure stress [MPa]

83.072

Effective failure strain [%]

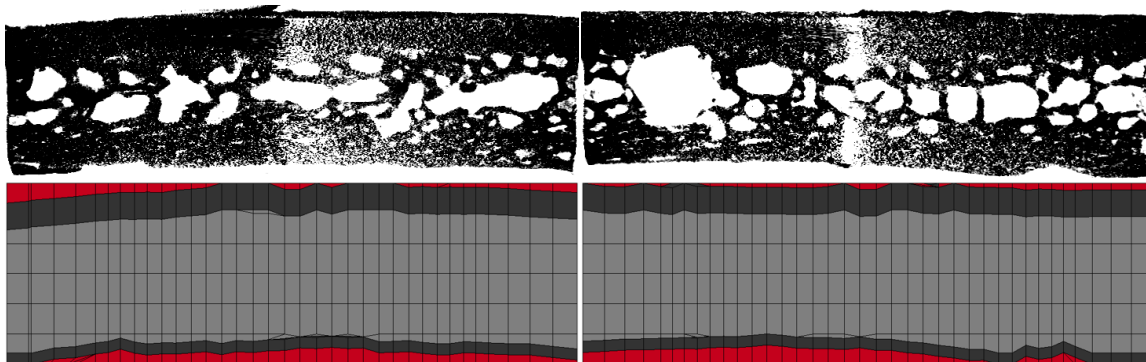
0.465

Bone modulus from BVF [GPa]

22.968

Bone modulus from μ FE [GPa]

17.549



ID – Source

0504 – Frontal

Trabecular bone volume fraction

0.404

Effective quasi-static modulus [MPa]

431.652

Diploe quasi-static modulus [MPa]

257.755

Diploe viscoelastic modulus [MPa @ 50 kHz]

1038.377



050401

050402 Same depth

Bone volume fraction

0.793

0.816

Effective modulus [GPa]

11.730

13.487

Effective failure stress [MPa]

43.763

55.950

Effective failure strain [%]

0.413

0.420

Bone modulus from BVF [GPa]

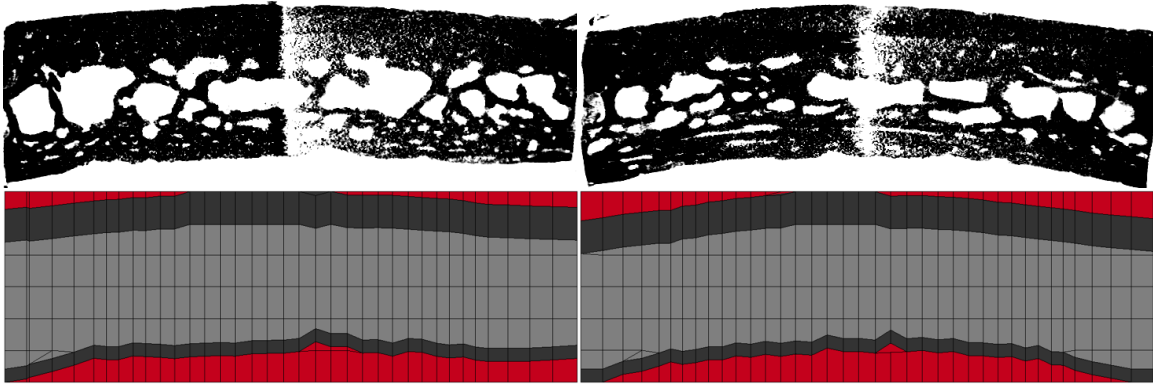
19.583

21.182

Bone modulus from μ FE [GPa]

15.685

16.905



ID – Source

0505 – Parietal

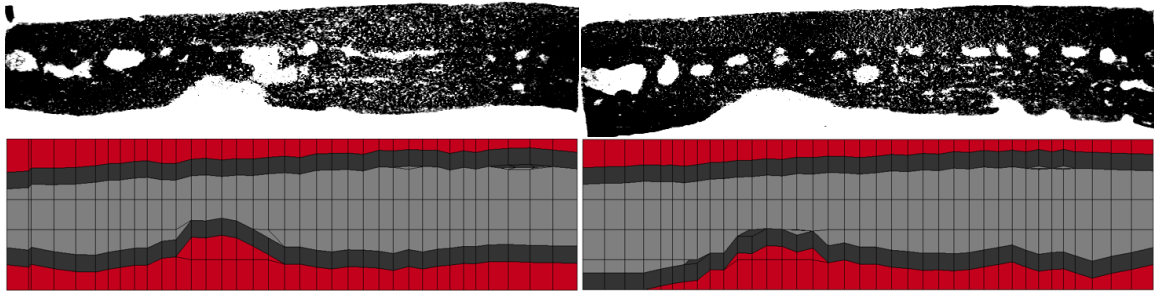
Trabecular bone volume fraction	0.489
Effective quasi-static modulus [MPa]	362.854
Diploe quasi-static modulus [MPa]	190.516
Diploe viscoelastic modulus [MPa @ 50 kHz]	1010.549



050501

050502 Same depth

Bone volume fraction	0.863	0.806
Effective modulus [GPa]	11.653	11.879
Effective failure stress [MPa]	54.713	44.633
Effective failure strain [%]	0.446	0.391
Bone modulus from BVF [GPa]	16.139	19.178
Bone modulus from μ FE [GPa]	14.015	16.588



ID – Source

0506 – Frontal

Trabecular bone volume fraction

0.822

Effective quasi-static modulus [MPa]

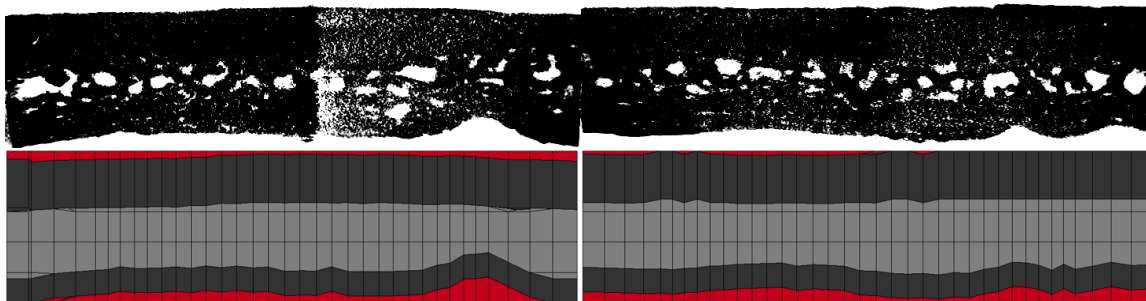
423.969

Diploe quasi-static modulus [MPa]

208.646

Diploe viscoelastic modulus [MPa @ 50 kHz]

763.434



ID – Source

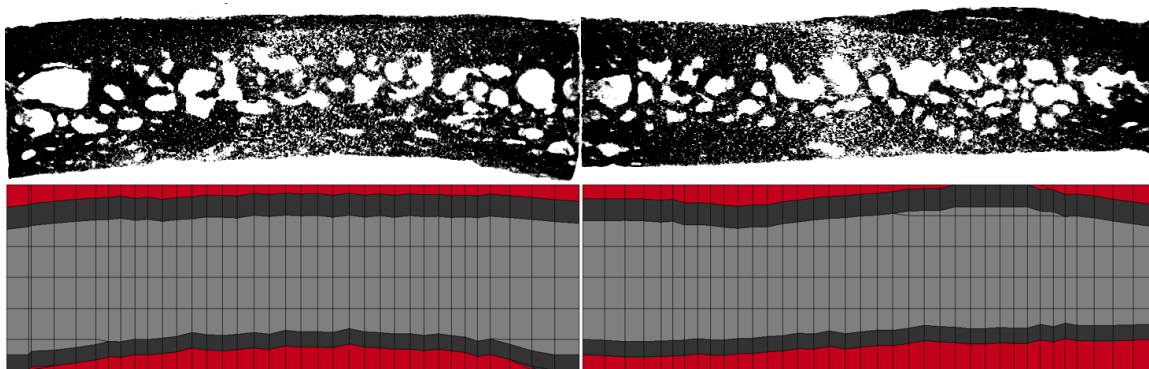
0507 – Frontal

Trabecular bone volume fraction	0.825
Effective quasi-static modulus [MPa]	512.489
Diploe quasi-static modulus [MPa]	174.758
Diploe viscoelastic modulus [MPa @ 50 kHz]	621.192



050701

Bone volume fraction	0.839
Effective modulus [GPa]	15.488
Effective failure stress [MPa]	82.358
Effective failure strain [%]	0.498
Bone modulus from BVF [GPa]	22.834
Bone modulus from μ FE [GPa]	20.468



ID – Source

0508 – Parietal

Trabecular bone volume fraction

0.470

Effective quasi-static modulus [MPa]

457.372

Diploe quasi-static modulus [MPa]

267.706

Diploe viscoelastic modulus [MPa @ 50 kHz]

855.211



050801

050802 Different depth

050803 Same depth

050804 Different depth

Bone volume fraction

0.856

0.838

0.883

0.865

Effective modulus [GPa]

14.446

17.389

15.732

18.838

Effective failure stress [MPa]

61.819

87.342

68.486

76.931

Effective failure strain [%]

0.411

0.519

0.441

0.341

Bone modulus from BVF [GPa]

20.405

25.726

20.748

25.995

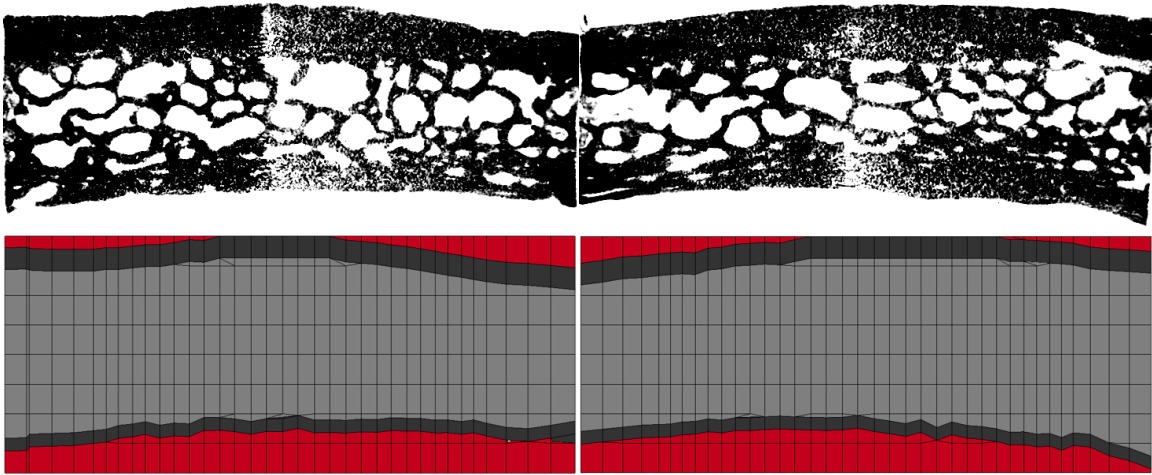
Bone modulus from μ FE [GPa]

19.580

22.667

17.447

21.506



ID – Source

0509 – Parietal

Trabecular bone volume fraction

0.368

Effective quasi-static modulus [MPa]

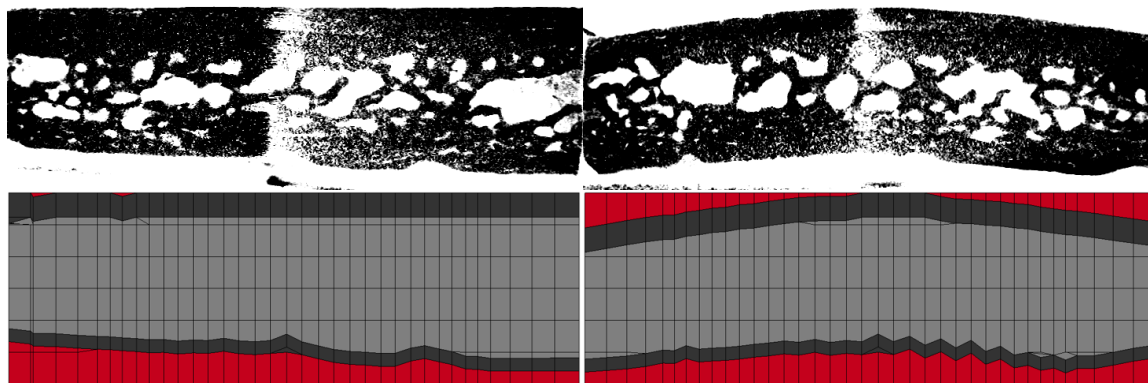
489.773

Diploe quasi-static modulus [MPa]

329.965

Diploe viscoelastic modulus [MPa @ 50 kHz]

1232.724



ID – Source

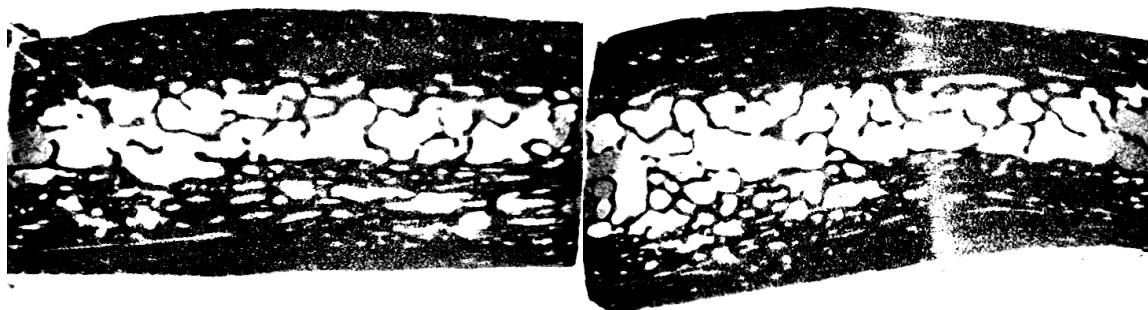
0510 – Parietal

Trabecular bone volume fraction	0.496
Effective quasi-static modulus [MPa]	555.203
Diploe quasi-static modulus [MPa]	347.367
Diploe viscoelastic modulus [MPa @ 50 kHz]	632.728



051001

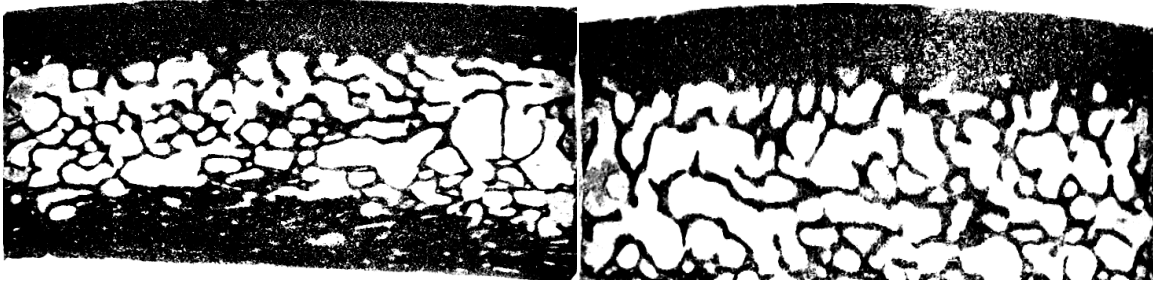
Bone volume fraction	0.758
Effective modulus [GPa]	7.428
Effective failure stress [MPa]	34.347
Effective failure strain [%]	0.455
Bone modulus from BVF [GPa]	13.707
Bone modulus from μ FE [GPa]	14.878



ID – Source	0602 – Parietal
Trabecular bone volume fraction	0.255
Effective quasi-static modulus [MPa]	288.706
Diploe quasi-static modulus [MPa]	180.739
Diploe viscoelastic modulus [MPa @ 50 kHz]	665.227



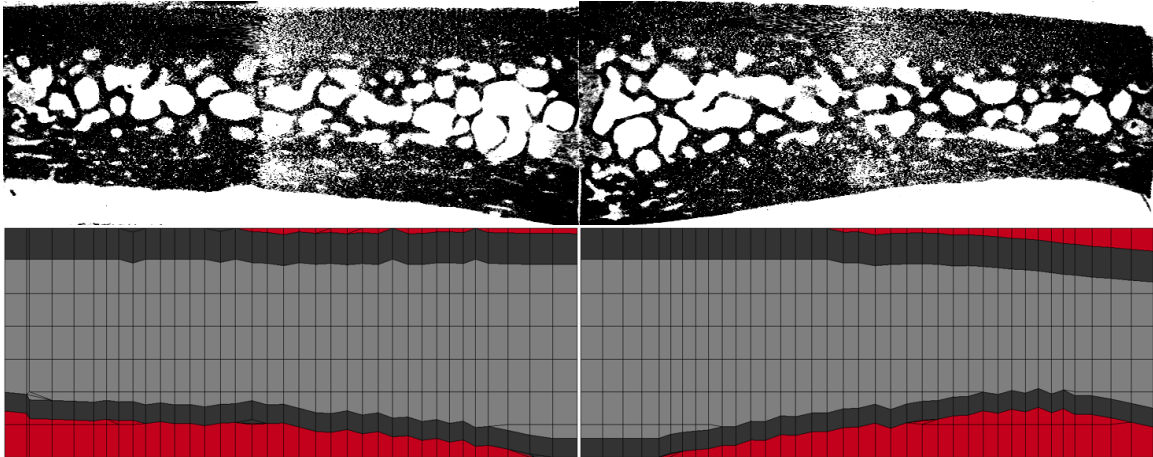
060201	060202 Different depth	060203 Same depth	
Bone volume fraction	0.875	0.747	0.853
Effective modulus [GPa]	15.602	10.941	8.905
Effective failure stress [MPa]	64.900	53.363	53.826
Effective failure strain [%]	0.396	0.546	0.655
Bone modulus from BVF [GPa]	20.957	20.882	12.679
Bone modulus from μ FE [GPa]	20.022	22.807	12.805



ID – Source	0603 – Parietal
Trabecular bone volume fraction	0.276
Effective quasi-static modulus [MPa]	439.160
Diploe quasi-static modulus [MPa]	292.827
Diploe viscoelastic modulus [MPa @ 50 kHz]	1300.797



060301	060302 Same depth	060303 Different depth	
Bone volume fraction	0.780	0.856	0.734
Effective modulus [GPa]	8.277	14.452	9.678
Effective failure stress [MPa]	65.543	80.417	40.488
Effective failure strain [%]	0.636	0.572	0.429
Bone modulus from BVF [GPa]	14.367	20.396	19.192
Bone modulus from μ FE [GPa]	14.454	18.313	19.450



ID – Source

0604 – Parietal

Trabecular bone volume fraction

0.378

Effective quasi-static modulus [MPa]

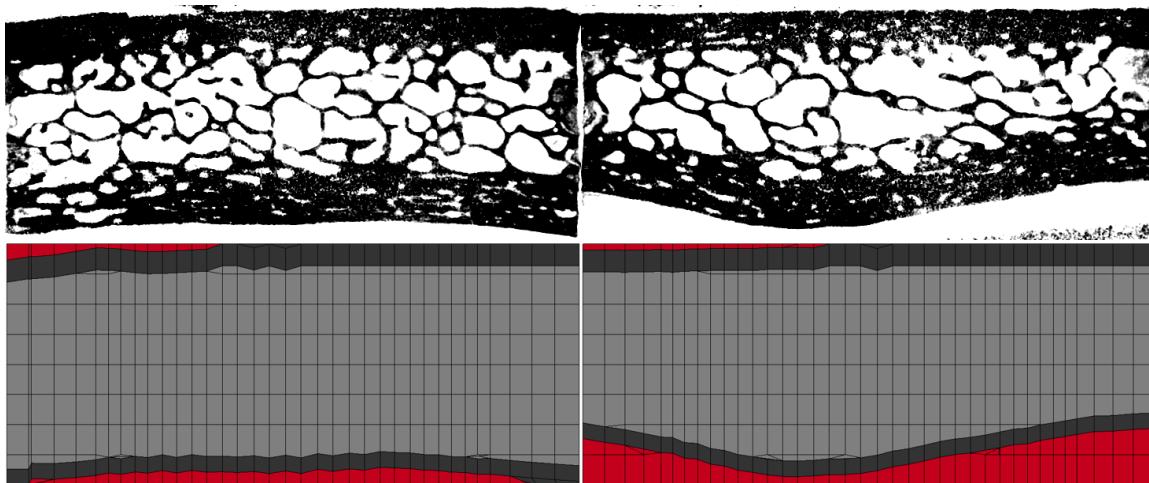
404.878

Diploe quasi-static modulus [MPa]

236.751

Diploe viscoelastic modulus [MPa @ 50 kHz]

848.266



ID – Source

0605 – Frontal

Trabecular bone volume fraction

0.219

Effective quasi-static modulus [MPa]

311.762

Diploe quasi-static modulus [MPa]

199.041

Diploe viscoelastic modulus [MPa @ 50 kHz]

1545.862



060501

Bone volume fraction

0.785

Effective modulus [GPa]

9.973

Effective failure stress [MPa]

66.101

Effective failure strain [%]

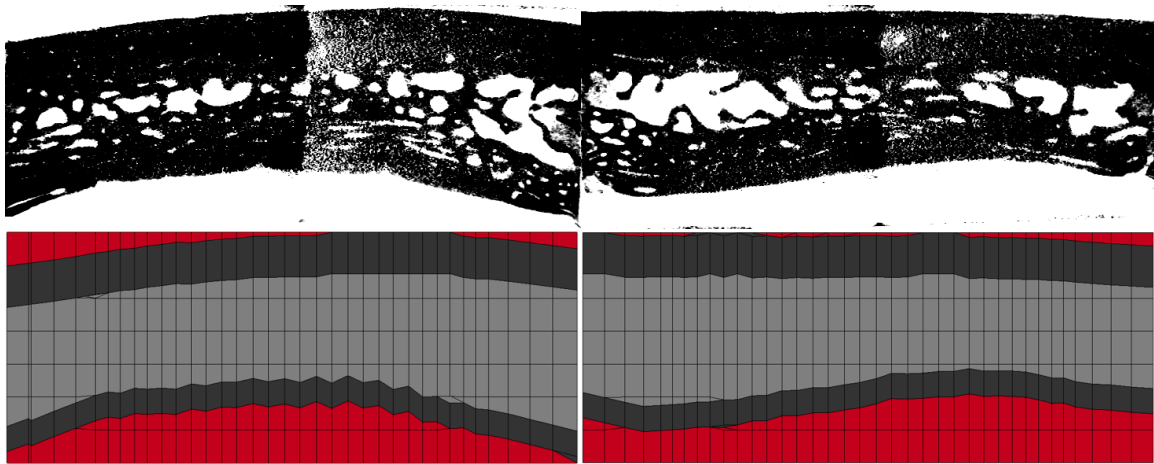
0.365

Bone modulus from BVF [GPa]

17.031

Bone modulus from μ FE [GPa]

15.718



ID – Source

0606 – Parietal

Trabecular bone volume fraction

0.514

Effective quasi-static modulus [MPa]

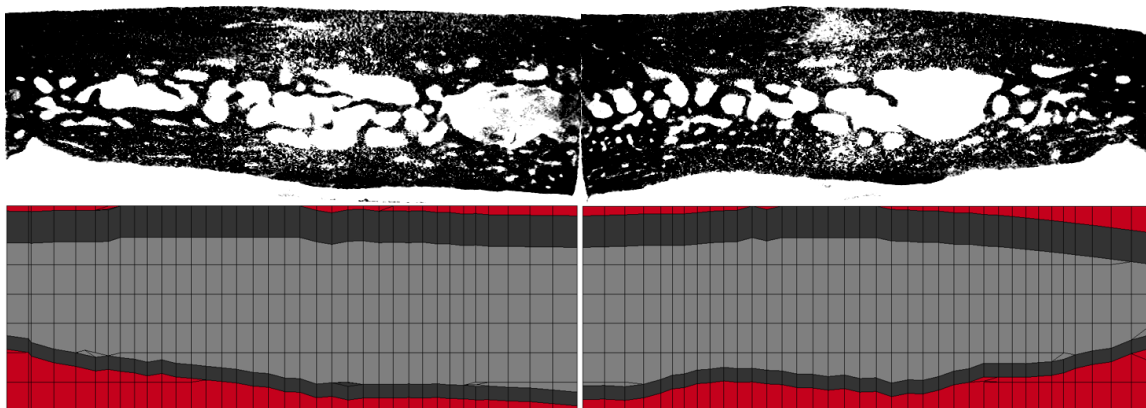
363.410

Diploe quasi-static modulus [MPa]

167.096

Diploe viscoelastic modulus [MPa @ 50 kHz]

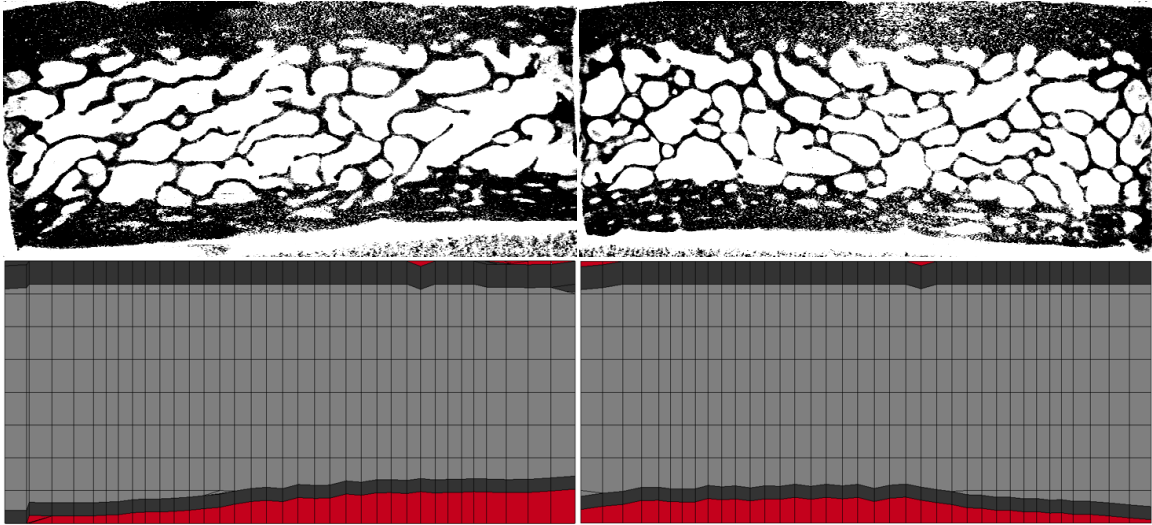
847.270



ID – Source	0608 – Parietal
Trabecular bone volume fraction	0.454
Effective quasi-static modulus [MPa]	390.991
Diploe quasi-static modulus [MPa]	215.236
Diploe viscoelastic modulus [MPa @ 50 kHz]	1286.281



060801	060802 Same depth	
Bone volume fraction	0.875	0.886
Effective modulus [GPa]	20.551	10.484
Effective failure stress [MPa]	127.622	62.543
Effective failure strain [%]	0.572	0.555
Bone modulus from BVF [GPa]	27.656	13.707
Bone modulus from μ FE [GPa]	25.512	12.466



ID – Source

0609 – Frontal

Trabecular bone volume fraction

0.212

Effective quasi-static modulus [MPa]

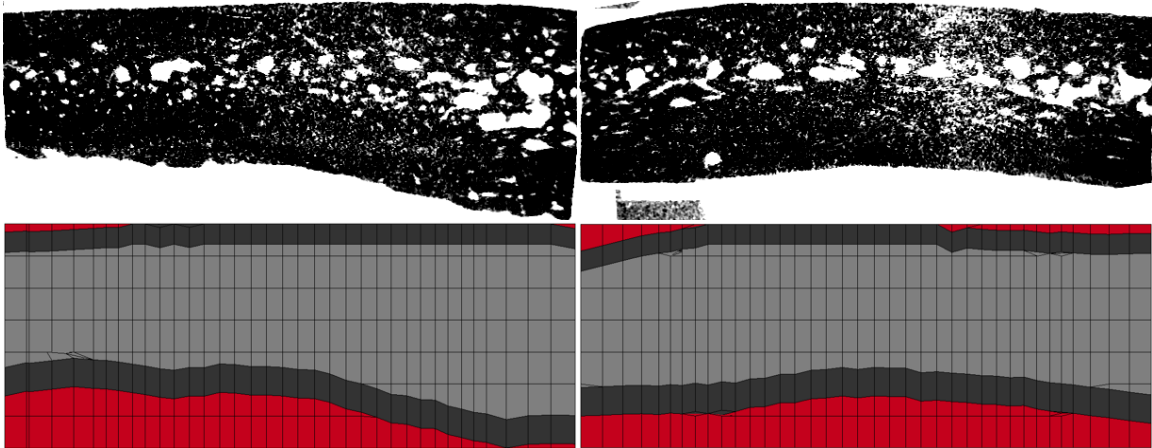
269.556

Diploe quasi-static modulus [MPa]

184.316

Diploe viscoelastic modulus [MPa @ 50 kHz]

1819.587



ID – Source

0701 – Parietal

Trabecular bone volume fraction

0.701

Effective quasi-static modulus [MPa]

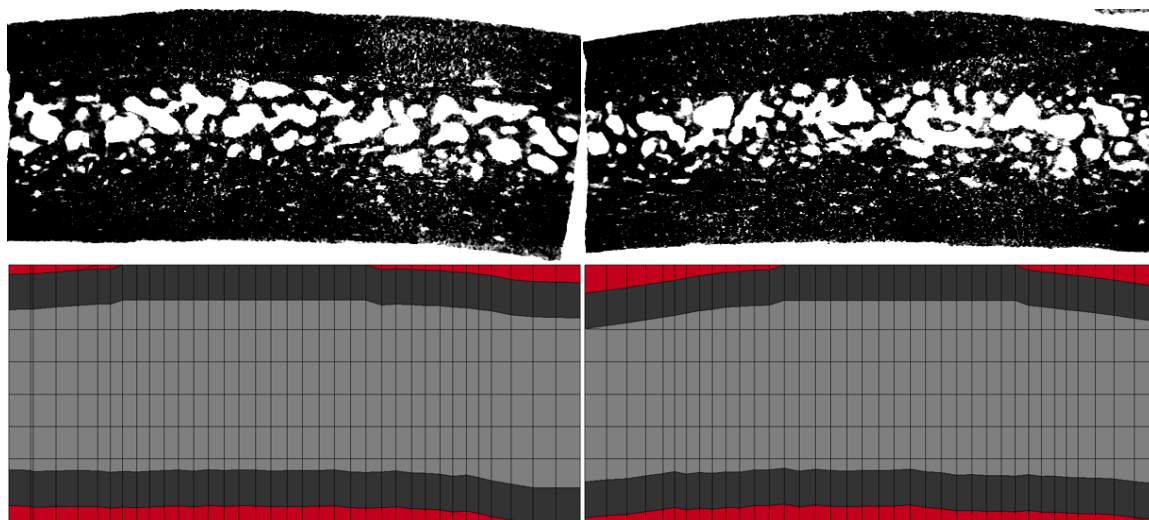
449.696

Diploe quasi-static modulus [MPa]

253.779

Diploe viscoelastic modulus [MPa @ 50 kHz]

1451.587



ID – Source

0702 – Parietal

Trabecular bone volume fraction

0.425

Effective quasi-static modulus [MPa]

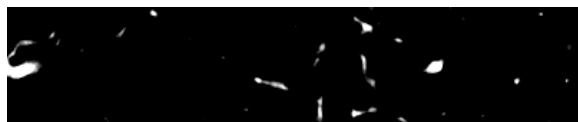
495.392

Diploe quasi-static modulus [MPa]

278.802

Diploe viscoelastic modulus [MPa @ 50 kHz]

550.414



070201

070202 Same depth

Bone volume fraction

0.837

0.840

Effective modulus [GPa]

13.224

15.219

Effective failure stress [MPa]

89.156

90.093

Effective failure strain [%]

0.681

0.573

Bone modulus from BVF [GPa]

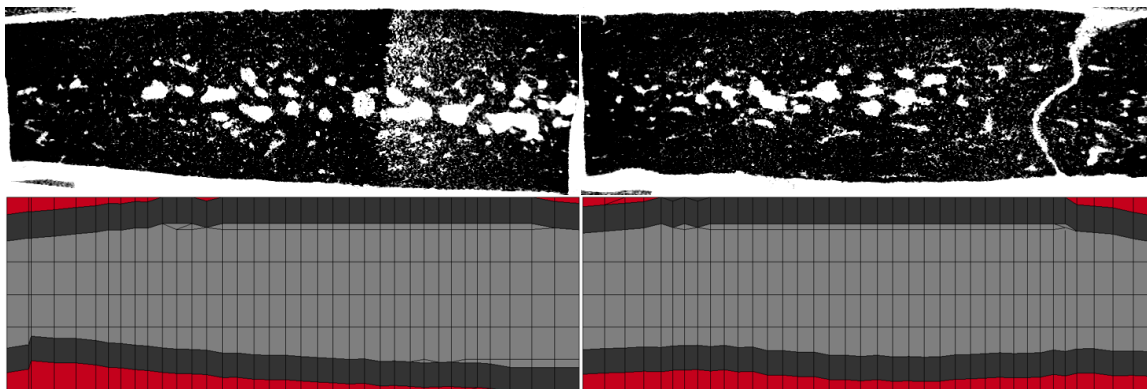
19.628

22.420

Bone modulus from μ FE [GPa]

21.458

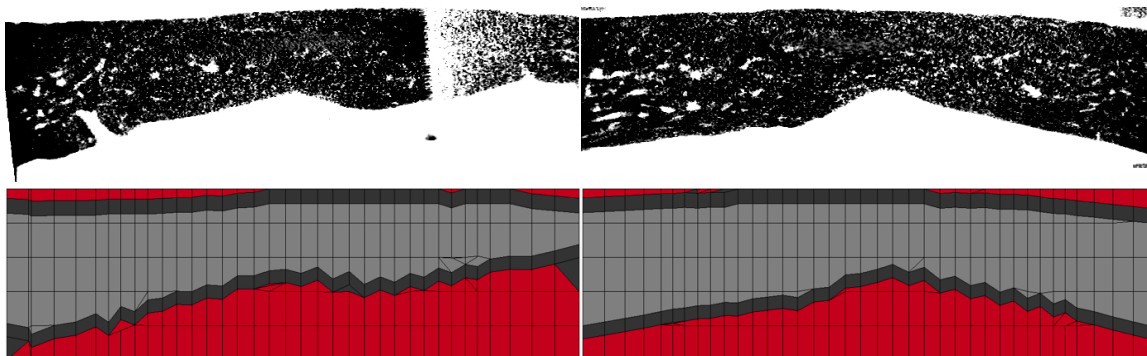
18.193



ID – Source	0703 – Parietal
Trabecular bone volume fraction	0.736
Effective quasi-static modulus [MPa]	514.046
Diploe quasi-static modulus [MPa]	282.945
Diploe viscoelastic modulus [MPa @ 50 kHz]	254.457



070301	
Bone volume fraction	0.845
Effective modulus [GPa]	12.992
Effective failure stress [MPa]	75.991
Effective failure strain [%]	0.548
Bone modulus from BVF [GPa]	18.884
Bone modulus from μ FE [GPa]	15.643



ID – Source

0704 – Parietal

Trabecular bone volume fraction

0.819

Effective quasi-static modulus [MPa]

337.562

Diploe quasi-static modulus [MPa]

163.920

Diploe viscoelastic modulus [MPa @ 50 kHz]

581.396



070401

070402 Same depth

Bone volume fraction

0.766

0.834

Effective modulus [GPa]

10.778

11.013

Effective failure stress [MPa]

66.949

69.912

Effective failure strain [%]

0.656

0.740

Bone modulus from BVF [GPa]

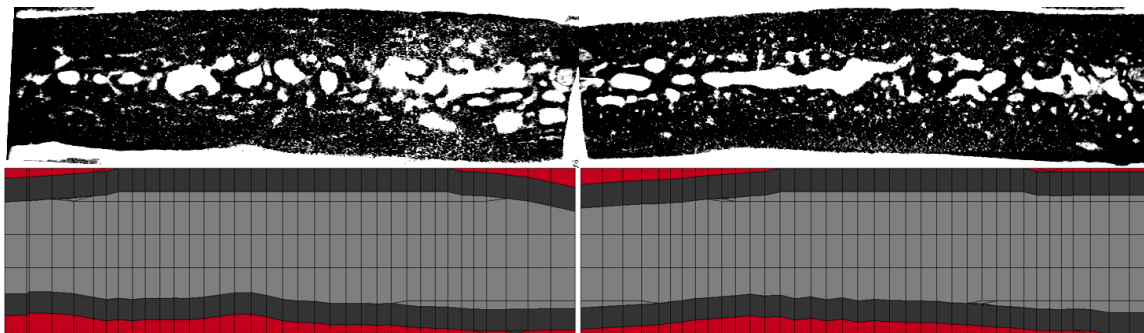
19.477

16.482

Bone modulus from μ FE [GPa]

18.904

18.553



ID – Source

0705 – Parietal

Trabecular bone volume fraction

0.570

Effective quasi-static modulus [MPa]

456.628

Diploe quasi-static modulus [MPa]

239.692

Diploe viscoelastic modulus [MPa @ 50 kHz]

589.450



070501

070502 Same depth

Bone volume fraction

0.834

0.786

Effective modulus [GPa]

12.030

10.156

Effective failure stress [MPa]

60.198

59.387

Effective failure strain [%]

0.586

0.730

Bone modulus from BVF [GPa]

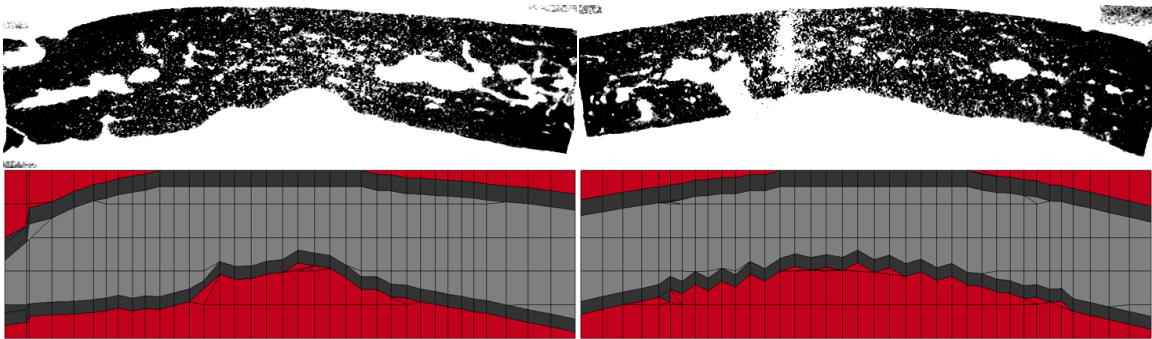
17.966

17.333

Bone modulus from μ FE [GPa]

18.937

15.775



ID – Source

0706 – Parietal

Trabecular bone volume fraction

0.717

Effective quasi-static modulus [MPa]

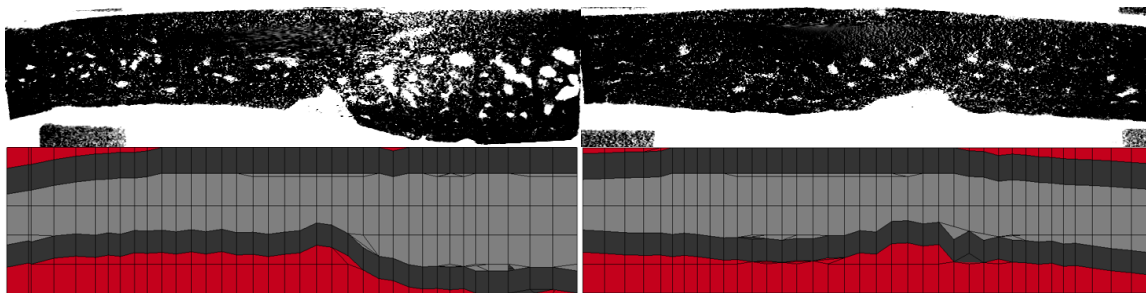
305.361

Diploe quasi-static modulus [MPa]

147.950

Diploe viscoelastic modulus [MPa @ 50 kHz]

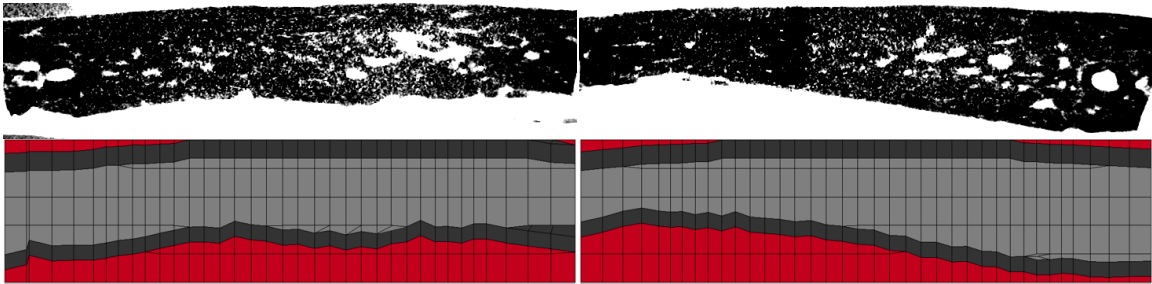
994.160



ID – Source	0707 – Parietal
Trabecular bone volume fraction	0.892
Effective quasi-static modulus [MPa]	203.640
Diploe quasi-static modulus [MPa]	67.415
Diploe viscoelastic modulus [MPa @ 50 kHz]	585.035



070701	
Bone volume fraction	0.653
Effective modulus [GPa]	5.395
Effective failure stress [MPa]	25.986
Effective failure strain [%]	0.570
Bone modulus from BVF [GPa]	13.868
Bone modulus from μ FE [GPa]	27.185



ID – Source

0708 – Parietal

Trabecular bone volume fraction

0.786

Effective quasi-static modulus [MPa]

295.095

Diploe quasi-static modulus [MPa]

129.451

Diploe viscoelastic modulus [MPa @ 50 kHz]

447.052



070801

Bone volume fraction

0.824

Effective modulus [GPa]

12.406

Effective failure stress [MPa]

42.885

Effective failure strain [%]

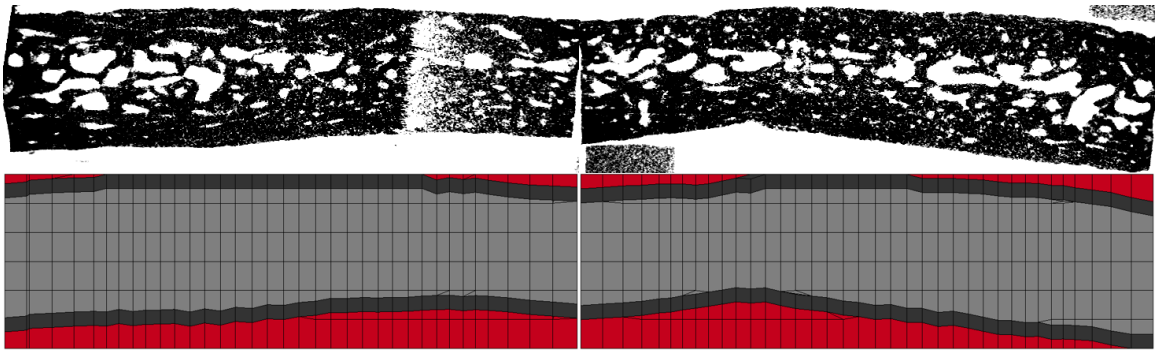
0.400

Bone modulus from BVF [GPa]

19.044

Bone modulus from μ FE [GPa]

18.391



ID – Source

0709 – Frontal

Trabecular bone volume fraction

0.563

Effective quasi-static modulus [MPa]

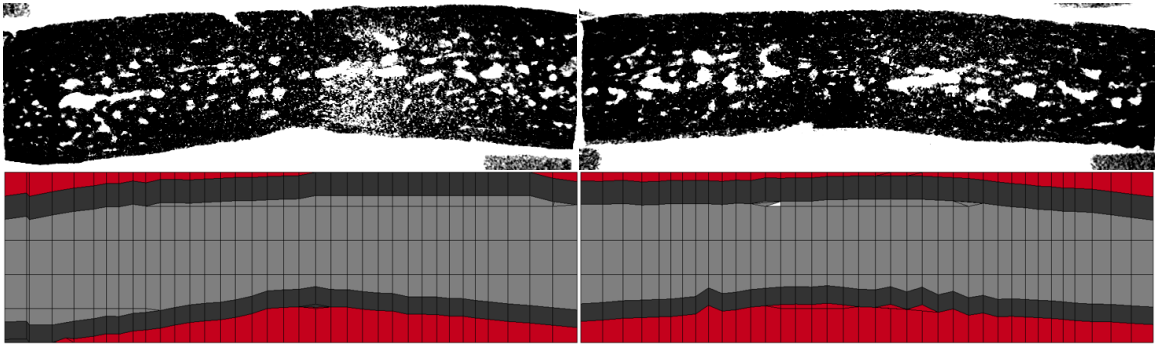
439.533

Diploe quasi-static modulus [MPa]

263.196

Diploe viscoelastic modulus [MPa @ 50 kHz]

1044.337



ID – Source

0710 – Parietal

Trabecular bone volume fraction

0.710

Effective quasi-static modulus [MPa]

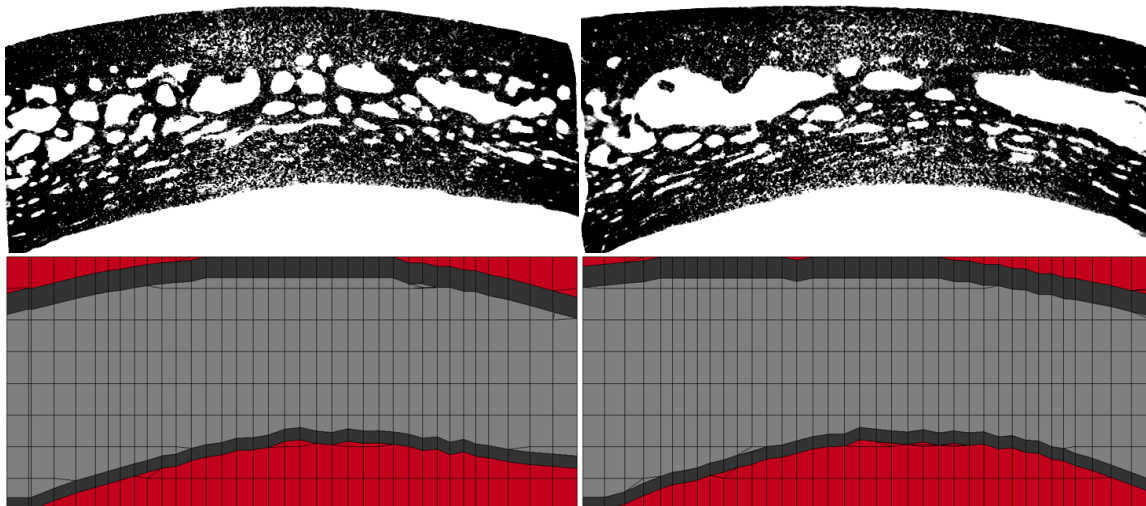
362.980

Diploe quasi-static modulus [MPa]

181.545

Diploe viscoelastic modulus [MPa @ 50 kHz]

913.742



ID – Source

0801 – Parietal

Trabecular bone volume fraction

0.446

Effective quasi-static modulus [MPa]

529.543

Diploe quasi-static modulus [MPa]

376.844

Diploe viscoelastic modulus [MPa @ 50 kHz]

707.573



080101

Bone volume fraction

0.828

Effective modulus [GPa]

11.271

Effective failure stress [MPa]

62.010

Effective failure strain [%]

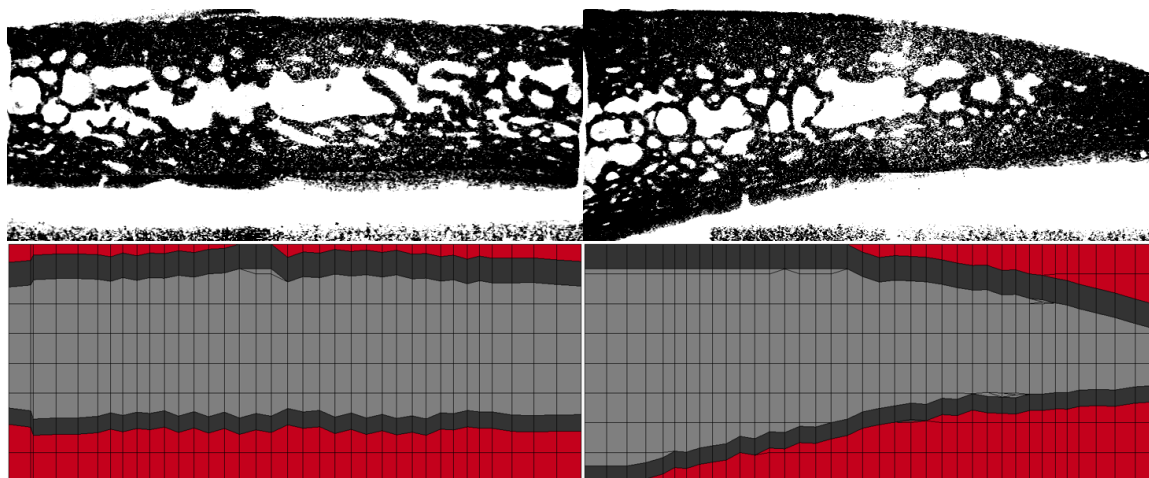
0.617

Bone modulus from BVF [GPa]

17.112

Bone modulus from μ FE [GPa]

19.172



ID – Source

0802 – Parietal

Trabecular bone volume fraction

0.521

Effective quasi-static modulus [MPa]

408.261

Diploe quasi-static modulus [MPa]

233.904

Diploe viscoelastic modulus [MPa @ 50 kHz]

749.542



080201

Bone volume fraction

0.816

Effective modulus [GPa]

10.240

Effective failure stress [MPa]

74.828

Effective failure strain [%]

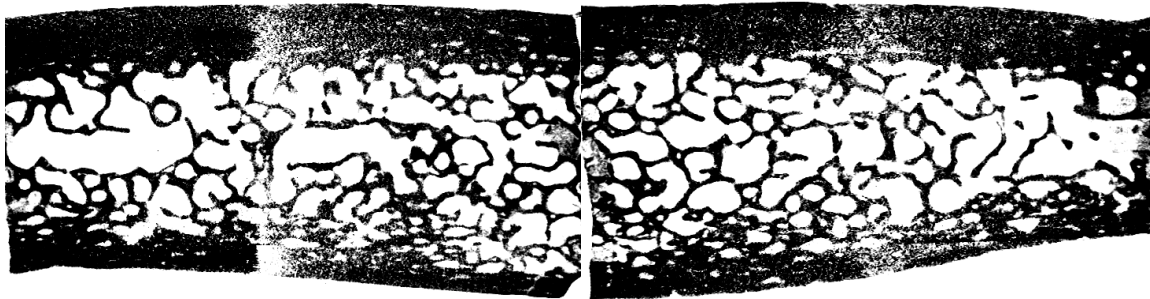
0.824

Bone modulus from BVF [GPa]

16.080

Bone modulus from μ FE [GPa]

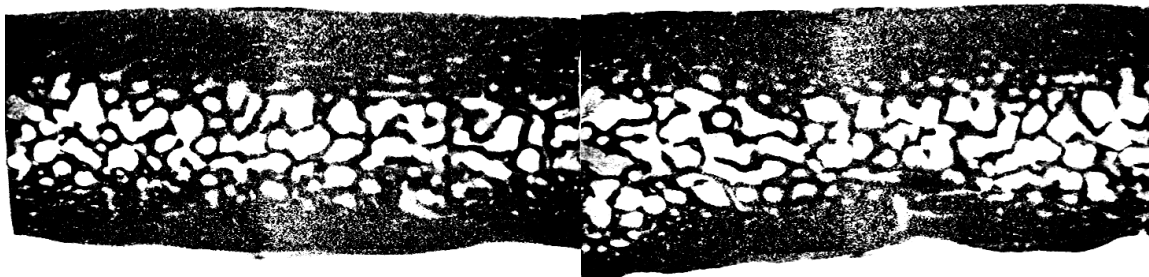
15.068



ID – Source	0803 – Parietal
Trabecular bone volume fraction	0.290
Effective quasi-static modulus [MPa]	498.032
Diploe quasi-static modulus [MPa]	361.246
Diploe viscoelastic modulus [MPa @ 50 kHz]	640.282



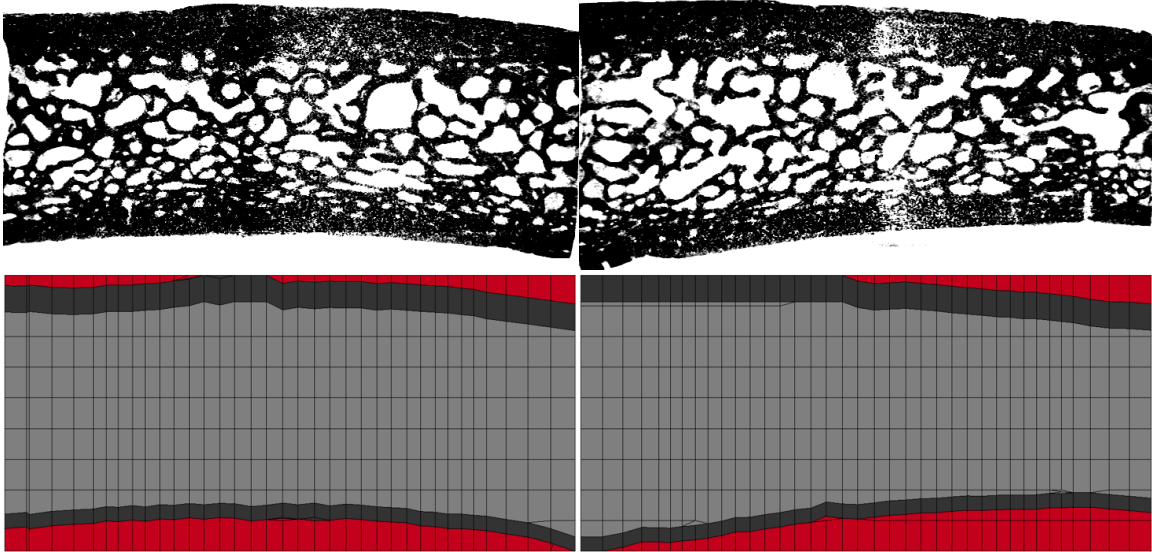
080301	
Bone volume fraction	0.883
Effective modulus [GPa]	15.029
Effective failure stress [MPa]	98.628
Effective failure strain [%]	0.764
Bone modulus from BVF [GPa]	19.799
Bone modulus from μ FE [GPa]	18.508



ID – Source	0804 – Parietal
Trabecular bone volume fraction	0.349
Effective quasi-static modulus [MPa]	394.558
Diploe quasi-static modulus [MPa]	244.813
Diploe viscoelastic modulus [MPa @ 50 kHz]	650.467



080401	
Bone volume fraction	0.859
Effective modulus [GPa]	12.890
Effective failure stress [MPa]	80.079
Effective failure strain [%]	0.614
Bone modulus from BVF [GPa]	18.035
Bone modulus from μ FE [GPa]	20.724



ID – Source

0805 – Parietal

Trabecular bone volume fraction

0.424

Effective quasi-static modulus [MPa]

501.388

Diploe quasi-static modulus [MPa]

348.636

Diploe viscoelastic modulus [MPa @ 50 kHz]

603.024



080501

Bone volume fraction

0.880

Effective modulus [GPa]

11.102

Effective failure stress [MPa]

70.672

Effective failure strain [%]

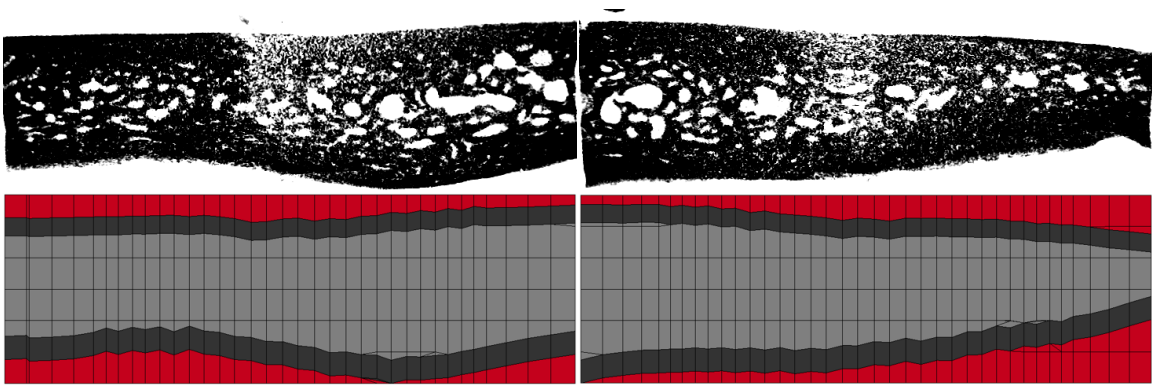
0.688

Bone modulus from BVF [GPa]

14.732

Bone modulus from μ FE [GPa]

15.030



ID – Source

0806 – Frontal

Trabecular bone volume fraction

0.664

Effective quasi-static modulus [MPa]

545.941

Diploe quasi-static modulus [MPa]

312.417

Diploe viscoelastic modulus [MPa @ 50 kHz]

1083.259



080601

Bone volume fraction

0.857

Effective modulus [GPa]

11.875

Effective failure stress [MPa]

103.322

Effective failure strain [%]

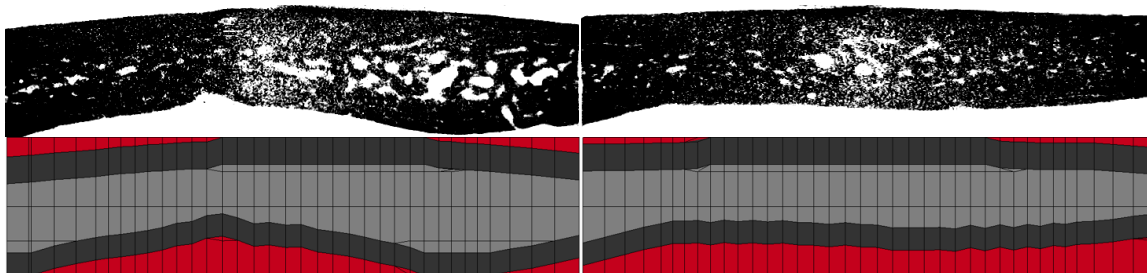
0.962

Bone modulus from BVF [GPa]

16.708

Bone modulus from μ FE [GPa]

17.040



ID – Source

0808 – Parietal

Trabecular bone volume fraction

0.816

Effective quasi-static modulus [MPa]

211.475

Diploe quasi-static modulus [MPa]

72.797

Diploe viscoelastic modulus [MPa @ 50 kHz]

583.784



080801

Bone volume fraction

0.833

Effective modulus [GPa]

9.902

Effective failure stress [MPa]

62.493

Effective failure strain [%]

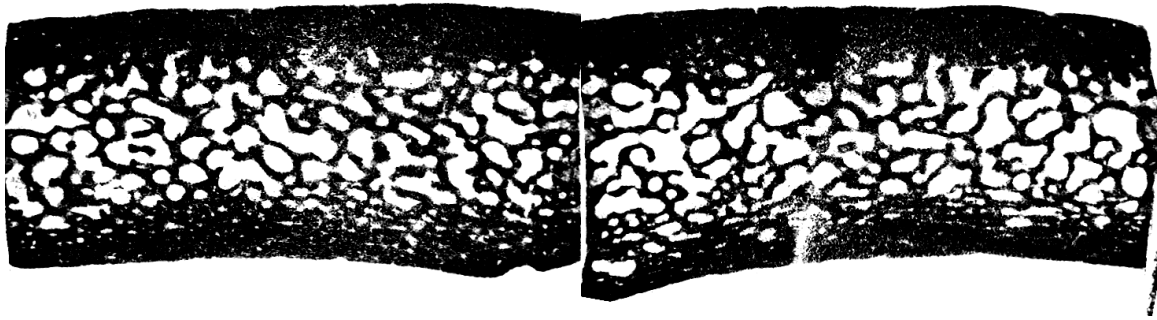
0.649

Bone modulus from BVF [GPa]

14.852

Bone modulus from μ FE [GPa]

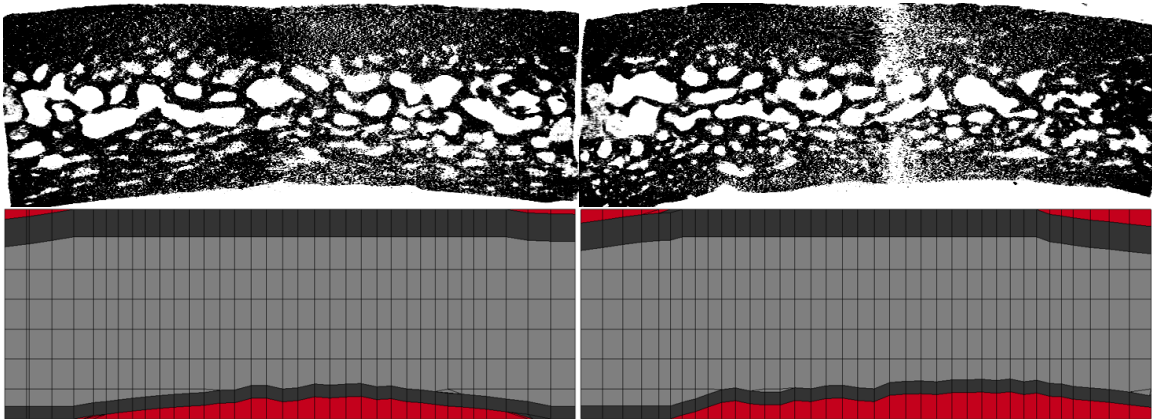
15.918



ID – Source	0809 – Parietal
Trabecular bone volume fraction	0.404
Effective quasi-static modulus [MPa]	711.570
Diploe quasi-static modulus [MPa]	528.751
Diploe viscoelastic modulus [MPa @ 50 kHz]	598.524



080901	
Bone volume fraction	0.894
Effective modulus [GPa]	12.036
Effective failure stress [MPa]	59.056
Effective failure strain [%]	0.480
Bone modulus from BVF [GPa]	15.439
Bone modulus from μ FE [GPa]	14.175



ID – Source

0810 – Frontal

Trabecular bone volume fraction

0.454

Effective quasi-static modulus [MPa]

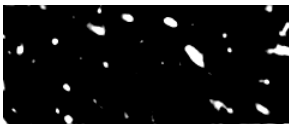
518.957

Diploe quasi-static modulus [MPa]

330.339

Diploe viscoelastic modulus [MPa @ 50 kHz]

669.394



081001

Bone volume fraction

0.826

Effective modulus [GPa]

13.343

Effective failure stress [MPa]

63.818

Effective failure strain [%]

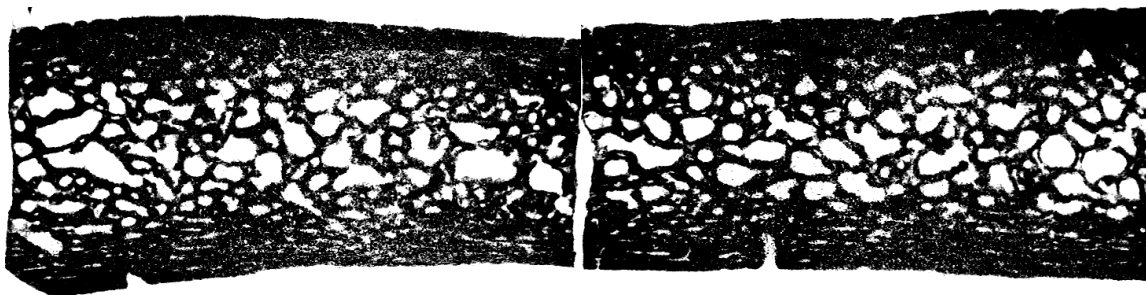
0.479

Bone modulus from BVF [GPa]

20.374

Bone modulus from μ FE [GPa]

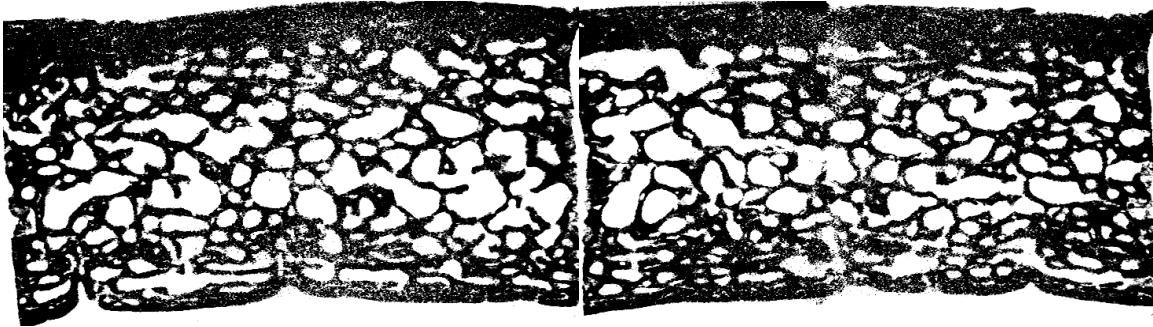
19.034



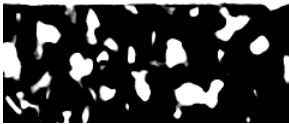
ID – Source	0904 – Parietal
Trabecular bone volume fraction	0.494
Effective quasi-static modulus [MPa]	715.879
Diploe quasi-static modulus [MPa]	528.740
Diploe viscoelastic modulus [MPa @ 50 kHz]	2279.957



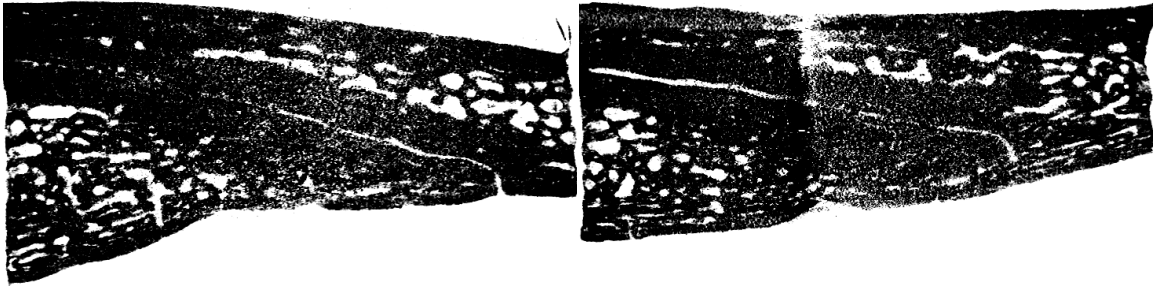
090401	
Bone volume fraction	0.720
Effective modulus [GPa]	5.565
Effective failure stress [MPa]	20.967
Effective failure strain [%]	0.431
Bone modulus from BVF [GPa]	11.521
Bone modulus from μ FE [GPa]	16.309



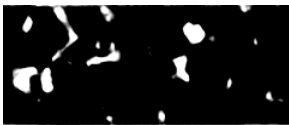
ID – Source	0905 – Parietal
Trabecular bone volume fraction	0.413
Effective quasi-static modulus [MPa]	531.070
Diploe quasi-static modulus [MPa]	412.954
Diploe viscoelastic modulus [MPa @ 50 kHz]	2110.837



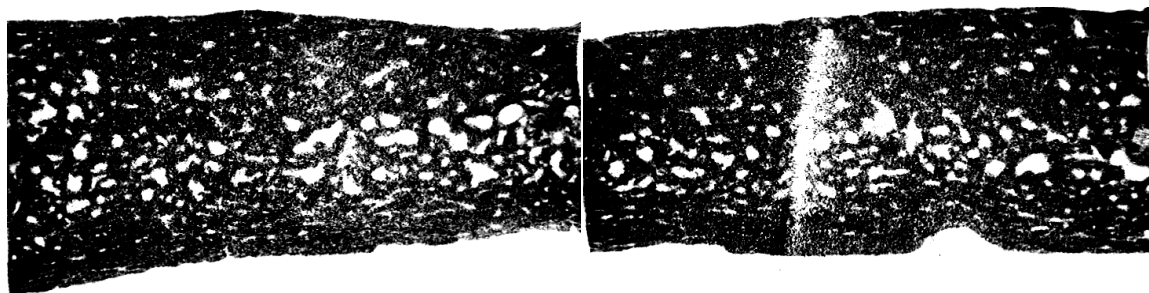
090501	
Bone volume fraction	0.699
Effective modulus [GPa]	6.054
Effective failure stress [MPa]	20.347
Effective failure strain [%]	0.624
Bone modulus from BVF [GPa]	13.391
Bone modulus from μ FE [GPa]	14.488



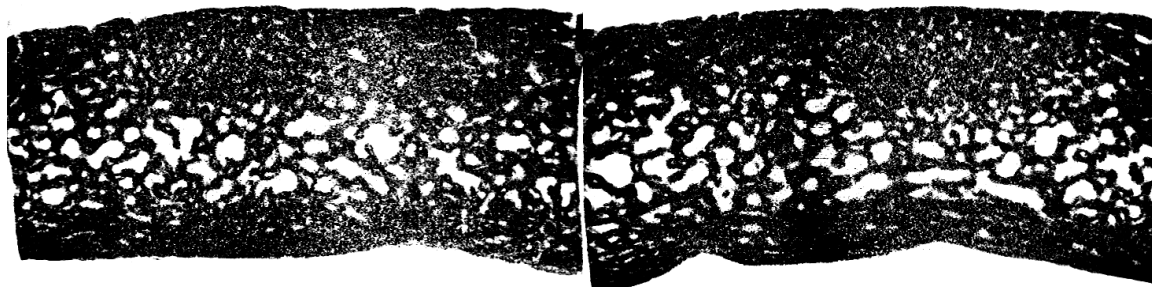
ID – Source	0906 – Frontal
Trabecular bone volume fraction	0.778
Effective quasi-static modulus [MPa]	433.821
Diploe quasi-static modulus [MPa]	293.627
Diploe viscoelastic modulus [MPa @ 50 kHz]	2504.847



090601	
Bone volume fraction	0.784
Effective modulus [GPa]	9.093
Effective failure stress [MPa]	49.947
Effective failure strain [%]	0.581
Bone modulus from BVF [GPa]	15.583
Bone modulus from μ FE [GPa]	16.121



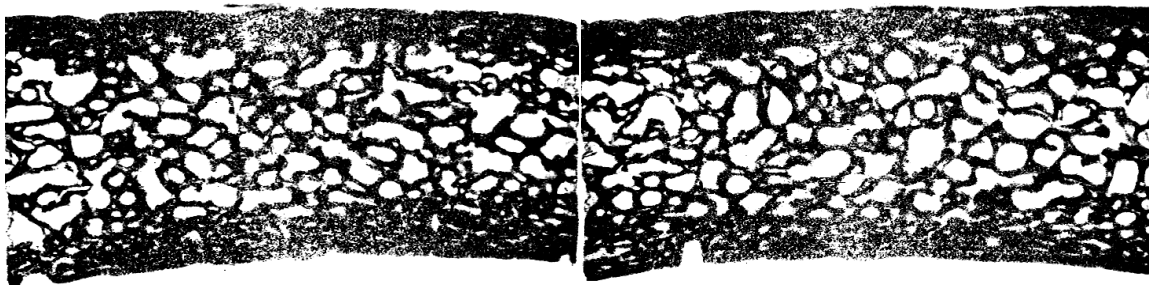
ID – Source	0907 – Frontal
Trabecular bone volume fraction	0.678
Effective quasi-static modulus [MPa]	427.666
Diploe quasi-static modulus [MPa]	298.027
Diploe viscoelastic modulus [MPa @ 50 kHz]	1995.501



ID – Source	0908 – Frontal
Trabecular bone volume fraction	0.601
Effective quasi-static modulus [MPa]	912.212
Diploe quasi-static modulus [MPa]	751.083
Diploe viscoelastic modulus [MPa @ 50 kHz]	1450.953



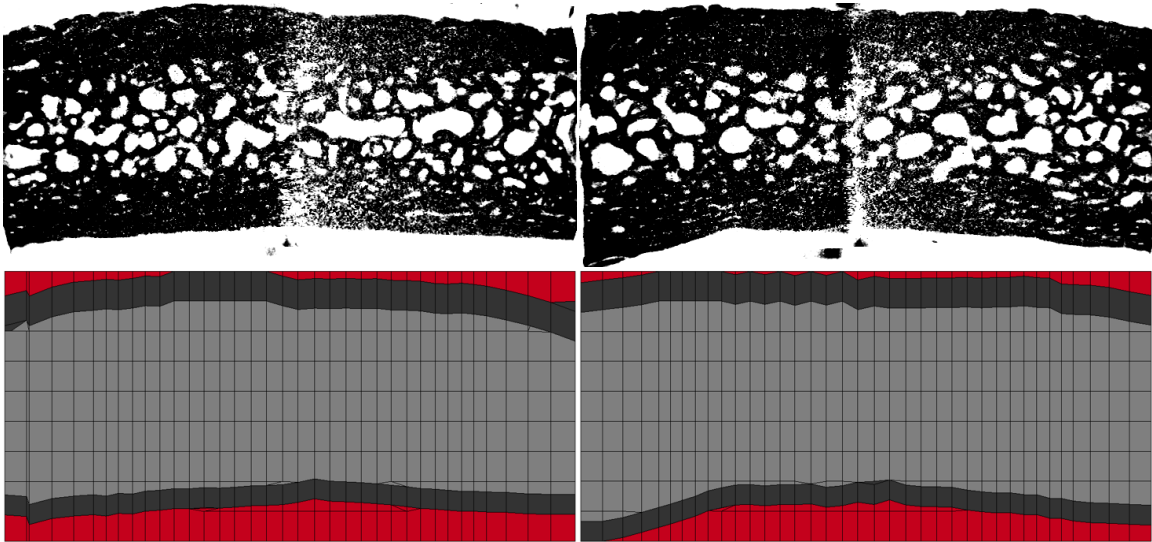
090801	
Bone volume fraction	0.813
Effective modulus [GPa]	8.911
Effective failure stress [MPa]	51.575
Effective failure strain [%]	0.591
Bone modulus from BVF [GPa]	14.113
Bone modulus from μ FE [GPa]	15.107



ID – Source	0909 – Frontal
Trabecular bone volume fraction	0.443
Effective quasi-static modulus [MPa]	656.478
Diploe quasi-static modulus [MPa]	542.513
Diploe viscoelastic modulus [MPa @ 50 kHz]	1980.572



090901	
Bone volume fraction	0.652
Effective modulus [GPa]	8.319
Effective failure stress [MPa]	43.001
Effective failure strain [%]	0.572
Bone modulus from BVF [GPa]	21.440
Bone modulus from μ FE [GPa]	19.463



ID – Source

0910 – Parietal

Trabecular bone volume fraction

0.541

Effective quasi-static modulus [MPa]

797.156

Diploe quasi-static modulus [MPa]

583.554

Diploe viscoelastic modulus [MPa @ 50 kHz]

1766.755



091001

Bone volume fraction

0.833

Effective modulus [GPa]

12.489

Effective failure stress [MPa]

74.638

Effective failure strain [%]

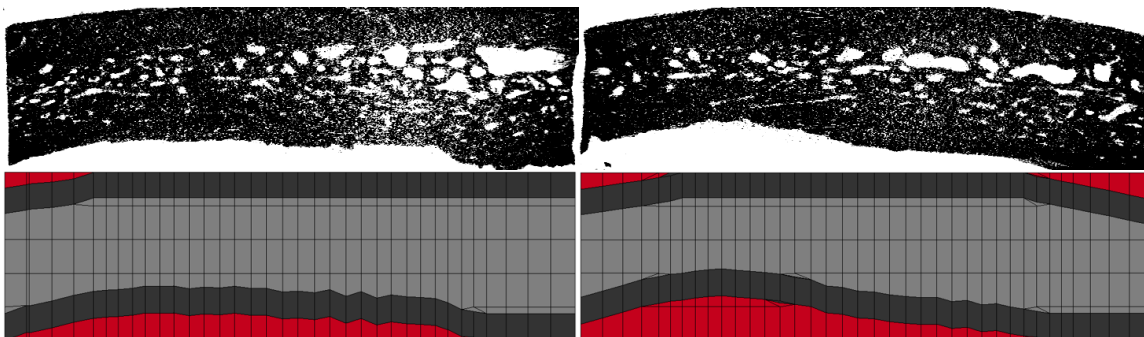
0.654

Bone modulus from BVF [GPa]

18.710

Bone modulus from μ FE [GPa]

15.936



ID – Source

1001 – Frontal

Trabecular bone volume fraction

0.713

Effective quasi-static modulus [MPa]

347.782

Diploe quasi-static modulus [MPa]

161.907

Diploe viscoelastic modulus [MPa @ 50 kHz]

842.776



100101

Bone volume fraction

0.706

Effective modulus [GPa]

14.996

Effective failure stress [MPa]

39.711

Effective failure strain [%]

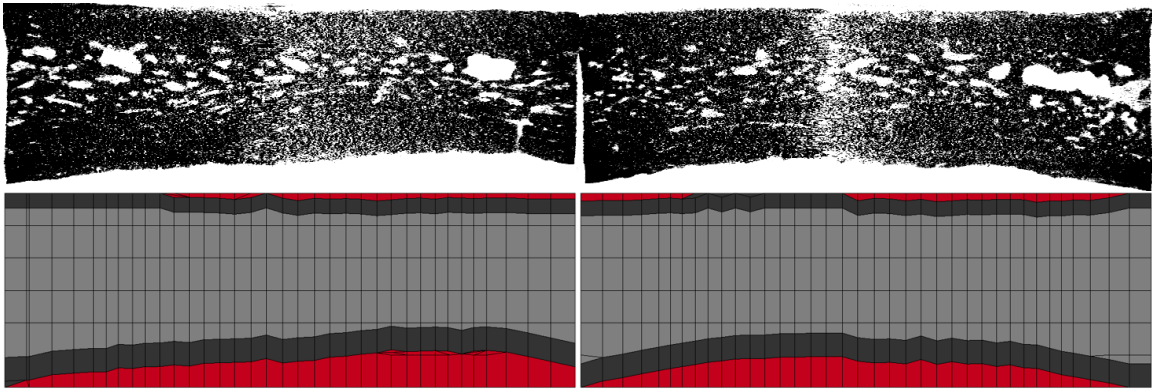
0.311

Bone modulus from BVF [GPa]

32.479

Bone modulus from μ FE [GPa]

27.723



ID – Source

1002 – Frontal

Trabecular bone volume fraction

0.710

Effective quasi-static modulus [MPa]

417.544

Diploe quasi-static modulus [MPa]

248.943

Diploe viscoelastic modulus [MPa @ 50 kHz]

1052.338



100201

Bone volume fraction

0.783

Effective modulus [GPa]

13.709

Effective failure stress [MPa]

74.945

Effective failure strain [%]

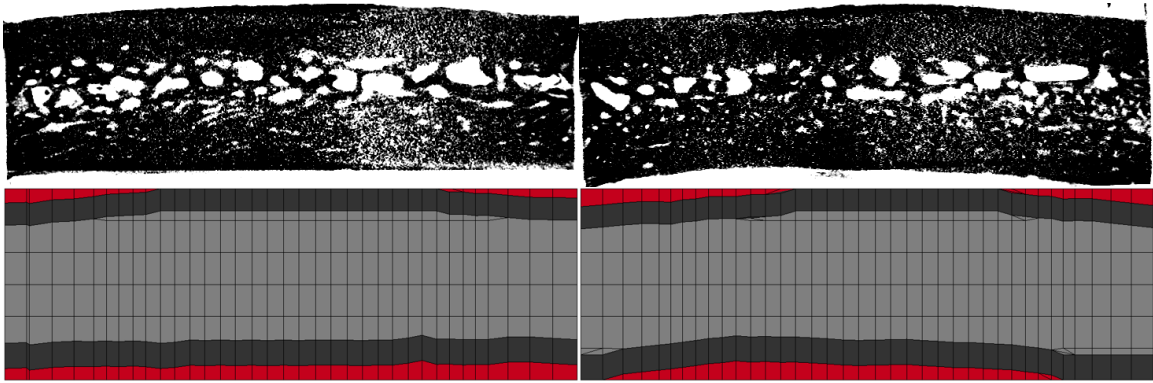
0.660

Bone modulus from BVF [GPa]

23.591

Bone modulus from μ FE [GPa]

20.041



ID – Source

1004 – Parietal

Trabecular bone volume fraction

0.586

Effective quasi-static modulus [MPa]

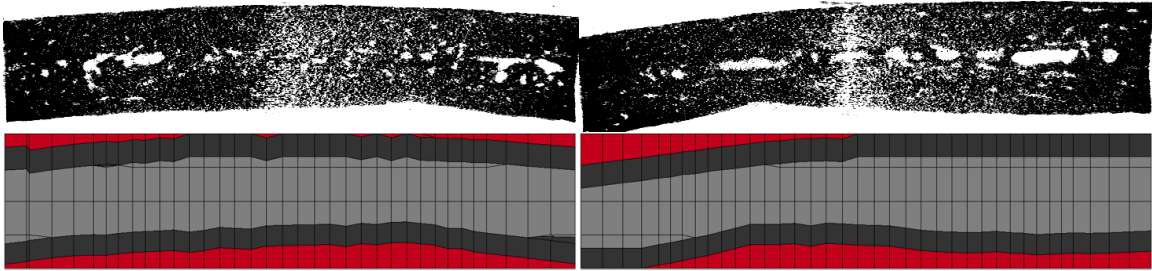
586.153

Diploe quasi-static modulus [MPa]

337.324

Diploe viscoelastic modulus [MPa @ 50 kHz]

963.873



ID – Source

1005 – Parietal

Trabecular bone volume fraction

0.850

Effective quasi-static modulus [MPa]

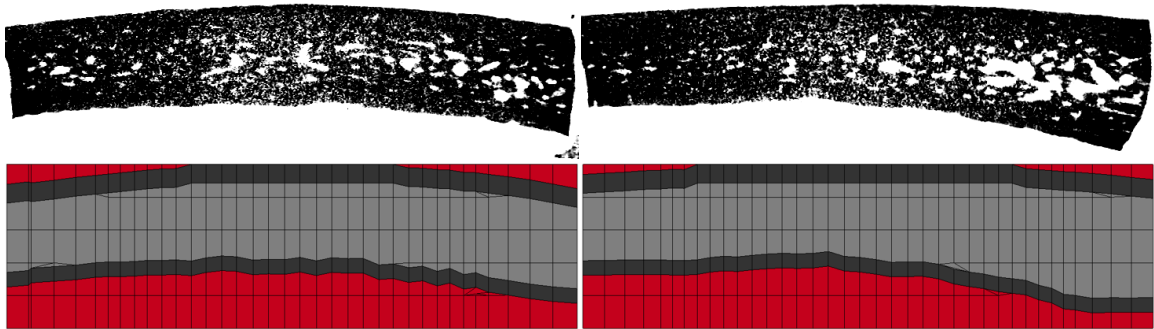
291.456

Diploe quasi-static modulus [MPa]

119.539

Diploe viscoelastic modulus [MPa @ 50 kHz]

618.357



ID – Source

1008 – Parietal

Trabecular bone volume fraction

0.750

Effective quasi-static modulus [MPa]

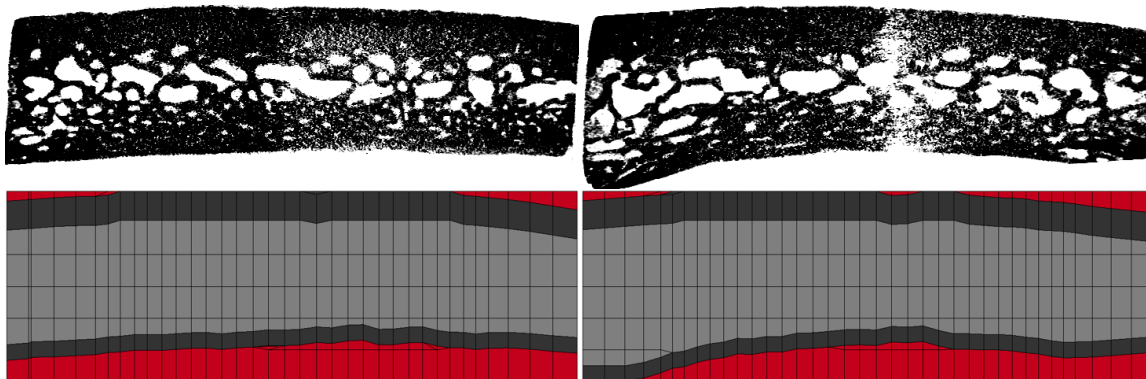
225.321

Diploe quasi-static modulus [MPa]

92.520

Diploe viscoelastic modulus [MPa @ 50 kHz]

760.906



ID – Source

1009 – Parietal

Trabecular bone volume fraction

0.491

Effective quasi-static modulus [MPa]

408.815

Diploe quasi-static modulus [MPa]

216.840

Diploe viscoelastic modulus [MPa @ 50 kHz]

378.605



100901

Bone volume fraction

0.721

Effective modulus [GPa]

10.129

Effective failure stress [MPa]

32.712

Effective failure strain [%]

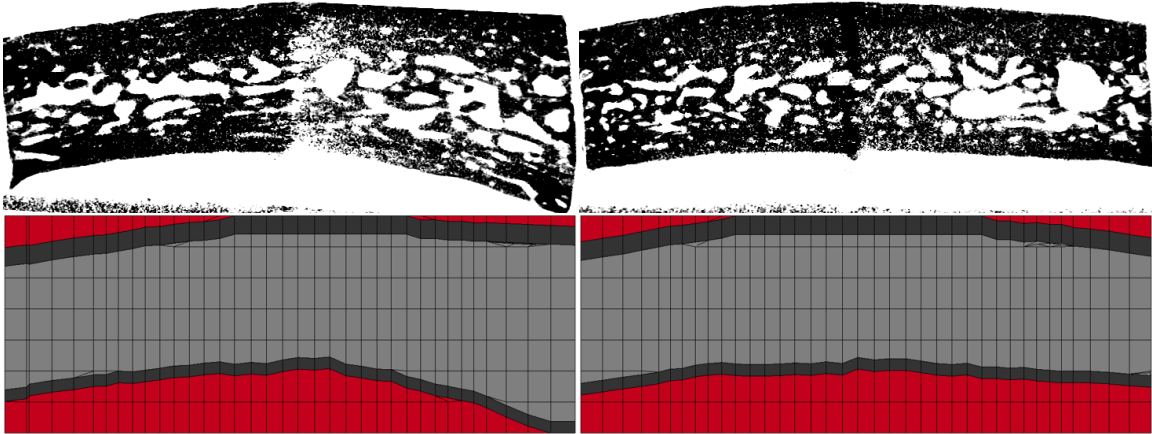
0.364

Bone modulus from BVF [GPa]

20.886

Bone modulus from μ FE [GPa]

20.395



ID – Source

1010 – Frontal

Trabecular bone volume fraction

0.439

Effective quasi-static modulus [MPa]

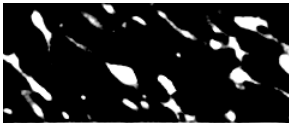
535.408

Diploe quasi-static modulus [MPa]

360.029

Diploe viscoelastic modulus [MPa @ 50 kHz]

1407.902



101001

Bone volume fraction

0.774

Effective modulus [GPa]

11.252

Effective failure stress [MPa]

53.723

Effective failure strain [%]

0.538

Bone modulus from BVF [GPa]

19.834

Bone modulus from μ FE [GPa]

18.917

14.5 Core compression testing

14.5.1 Experimental data

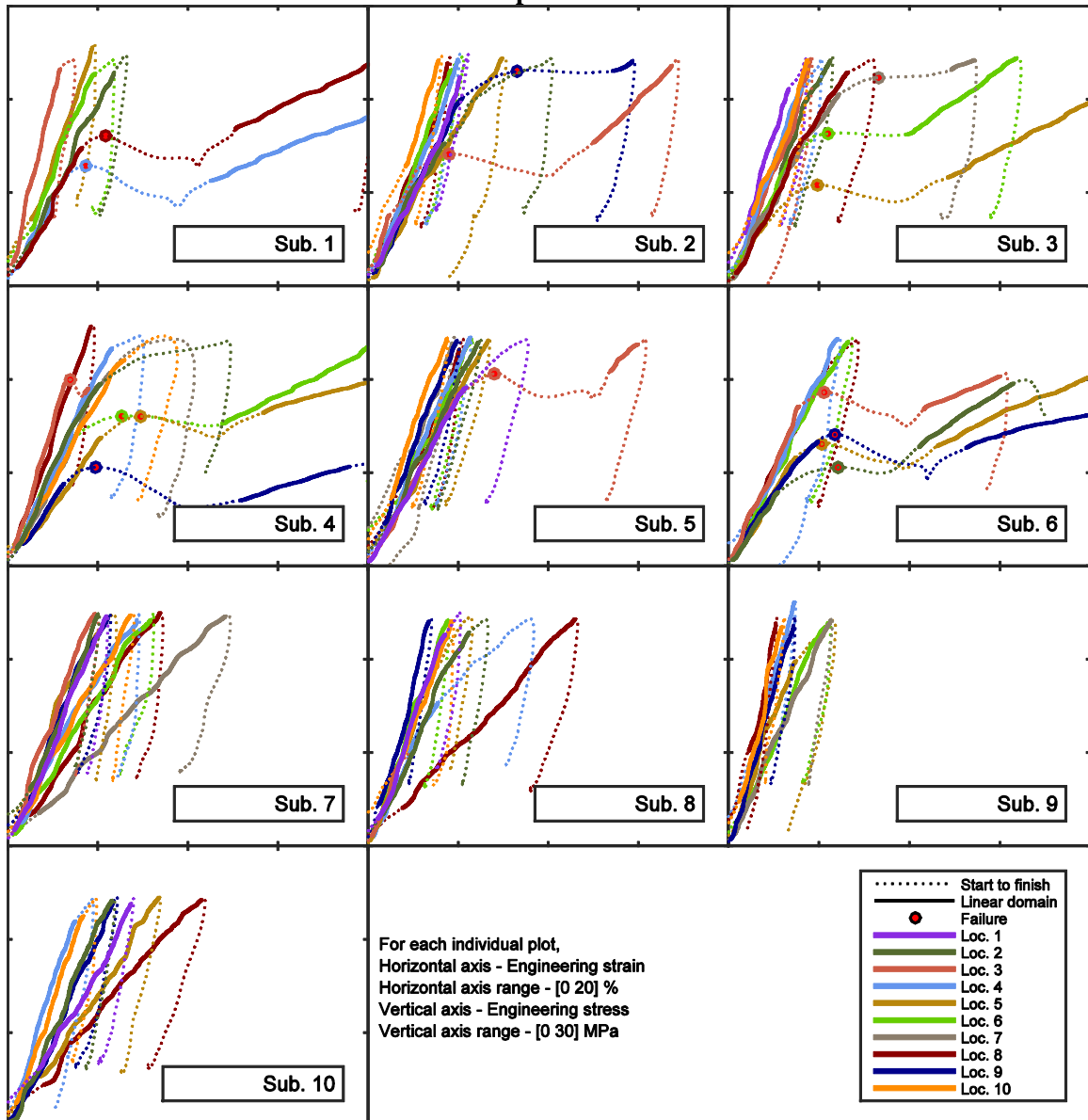


Figure A.13 Stress vs. strain for core compression tests combined by subject

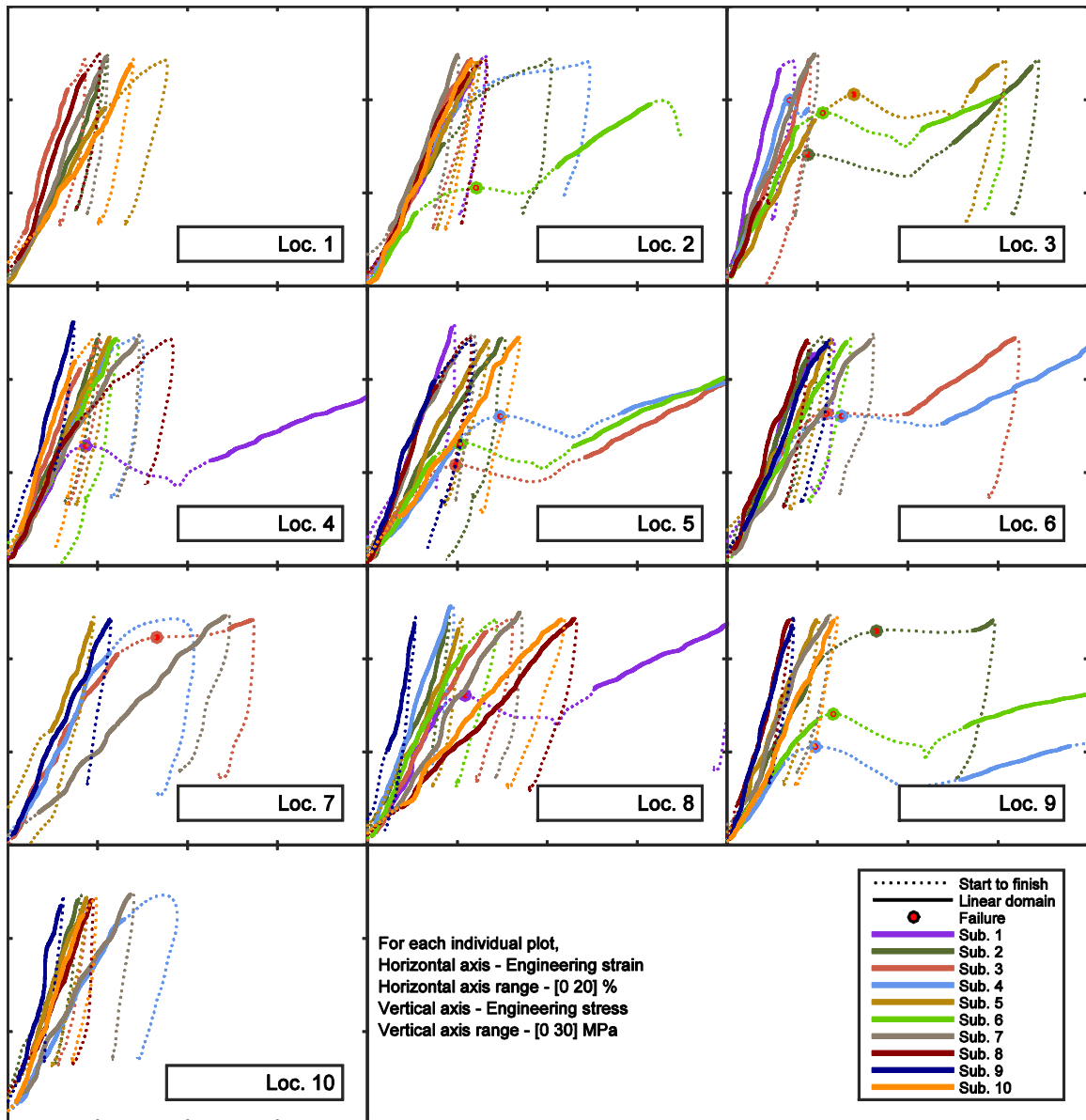


Figure A.14 Stress vs. strain for core compression tests combined by location

14.5.2 Tabulated results

Table A.27 List of core samples and their quasi-static mechanical properties.

ID	Composite modulus [MPa]	Composite failure stress [MPa]	Composite failure strain [%]	Diploe modulus [MPa]
0102	387.00			222.05
0103	797.58			698.95
0104	365.22	12.88	4.87	240.00
0105	543.57			336.98
0106	470.03			338.48
0108	357.86	16.11	6.99	251.27
0201	438.42			261.40
0202	360.21			222.56
0203	640.54	14.14	5.33	449.86
0204	485.35			196.02
0205	327.41			178.74
0206	501.36			247.88
0208	541.27			226.41
0209	384.29	23.02	9.33	192.00
0210	615.75			335.51

Table A.27 List of core samples and their quasi-static mechanical properties continued...

ID	Composite modulus [MPa]	Composite failure stress [MPa]	Composite failure strain [%]	Diploe modulus [MPa]
0301	632.55			431.27
0302	428.64			258.54
0303	535.15			304.39
0304	522.55			304.49
0305	321.45	10.85	5.48	200.70
0306	392.64	16.33	6.72	232.51
0307	335.88	22.29	8.41	180.54
0308	346.66			176.04
0310	556.38			406.09
0402	379.12			220.76
0403	615.03	20.00	4.10	421.26
0404	402.29			205.91
0405	265.26	16.00	10.58	168.20
0406	407.82	16.07	7.32	229.66
0407	363.95			199.46
0408	555.80			359.67
0409	281.32	10.61	5.23	204.97
0410	341.30			193.43

Table A.27 List of core samples and their quasi-static mechanical properties continued...

ID	Composite modulus [MPa]	Composite failure stress [MPa]	Composite failure strain [%]	Diploe modulus [MPa]
0501	351.62			214.13
0502	390.68			157.47
0503	367.11	20.60	8.36	201.53
0504	431.65			257.76
0505	362.85			190.52
0506	423.97			208.65
0507	512.49			174.76
0508	457.37			267.71
0509	489.77			329.97
0510	555.20			347.37
0602	288.71	10.58	6.18	180.74
0603	439.16	18.63	5.78	292.83
0604	404.88			236.75
0605	311.76	13.06	5.86	199.04
0606	363.41			167.10
0608	390.99			215.24
0609	269.56	14.11	6.23	184.32

Table A.27 List of core samples and their quasi-static mechanical properties continued...

ID	Composite modulus [MPa]	Composite failure stress [MPa]	Composite failure strain [%]	Diploe modulus [MPa]
0701	449.70			253.78
0702	495.39			278.80
0703	514.05			282.95
0704	337.56			163.92
0705	456.63			239.69
0706	305.36			147.95
0707	203.64			67.42
0708	295.09			129.45
0709	439.53			263.20
0710	362.98			181.55
0801	529.54			376.84
0802	408.26			233.90
0803	498.03			361.25
0804	394.56			244.81
0805	501.39			348.64
0806	545.94			312.42
0808	211.48			72.80
0809	711.57			528.75
0810	518.96			330.34

Table A.27 List of core samples and their quasi-static mechanical properties continued...

ID	Composite modulus [MPa]	Composite failure stress [MPa]	Composite failure strain [%]	Diploe modulus [MPa]
0904	715.88			528.74
0905	531.07			412.95
0906	433.82			293.63
0907	427.67			298.03
0908	912.21			751.08
0909	656.48			542.51
0910	797.16			583.55
1001	347.78			161.91
1002	417.54			248.94
1004	586.15			337.32
1005	291.46			119.54
1008	225.32			92.52
1009	408.81			216.84
1010	535.41			360.03

14.5.3 Statistical test results

Table A.28 Results of normality tests (p-values from Shapiro-Wilk test) of quasi-static mechanical properties of the core samples for each subject.

Sub	Composite Modulus	Diploe quasi-static modulus
1	0.084	0.012
2	0.752	* 0.037
3	0.363	0.273
4	0.252	* 0.006
5	0.575	0.276
6	0.686	0.314
7	0.589	0.337
8	0.454	0.646
9	0.635	0.598
10	0.885	0.625

Significant values ($\alpha=0.05$) are shown in bold and marked with an asterisk.

Table A.29 Results of one-way within subjects ANOVA tests of quasi-static mechanical properties of the core samples.

Dependent variable	DF	SS	MS	F	p	ges	
Main effect – Subject							
Composite modulus	9	421k	47k	3.231	* 0.002	0.285	
Diploe quasi-static modulus	9	492k	55k	5.022	* 0.000	0.382	
Dependent variable	DFn	DFd	SSn	SSd	F	p	ges
Main effect – is frontal, random effect – Subject							
Composite modulus	1	8	15k	27k	4.405	0.069	0.192
Diploe quasi-static modulus	1	8	16k	17k	7.977	* 0.022	0.210
Main effect – is superior, random effect – Subject							
Composite modulus	1	9	5k	43k	1.103	0.321	0.031
Diploe quasi-static modulus	1	9	9k	27k	3.070	0.114	0.053
Significant values ($\alpha=0.05$) are shown in bold and marked with an asterisk.							

14.5.4 Distribution of quasi-static modulus over the calvarium of each subject

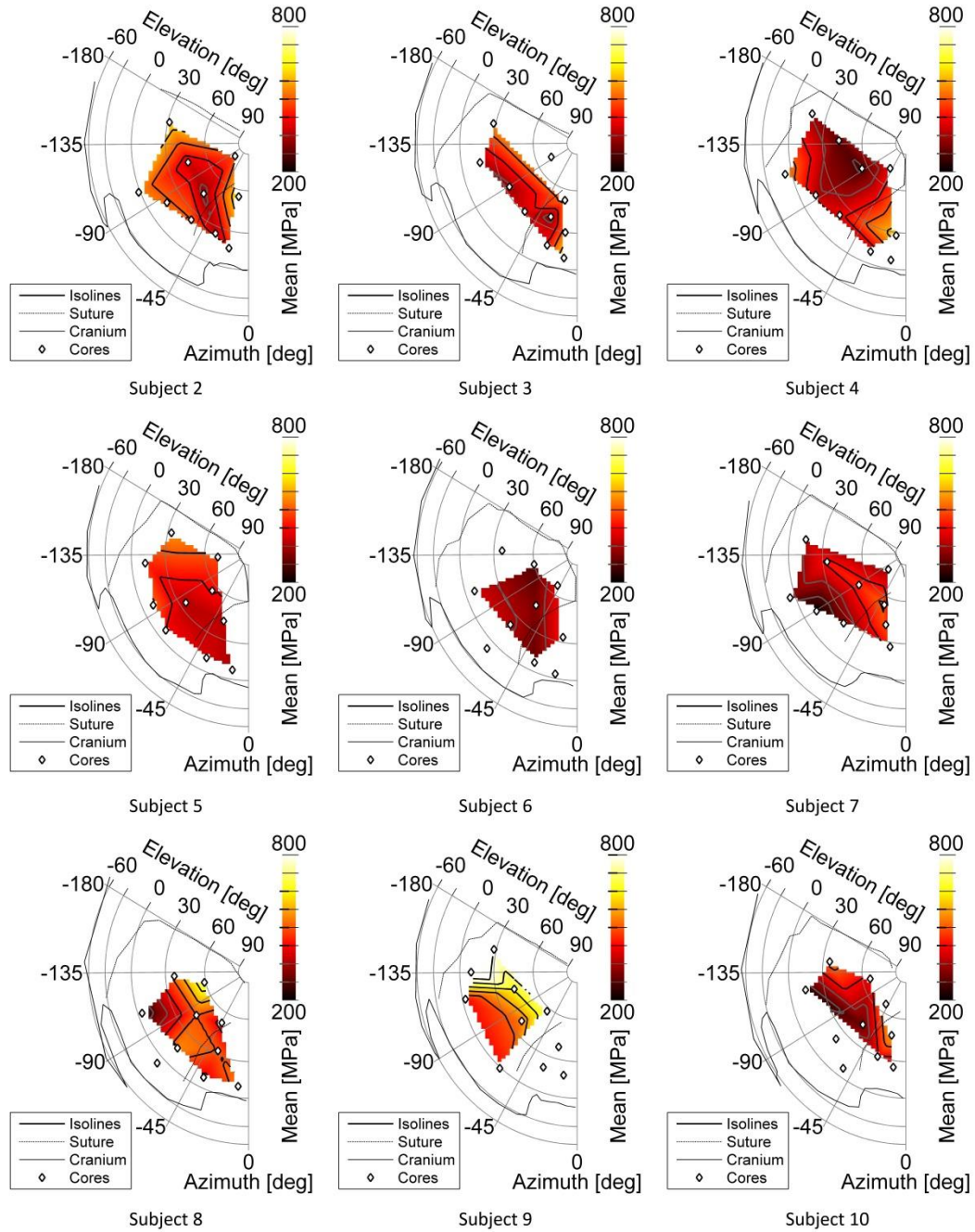


Figure A.15 Effective composite through-the-thickness modulus.

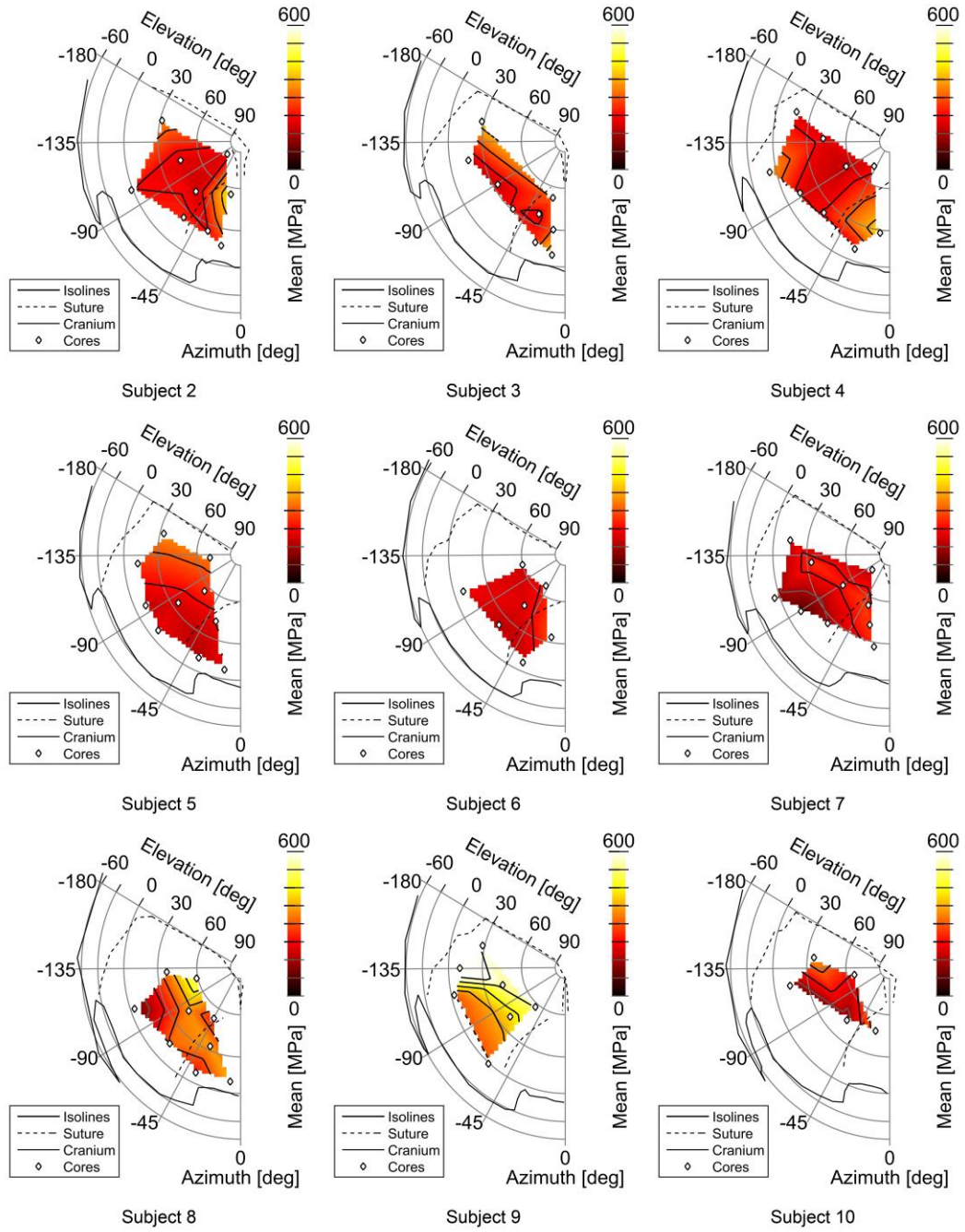
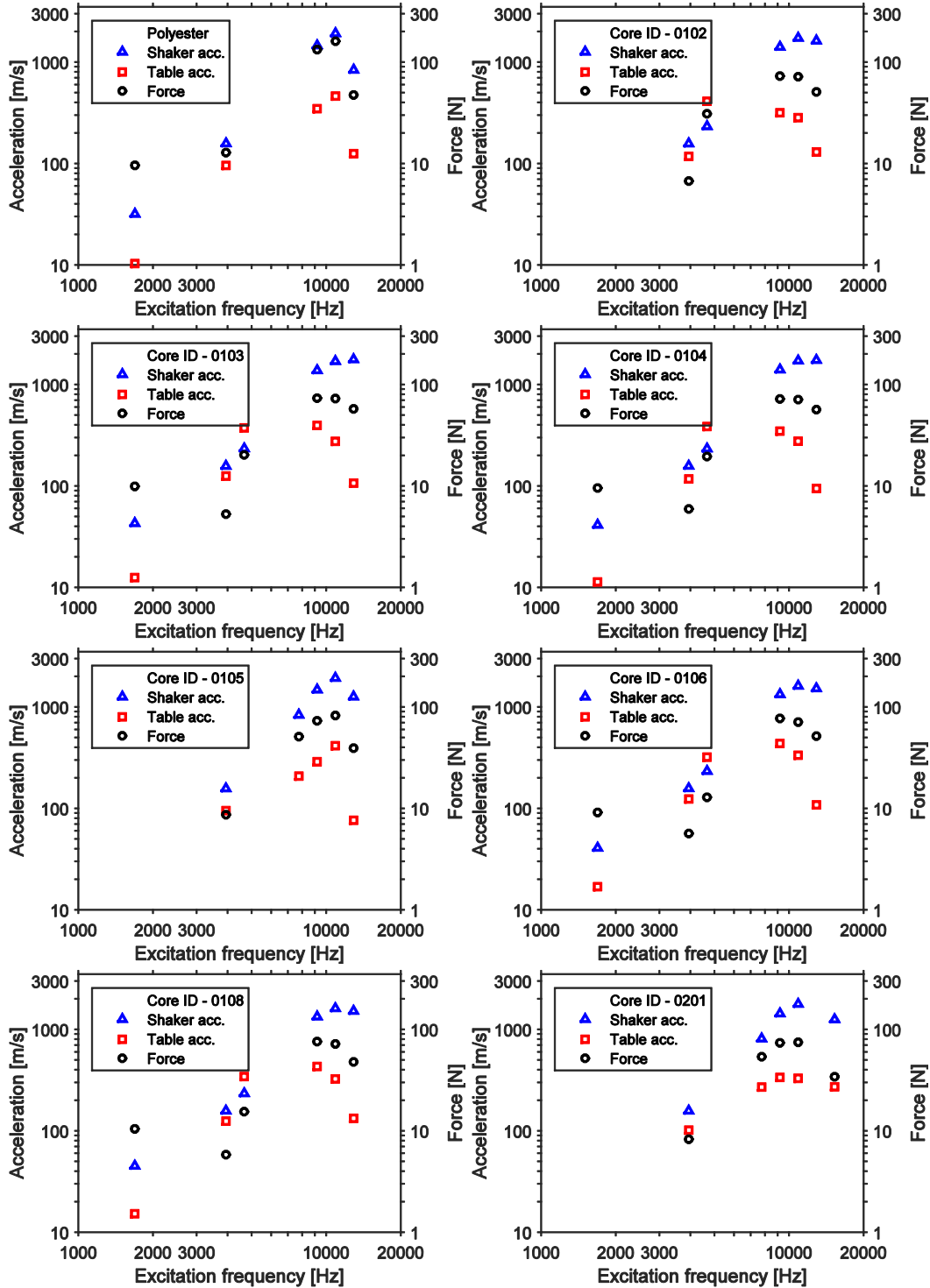
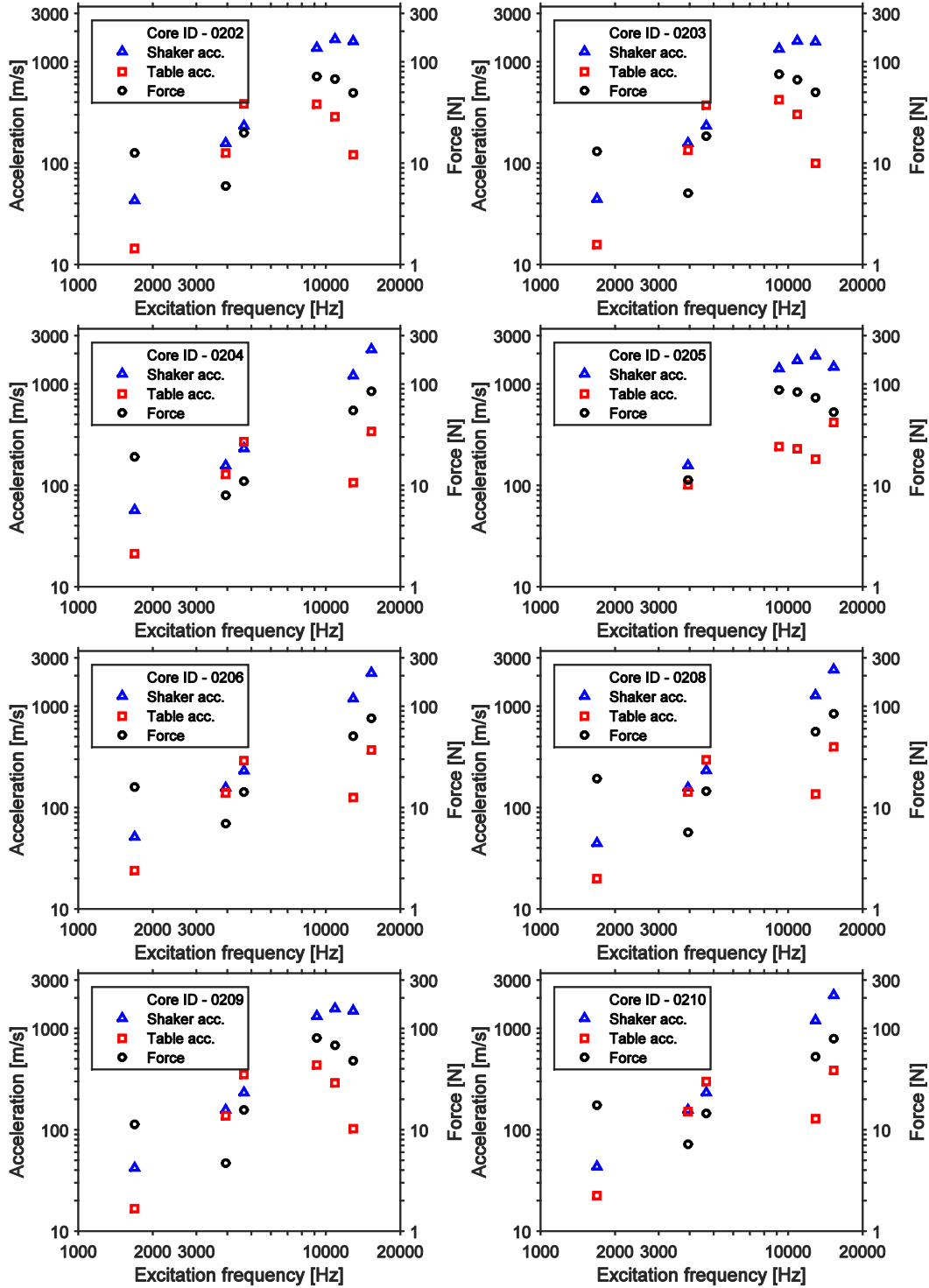


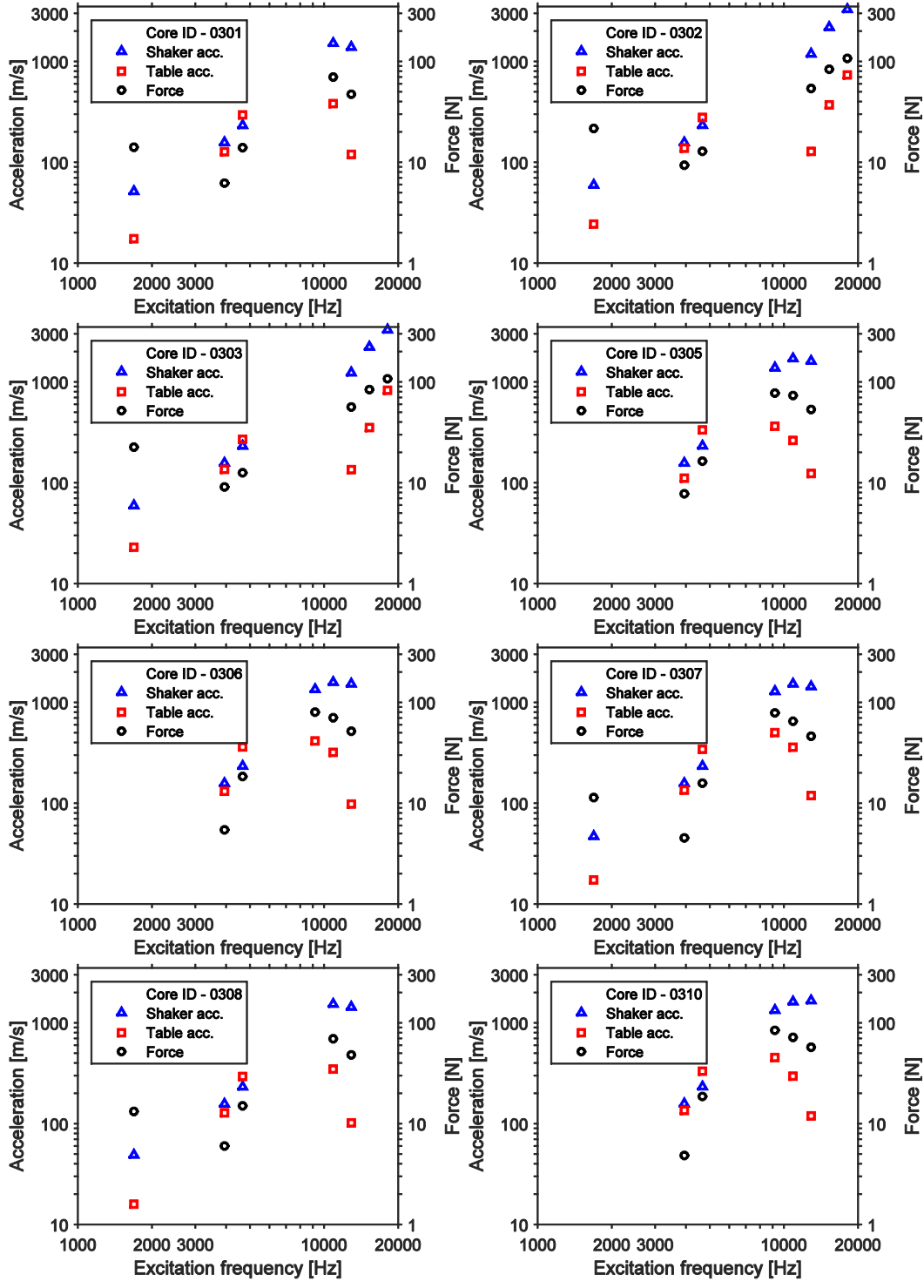
Figure A.16 Effective cancellous layer modulus derived using implicit FE models.

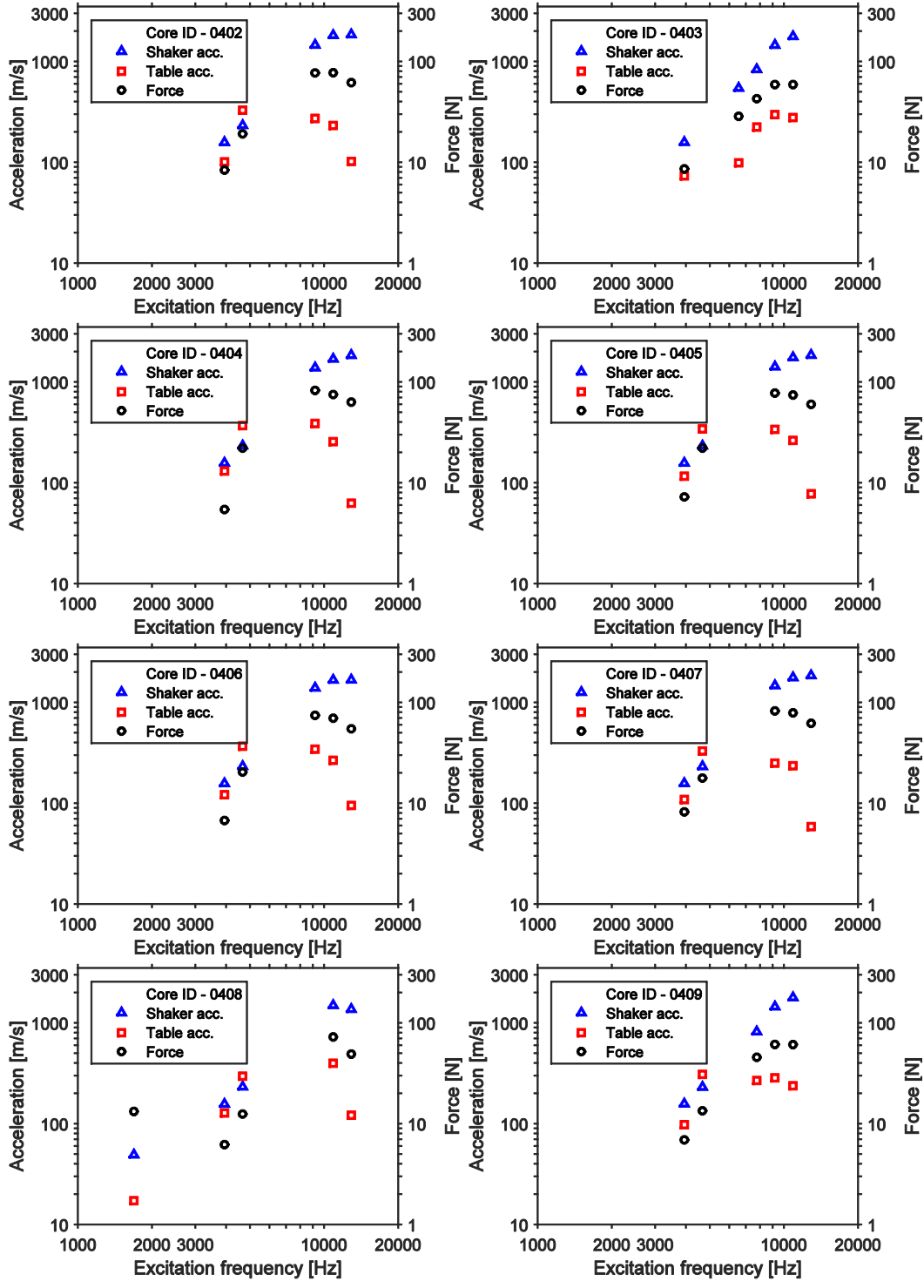
14.6 Core transmissibility testing

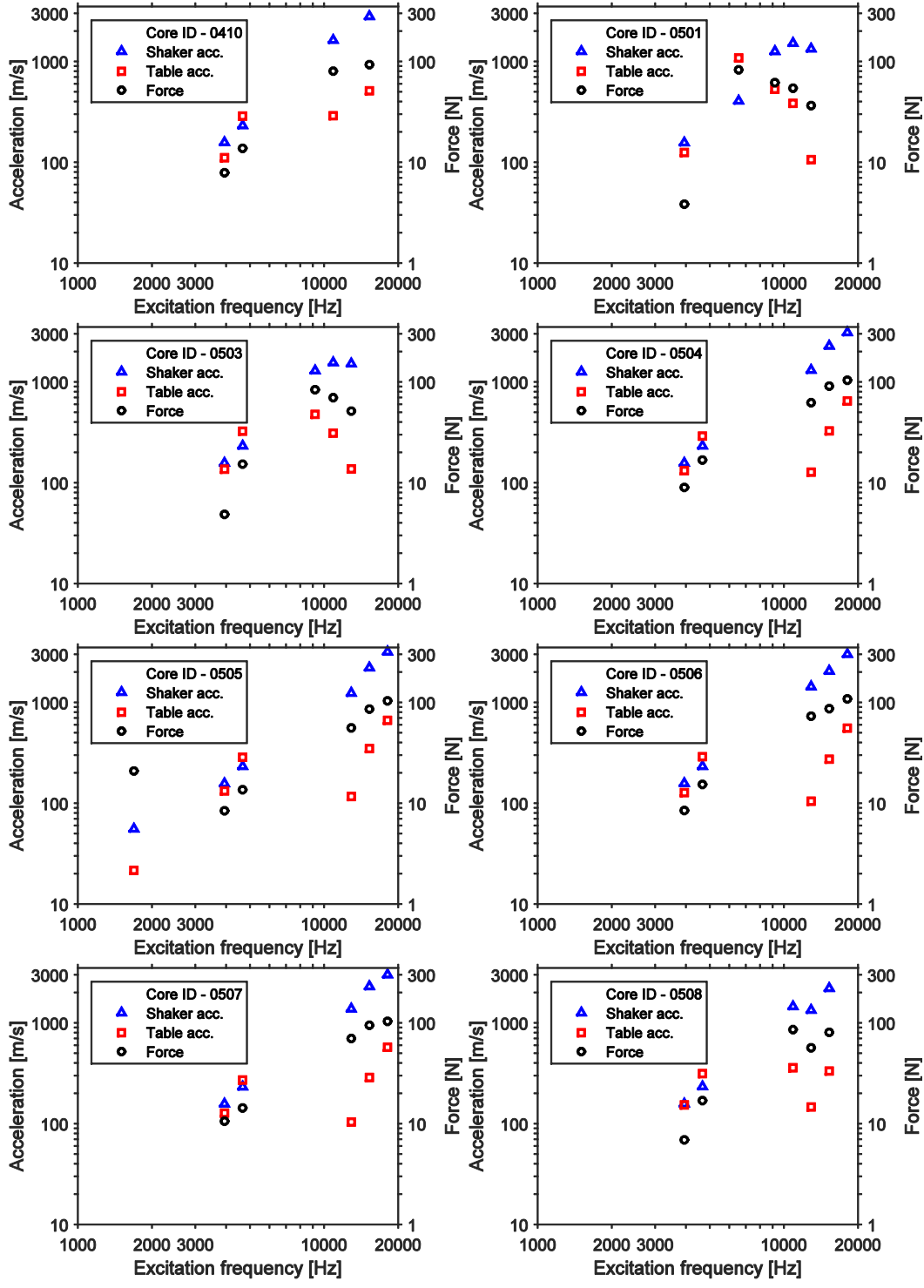
14.6.1 Sample wise Force and Acceleration magnitude spectra

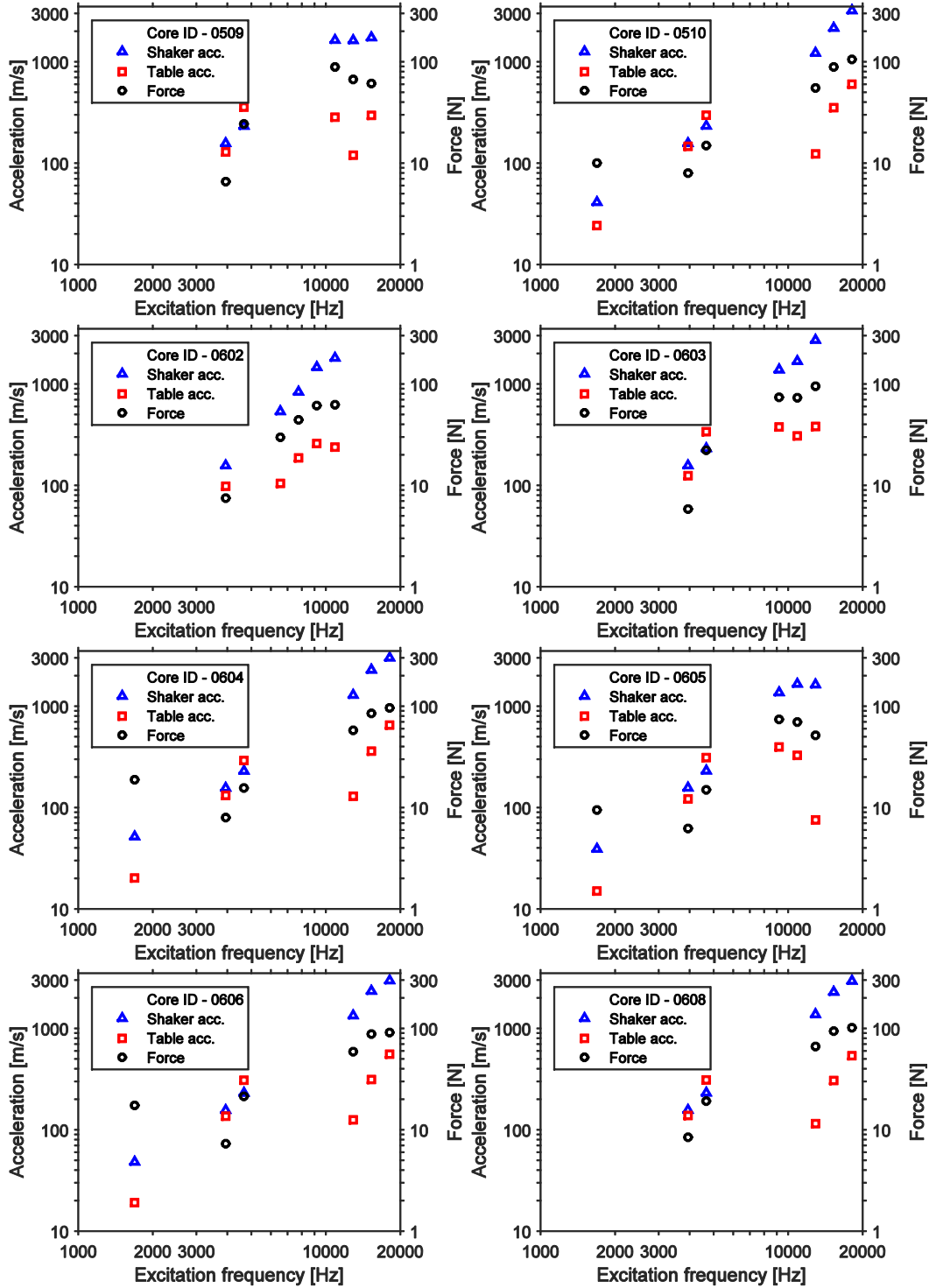


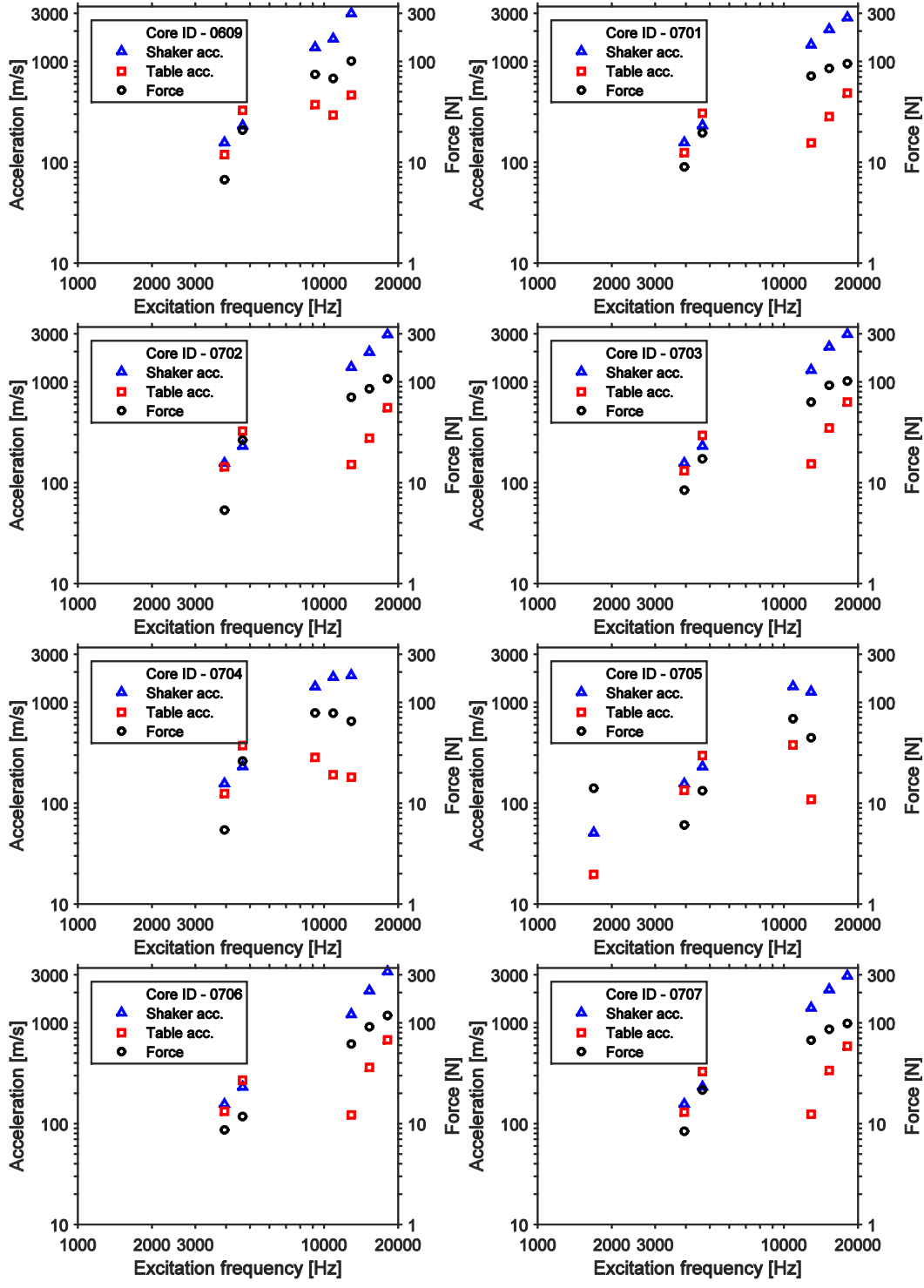


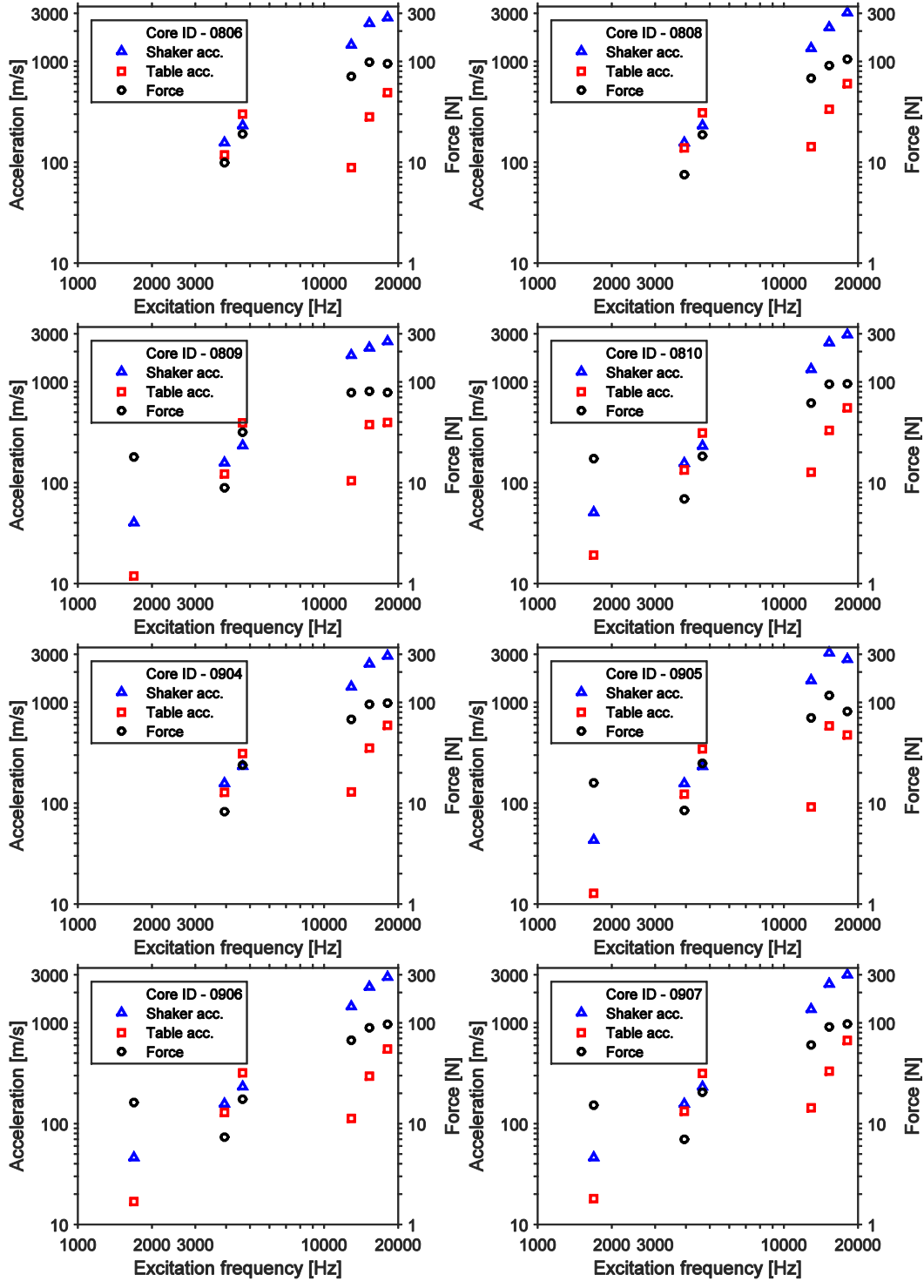


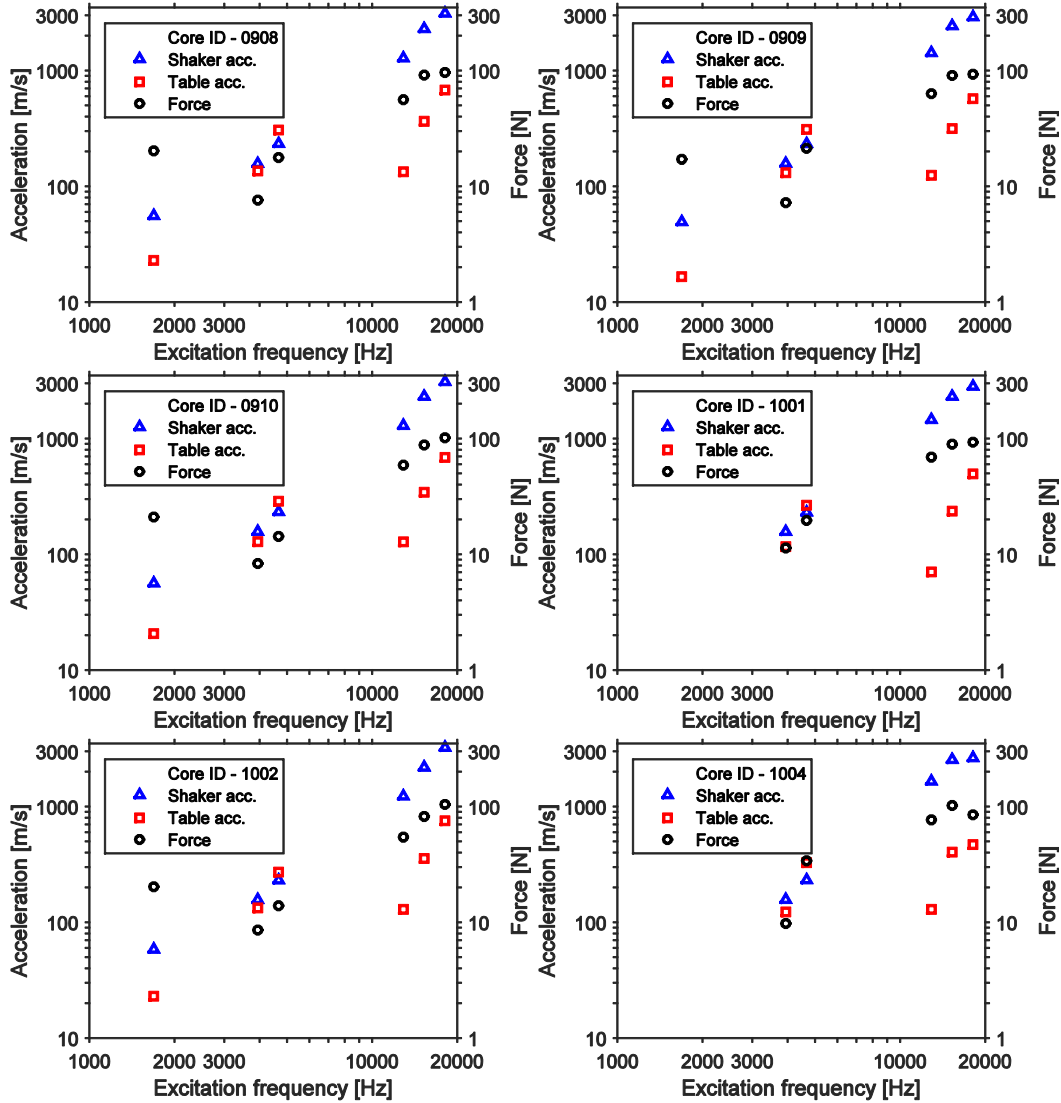


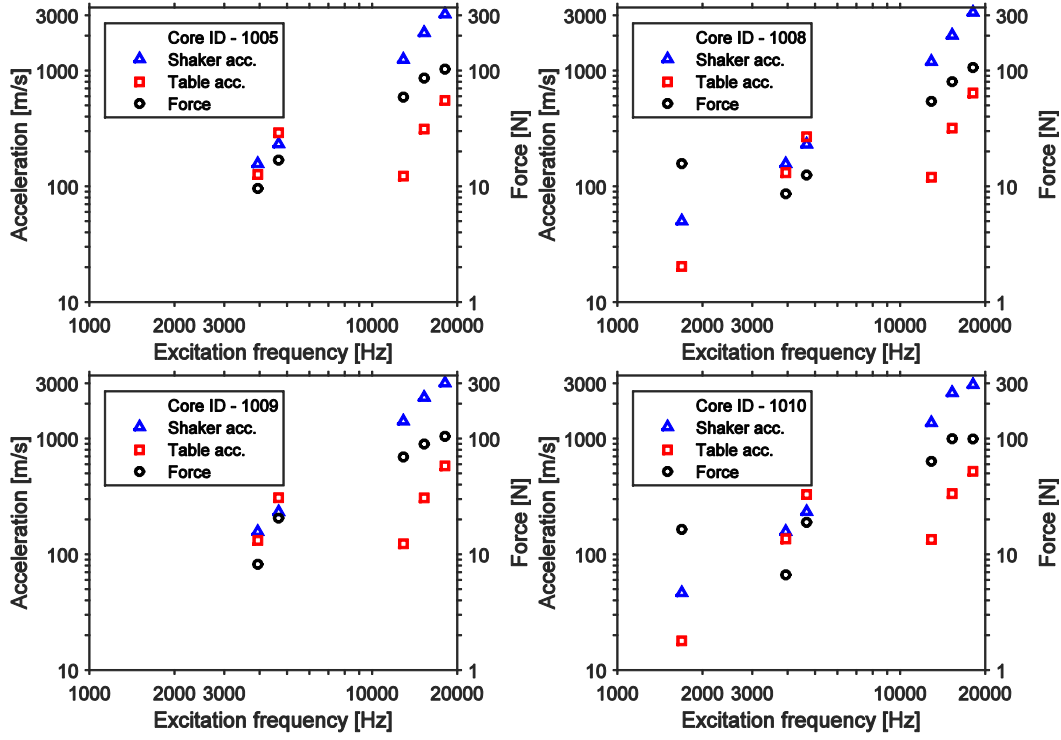




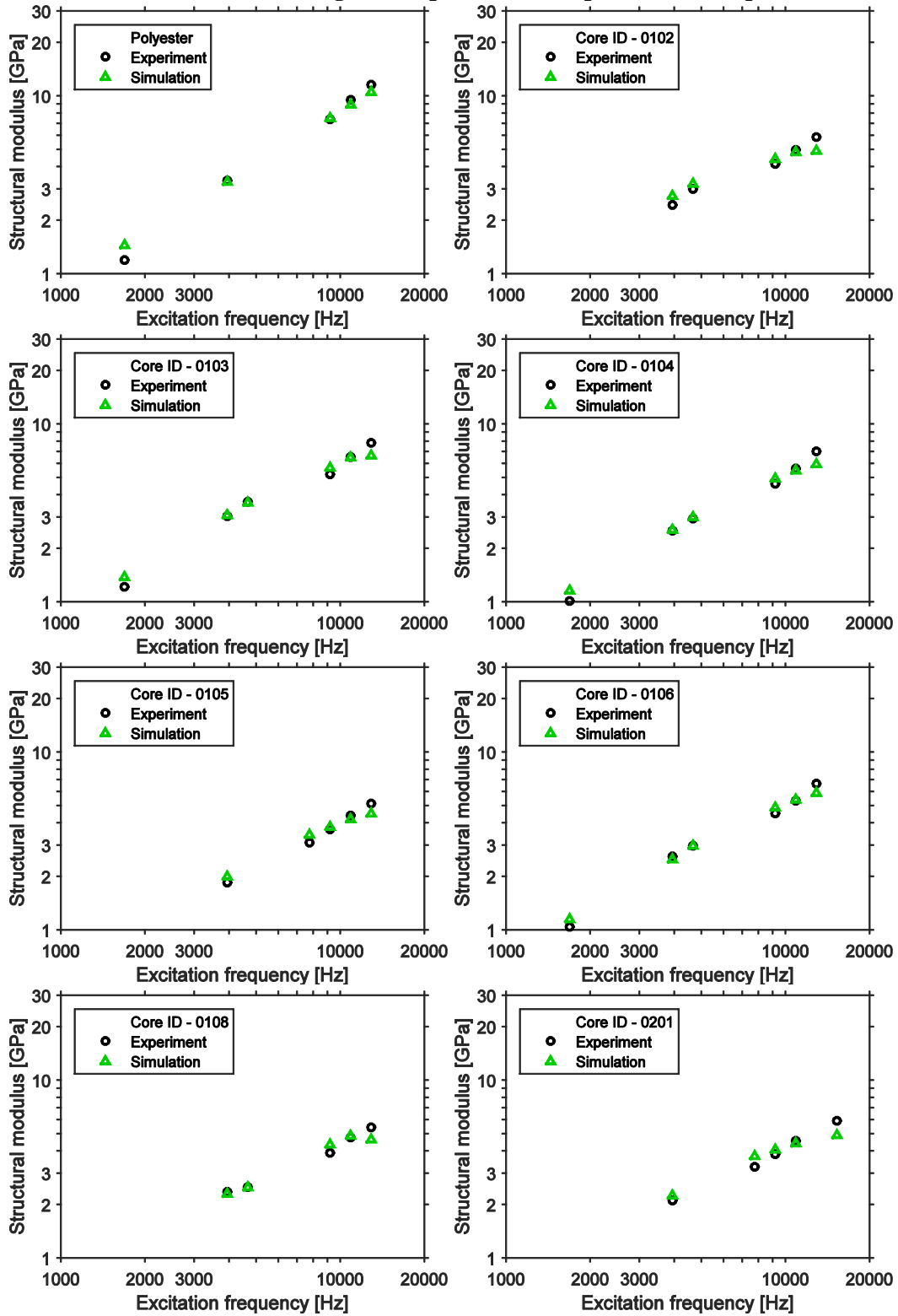


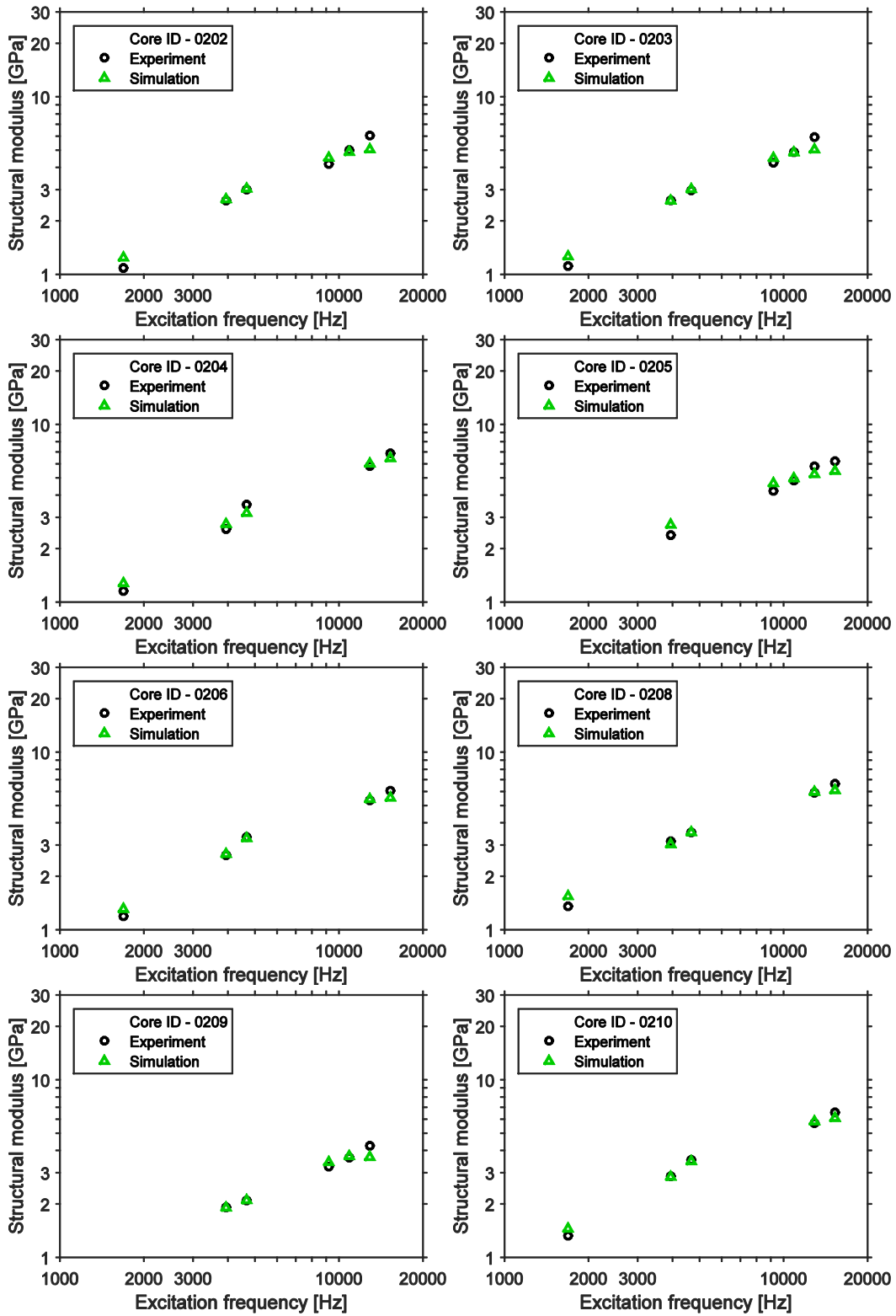


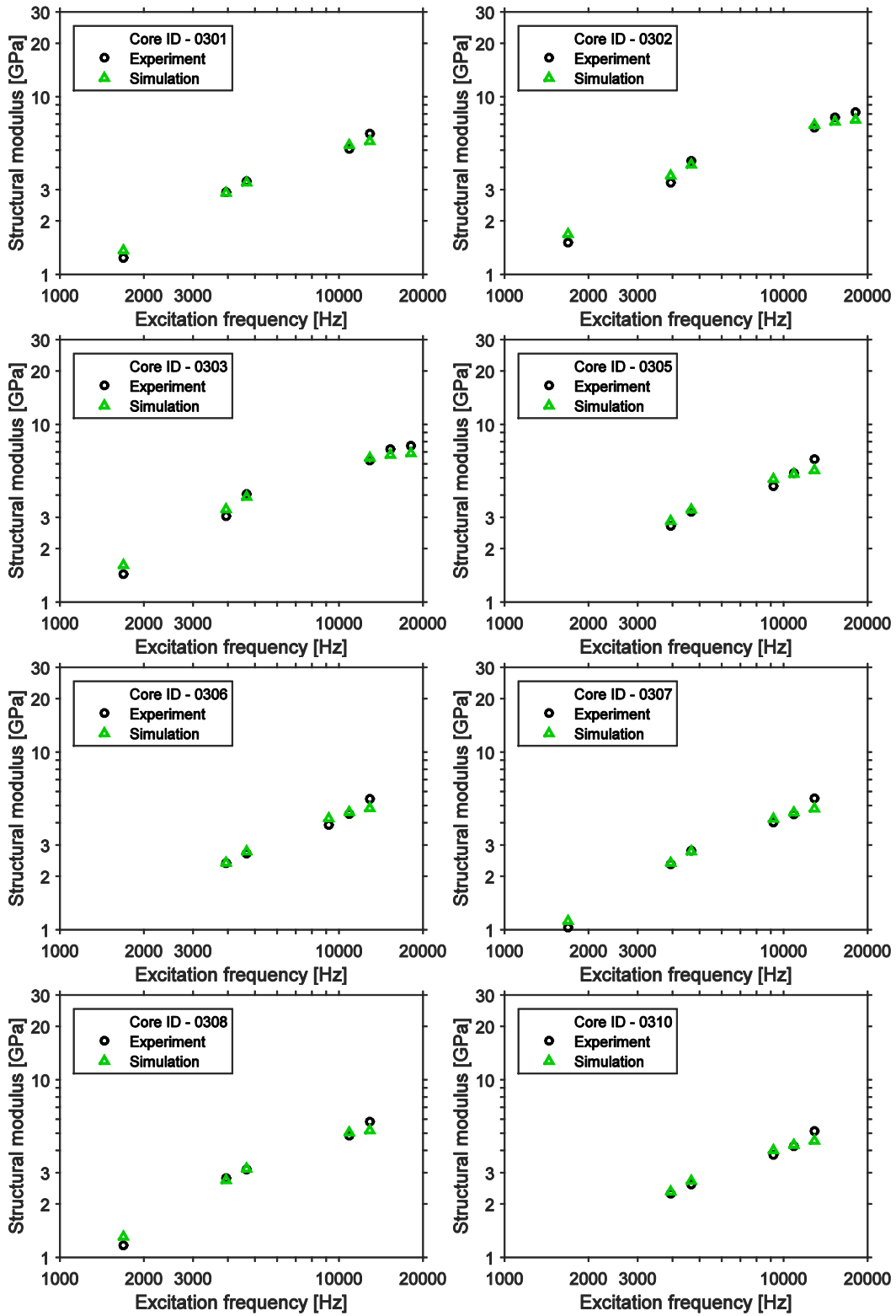


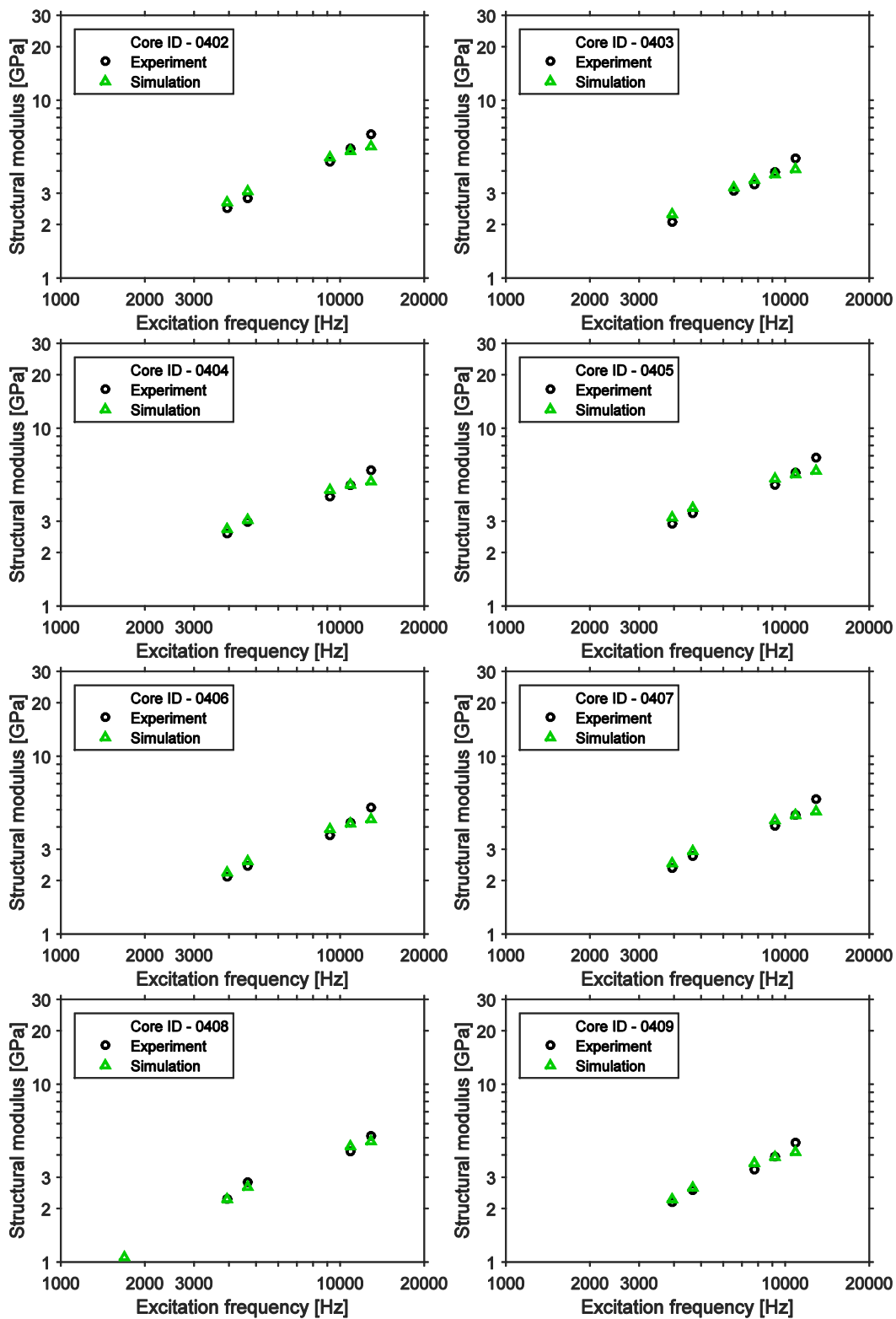


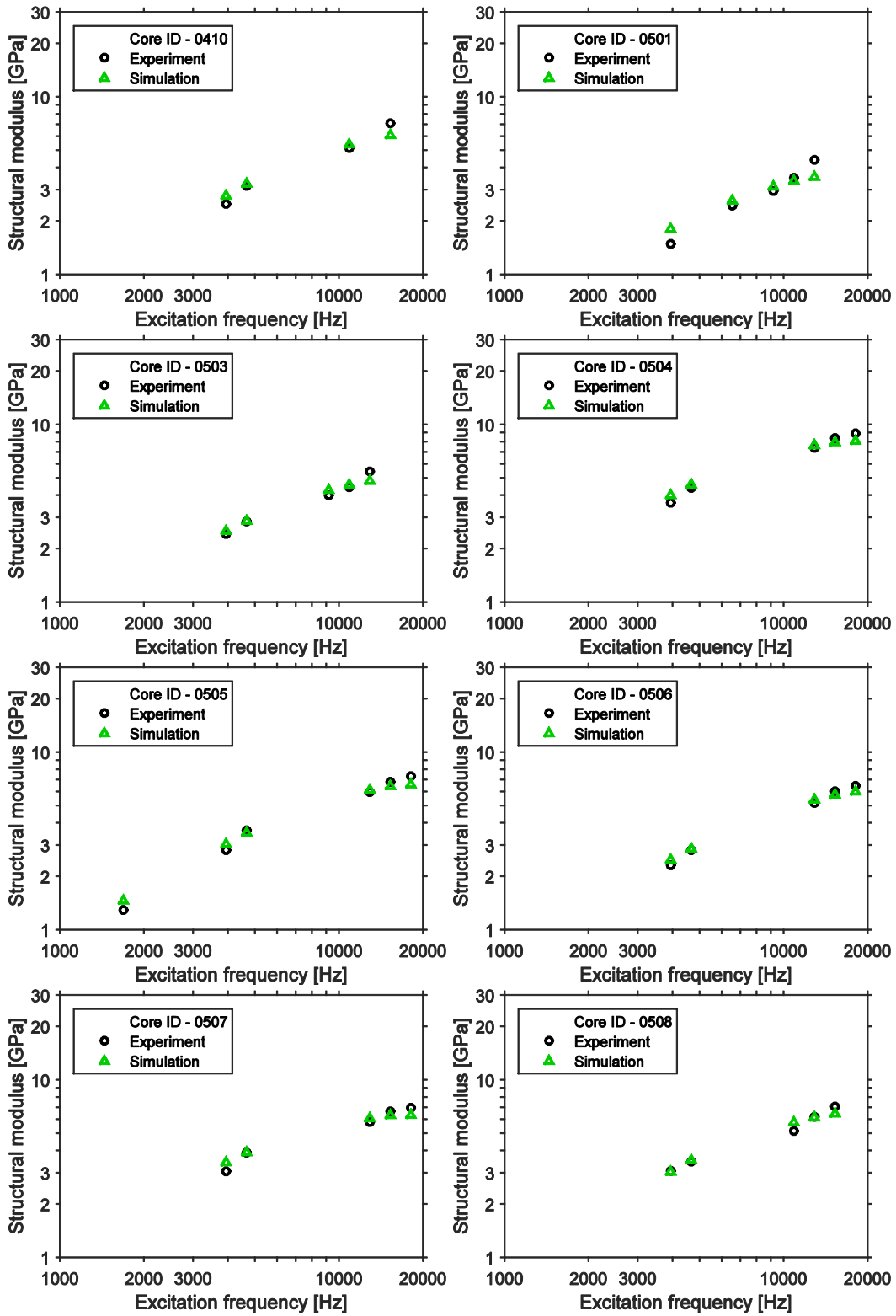
14.6.2 Resultant Modulus magnitude spectra from experiment and optimized simulations

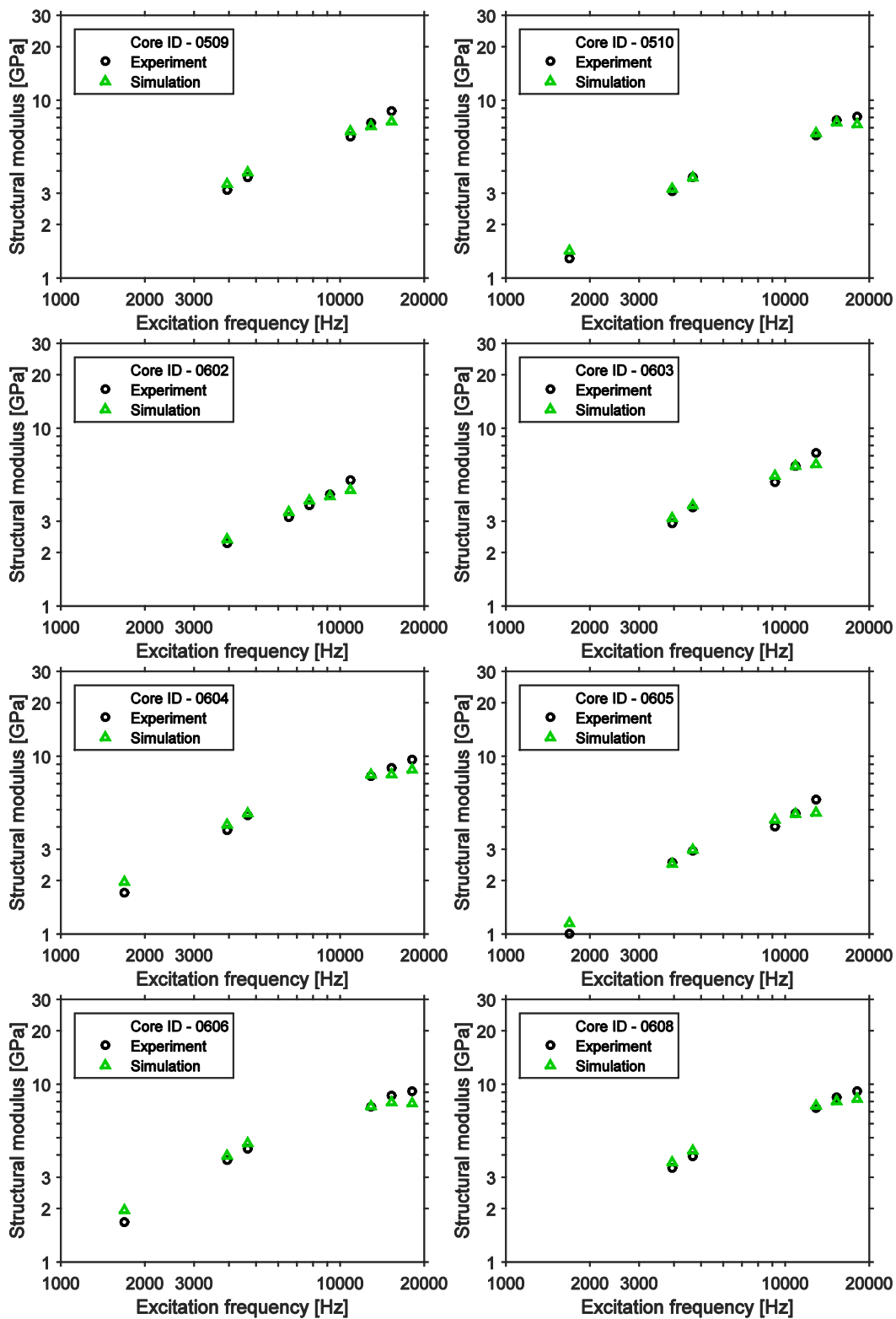


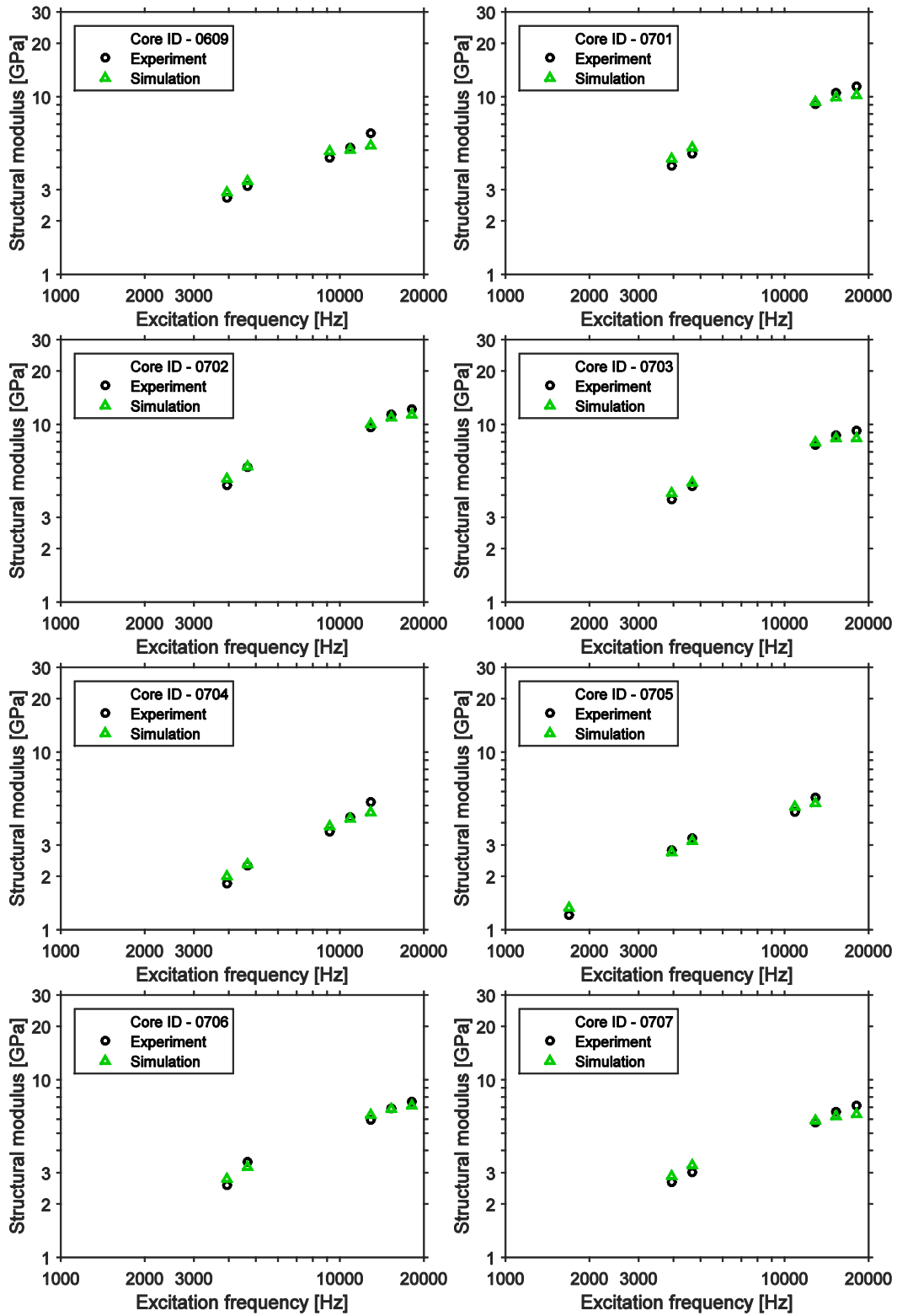


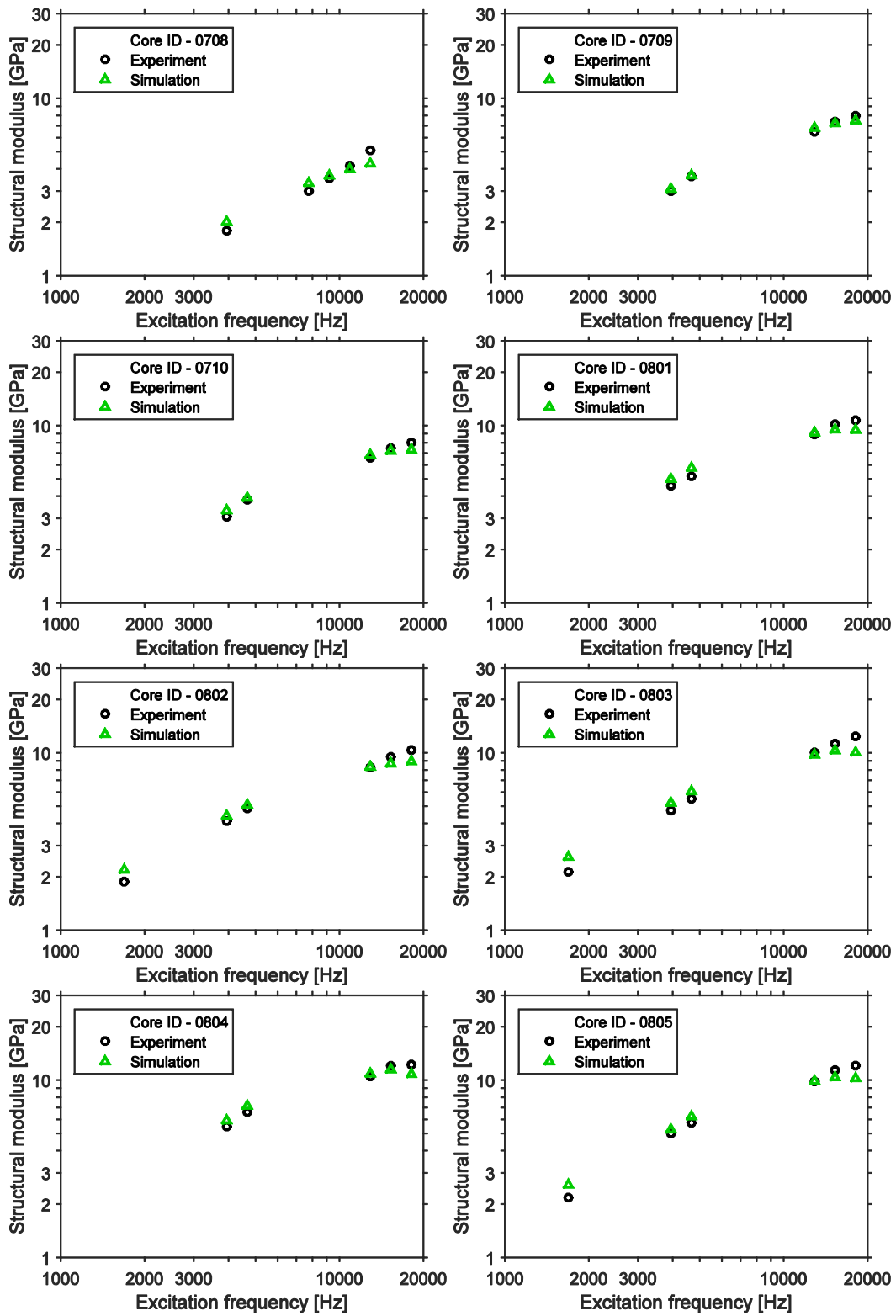


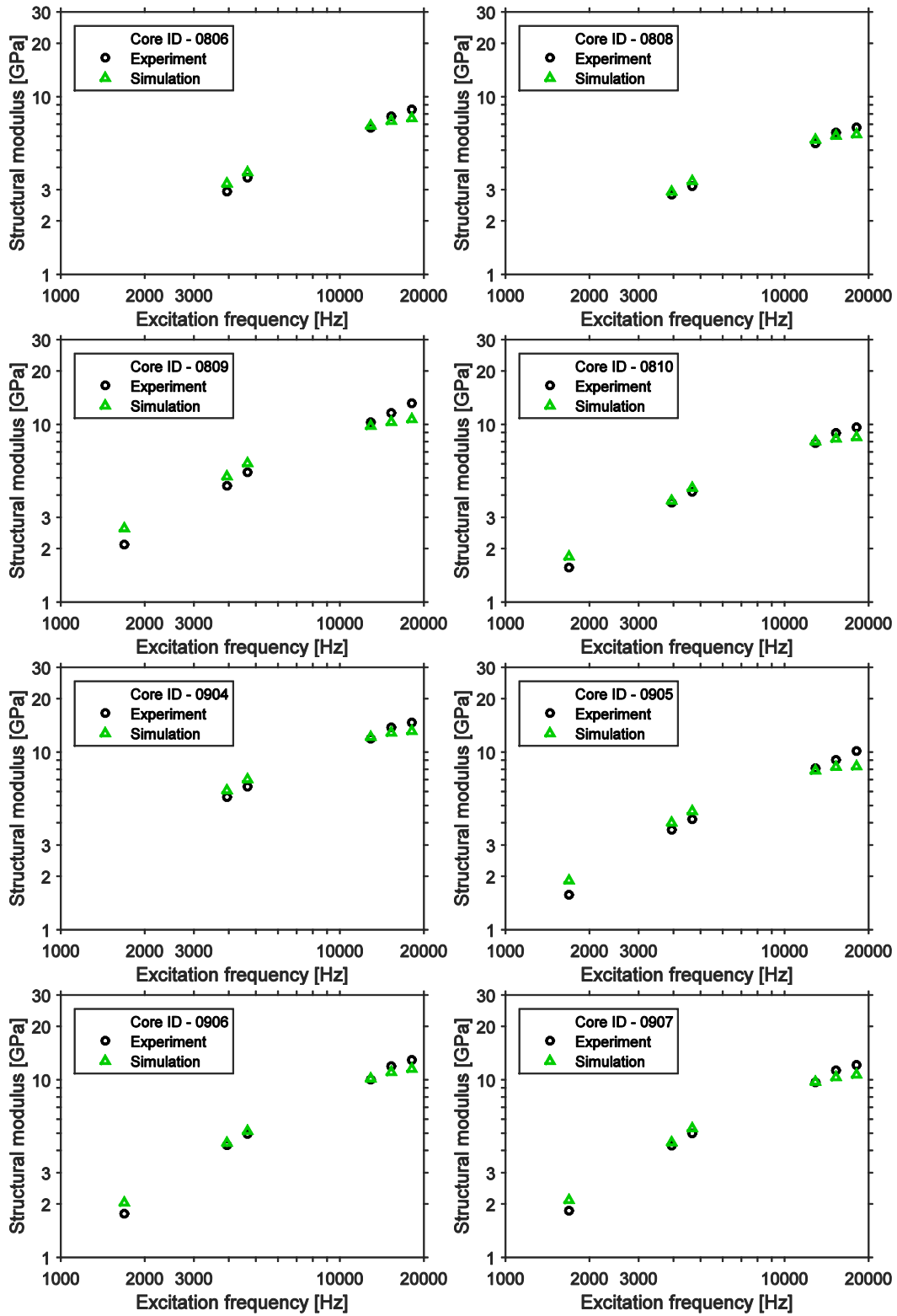


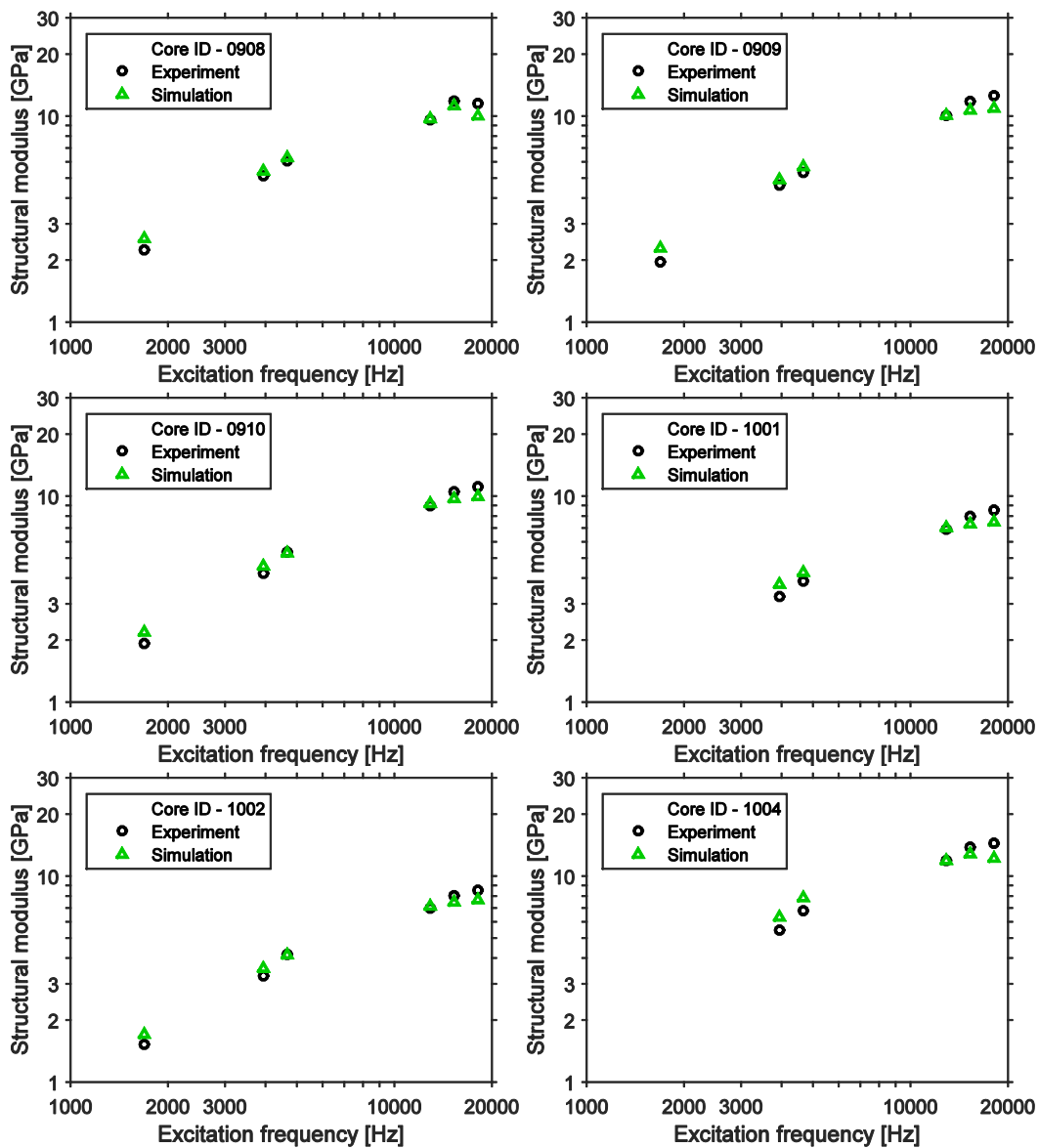


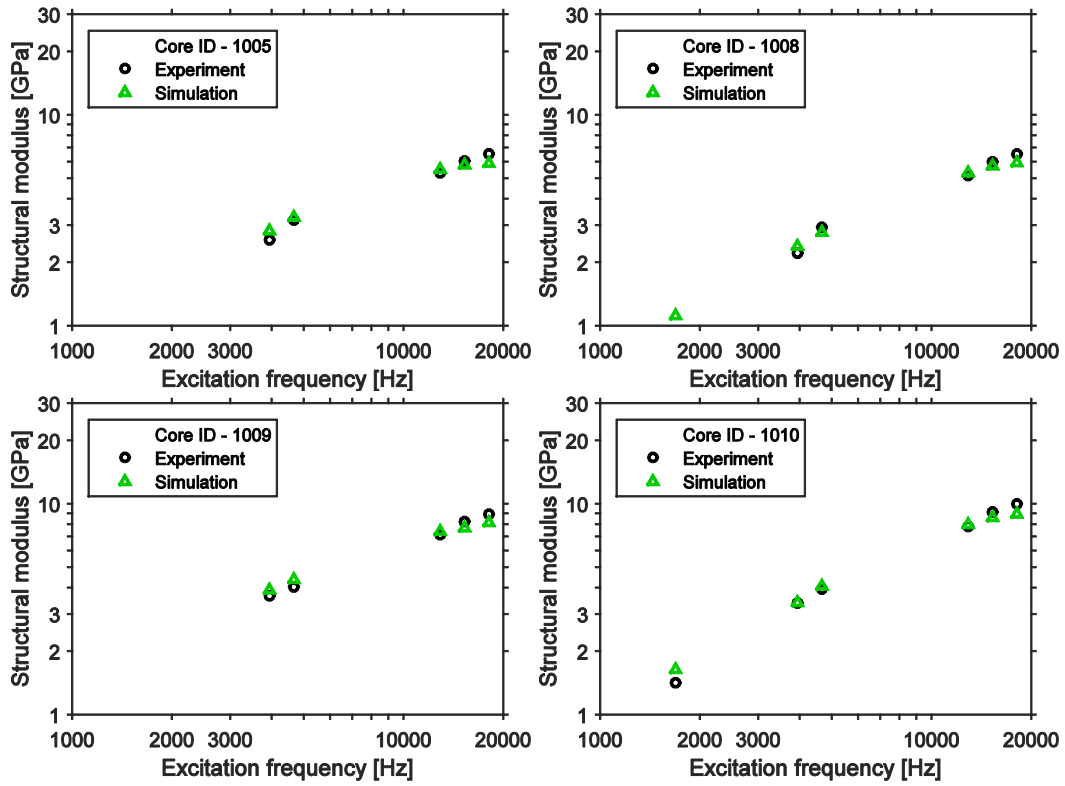




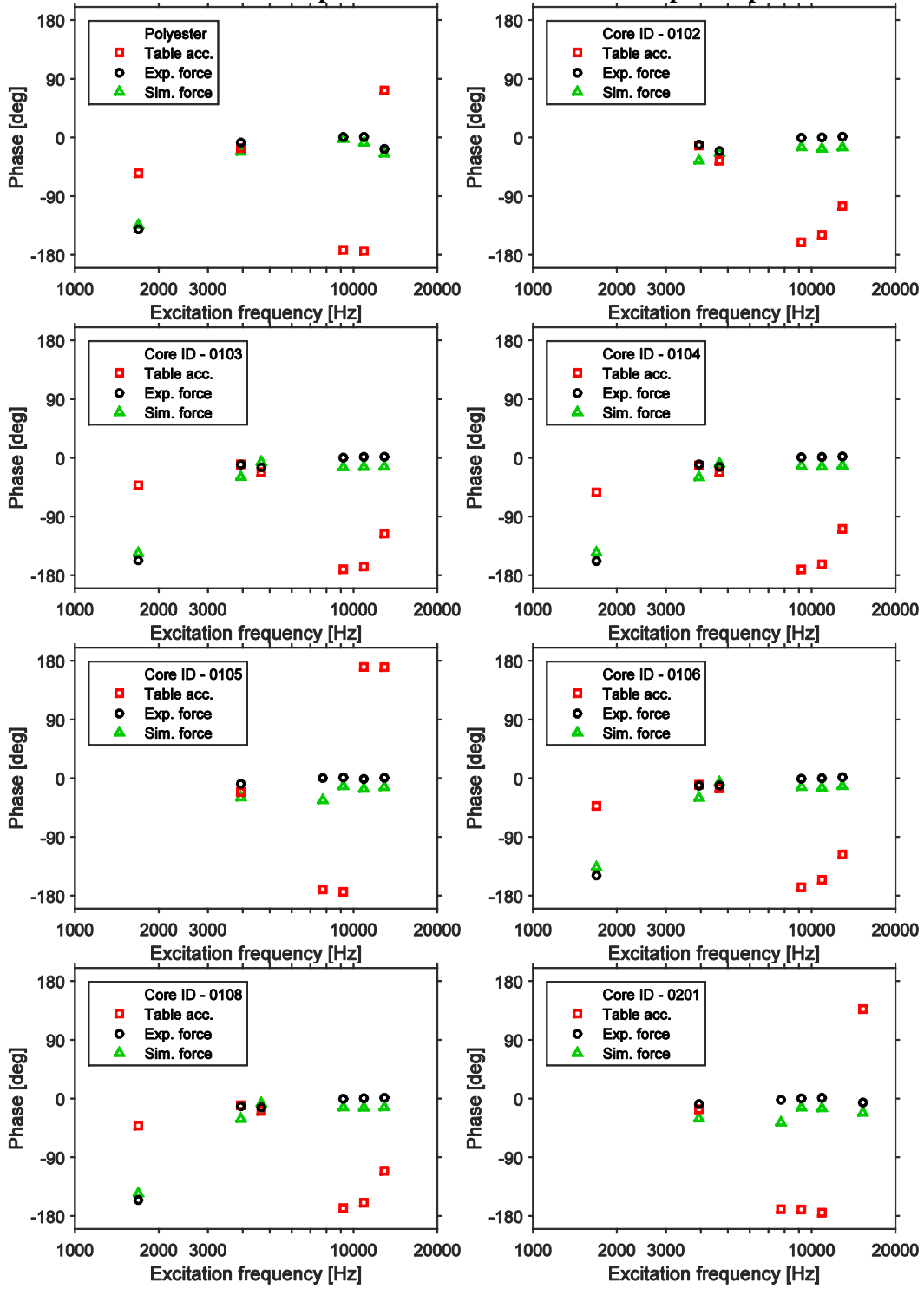


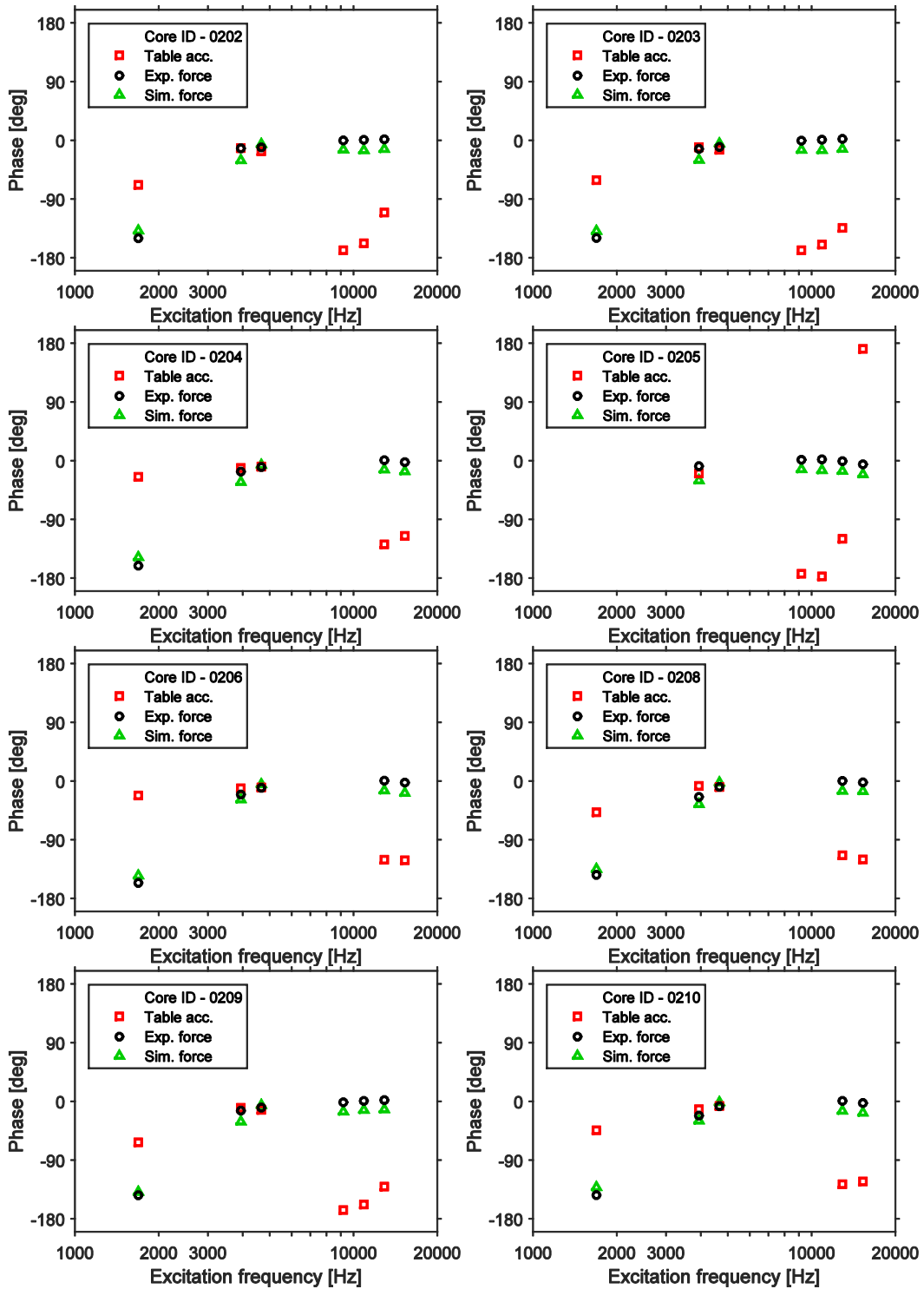


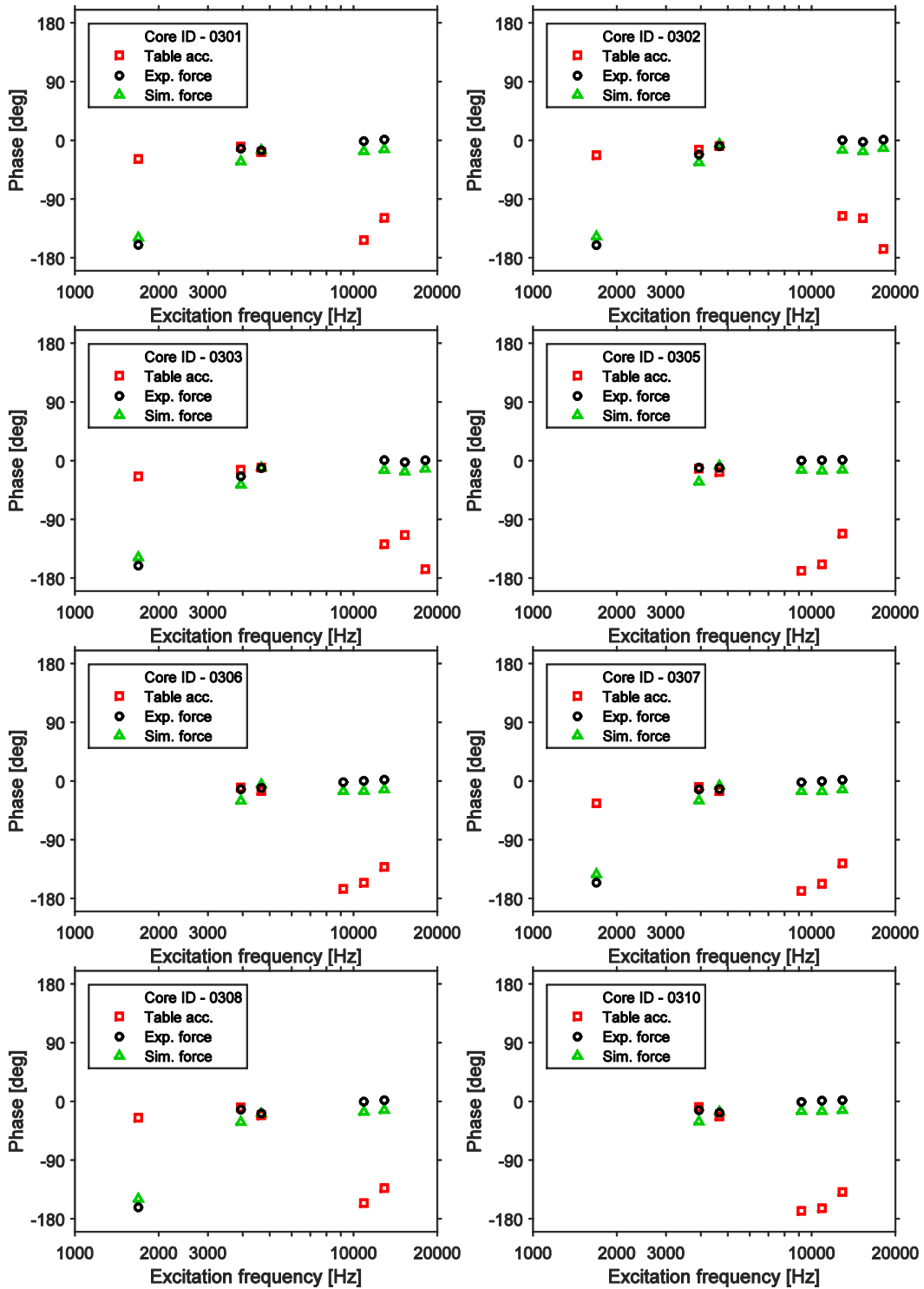


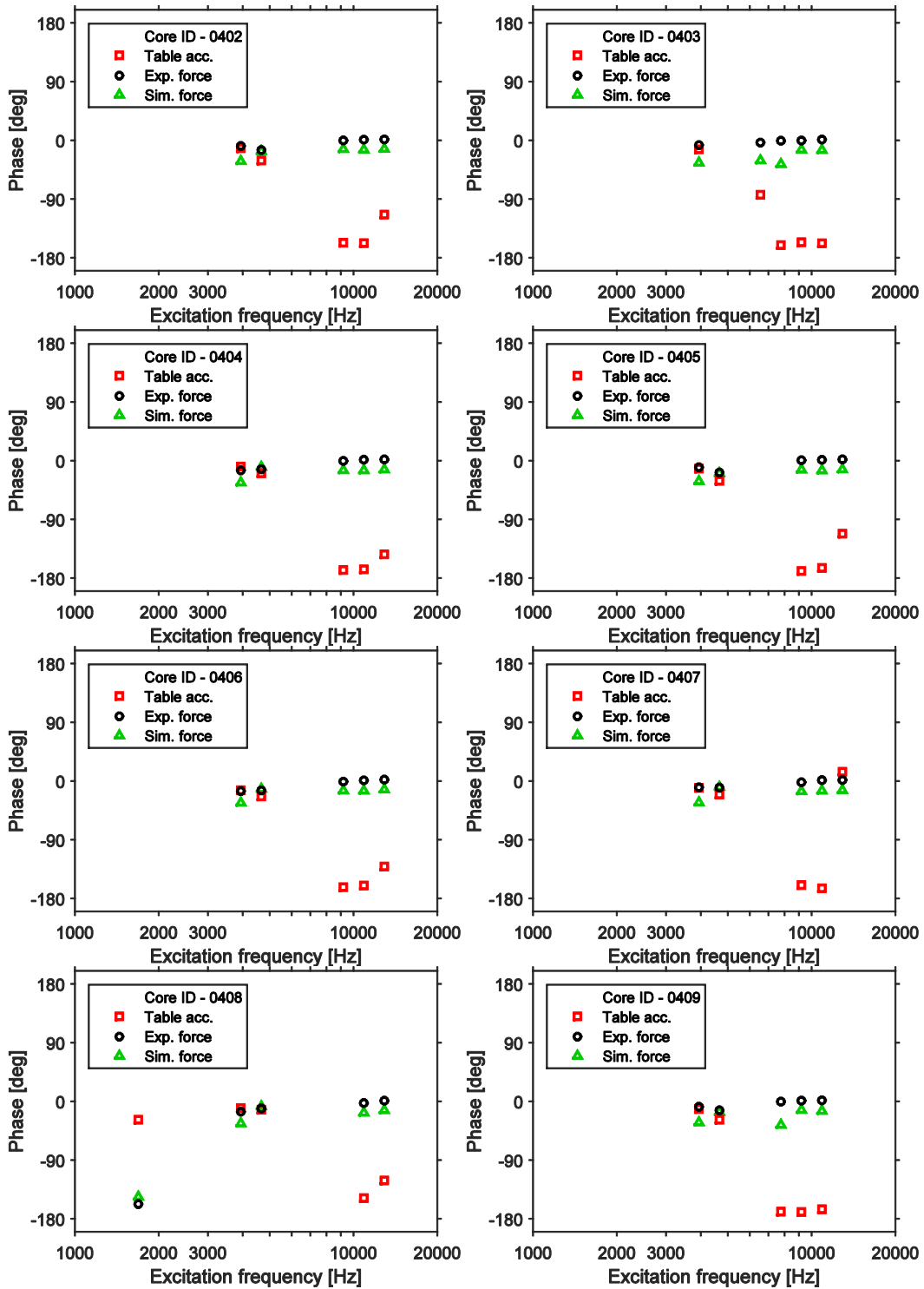


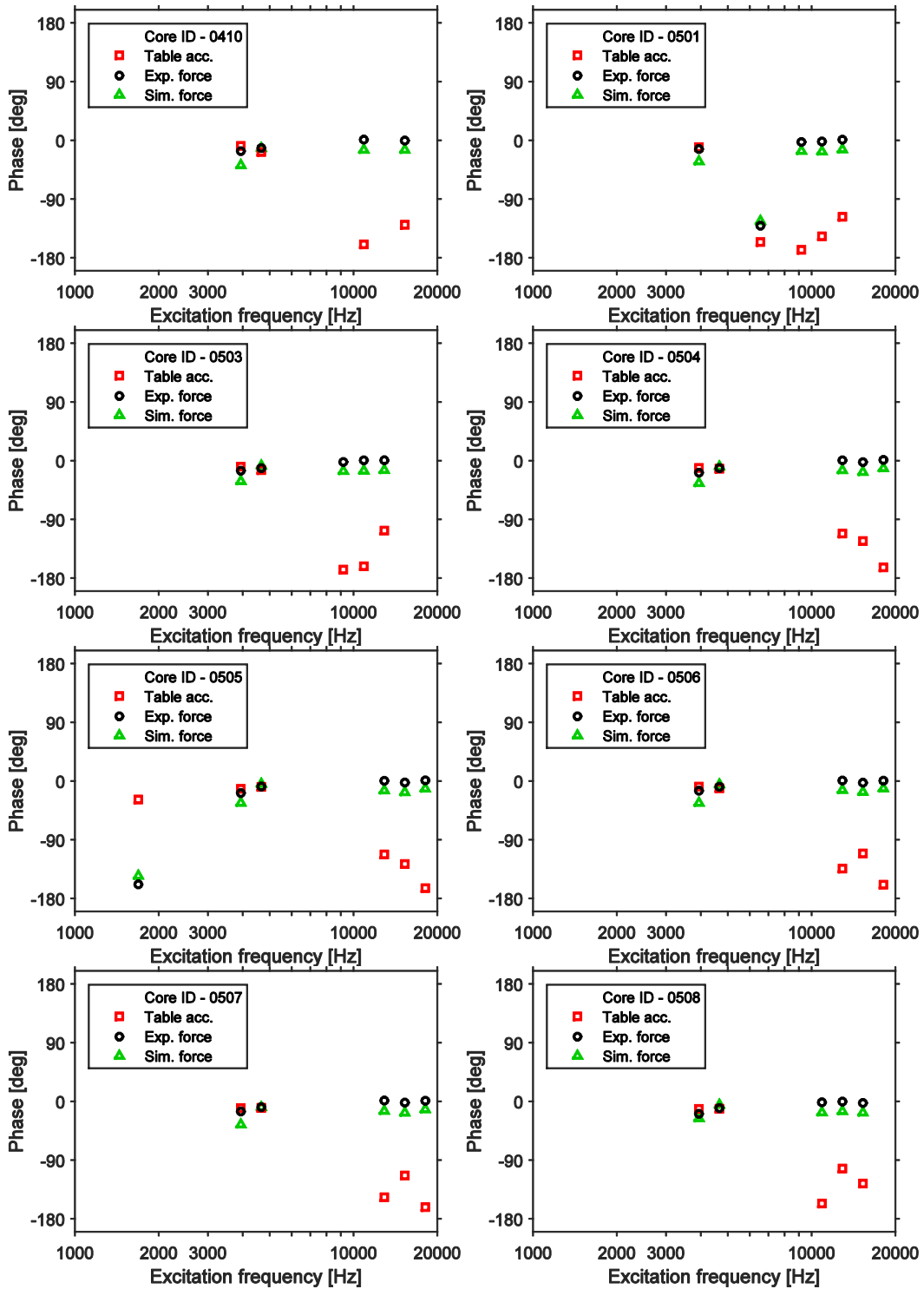
14.6.3 Sample wise Force and Acceleration phase spectra

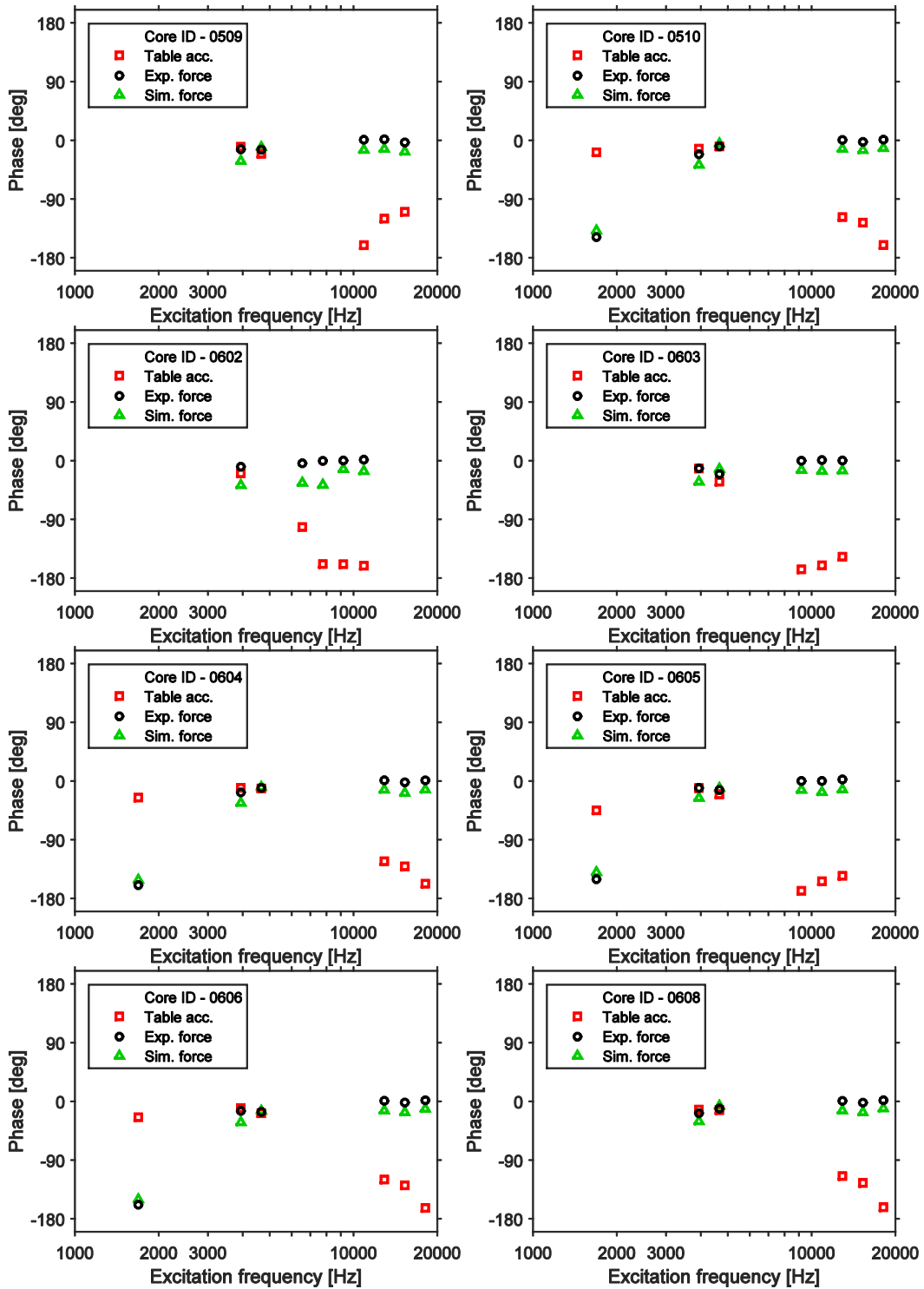


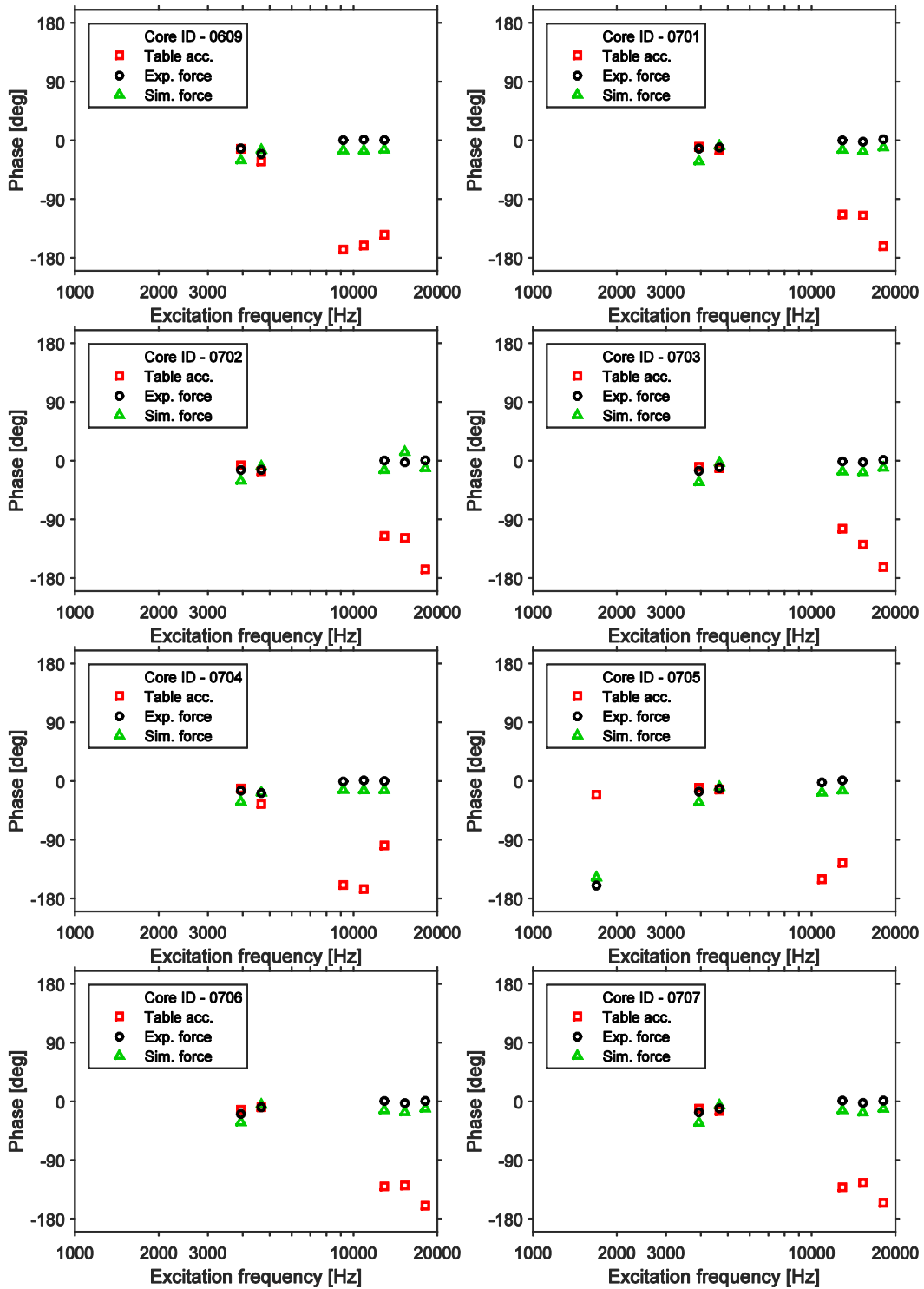


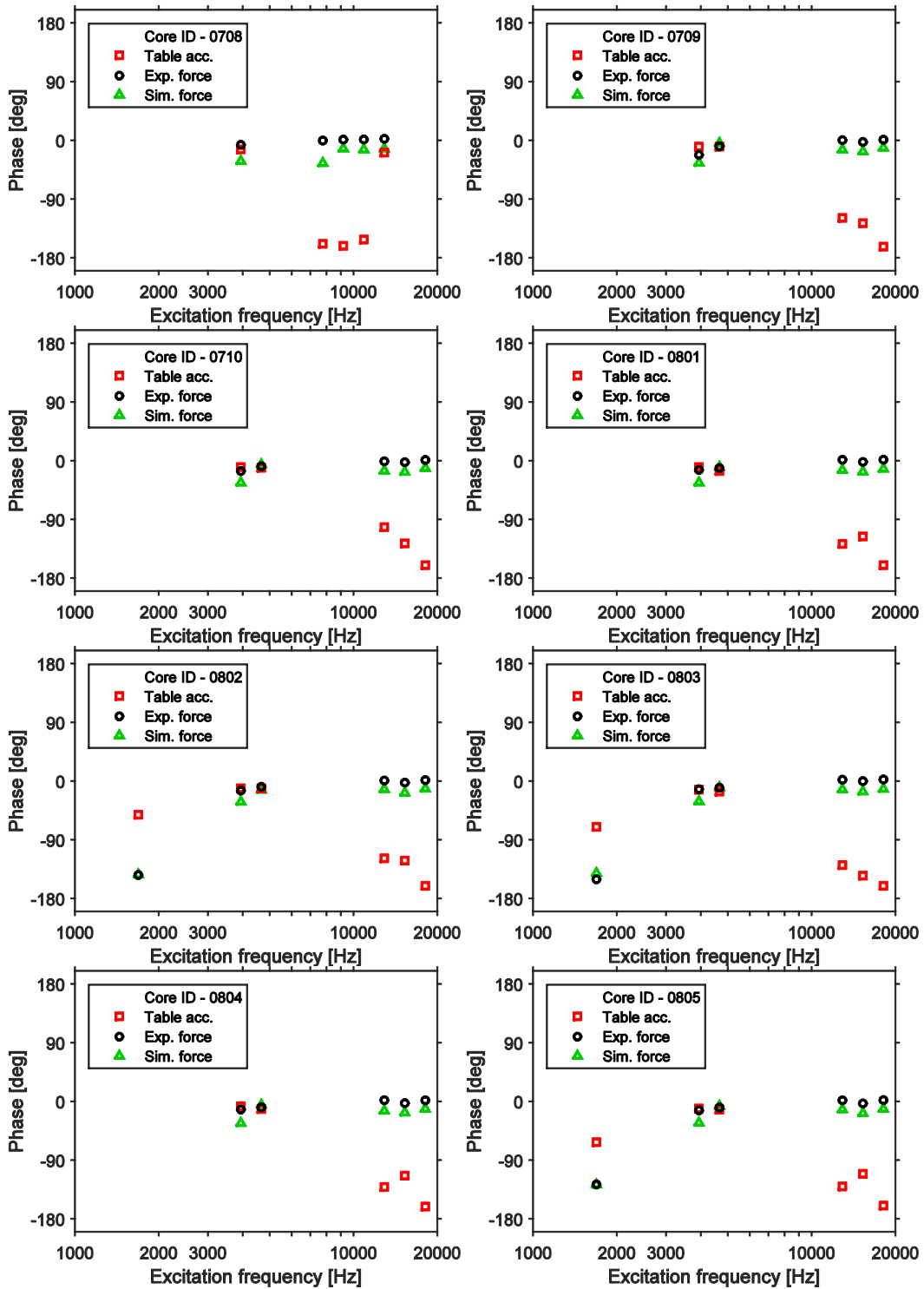


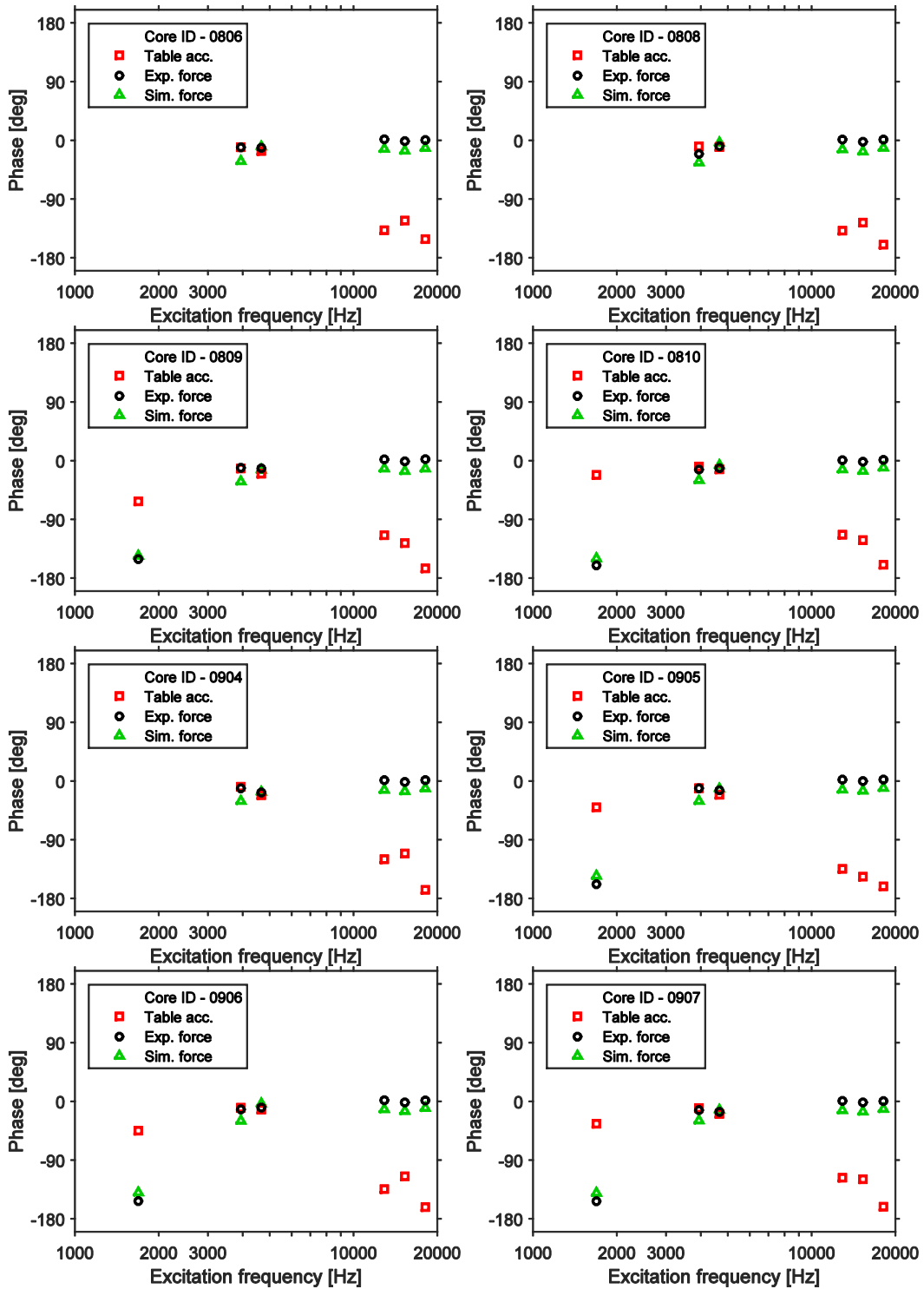


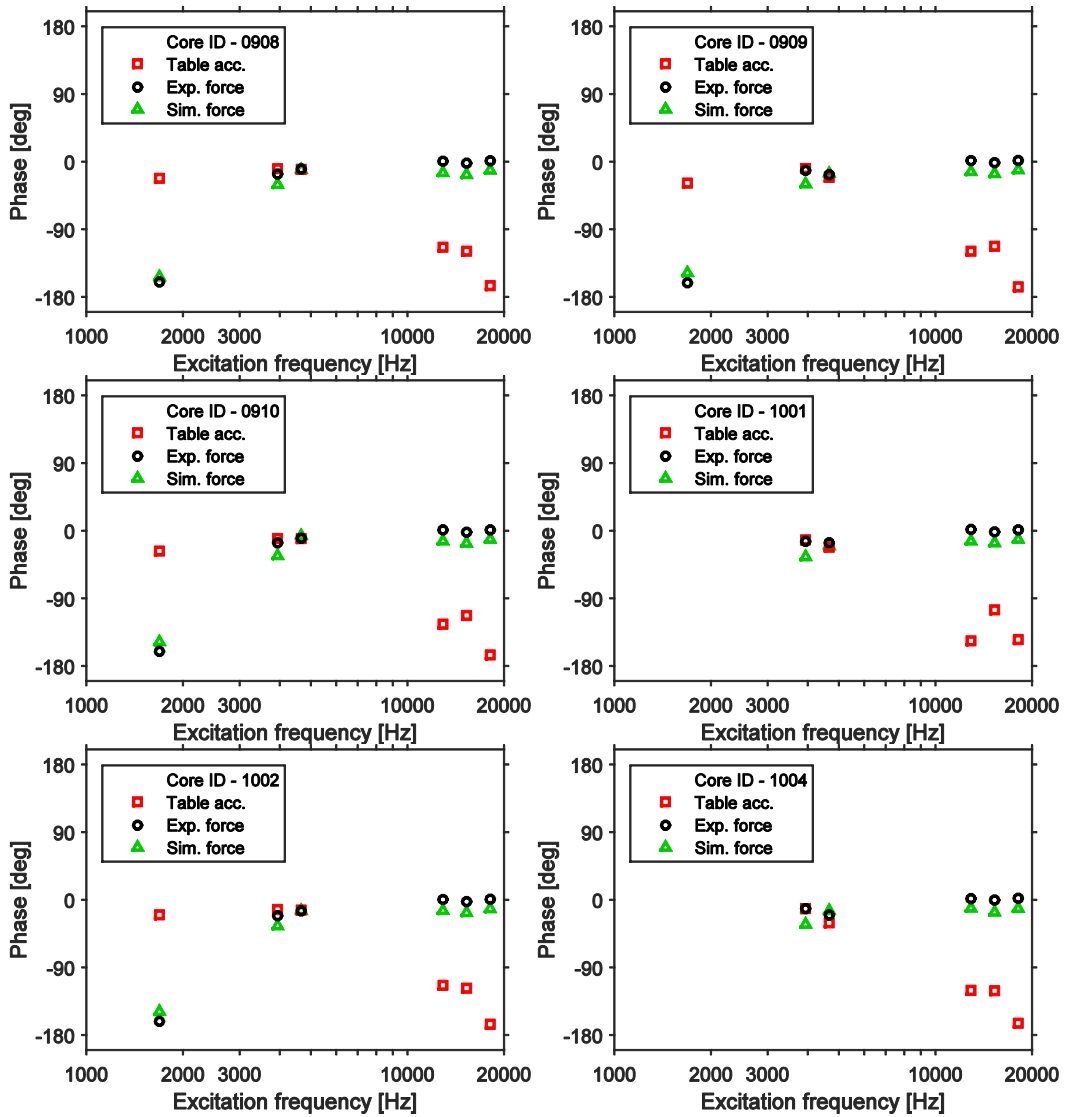












14.6.4 Tabulated results

Table A.30 List of core samples and their viscoelastic properties.

ID	Viscoelastic modulus [50 kHz, 20 μ s]	
	Absolute [MPa]	Fractional
0102	817.75	3.68
0103	1033.07	1.48
0104	1020.97	4.25
0105	877.51	2.60
0106	1129.25	3.34
0108	1153.47	4.59
0201	727.77	2.78
0202	815.83	3.67
0203	779.68	1.73
0204	532.59	2.72
0205	715.23	4.00
0206	561.64	2.27
0208	581.66	2.57
0209	868.72	4.52
0210	764.84	2.28

Table A.30 List of core samples and their viscoelastic properties continued...

ID	Viscoelastic modulus [50 kHz, 20 μ s]	
	Absolute [MPa]	Fractional
0301	670.94	1.56
0302	1265.62	4.90
0303	838.11	2.75
0305	842.56	4.20
0306	737.98	3.17
0307	663.85	3.68
0308	699.36	3.97
0310	935.82	2.30
0402	821.87	3.72
0403	605.98	1.44
0404	617.03	3.00
0405	951.42	5.66
0406	653.12	2.84
0407	736.01	3.69
0408	646.09	1.80
0409	762.85	3.72
0410	943.94	4.88

Table A.30 List of core samples and their viscoelastic properties continued...

ID	Viscoelastic modulus [50 kHz, 20 μ s]	
	Absolute [MPa]	Fractional
0501	538.89	2.52
0503	709.16	3.52
0504	1038.38	4.03
0505	1010.55	5.30
0506	763.43	3.66
0507	621.19	3.55
0508	855.21	3.19
0509	1232.72	3.74
0510	632.73	1.82
0602	665.23	3.68
0603	1300.80	4.44
0604	848.27	3.58
0606	847.27	5.07
0608	1286.28	5.98

Table A.30 List of core samples and their viscoelastic properties continued...

ID	Viscoelastic modulus [50 kHz, 20 μ s]	
	Absolute [MPa]	Fractional
0701	1451.59	5.72
0702	550.41	1.97
0703	254.46	0.90
0704	581.40	3.55
0705	589.45	2.46
0708	447.05	3.45
0709	1044.34	3.97
0710	913.74	5.03
0801	707.57	1.88
0802	749.54	3.20
0803	640.28	1.77
0804	650.47	2.66
0805	603.02	1.73
0806	1083.26	3.47
0809	598.52	1.13
0810	669.39	2.03

Table A.30 List of core samples and their viscoelastic properties continued...

ID	Viscoelastic modulus [50 kHz, 20 μ s]	
	Absolute [MPa]	Fractional
0904	2279.96	4.31
0905	2110.84	5.11
0908	1450.95	1.93
0909	1980.57	3.65
0910	1766.75	3.03
1001	842.78	5.21
1002	1052.34	4.23
1004	963.87	2.86
1005	618.36	5.17
1009	378.60	1.75
1010	1407.90	3.91

14.6.5 Statistical test results

Table A.31 Results of normality tests (p-values from Shapiro-Wilk test) of viscoelastic modulus of the diploe layer for each subject.

Sub	Absolute	Fractional
1	0.510	0.951
2	0.387	* 0.015
3	* 0.046	0.832
4	0.172	0.767
5	0.604	0.697
6	0.180	0.351
7	0.465	0.955
8	* 0.003	0.700
9	0.895	0.927
10	0.992	0.263

Significant values ($\alpha=0.05$) are shown in bold and marked with an asterisk.

Table A.32 Results of one-way within subjects ANOVA tests of viscoelastic modulus of the diploe layer.							
Dependent variable	DF	SS	MS	F	p	ges	
Main effect – Subject							
Absolute	9	6423k	714k	12.36	* 0.000	0.638	
Fractional	9	10.04	1.12	2.46	* 0.018	0.260	
Dependent variable	DFn	DFd	SSn	SSd	F	p	ges
Main effect – is frontal, random effect – Subject							
Absolute	1	8	0k	69k	0.002	0.970	0.000
Fractional	1	8	0.945	1.287	5.871	* 0.042	0.114
Main effect – is superior, random effect – Subject							
Absolute	1	9	1k	265k	0.036	0.853	0.000
Fractional	1	9	0.248	7.049	0.316	0.588	0.019
Significant values ($\alpha=0.05$) are shown in bold and marked with an asterisk.							

14.6.6 Distribution of viscoelastic modulus over the calvarium of each subject

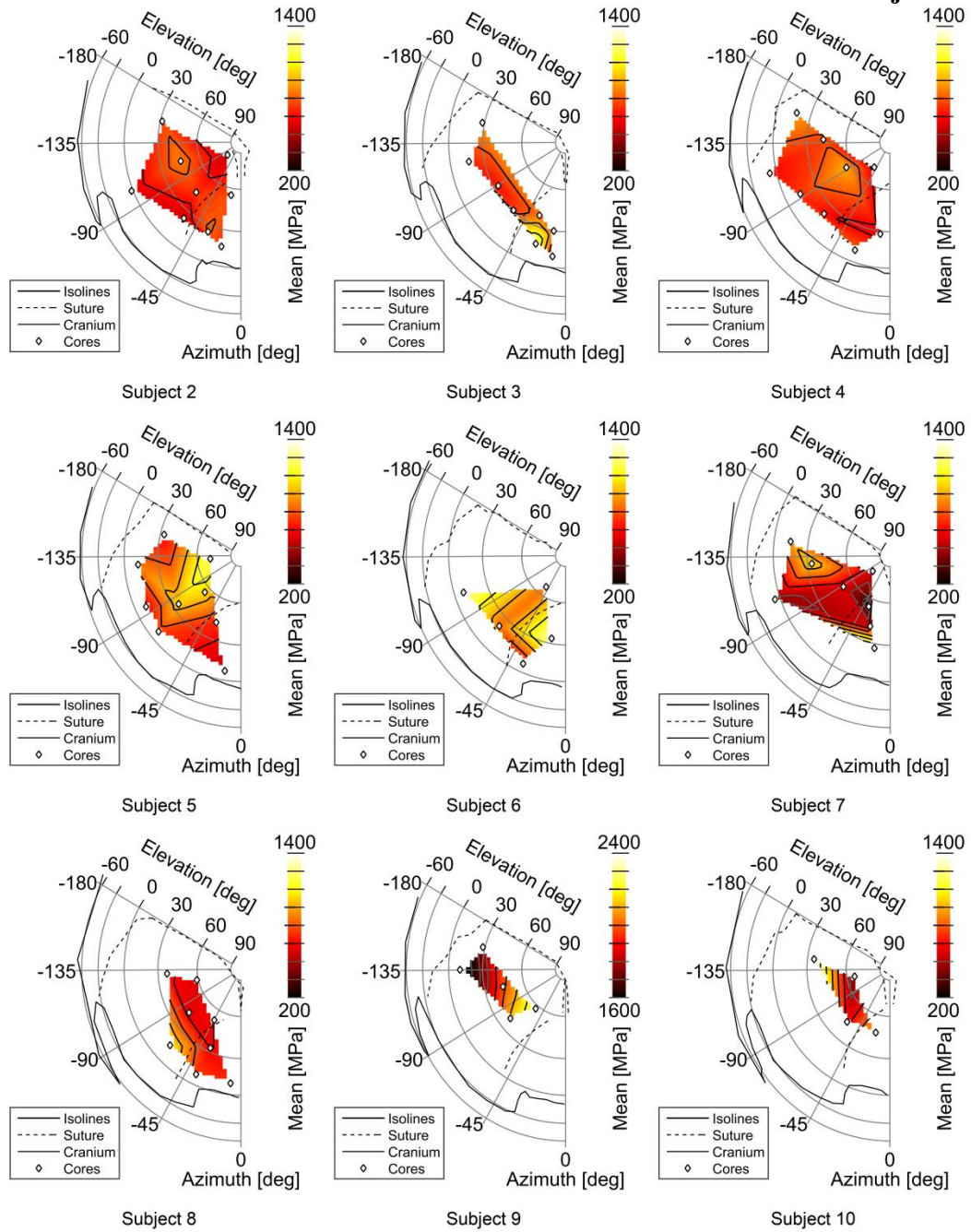


Figure A.17 Effective diploe layer viscoelastic modulus (absolute values).

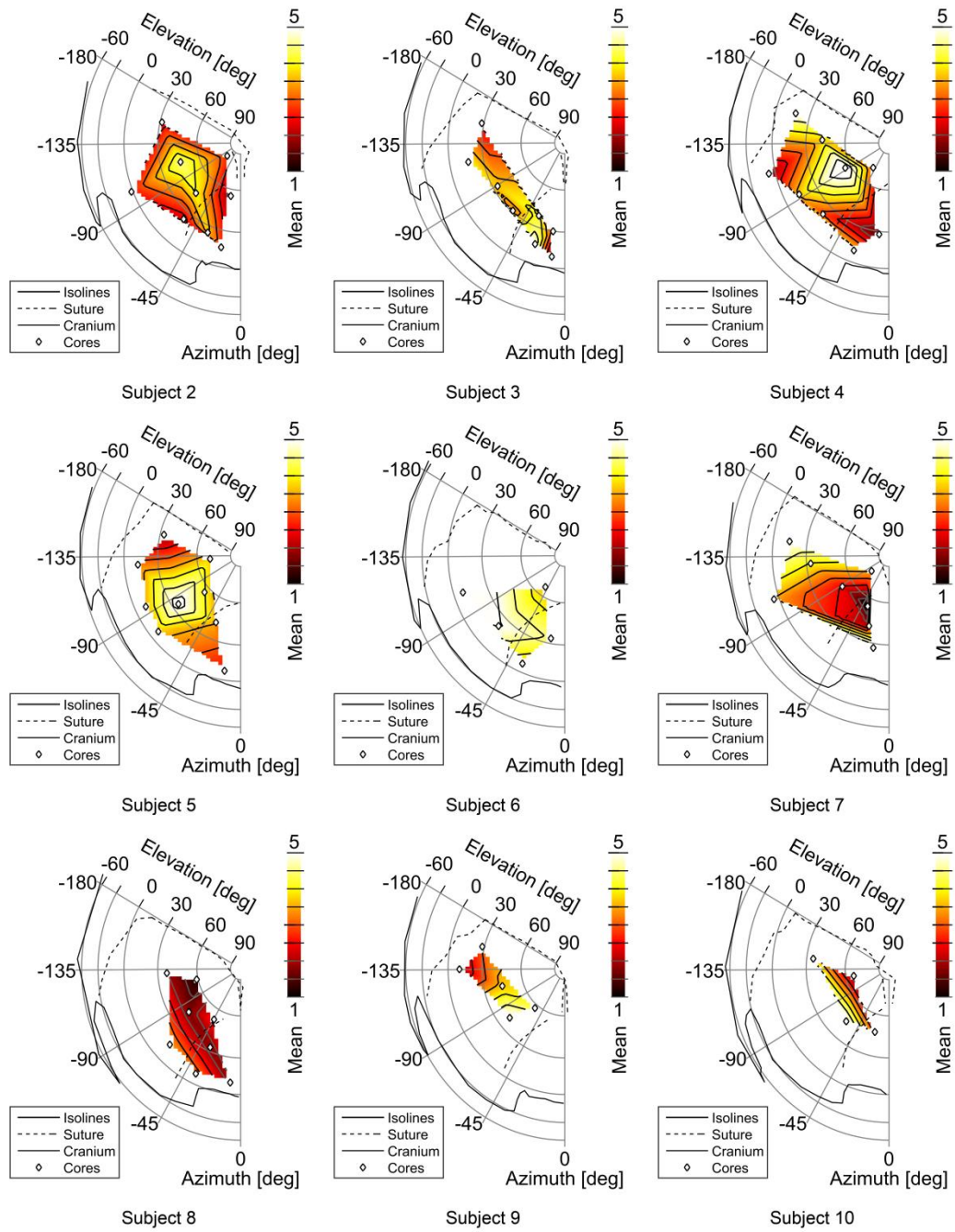
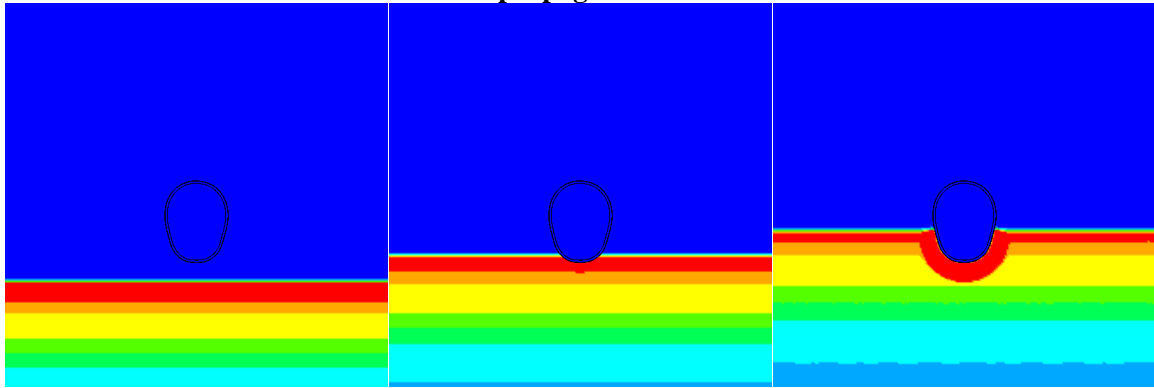


Figure A.18 Effective diploe layer viscoelastic modulus (fractional value relative to quasi-static modulus).

14.7 Simplified plane-strain blast model

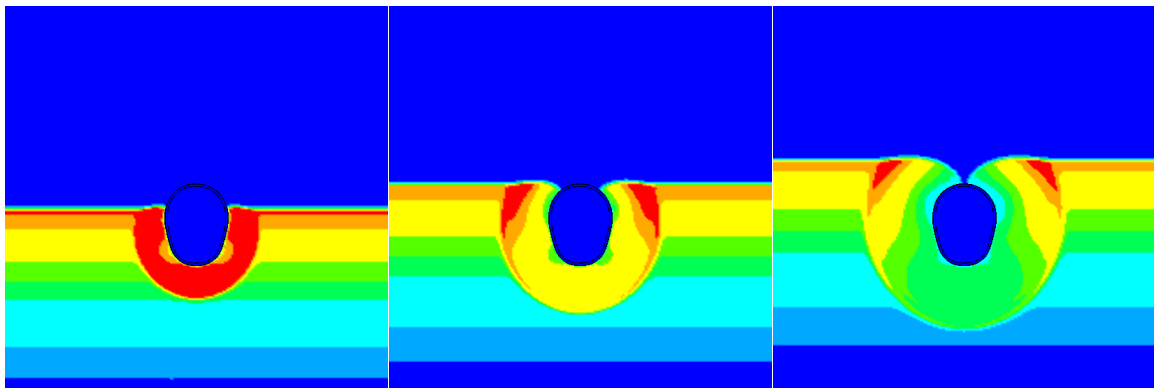
14.7.1 Shock wave propagation in Eulerian air mesh



$t = 0.4$ ms

$t = 0.5$ ms

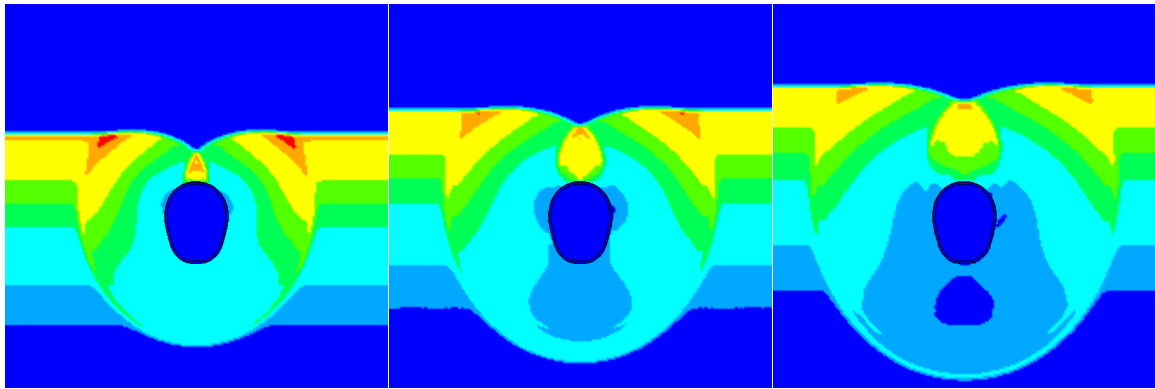
$t = 0.6$ ms



$t = 0.7$ ms

$t = 0.8$ ms

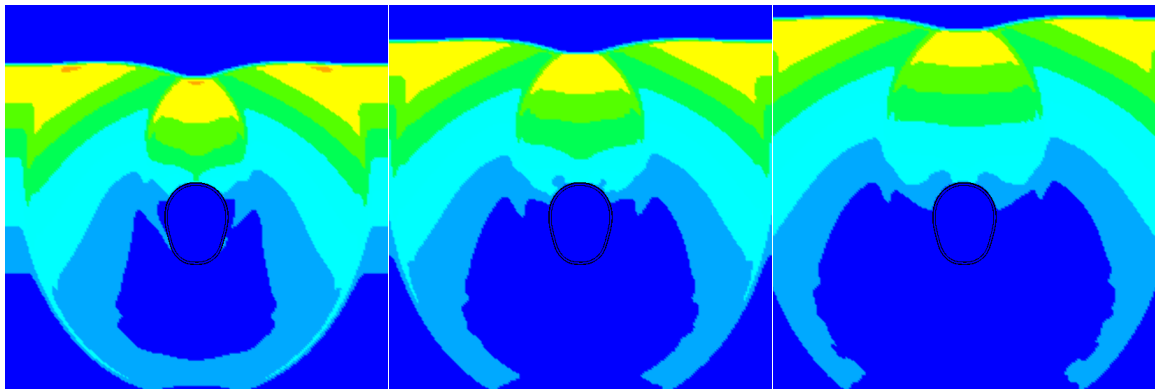
$t = 0.9$ ms



t = 1.0 ms

t = 1.1 ms

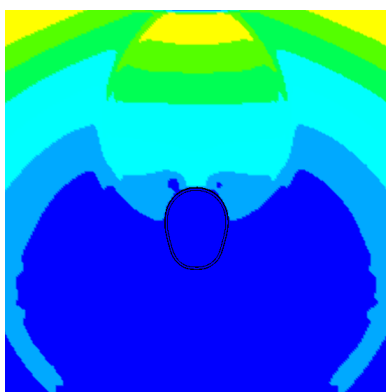
t = 1.2 ms



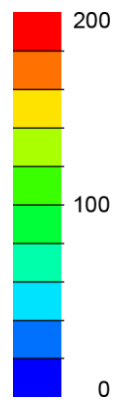
t = 1.3 ms

t = 1.4 ms

t = 1.5 ms



t = 1.6 ms



200 Contours of pressure in Eulerian mesh (kPa).

Pressure in Lagrangian skull-brain mesh is not shown.

100

0

14.7.2 Statistical results

14.7.2.1 Peak pressure

Table A. 33 Case wise spatial distributions (as percentiles) of peak pressure [kPa]

Case	5 th	25 th	50 th	75 th	95 th
Median	234.860	96.293	116.917	166.380	204.693
OCT -	241.236	94.861	127.110	175.597	209.017
OCT +	229.732	96.874	106.963	160.407	200.900
DT -	232.119	97.322	99.889	171.003	201.510
DT +	246.428	96.696	132.973	173.587	215.607
ICT -	237.266	95.748	119.817	169.983	206.377
ICT +	230.579	96.000	108.920	161.643	201.650
DQM -	237.351	99.055	115.363	165.353	208.190
DQM +	231.630	94.577	113.063	166.850	200.527
DVM -	242.613	102.085	116.763	166.990	213.227
DVM +	232.310	95.043	115.143	166.213	201.680
NCNS	240.162	102.288	96.473	176.970	216.507
DEM Q	253.698	98.621	129.263	181.890	224.173
DEM I	244.669	93.775	134.647	175.267	214.443

OCT – Outer cortical thickness; DT – Diploe thickness; ICT – Inner cortical thickness; DQM – Diploe quasi-static modulus; DVM – Diploe viscoelastic modulus; NCNS – No CSF and no scalp; DEM Q – Diploe elastic modulus quasi-static DEM I – Diploe elastic modulus instantaneous

14.7.2.2 Peak Von-Mises stress

Table A. 34 Case wise spatial distributions (as percentiles) of peak Von-Mises stress [kPa]					
Case	5 th	25 th	50 th	75 th	95 th
Median	0.774	1.363	1.827	2.169	2.682
OCT -	0.840	1.456	1.989	2.365	2.792
OCT +	0.724	1.290	1.709	2.017	2.599
DT -	1.265	2.065	2.830	3.322	4.023
DT +	0.657	1.100	1.453	1.672	2.054
ICT -	0.832	1.437	1.961	2.343	2.804
ICT +	0.686	1.243	1.632	1.900	2.523
DQM -	0.784	1.401	1.906	2.286	2.769
DQM +	0.777	1.343	1.769	2.085	2.615
DVM -	0.809	1.401	1.884	2.247	2.766
DVM +	0.759	1.348	1.801	2.140	2.644
NCNS	0.855	1.550	1.953	2.407	3.522
DEM Q	0.878	1.471	2.000	2.399	2.882
DEM I	0.850	1.343	1.764	2.119	2.702

OCT – Outer cortical thickness; DT – Diploe thickness; ICT – Inner cortical thickness; DQM – Diploe quasi-static modulus; DVM – Diploe viscoelastic modulus; NCNS – No CSF and no scalp; DEM Q – Diploe elastic modulus quasi-static DEM I – Diploe elastic modulus instantaneous

14.7.2.3 Peak maximum shear strain

Table A. 35 Case wise spatial distributions (as percentiles) of peak maximum shear strain [%]

Case	5 th	25 th	50 th	75 th	95 th
Median	0.176	0.315	0.434	0.498	0.569
OCT -	0.199	0.344	0.479	0.549	0.630
OCT +	0.158	0.292	0.398	0.456	0.524
DT -	0.314	0.515	0.680	0.787	0.914
DT +	0.140	0.235	0.321	0.373	0.412
ICT -	0.193	0.339	0.473	0.539	0.621
ICT +	0.148	0.276	0.373	0.427	0.500
DQM -	0.181	0.330	0.456	0.525	0.605
DQM +	0.171	0.302	0.412	0.474	0.537
DVM -	0.185	0.322	0.446	0.510	0.589
DVM +	0.172	0.311	0.428	0.493	0.560
NCNS	0.184	0.341	0.436	0.509	0.662
DEM Q	0.199	0.334	0.460	0.528	0.615
DEM I	0.179	0.293	0.390	0.455	0.537

OCT – Outer cortical thickness; DT – Diploe thickness; ICT – Inner cortical thickness; DQM – Diploe quasi-static modulus; DVM – Diploe viscoelastic modulus; NCNS – No CSF and no scalp; DEM Q – Diploe elastic modulus quasi-static DEM I – Diploe elastic modulus instantaneous

14.7.2.4 Peak maximum shear strain rate

Table A. 36 Case wise spatial distributions (as percentiles) of peak maximum shear strain rate [s^{-1}]

Case	5 th	25 th	50 th	75 th	95 th
Median	4.168	5.531	7.777	9.796	15.092
OCT -	4.261	5.914	8.204	10.092	14.878
OCT +	4.074	5.329	7.396	9.489	15.118
DT -	4.539	7.540	10.695	14.133	17.454
DT +	3.919	4.982	7.023	8.633	13.694
ICT -	4.205	5.820	8.120	10.079	15.102
ICT +	4.062	5.245	7.169	9.250	15.158
DQM -	4.138	5.706	7.990	9.865	15.412
DQM +	4.221	5.534	7.764	9.777	15.029
DVM -	4.186	5.662	8.070	10.202	15.888
DVM +	4.155	5.498	7.638	9.675	14.755
NCNS	4.690	7.022	9.699	14.648	27.858
DEM Q	4.458	6.075	8.973	12.349	18.633
DEM I	4.577	6.124	8.650	12.436	17.451

OCT – Outer cortical thickness; DT – Diploe thickness; ICT – Inner cortical thickness; DQM – Diploe quasi-static modulus; DVM – Diploe viscoelastic modulus; NCNS – No CSF and no scalp; DEM Q – Diploe elastic modulus quasi-static DEM I – Diploe elastic modulus instantaneous